Perturbation studies of intrinsic point defects in synthetic diamond

Smith, Hannah Elaine

Perturbation Studies of Intrinsic Point Defects in Synthetic Diamond

Hannah E Smith

A thesis submitted for the degree of Doctor of Philosophy

in the University of London

at

King's College London

Strand, London, United Kingdom WC2R 2LS

July 2004

Abstract

Intrinsic point defects produced in synthetic diamond by electron irradiation have been studied, using optical absorption spectroscopy in the visible and near infrared region. The symmetry and energy level structure of these defects have been probed using isotopic substitution, temperature dependence, annealing and uniaxial stress perturbations. The major focus of this study is the neutral carbon $\langle 001 \rangle$ split interstitial, which is examined in great detail. The absorption features studied are the 1685 and 1859 meV lines due to the interstitial. The isotope shift of the 1859 meV line is measured and identifies it as a local mode of vibration of the interstitial. An energy level doublet split by a few meV, is characterised in the ground state of the interstitial, first through the complementary temperature dependence of the 1685 and 1859 meV lines and then confirmed through a transition induced at 1692 meV under uniaxial stress. Another closely spaced doublet is identified in the excited state through the stress, isotope and temperature dependence of transitions induced at 1864 and 1690 meV under uniaxial stress. These data are fitted quantitatively in terms of the interstitial tunnelling rapidly between equivalent D_2 and equivalent C_{2v} configurations, in its ground and excited states respectively, with their average D_{2d} symmetry observed on the timescale of the optical transitions. Also studied briefly are the neutral vacancy and 3H defects. Finally, the production of neutral $\langle 001 \rangle$ split interstitials by electron irradiation in diamond, is studied as a function of increasing concentrations of single substitutional nitrogen and is found to be dramatically enhanced at high concentrations. The interstitials in this material are highly strained but produce distinctive absorption features which are quantitatively modelled.

Acknowledgements

I would like to thank:

Professor Gordon Davies for continually challenging, supporting and guiding me throughout my undergraduate and postgraduate careers. For his invaluable input into my research, sharing his experience and patiently explaining the same thing many times. Most of all for giving up so much of his valuable time.

Dr Mark Newton for excellent supervision, designing inspiring projects, obtaining samples and setting up experiments expertly. For patiently supporting my professional development and research on every level.

Professor Alison Mainwood for discussions, general guidance and for providing the funding for my work through the EPSRC grant GR/M77826/01.

Professor Alan Collins for sharing his experimental skill, being an effective second supervisor and for helpful discussions and providing additional data for the Nirrad chapter. Also Dr Kostya Iakoubovskii for discussions and providing additional data.

Bill Luckhurst and Alex Conner for repeatedly helping with two person jobs, heavy lifting and fixing things.

Claire Glover, Thomas Graf, Ruth Harding and the rest of the Solid State Group for friendship, encouragement and general support. Dr Karl Johnston for early experimental instruction and for being a good listener and supportive friend.

The scientists of the Diamond Trading Company Research Centre, H. Kanda of NIMS (Japan) and T. R. Anthony of GEC (USA) for providing the samples used in my experimental work.

Chris Kelly, Andy Taylor, Samantha Quinn and Jacques Jones of the Diamond Trading Company Research Centre for invaluable sample preparation and characterisation.
Dr David Fisher of the DTC Research Centre for the kind provision of his one-phonon defect spectra deconvolution program and Alex Smith of KCL for modifications.
The EPSRC for a studentship (grant GR/M77826/01) and the DTC Research Centre for the provision of a CASE award.
My family for doing so much to support and encourage me throughout my education and finally Phil Buisson for his patience, loyalty, endless encouragement and technical support.

Publications

Structure of the self-interstitial in diamond
Hannah E Smith, Gordon Davies, M. E. Newton and H. Kanda
Physical Review B, 69 (2004) 045203

Mapping the energy levels of the self-interstitial in diamond
Hannah E Smith, Gordon Davies, M. E. Newton and H. Kanda
Physica B, 340-342 (2003) 111-115

The energy levels of the self-interstitial in diamond
Hannah E Smith, Gordon Davies, M. E. Newton and H. Kanda
Diamond and Related Materials, 13 (2004) 705-708

Self-interstitial in diamond
Gordon Davies, Hannah Smith and H. Kanda
Physical Review B, 62 (2000) 1528

The findings of chapters 5 and 7 have also been communicated through various oral presentations at: the De Beers Diamond Conferences, (July 2004/3/2); the 22nd International Conference on Defects in Semiconductors, Denmark (July 2003); the Physics of Group IV Semiconductors workshop, Exeter, UK (April 2003); the European Conference on Diamond, Diamond-Like Materials, Carbon Nanotubes, Nitrides and Silicon Carbides, Spain (September 2002). And a poster presentation at the workshop on Surface and bulk defects in CVD diamond films VII, Hasselt, Belgium (March 2002).

Table of Contents

List of Figures

List of Tables

Chapter 1

Introduction

1.1 Carbon Phase

At room temperature and pressure graphite is the thermodynamically stable form of carbon, but because of the high cohesive and solid-state transformation activation energies of carbon, diamond may endure indefinitely under these conditions [4]. Graphite also stubbornly persists at pressures far into the diamond stability region [4], except at very high temperatures. Dissolving the graphite first with the aid of transition metals may help overcome this barrier [5]. For a detailed review of the carbon phase diagram see Bundy et al [4].

The free energies of graphite and diamond are similar at atmospheric pressure, and both differ greatly to that for carbon vapour [4], so the condensation of carbon vapour may be expected to be equally likely to form graphite or diamond. This may allow carbon vapour to condense as diamond under low pressure, metastable conditions, given proper control of the reaction path and the nucleation conditions [4], including the reduction of graphite nucleation. Carbon vapour deposition from a plasma, containing atomic hydrogen as well as carbon vapour and hydrocarbon molecules, can reduce the competition of graphite nuclei allowing only diamond to exist and grow [4].

Synthetic diamonds can be grown from methane by Chemical Vapour Deposition

(CVD) or from graphite (or fine diamond powder) by High Pressure High Temperature (HPHT) synthesis with the addition of a metallic catalyst.

1.1.1 HPHT Growth

Nitrogen atoms readily substitute for carbon atoms during growth, so unless nitrogen getters are used it is grown into the diamond, mostly in dispersed single substitutional form. Diamonds may be grown by the HPHT temperature gradient method with less than 0.1 ppm of nitrogen, through the use of nitrogen getters such as aluminium, titanium and zirconium, (otherwise it is grown in to a concentration of 100-1000 ppm) and with boron incorporated by adding it to the solvent/catalyst [5]. Graphite has a greater solubility in transition metal melts than diamond under 5-6 GPa of pressure at 1300-1400°C, where these diamonds are synthesised [5]. As a result of this growth process, transition metals may also become incorporated into the diamond lattice in the form of point defects [6]. Using diamond powder instead of graphite minimises local decreases in pressure, since there is no conversion of graphite to diamond with the accompanying volume change, this allows stable growth and the production of large high quality diamonds [5]. Burns et al [5] review diamond growth at the De Beers Diamond Research Laboratory by the temperature gradient HPHT method. For another review of growth of gem quality diamonds using the HPHT and CVD processes focusing on the thermodynamics, kinetics of the growth processes and the apparatus see Choudhary et al [7].

1.1.2 CVD Growth

The basic science and technology underlying the chemical vapour deposition of diamond thin films is explained in reference [8]. CVD diamond growth by a variety of methods, nucleation, surface science and the mechanism of metastable growth at low pressure are reviewed by Tong Lee et al [9]. A review of CVD diamond from growth to applications, linking growth parameters to material properties is given by Gicquel et al [10].

Coe et al [11] review the properties of some of the different CVD diamond material grades commercially available, used in optical, thermal and mechanical applications.

1.2 Applications of Diamond

Among other properties, diamond is the hardest known material, has the highest thermal conductivity at room temperature, is transparent over a very wide wavelength range, is the stiffest material, the least compressible and is inert to most chemical reagents [8]. A review of many of the excellent properties and applications of diamond is given by May [8], some of these are listed below to give some indication of why this material is so worth studying.

The extreme hardness of diamond, coupled with its chemical inertness and wear resistance, makes it ideal for use as an abrasive as grit, chemically and mechanically robust coatings and for cutting tools, either through the attachment of grit or CVD diamond coated directly onto the surface of tool-pieces [8]. The one disadvantage that diamond has over other tool materials, is that it cannot be used to cut ferrous materials such as steel since it reacts with iron [8].

Free-standing diamond plates with their high transparency, durability and resistance to thermal shock, are useful for optical components such as infrared (IR) windows for use in harsh environments, since conventional IR materials are brittle and easily damaged [8].

Surface Acoustic Wave (SAW) filters transform radio frequency electronic signals into mechanical vibrations and vice versa and are used in the communications industry [8]. The limiting factor in most current SAW devices is the maximum speed with which signals can propagate through the device, this depends largely upon the speed of sound (the acoustic wave) along the surface of the device material, because the diamond lattice is so stiff, the speed of sound through it is extremely fast [8]. Some companies (such as Sumitomo in Japan) are already exploiting diamond-based SAW filters in commercial mobile phone equipment [8].

Because of its small (maybe even negative) electron affinity, diamond may be an excellent candidate for use in field emission displays [8].

Doped CVD diamond films are useful for electrochemical applications, especially in harsh or corrosive environments [8]. Conducting diamond electrodes, made by boron-doping CVD diamond films, have been found to have a very large potential window in water; a great advantage over other electrode materials which dissociate water at higher electrode potentials [8].

Being chemically inert and composed of carbon, diamond is also bio-compatible [12] and so is most useful for medical and bio-sensing applications where other materials, such as silicon, may prove poisonous or too readily degraded. Diamond may also find a use as a dosimeter for radiation exposure [8].

The outstanding thermal conductivity and high electrical resistivity has led to the development of diamond as a heat spreader for a variety of applications such as multichip modules (MCMs), high power laser diode arrays and power modules [13]. Research has also been done into the deposition of passive diamond layers for thermal management purposes directly within integrated electronic and optoelectronic circuits and microelectromechanical systems (MEMS) [14]. Modern high-power electronic and optoelectronic devices may produce large amounts of heat in a small area, so it is essential to spread the narrow heat flux by placing a layer of high thermal conductivity between the device and heat sink [8]. Diamond has a thermal conductivity that is far superior to copper over a wide temperature range and has the advantage of being an electrical insulator, making it ideal for a variety of thermal management applications such as constituting submounts for integrated circuits.

Strength, durability and very high thermal conductivity are not diamonds only extreme assets, it also boasts high carrier mobility, a large electronic band gap ($\sim$5.5 eV) and a high breakdown field strength, is readily p-type doped and may be n-type doped [12].

1.2.1 Diamond Electronics

Diamond is readily p type doped through the incorporation of Boron [5]. Hall effect measurements have shown that n-type semiconducting homoepitaxial diamond thin films have been grown [15] by microwave plasma CVD, through the addition of phosphine (PH_3) to the growth gas. This strongly influences the optimal growth conditions for diamond [15]. There has been great difficulty in growing n-type diamond because of passivation by the presence of hydrogen, which can be incorporated in large amounts when phosphine is present in the growth gas, or crystalline imperfection in the doped film [15].

The wide band gap of diamond allows the possibility of ultraviolet (UV) lightemitting devices. The successful fabrication of an ultraviolet light emitting diode has been reported, with the use of a diamond pn junction formed from a boron-doped p-type diamond layer and phosphorus-doped n-type diamond layer [16].

High carrier mobility (an improvement over that in polycrystalline CVD diamond and in the best natural diamonds), has been reported for single-crystal plasma-deposited diamond, encouraging research on and the development of diamond for high-performance electronics [17]. The presence of grain-boundaries and point defects impede electronic performance because defect scattering limits carrier mobility, so pure single crystal diamond is required for demanding electronic applications [17]. Chalker [18] gives a comparison of wide band gap semiconductor materials for high temperature electronics.

Advanced electronics involves defect engineering at the atomic level [19]. To control the behaviour of nearly every atom in the active area of a device requires a high degree of understanding of how crystal defects behave and interact [19].

1.2.2 Particle Detectors

The radiation hardness of diamond makes it an ideal material for detector applications in high energy experiments [20]. Behnke et al [20] give the results of one study of the

charge collection properties of CVD diamond, grown and primed under varying conditions. Priming, for example by irradiation of the material, is found to significantly enhance the charge collection properties of diamond films, through the passivation of traps [20]. Identification of electrically active defects (defects producing states in the band gap) incorporated during growth and their correlation to growth and processing parameters, is therefore useful for process control of high quality detector material [20].

High-performance diamond UV detectors have been demonstrated and are now in commercial production [8]. CVD diamond micro strip and pixel radiation sensors have also been fabricated and studied, for use as charged particle tracking detectors in high luminosity experiments, by the RD42 collaboration [21]. A review of these studies is published in reference [21], giving a favourable comparison of the properties of diamond detectors to the equivalent in silicon and reporting on charge collection properties and radiation hardness. A later publication by the same collaboration reported that diamond is roughly an order of magnitude radiation harder than silicon [22]. Radiation damage to CVD diamond by particles mainly consists of vacancies (where a carbon atom is absent from its lattice site) and self-interstitials (carbon atoms occupying interstitial/non-lattice sites). These defects can act as charge carrier traps and the charge collection distance depends upon the presence of such traps [22]. Predicting the long term effects of radiation damage on diamond detectors is therefore important.

1.3 Ion-Implantation

Ion-implantation doping offers the possibility of precise control of dopant concentration and depth, while spatially selective doping is achievable using masking techniques [23]. The tightness of the strong sp3 bonded diamond crystal makes diffusion-doping or doping during HPHT growth very difficult, prompting the use of ion-implantation

and attempts to control its effects, to produce diamond for use as an electronic material [24]. Ion-implantation has found widespread use in the manufacture of semiconductor devices and the technique is well established [23]. Ion-implantation in diamond is complicated since unintended damage defects are created alongside the dopant incorporation, which can give rise to non-doping related electrical conductivity. Appropriate annealing can repair damage (through recombination of vacancies and interstitials) and drive the dopants onto the required lattice sites (usually substitutional) [24] through reactions with vacancies or interstitials. The problem is that diamond is metastable with respect to graphite and so has a tendency to revert to graphite at high temperatures and or doses [23, 24], doping via this method is therefore less straightforward for diamond than for silicon. For reviews of doping diamond films by ion-implantation see Prawer [23] (1995) and Kalish [24] (1997), these references include a description of the CIRA doping technique (Cold Implantation followed by Rapid Annealing). In the introduction of reference [24] some of the electronic properties of diamond are also listed and compared favourably with those in Si and GaAs. In addition to the CIRA technique, pulsed laser annealing of deeply buried ion-implanted layers has been employed to achieve very high annealing temperatures while still preventing graphitization [23].

Aside from doping, damage alone can be useful, various permanent identifying patterns can be fabricated into diamond gemstones by ion implantation using suitable masks [23]. These patterns may only become visible once the implanted diamond is electrostatically charged and dusted with fine powders, since it is possible to select an ion dose which does not impart any visible damage into the gemstone, but only alters the ability of the diamond to hold an electrostatic charge [23]. Implantation with high doses of MeV ions may even be used to created a highly damaged layer at some depth in a diamond, this graphitizes upon thermal annealing and may then be etched away resulting in a novel method for the removal of a thin (maybe relatively large area) diamond layer [23]. The layer will have been relatively undamaged, so the annealing will have served to repair most of this damage, rather than worsen it as

occurs for high levels of damage [23].

Controlling the number and type of defects and dopant profiles is therefore an important part of successful exploitation of the excellent properties of diamond. This provides a driving force for studying these defects, their stability and interactions. Radiation damage products and their evolution with treatment form a significant part of this field.

1.4 Point Defects

Many of the reasons for studying point defects in diamond have already been covered. In addition, there is a considerable difference in monetary value between untreated natural and synthetic or treated natural diamonds. The study of point defects by optical absorption spectroscopy facilitates distinction between these stones; this area of study has recently been reviewed [25].

Like diamond, silicon is an elemental group-IV semiconductor and has the same lattice structure [26]. Much has been learned in silicon about intrinsic defects and their interactions with other defects, due to the ability to grow large single crystals of high chemical and structural perfection and to dope them in a controlled manner allowing systematic study [26]. The presence of the naturally occurring 4.7% abundant ^{29}Si isotope, with nuclear spin I=1/2, has helped considerably with the identification and characterisation of defects using epr, this is not so easy in diamond with only the naturally occurring 1% abundant ^{13}C, I=1/2, isotope [26]. A review of epr in diamond is given by Reynhardt et al [27]. The availability of high quality synthetic single crystal diamonds enriched with ^{13}C, has created the opportunity to determine the structures of intrinsic irradiation damage defects using hyperfine structure in epr [28], this has led to a substantial advancement in our knowledge of point defects in diamond [26] including the recent identification of the isolated self-interstitial [28].

For a review of intrinsic defects in silicon and comparison to diamond see Watkins

[26]. Interstitials and vacancies are both highly mobile well below room temperature in silicon, but are considerably more stable in diamond [26]. The isolated self-interstitial in silicon has not been identified [26].

The structure of the isolated neutral self-interstitial in diamond identified with the epr centre R2, is ⟨001⟩-split ($\mathbf{I}^0_{\langle 001\rangle}$). This was determined [28] through measurement of the angular variation of the line width and ^{13}C hyperfine structure.

The intensities of lines observed in optical absorption at 1685 and 1859 meV correlate with the concentration of R2 observed in epr [28, 29]. These lines also show the same annealing behaviour as R2 [28, 29] identifying them with the self-interstitial. So the isolated neutral self-interstitial in diamond may be identified using both epr and optical absorption spectroscopies.

The calibrations linking the concentrations of damage centres to their optical absorption are known for the vacancy and vacancy-nitrogen centres and for self-interstitials, as well as for nitrogen centres present before irradiation [30]. This means the rates of production of damage may be studied and it is known that the presence of nitrogen impurities plays an important role in the amount and nature of damage produced [30]. The ^{13}C isotope shift in the optical absorption of many radiation damage defects in diamond, which gives information about their configurations, are tabulated in a review by Davies [30]. Diamond was the first semiconductor where samples were studied for which the isotope of the host material had been totally changed, [31] changing the vibrational frequencies of all modes involving the motion of only carbon atoms in the approximate ratio $\sqrt{(12/13)}$ and so allowing the identification of local modes and any impurity content of the defect from which they arise. Vibronic effects are significant at defects in diamond [32], they can be of great importance in understanding the optical properties of defects (e.g. the H3 centre [33]) and their study is well established [32] and will be made use of in this thesis.

It is clear from the last few sections that the fundamental study of radiation damage in diamond, is of potentially substantial importance to the full exploitation of the excellent properties of diamond in a great number of applications. The simplest

and most fundamental primary products of irradiation in diamond are vacancies, where a carbon atom is absent from its lattice site and self-interstitials, carbon atoms occupying interstitial (non-lattice) sites. The production and effect of these defects in diamond is determined by the presence of other defects. Interstitials and vacancies are not just produced by irradiation either, they may occur during growth or be released into the diamond during heat treatment from slip planes, other extended defects or even point defects such as transition metals, which due to their size can lower their energy by occupying two lattice sites instead of one (a semi-divacancy configuration) [34, 35, 36].

To study all these reactions effectively it is necessary to have a detailed understanding of defect structures and stability and know how to identify these fundamental defects, to quantify their concentration and understand how they may be perturbed. The isolated neutral vacancy was identified in diamond in 1973 [37] and has been extensively studied. The isolated neutral interstitial was identified much more recently [28] thanks to improvements in diamond quality, availability and most significantly isotopic control. This is the only isolated self-interstitial identified in a group IV semiconductor and provides a unique opportunity to study a fundamental defect. Before this, interstitials were thought to be mobile in diamond at low temperature and so were assumed not to be present in their isolated form but only as part of complexes. This recent identification casts new light on all sorts of defect processes in diamond, but perturbation studies of the interstitial are incomplete. Understanding how interstitials may be perturbed may help illuminate their role in defect processes. Completing these studies is the main aim of this thesis.

Chapter 2

Theory

In this chapter the physics relevant the studies reported in this thesis is explained. Further information on the theory of optical properties of point defects, including isotopic substitution, uniaxial stress and vibronic coupling is given by Davies [38]. An accessible discussion of absorption by semiconductors is given in chapter 1 of reference [39]. Extensive and quantitative detail of the theory uniaxial stress effects in cubic crystals is given by Mohammed et al [40] and Kaplyanskii [41, 42]. These are acknowledged as the primary sources for this chapter.

2.1 Structure and Mechanisms of Optical Absorption in Diamond

Electromagnetic (em) radiation can be absorbed by a diamond on passing through it. The amount of absorption (its intensity) may be recorded as a function of energy in an absorption spectrum, whose structure is determined by the origin and mechanisms of the absorption within the material. This is the major experimental technique used in this thesis, so some understanding of the origin of structure in diamond absorption spectra is required.

Absorption of EM Radiation

In general, absorption of electromagnetic radiation by a material requires an electric dipole moment. For an electric dipole transition to occur at a molecule or defect it must have the ability to respond to an electric field and to acquire an electric dipole moment [43]. The square of the effective dipole moment of a transition determines the absorption coefficient [44].

Consider the vibrational spectrum. The dipole moment of a defect can be expressed in terms of a differential power series of a change in induced dipole with respect to a change in length[1] [45]. States with different energies are orthogonal with no overlap, so that absorption at a static dipole (first order term in dipole moment) does not occur. A transition may occur between rotational states at a static dipole, but not at a defect in a solid since it is not free to rotate [45]. Absorption at a defect in a crystal must therefore arise from a vibration (second order term in dipole moment) which transforms the states to give a non-zero overlap. The rate of change of the dipole moment of a defect with the displacement in a vibration, therefore determines whether absorption will occur at the defect [45].

All the atoms in an intrinsic diamond molecule are covalently bonded equally to four neighbours. The four bonds at any one atom are a translation of those at its second nearest neighbour but differ in orientation from those at the next atom. In the diamond structure there are then 2 atoms per unit cell, Fig. 2.1. For absorption to occur energy and momentum must be conserved, but for a single phonon (vibrational quantum) these two atoms have displacements and hence polarisations that are exactly equal and opposite and π out of phase [39]. The inversion symmetry of the perfect diamond structure, therefore prevents the creation of an induced dipole moment by a single phonon and for this simple reason of symmetry, there can be no coupling to IR radiation through the creation of just one phonon in intrinsic diamond.

Diamond has a large indirect band gap so there is no electronic excitation (valence band to conduction band) of intrinsic diamond until about 5.5eV. This means optical

[1] for example, the length of the orbit of an electron in and around an absorbing defect

absorption by diamond up to 5.5 eV in the UV, visible and IR regions generally arises from a dipole moment induced in the diamond by a defect. There is some intrinsic absorption due to bulk diamond in the mid IR. This is due to multiple phonon processes which are IR active if they produce charge deformation.

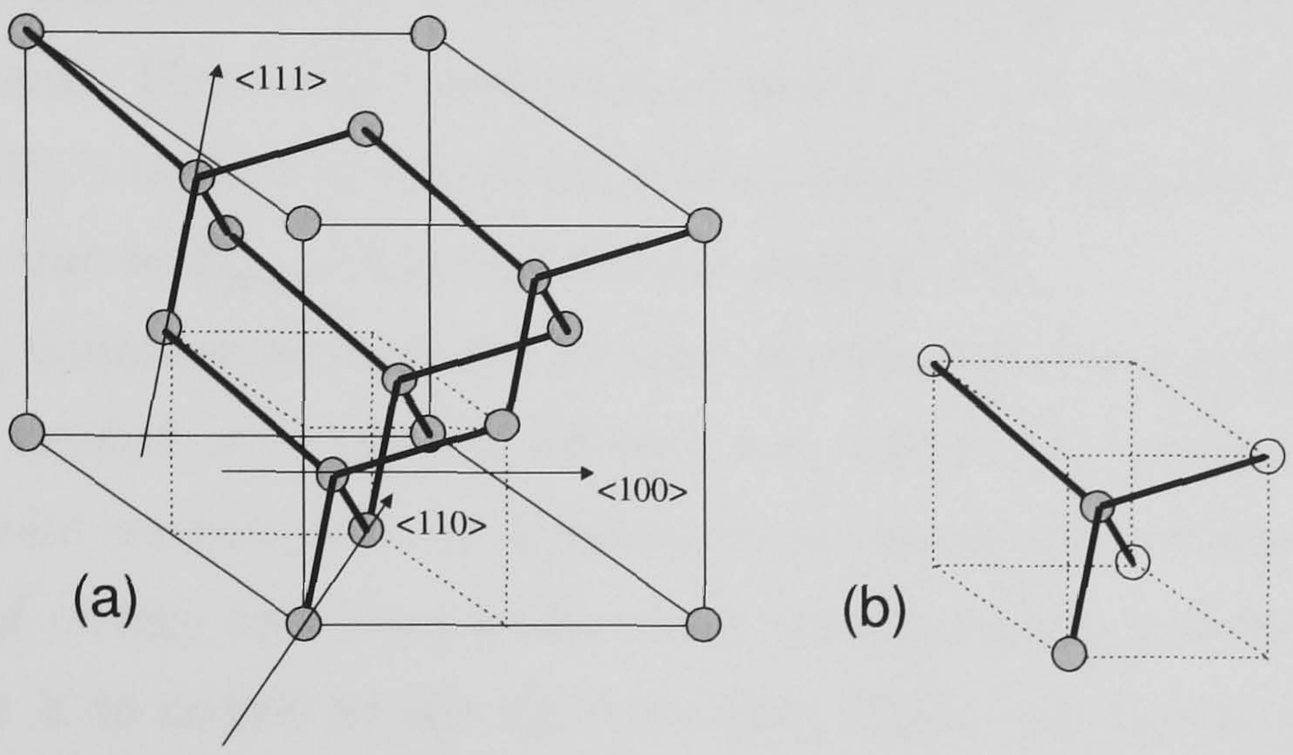

Figure 2.1: (a) Cubic unit cell in diamond = 2 interpenetrating FCC lattices. (b) Filled atoms constitute the unit cell.

One-phonon lattice absorption is forbidden in intrinsic diamond but may be activated by the presence of defects that destroy lattice symmetry. Point defects, which are the subject of this thesis, then manifest optically in the defect-induced one-phonon absorption region and/or through an electronic transition plus vibronic structure.

Defect Induced Absorption

There are two ways in which the presence of a defect in the lattice may induce a dipole moment which results in extrinsic absorption. They may be separated into vibrational and electronic/vibronic.

Electronic states may be introduced into the band gap by the altered electronic configuration at a defect, as it breaks the periodic bonding structure of the lattice allowing a dipole moment with a non-zero second order term. A direct electronic transition may then occur between these defect states within the band gap, absorbing

a photon with quantum, $h\nu$, equal to the energy separation of the states, provided that there is a non-zero rate of change in the dipole moment of the defect in the time it takes to transit between the states, i.e subject to the quantum mechanical constraint, $\langle$ state 1 | dipole moment | state 2 $\rangle \neq 0$ (basically a symmetry constraint). The states are directly coupled by the em radiation and the frequency, ν, of this absorption is then well defined. These sharp absorption features are zero phonon lines (ZPL's). Examples of ZPL's studied in this thesis are the GR1 (1673 meV) due to $\mathbf{V}^0$ and the 1685 meV line due to $\mathbf{I}^0_{\langle 001 \rangle}$, Chapters 4 and 5 respectively.

Vibrations, quantised as phonons, are also important in diamond absorption spectra. Atoms in crystals are vibrating all the time, even at low temperature they will have a zero point motion, but for a vibration to absorb electromagnetic-radiation conservation of energy and momentum must be maintained and there must be a mechanism for it to couple to the em wave [39]. There are two main mechanisms through which this may occur. The first occurs when a vibration is able to couple to electronic defect states adding vibronic structure to electronic absorption induced by the defect [38]. The mechanism of this coupling is discussed in detail later in this section.

The second mechanism is for a vibration at a defect, of the correct symmetry, to induce an oscillating dipole, producing a second order dipole moment. When it can be driven by the oscillating em field of the radiation, this produces absorption that can occur even in the forbidden one-phonon region of the diamond spectrum, since the defect destroys the periodicity of the lattice. Through this mechanism an em wave of the right frequency can directly excite single phonons, hence the lattice absorbs energy.

Lattice Modes and LVM's

If the natural resonance of a defect is greater than the highest allowed lattice frequency - the cutoff - i.e. if the frequency of a mode of vibration of the defect is very different from the lattice frequencies, then the vibration is unable to propagate into the crystal

and is localised in frequency and in space, involving just a few atoms at and around the defect [38]. Local vibrational modes (LVM's) therefore appear in the spectrum as sharp features which are well defined in frequency. They usually occur at light impurities, that is, impurities lighter than carbon and at strongly bound defects since vibrations are heavily damped by strong bonds. LVM's can interact with extended modes of vibration of the crystal and decay by breaking into extended vibrations of lower frequency involving more and more atoms of the crystal [38]. The line width of an LVM is determined by the lifetime of the vibration and lifetimes increase at low temperatures, so the lines narrow as the material is cooled. For this reason some sharp or weak lines may be observed accurately only at low temperature.

If the mass of the defect is greater than the mass of the host lattice, or the defect is weakly bound, then its absorbing modes will be in the phonon continuum of the diamond; all the band modes can then be activated. These effects will be observed as resonances in the bulk absorption spectrum. Heavy impurities in diamond (heavier than carbon) such as nitrogen have these resonant modes in the bulk diamond absorption band. They appear as broad peaks, so for broader resonances at low defect concentrations these features may be relatively hard to observe. The presence of heavy impurities can sometimes be inferred from local vibrational modes of lighter impurities attached to them [46].

Electron-Phonon Coupling

When a transition between electronic states plus a vibration produces absorption, this is called electron-phonon coupling. Strain at a defect may perturb electronic orbitals and change the energy of an electronic state by an amount which, for an isolated electronic state, is linear in the strain. The energy of the state therefore may be reduced by movement of the atoms that causes strain of the appropriate sign, relative to the sign of the change in energy with strain. This will only couple a state if the strain is totally symmetric. As well as lowering the energy of the state continuously with an increasing magnitude of strain, by distorting the orbital component of the

wavefunction, the strain stretches bonds and distorts the surrounding lattice. This results in an increase in elastic energy that varies as the displacement of the atoms squared. The potential surface of this distortion is therefore parabolic in the displacement with the minimum at the equilibrium displacement of strain versus elastic constraint. The result is harmonic motion about this equilibrium point driven by the reduction in energy. Electronic states of a defect may be coupled to vibrations of the centre in this way. The change in energy of a state with strain will vary from state to state, so this equilibrium position may be different in the ground and excited states. Transitions between these states can then occur with the absorption of a photon and simultaneous creation of a phonon.

The consequence of this effect in the absorption spectrum is that a vibronic side-band may be observed to higher energy beyond the zero-phonon line e.g. $\mathbf{V}^0$ Fig. 2.2. This may consist of one-phonon resonances (or optic modes) superimposed on a one-phonon lattice continuum. The required movement of the atoms may also be achieved through a sum of band-modes (allowed lattice vibrations) giving rise to multiple-phonon structure. To higher energy of the one-phonon continuum band, local modes of the defect may give rise to one-phonon side-bands, which may be duplicated to higher energy at intervals equal to the phonon quantum as 2, 3, 4... phonon replicas [38]. These will be sharp lines due to their local nature but their width must be at least equal to the width of the zero-phonon line. Considerable vibronic structure is observed following electronic transitions in the optical absorption spectra of most defects in diamond, since coupling of a vibration to a defect electronic state, often lowers the energy of the state by an amount that is comparable to phonon energies in diamond.

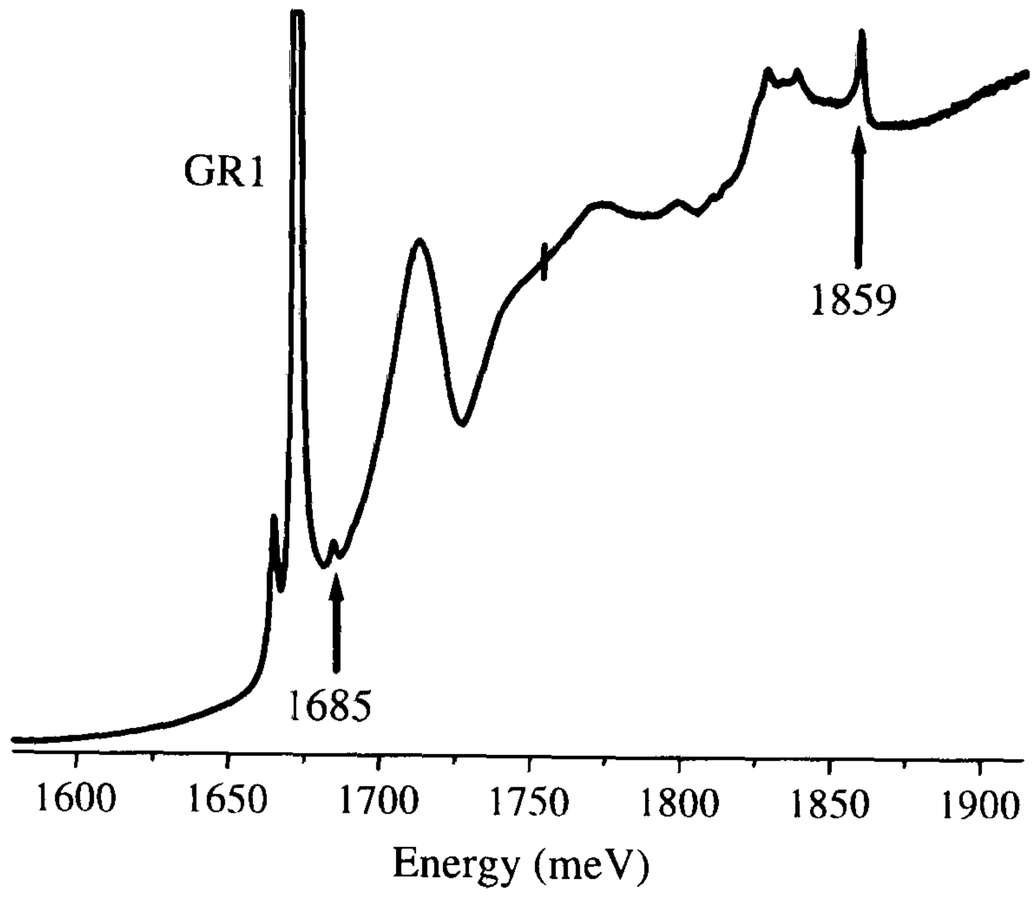

Figure 2.2: The 1685 and 1859 meV lines due to $\mathbf{I}^0_{\langle 001 \rangle}$ superimposed on the vibronic sideband of the GR1 ZPL due to $\mathbf{V}^0$ including two optic modes just to lower energy from the 1859 meV line. Spectrum recorded at 77K.

Distortions

Alternatively a vibration of a different symmetry may distort the defect and couple degenerate or nearly degenerate electronic states to each other. This is a dynamic distortion and occurs when the distortion energy is comparable to the zero-point energy of the vibration. This will be discussed in more detail later and is an important concept in this thesis. The 1859 meV transition at $\mathbf{I}^0_{\langle 001 \rangle}$ is an LVM plus an electronic transition - a one-phonon vibronic sideband. Only a few meV above the phonon cutoff for diamond the vibration involved is just localised at the interstitial and produces a dynamic distortion that strongly couples its states (Section 5.2.2) [47]. The two minima in this case are inversions of one another and vibrations dynamically inverting the defect may be compared to the inversion doubling behaviour of the ammonia molecule.

The Jahn-Teller theorem states that any symmetric, non-linear molecule or point defect with degenerate electronic energy levels will distort in order to lift the orbital

degeneracy and lower its energy. If the temperature is high enough and/or the energy barrier is low enough, rapid re-orientation between equivalent distortions may occur effectively restoring the original symmetry; the electronic degeneracy is then replaced by an equivalent vibronic degeneracy. If the barrier is too high for this to occur, particularly at low temperatures, there will be a static distortion to a lower symmetry with greater orientational degeneracy, separating the degenerate states in energy so lifting the orbital degeneracy. These effects are important at the neutral vacancy $\mathbf{V}^0$.

Stress and Symmetry

The dipole moment induced in the lattice by a defect is directional relative to the high symmetry of its environment and so may have orientational degeneracy. The electronic states of the defect may also be degenerate. Strains interact with the orbital components of electronic states, so the application of uniaxial stress can lift this degeneracy; sharp absorption features are observed to split. This stress dichroism indicates the symmetry of the defect and gives information about the nature of the states and any vibrations involved in the transition. Temperature dependence of the intensity of absorption under an applied stress can identify degeneracy in the ground state, since as they are split, the population in each component will vary with temperature.

Knowing the symmetry and energy level structure of a defect is useful for identifying its physical structure and places constraints on its properties; simple symmetry arguments from group theory can be invaluable in simplifying the quantum mechanics and identifying selection rules. The extent of perturbation with stress can give information about the defect in addition to that given by lines splitting, since the amount of strain per unit stress depends on the elastic constants near the defect. These will be different from elsewhere in the bulk. Vacancies 'soften' the crystal (by making holes in it), whilst interstitials increase the local density and so might be expected to 'harden' the crystal [38]. Generally, larger linear changes in energy per unit stress may be expected from vacancy related centres than from interstitial related centres.

Also, knowing the stress dependence of a centre allows its line-shape and width, perhaps even shift, in a given sample to be used to ascertain the local strains inherent in the sample; some ZPL's are observed to split even in as-grown samples where there is a large amount of internal strain due to defects arising from the growth process.

Isotopes

The behaviour of an absorption line upon changing the carbon isotope can also reveal information about the nature of the transition (as we will see in Section 5.2.2). Also the relative intensities of the components of a line split by the use of mixed isotopes of a given species, can imply the number of equivalent atoms of that species involved in the absorbing defect. In the case of carbon isotope doping this can be indicative of the local symmetry of the defect. The natural abundance of species with higher atomic number may prove useful without the need for doping, for example the correspondence of the intensity ratio of split components of the 1.4 eV line, to the natural abundance ratio of isotopes of Ni, determines that the defect consists of at least one Ni atom [48]. Uniaxial stress perturbations and isotopic substitution are the major experimental tools of this thesis.

Concentrations and Annealing

The intensity of absorption due to a given defect is directly related to the number of such defects which are absorbing. This means measurement of absorption features can be used to calculate the concentration of the defect absorbing and to characterise a sample. Moving the focus of the light in an experiment across a sample provides a test of the homogeneity of defects and inhomogeneity affects the accuracy of bulk concentration determination by optical spectroscopy.

Annealing is a useful technique in identifying different lines that originate at the same defect. The intensity of an absorption line changes proportionately with the concentration of the defect responsible, with annealing. Such changes occur as defects migrate, are trapped, trap other defects or even just get too close to other defects

and are distorted by strain or electrostatic interaction beyond recognition. If lines are associated with the same defect they will not anneal independently e.g. annealing of the 1859 meV line has been correlated with annealing of the R2 epr defect [28] and showed it is not associated with the GR1 [37]. This result was useful in identifying the self-interstitial in optical absorption and the technique is used again in this thesis, in conjunction with uniaxial stress in Chapter 5, to further our understanding of this absorption.

2.2 Defect Symmetry

2.2.1 Symmetry Groups

The symmetry of molecules can be described in terms of distinct point groups. The symmetry of a point defect in a crystal is restricted by the high symmetry of its environment, such that defects may belong to any of only 32 distinct point groups possible in a cubic crystal [49]. Identifying the point group to which a particular defect belongs can help identify its structure, atomic configuration and electronic properties.

Each atom in diamond makes 4 equal, sp^3 hybrid bonds in a tetrahedral arrangement [50] so that the point group of an individual lattice site in the pure crystal is T_d (tetrahedral). The diamond lattice consists of two interpenetrating face centred cubic structures, displaced along the diagonal by one quarter of the diagonal of a unit cell, Fig. 2.1. The environment of any given atom then differs in orientation from the environment of any of the atoms it is bonded to, (while the next nearest neighbours have the same orientation) so that the point group of the bulk crystal is O_h, (all defects must belong to subgroups of this point group). There are therefore two inequivalent orientations, one an inversion of the other, of a defect with T_d symmetry in diamond, such as the neutral vacancy. In general the total number of inequivalent orientations in the lattice, for a defect of a given symmetry, is given by the total number of symmetry elements in the O_h point group of the diamond lattice (which

is 48) divided by the total number of symmetry elements in the point group of the defect. Besides T_d there are the three other point groups of particular importance in the analysis that follows in this thesis, these are D_{2d} (tetragonal), C_{2v} and D_2 (orthorhombic, or rhombic I and rhombic II respectively). The group tables for these four point groups are given in Tables 2.1, 2.2, 2.3 and 2.4. These are standard tables. Summing their symmetry elements (listed in these tables - across the top) gives 24, 8, 4 and 4 respectively. There are therefore 6 inequivalent orientations of centres with tetragonal symmetry and 12 orientations of centres with orthorhombic symmetry. In the D_{2d} (tetragonal) point group these are the three listed in Table 2.6 plus their inversions and for the D_2 (rhombic II) and C_{2v} (rhombic I) point groups, 6 are listed in Tables 2.7 and 2.8 and the remaining 6 are their inversions. The distinct orientations listed in these tables, are those of importance in a uniaxial stress experiment, where they cannot be distinguished from their inversions. Since they simply mirror their counterparts' response to stress this does not matter.

	E	$8C_3$	$3C_2$	$6S_4$	$6\sigma_d$		
A_1	1	1	1	1	1		x^2, y^2, z^2
A_2	1	1	1	-1	-1		
E	2	-1	2	0	0		$(2z^2 - x^2 - y^2, x^2 - y^2)$
T_1	3	0	-1	1	-1	(R_x, R_y, R_z)	
T_2	3	0	-1	-1	1	(x, y, z)	(xy, xz, yz)

Table 2.1: T_d Group Character Table

	E	$2S_4$	C_2	$2C_2'$	$2\sigma_d$		
A_1	1	1	1	1	1		$x^2 + y^2, z^2$
A_2	1	1	1	-1	-1	R_z	
B_1	1	-1	1	1	-1		$x^2 - y^2$
B_2	1	-1	1	-1	1	z	xy
E	2	0	-2	0	0	$(x, y)\,;(R_x, R_y)$	(xz, yz)

Table 2.2: D_{2d} Group Character Table

	E	$C_2(z)$	$C_2(y)$	$C_2(x)$		
A	1	1	1	1		x^2, y^2, z^2
B_1	1	1	-1	-1	z, R_z	xy
B_2	1	-1	1	-1	y, R_y	xz
B_3	1	-1	-1	1	x, R_x	yz

Table 2.3: D_2 Group Character Table

	E	C_2	$\sigma_v(xz)$	$\sigma_v(yz)$		
A_1	1	1	1	1	z	x^2, y^2, z^2
A_2	1	1	-1	-1	R_z	xy
B_1	1	-1	1	-1	x, R_y	xz
B_2	1	-1	-1	1	y, R_x	yz

Table 2.4: C_{2v} Group Character Table

The relevant symmetry elements and their definitions are listed in the following table:

E	Identity transformation.
Primary axis	Axis with highest symmetry.
C_2	180° rotation (2 fold) axis.
S_4	90° rotation and inversion (4 fold) axis.
σ_v	Vertical reflection (plane contains primary axis and C_2 axis.).
σ_d	Diagonal reflection (plane contains primary axis diagonal to 2 C_2 axes).
Prime	Distinguish inequivalent operations of the same type.

Table 2.5: Symmetry elements and definitions.

2.2.2 Point Groups and Symmetry Operations Related to the Atomic Configuration of a Defect

An ⟨001⟩-split interstitial consists of two atoms (the principal atoms) sharing a lattice site split and aligned along ⟨001⟩, Fig. 2.3.

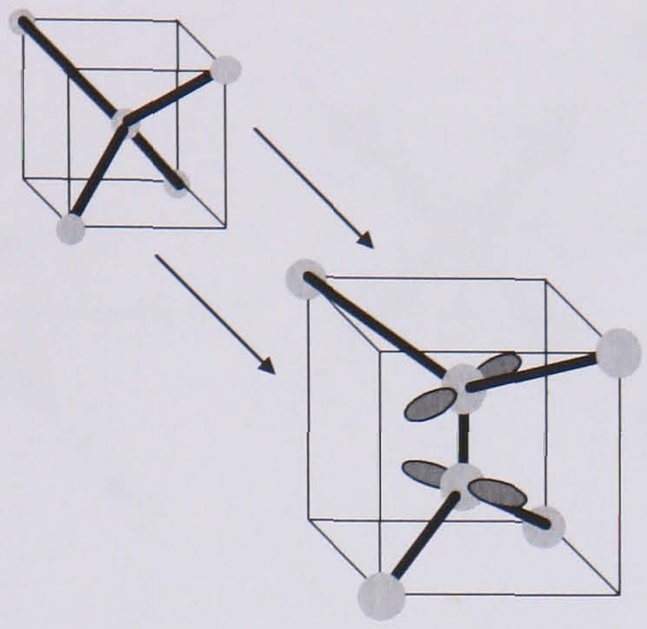

Figure 2.3: An ⟨001⟩-split self-interstitial: two carbon atoms sharing a lattice site.

A defect with D_{2d} symmetry has a C_2 rotation axis as its principal z axis. For an ⟨001⟩ split interstitial with D_{2d} symmetry, this would be the ⟨001⟩ axis. It is then convenient to take x and y along ⟨100⟩ and ⟨010⟩ respectively. In the D_{2d} point group there are also 2 S_4 improper rotation axes (rotation plus inversion), for $\mathbf{I}^0_{\langle 001\rangle}$ these are also the ⟨001⟩ axis. An ⟨001⟩-split interstitial can have this symmetry operation provided: the four atoms to which the principal atoms are bonded, are at equal distances from and make the same angle with, the principal atom to which they bond. This means that, viewing down the ⟨001⟩ direction, these four atoms form the corners of a square (Fig. 2.4) and are equivalent under a (4 fold) 90° rotation and inversion. Other consequences of this high symmetry are two 2-fold rotation axes x and y, Fig. 2.4, these are the two C_2 axes (Table 2.2) and 2 reflection planes along the diagonals of the square ($2\sigma_d$, Table 2.2), Fig. 2.4.

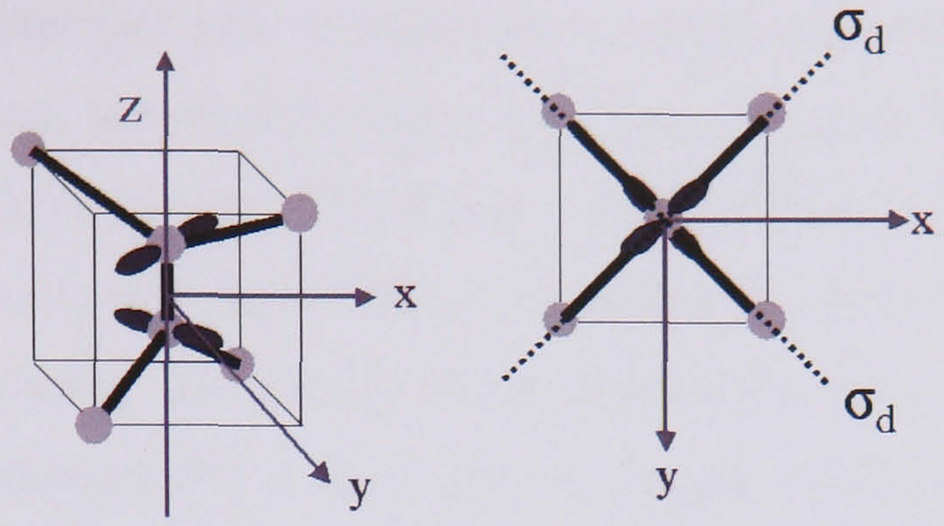

Figure 2.4: An ⟨001⟩-split interstitial with D_{2d} symmetry from the side and end on.

If the symmetry is lowered to D_2 the square becomes a rectangle, the reflection planes are lost and the x and y C_2 rotation axes become inequivalent, Fig. 2.5. The 4 fold improper rotation also breaks down since a rectangle does not have 4 fold rotational symmetry. The symmetry operations that make up the D_2 point group are then C_2^x, C_2^y, C_2^z (Table 2.3). This inequivalence of the x and y dimensions means there are now 2 distinct D_2 centres for each parent D_{2d} centre leading to the 12 possible orientations for D_2 determined previously compared to the 6 for D_{2d}. It is still convenient to use the crystal axes and to choose x, y and z to make a right-handed set.

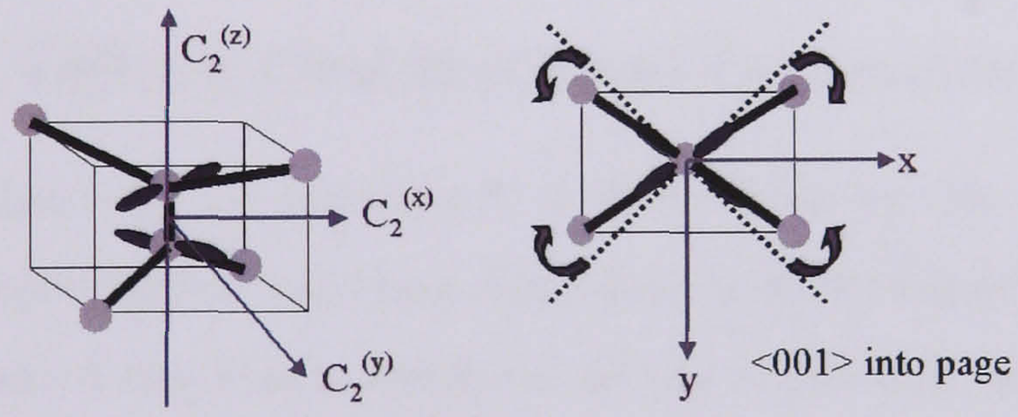

Figure 2.5: An ⟨001⟩-split interstitial with D_2 symmetry from the side and end on.

Alternately, if the symmetry is lowered to C_{2v} from D_{2d}, the square becomes a rhombus, Fig. 2.6, the angles and lengths of the bonds between the principal and outer atoms now differ from one principal atom to the other. However, the two bonds to outer atoms on each of the principal atoms do retain the same length and make the

same angle to the principal axis as each other, so the reflection planes are maintained although inequivalent, see σ_v(xz) and σ_v(yz) Fig. 2.6 and Table 2.4. Note that, for convenience in this point group, the x and y axes in this point group are along ⟨110⟩ type directions (the z is still along ⟨001⟩) compared to the ⟨100⟩ type directions in the D_{2d} and D_2 point groups. The bonds above and below the xy plane are now different so a 180° rotation around the x or y axes no longer returns the same configuration; as a result, with the exception of the principal axis, the C_2 axes are lost and so is the improper rotation axis. The longer diagonal of the rhombus can be along either the x or the y axis, so again there are two inequivalent centres for each parent D_{2d} centre.

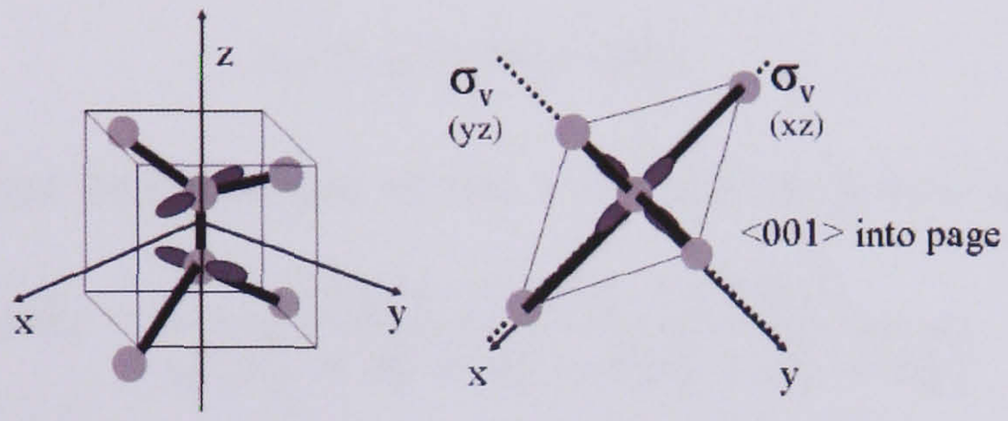

Figure 2.6: An ⟨001⟩-split interstitial with C_{2v} symmetry from the side and end on.

2.2.3 Uniaxial Stress Perturbations of Non-Degenerate States: Lifting Orientational Degeneracy

Non-degenerate states may be perturbed to first order by the application of stress. The effect of the perturbation on the transitions is determined by the symmetry of the perturbation and of the states involved in the transition and is small compared to the energy of the transition. The symmetry of the perturbation is determined by the direction of stress relative to the orientation of the defect, so uniaxial stress can lift the orientational degeneracy of the centres.

The application of stress along the crystal axes cannot lift the orientational degeneracy of a T_d centre, such as $\mathbf{V}^0$, only the electronic degeneracy; this is discussed in the next section. It can however, lift the orientational degeneracy of tetragonal and orthorhombic centres such as $\mathbf{I}^0_{\langle 001\rangle}$ and 3H studied in this thesis. The applied strains

are much smaller than the typical zero point motions of an atom but are generally sufficient in diamond to produce measurable shifts of the order of meV.

Electronic dipole transitions occur when the electric field vector of the light has a component parallel to the axis of the electric dipole. In D_{2d} and D_2, this is the z direction. In C_{2v} it can be the z or the x/y direction, as will be shown later for a statically distorted $\mathbf{I}^0_{\langle 001\rangle}$ and the 3H defect respectively. The use of a polariser can therefore distinguish between the effects of stress on centres with different orientations relative to that stress and be used to identify the orientation of the dipole of a centre.

The stress tensor components are determined by;

$$s_{ij} = |s| cos\theta_i . cos\theta_j \tag{2.1}$$

where i and j are some combination of the local axes x, y or z of the defect and

$$cos\theta_a = \frac{(s_X a_X + s_Y a_Y + s_Z a_Z)}{\sqrt{(s_X^2 + s_Y^2 + s_Z^2)}\sqrt{(a_X^2 + a_Y^2 + a_Z^2)}} \tag{2.2}$$

where θ_a = angle between the applied stress $\bar{s} = (s_X, s_Y, s_Z)$ and the local axis a of the defect oriented along $\bar{a} = (a_X, a_Y, a_Z)$ and X, Y, Z are the crystal axes [100], [010] and [001].

The perturbation of the energy of a state as a function of stress can be written down for each symmetry group from their group Tables 2.1, 2.2, 2.3 and 2.4 in terms of electronic operators and stress tensor components, as follows:

$$\begin{aligned} \Delta T_d: \quad H_s = {} & \hat{a_1}\left(s_{xx} + s_{yy} + s_{zz}\right) + \hat{e_\theta}\left(2s_{zz} - s_{xx} - s_{yy}\right) \\ & + \sqrt{2}\hat{e_\epsilon}\left(s_{xx} - s_{yy}\right) + \hat{t_2} s_{yz} + \hat{t_2'} s_{zx} + \hat{t_2''} s_{xy} \end{aligned} \tag{2.3}$$

$$\begin{aligned} \Delta D_{2d}: \quad H_s = {} & \widehat{a_1} s_{zz} + \widehat{a_1'}\left(s_{xx} + s_{yy}\right) + \widehat{b_1}\left(s_{xx} - s_{yy}\right) \\ & + \widehat{b_2} s_{xy} + \widehat{e_x} s_{yz} + \widehat{e_y} s_{xz} \end{aligned} \tag{2.4}$$

$$\Delta D_2: \quad H_s = \widehat{a_1} s_{zz} + \widehat{a_1'} s_{xx} + \widehat{a_1''} s_{yy} + \widehat{b_1} s_{xy} + \widehat{b_2} s_{xz} + \widehat{b_3} s_{yz} \tag{2.5}$$

$$\Delta C_{2v}: \quad H_s = \widehat{a_1} s_{zz} + \widehat{a_1'} s_{xx} + \widehat{a_1''} s_{yy} + \widehat{a_2} s_{xy} + \widehat{b_1} s_{xz} + \widehat{b_2} s_{yz} \tag{2.6}$$

The a's and b's are electronic operators that transform the states of the defect as indicated by the letter and subscript (e.g. $\widehat{a_1}$, $\widehat{a_1'}$ and $\widehat{a_1''}$ transform as A_1 while $\widehat{b_1}$ transforms as B_1 and so on), a prime indicates a different transformation of the same symmetry. The x, y and z refer to the local axes of the orientation of defect on which the perturbation H_s acts and their relation to the crystal axes is listed in Tables 2.6, 2.7 and 2.8 for each distinguishable orientation in the given point group. Note that for the first two point groups these are all some combination of the crystal axes [100], [010] and [001], while for C_{2v}, x and y are directed along $\langle 110 \rangle$ type directions.

	Axis Orientation		
Defect \ Local Axis	x	y	z
1	100	010	001
2	010	001	100
3	001	100	010

Table 2.6: D_{2d} Orientations

	Axis Orientation		
Defect \ Local Axis	x	y	z
1	100	010	001
2	010	100	$00\bar{1}$
3	010	001	100
4	001	010	$\bar{1}00$
5	001	100	010
6	100	001	$0\bar{1}0$

Table 2.7: D_2 Orientations

Defect \ Local Axis	Axis Orientation		
	x	y	z
1	110	$\bar{1}10$	001
2	$\bar{1}10$	110	$00\bar{1}$
3	011	$0\bar{1}1$	100
4	$01\bar{1}$	$0\bar{1}\bar{1}$	$\bar{1}00$
5	101	$10\bar{1}$	010
6	$\bar{1}01$	$\bar{1}0\bar{1}$	$0\bar{1}0$

Table 2.8: C_{2v} Orientations

The electronic operators operate on the states of the defect according to symmetry rules laid out in Tables 2.10, 2.11, 2.12 and 2.13 given in the next section. The electric dipole operator transforms as B_2(z) in D_{2d}, B_1(z) in D_2 and A_1(z) or B_{1or2}(x or y) in C_{2v} for $\langle 001 \rangle$ and $\langle 110 \rangle$ type dipoles respectively - see Tables 2.2, 2.3 and 2.4. For a transition between two states of a defect to be dipole allowed, the product of their symmetries with the symmetry of the dipole must be totally symmetric i.e. transform as A_1, so that $\langle \text{symmetry}_{ground} | \text{dipole operator} | \text{symmetry}_{excited} \rangle = A_1$ according to the product rules laid out in Tables 2.10, 2.11, 2.12 and 2.13. So for example, a B_1 to A_2 transition is dipole allowed in the D_{2d} point group while a B_1 to B_2 transition is forbidden.

The quantum mechanical constraints that determine the transitions which may occur between states, essentially boil down to these symmetry requirements and may be simply determined through the use of group theory. However, while group theory can determine if a term must be zero it can not determine how large a non-zero term will be, so if a transition is not observed this doesn't mean it is not allowed.

When states interact under stress and are mixed into each other, these symmetry rules can have implications for which transitions occur/are observed at the perturbed defect and their relative probabilities/intensities. These implications are worked through in some detail in the next section.

2.2.4 Interactions of Degenerate and Near Degenerate States Under Symmetry Lowering Transformations: Lifting Electronic Degeneracy

The electrostatic field of the diamond crystal quenches orbital angular momentum so that the maximum orbital degeneracy is three in T_d, two in D_{2d} and C_{3v} and one in other subgroups of T_d [51]. Defects with tetrahedral T_d symmetry therefore have orientational degeneracy that can not be lifted by deforming along crystal axes and electronic degeneracy that can, (Ref. [40], p38). Defects with trigonal or tetragonal symmetry can display stress effects due to both orientational and electronic degeneracy. Defects with lower symmetry can only possess non-degenerate states, but due to their low symmetry may have considerable orientational degeneracy.

In the Mulliken system of notation A and B electronic states are non-degenerate while E and T states are doubly and triply degenerate respectively [51]. If the state is left invariant under a C_n rotation about the principal n-fold axis A is used, if it changes sign B is used. If the state is unchanged by a 180° rotation perpendicular to the principal axis the subscript is 1 and if it changes sign the subscript is 2 [52]. A_1 is therefore totally symmetric.

States can interact under perturbations of the right symmetry governed by the the rules of Tables 2.10, 2.11, 2.12 and 2.13. The symmetry of the perturbation giving rise to the interaction therefore reveals information about the symmetry of the states which are interacting. The strength of the interaction falls off as the square of the initial energy separation of the states, so only the components of degenerate and near-degenerate states will interact appreciably. States referred to as near-degenerate in this thesis are singlet states separated by a few meV.

For a doubly degenerate state (or two nearly degenerate states) the stress dependent perturbed hamiltonian may be written:

	ψ_1	ψ_2
ψ_1	$\langle \psi_1 \mid H_s \mid \psi_1 \rangle$	$\langle \psi_1 \mid H_s \mid \psi_2 \rangle$
ψ_2	$\langle \psi_2 \mid H_s \mid \psi_1 \rangle$	$\langle \psi_2 \mid H_s \mid \psi_2 \rangle$

Table 2.9: States 1 and 2 interacting under a static stress perturbation H_s.

where the H_s are given by Equations 2.3 to 2.6 and $\langle \psi_1 \mid H_s \mid \psi_2 \rangle = \langle \psi_2 \mid H_s \mid \psi_1 \rangle$ since the wavefunctions are real and hermitian. For a triply degenerate (T) state, (or a doubly degenerate state with a third state nearby) this is simply extended to a 3x3 matrix. Interactions between the states appear in the off-diagonal so that finding the determinant gives a perturbed energy that is quadratic (or higher) in the stress. Any curvature in the shift rate of lines under stress is therefore an indication of interacting states.

The sign of the quadratic is plus for the upper state and minus for the lower state since states repel when they interact under a perturbation, increasing their separation. States a and b (including when a=b) will only interact under a given symmetry of perturbation if $\langle \psi_a \mid H_s \mid \psi_b \rangle$ is totally symmetric, i.e. it transforms as A_1, according to the product rules, (for the point groups of interest here these are shown in Tables 2.10, 2.11, 2.12 and 2.13).

	A_1	A_2	E	T_1	T_2
A_1	A_1	A_2	E	T_1	T_2
A_2		A_1	E	T_2	T_1
E			$A_1 + [A_2] + E$	$T_1 + T_2$	$T_1 + T_2$
T_1				$A_1 + E + [T_1] + T_2$	$A_2 + E + T_1 + T_2$
T_2					$A_1 + E + [T_1] + T_2$

Table 2.10: T_d Products

	A_1	A_2	B_1	B_2	E
A_1	A_1	A_2	B_1	B_2	E
A_2		A_1	B_2	B_1	E
B_1			A_1	A_2	E
B_2				A_1	E
E					$A_1 + [A_2] + B_1 + B_2$

Table 2.11: D_{2d} Products

	A	B_1	B_2	B_3
A	A	B_1	B_2	B_3
B_1		A	B_3	B_2
B_2			A	B_1
B_3				A

Table 2.12: D_2 Products

	A_1	A_2	B_1	B_2	E_1	E_2
A_1	A_1	A_2	B_1	B_2	E_1	E_2
A_2		A_1	B_2	B_1	E_1	E_2
B_1			A_1	A_2	E_2	E_1
B_2				A_1	E_2	E_1
E_1					$A_1 + [A_2] + E_2$	$B_1 + B_2 + E_1$
E_2						$A_1 + [A_2] + E_1$

Table 2.13: C_{2v} Products

When states interact under stress they are mixed into each other. This means that previously forbidden transitions may be induced and the intensity of absorption lines may vary, as the transition probabilities vary with stress. These effects can be quantified. Consider two unperturbed states ψ_a and ψ_b, ΔE apart ($\Delta E = 0$ for a doubly degenerate state) with energies E_a and E_b such that $\Delta E = E_b - E_a$. If H_0 is the unperturbed Hamiltonian then:

$$H_0\psi_a = E_a\psi_a$$
$$H_0\psi_b = E_b\psi_b \tag{2.7}$$

For a stress perturbed Hamiltonian H where $H = H_0 + H_s$:

$$H\Psi_- = (E_a + E_-)\,\Psi_-$$
$$H\Psi_+ = (E_b + E_+)\,\Psi_+ \tag{2.8}$$

so that:

$$H_s\Psi_- = E_-\Psi_-$$
$$H_s\Psi_+ = E_+\Psi_+ \tag{2.9}$$

Under the perturbation H_s the original states may be mixed into each other such that:

$$\Psi_- = a^-\psi_a + b^-\psi_b$$
$$\Psi_+ = a^+\psi_a + b^+\psi_b \tag{2.10}$$

then from Equations 2.9 and 2.10 and Table 2.9:

$$\begin{pmatrix} \alpha - E & \gamma \\ \gamma & \beta + \Delta E - E \end{pmatrix} \begin{pmatrix} a \\ b \end{pmatrix} = 0 \tag{2.11}$$

and E_+ and E_- are the $\pm$ solutions of the quadratic:

$$\cdot \qquad \begin{vmatrix} \alpha - E & \gamma \\ \gamma & \beta + \Delta E - E \end{vmatrix} = 0 \tag{2.12}$$

and α, β and γ are stress dependent parameters. Since:

$$\int dr\Psi_+^*\Psi_+ = \int dr\Psi_-^*\Psi_- = 1$$

and:

$$\int dr\Psi_+^*\Psi_- = \int dr\Psi_-^*\Psi_+ = 0 \tag{2.13}$$

the values of the constants a and b are related. The relation can be written in terms of sin and cos of a single parameter θ:

$$\begin{aligned} a^- &= \cos\theta \quad & b^- &= \sin\theta \\ a^+ &= -\sin\theta \quad & b^+ &= \cos\theta \end{aligned} \tag{2.14}$$

From the Eqn. 2.12:

$$E_{\pm} = \frac{1}{2}\left(\alpha + \beta + \Delta E\right) \pm \frac{1}{2}\sqrt{\left(\beta + \Delta E - \alpha\right)^2 + 4\gamma^2} \tag{2.15}$$

and from Equations 2.11and 2.14:

$$\begin{aligned} E_+ \Rightarrow (\alpha - E_+)\cos\theta + \gamma\sin\theta = 0 \quad (A) \\ \gamma\cos\theta + (\beta + \Delta E - E_+)\sin\theta = 0 \quad (B) \\ E_- \Rightarrow (\gamma - E_-)(-\sin\theta) + \gamma\cos\theta = 0 \quad (C) \\ \gamma(-\sin\theta) + (\beta + \Delta E - E_-)\cos\theta = 0 \quad (D) \end{aligned} \tag{2.16}$$

Then multiplying A and C by sin and cos respectively and adding them:

$$(A)\sin\theta + (C)\cos\theta \tag{2.17}$$

or by multiplying B and D by cos and sin respectively and adding them:

$$(B)\cos\theta + (D)\sin\theta \tag{2.18}$$

and substituting for $E_{\pm}$ from Eqn. 2.15 gives:

$$\tan(2\theta) = \frac{2\gamma}{\alpha - \beta - \Delta E} \tag{2.19}$$

then:

$$\begin{aligned} \cos^2\theta &= \frac{1 - 1/\sqrt{\tan^2(2\theta) + 1}}{2} \\ \left(1 - \cos^2\theta\right) &= \frac{1 + 1/\sqrt{\tan^2(2\theta) + 1}}{2} \end{aligned} \tag{2.20}$$

An optical transition between two states of a defect is a perturbation that varies with time resulting from the effect of the electric field of the light on an electron associated with the defect. The electric field is constant over the defect at any given instant, since the wavelength of the light is much larger than the dimensions of the electronic orbitals. The perturbation produces a change, ΔV, in the potential energy of the electron. This is the work done by the electron changing its orbital, in moving

from the initial to the final state under the influence of the perturbing field. If the electric field is polarised along the z axis then, since work done is force times distance, $\Delta V =$ (electric field)ez where e is the electronic charge. Assuming the quantum of energy provided equals the separation of the states the probability, T, of an electric dipole transition from a perturbed state Ψ to a state c is given by:

$$\begin{aligned} T &= |\int dr \Psi \Delta V \psi_c|^2 \\ &= |\int dr\,(a\psi_a + b\psi_b)\,\Delta V \psi_c|^2 \\ &= |\,a\int dr \psi_a \Delta V \psi_c + b\int dr \psi_b \Delta V \psi_c\,|^2 \end{aligned} \tag{2.21}$$

If transitions between a and c are allowed without an applied stress, while transitions between b and c are forbidden then:

$$\int dr \psi_b \Delta V \psi_c = 0 \tag{2.22}$$

and:

$$\begin{aligned} T &= |a\int dr \psi_a \Delta V \psi_c|^2 \\ &= (a)^2\, T_{ac} \end{aligned} \tag{2.23}$$

From Equations 2.14 and 2.23 the probabilities, T_{-c} and T_{+c} of a transition from Ψ_- to ψ_c and from Ψ_+ to ψ_c at the perturbed defect are $(a^-)^2 = \cos^2\theta$ and $(a^+)^2 = (1-\cos^2\theta)$ respectively, times the probability, T_{ac}, at the unperturbed defect, where $\cos^2\theta$ and $(1-\cos^2\theta)$ are determined by Equation 2.20. A transition that is forbidden at zero stress then becomes allowed as the states are mixed under stress and will appear, starting at an energy shifted from the energy of the original transition by ΔE. This induced transition will then shift and increase in intensity with increasing stress as more probability is transferred.

The absorption line intensity is proportional to the transition probability, so the value of $\cos^2\theta$ is used to fit the fall in line intensity for the original transition and rise in intensity of the induced line as a function of stress, quantitatively, in terms of the same parameters ΔE, α, β and γ which also fit the energy shift rates, E_+ and E_-.

Temperature Dependence of Line Intensity under Stress.

The absorption line intensity may also depend on the temperature. When there is a state near in energy to the ground state (a few meV above) it may be thermally populated except at very low temperature, to an extent determined by a Boltzmann factor, which depends exponentially on the inverse of the energy separation, ΔE, of the states. The intensity of a line is determined by the population in the ground state of the transition as well as mixing under stress and so is dependent on and will vary with temperature. If the ground state of the transition is not the ground state of the defect it will de-populate at low temperature according to a Boltzmann distribution and thc intensity of the line will fall accordingly. The rate at which this occurs will be quantified later in this thesis, when it is required. The ground state will populate with decreasing temperature at the same rate. So transitions from the two states will display complementary behaviour. Since this temperature dependence is a function of ΔE this rate increases exponentially with increasing separation of the states. States of different symmetry respond differently to stress so applying stress is likely to split degenerate states or change the separation of nearly degenerate states. Temperature dependence of the intensity of stress split components of a line(s) is therefore an indication of a degenerate ground state. This may be used to identify the initial state of a transition and must be taken into account when interpreting component intensity variations with stress. Interactions in the excited states of a defect will give rise to changes in the relative line intensity, of the stress split components, that are entirely determined by .the magnitude of the stress applied and will not vary with the temperature.

2.3 Vibrational Coupling of Electronic States

A vibration is like a dynamic strain. So, a vibration of the right symmetry can perturb and couple the states of a defect in the same way as described in the last section for a static perturbation. The instantaneous strains produced at a defect by a vibration are

much greater than the strain that can be applied during a uniaxial stress experiment so states interact much more strongly and states with a greater energy separation are able to interact.

The Born-Oppenheimer approximation states that the total wavefunction for a molecule or defect may be factorised into an electronic part and a vibrational part. In general the total wavefunction is not known and for all but the simplest molecules (diamond doesn't qualify) may be excessively complicated. So this approximation is useful since it allows the derivation of important physical properties. The approximation is reasonable since the nuclei in a molecule are stationary in comparison to the electrons, which go through their orbits many times before the nuclei have moved appreciably, due to their difference in mass. That is: the electrons arrange themselves instantaneously around the nuclei.

Starting with an undistorted defect, with unperturbed electronic states 1 and 2, the vibronic progressions of these states can be written down as the Born-Oppenheimer products of their electronic wavefunctions $\phi_1(r)$ and $\phi_2(r)$ in co-ordinate r and vibrational parts $\chi_n(Q)$ and $\chi_p(Q)$ respectively, in co-ordinate Q with vibrational quanta n and p (number of phonons), see Fig. 2.7. In this uncoupled configuration where the vibrations are harmonic, the energy eigenvalues are:

$$E_n = (n + 1/2)\,\hbar\omega \tag{2.24}$$

and:

$$E_p = E_0 + (p + 1/2)\,\hbar\omega \tag{2.25}$$

for eigenstates $\phi_1(r)\,\chi_n(Q)$ and $\phi_2(r)\,\chi_p(Q)$ respectively, where E_0 is the energy separation of the uncoupled states 1 and 2.

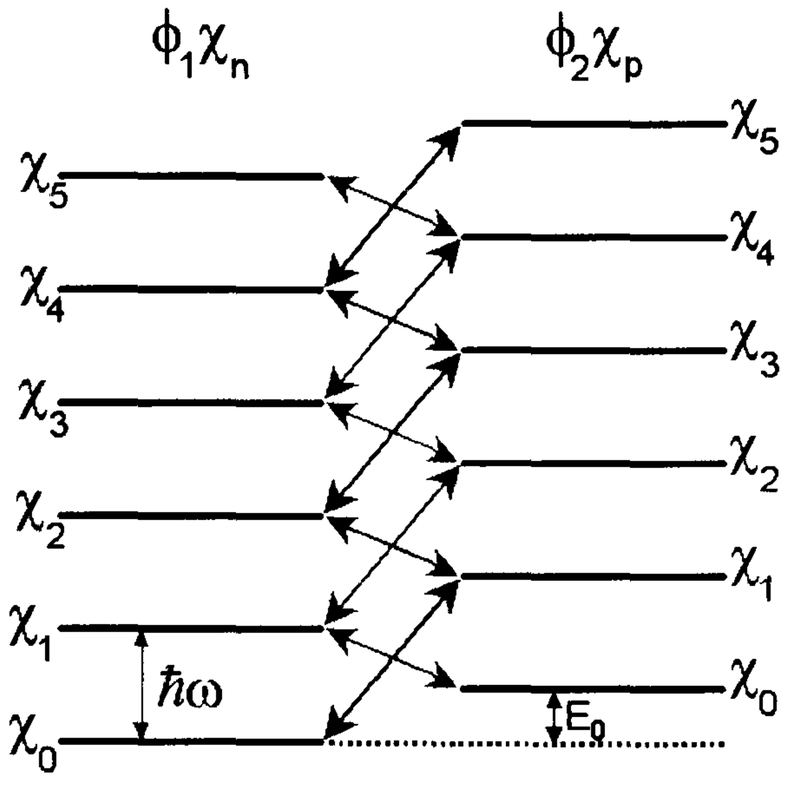

Figure 2.7: Schematic showing the coupling of the vibronic progressions of two electronic states. Arrows indicate which states couple to each other. Shown for $E_0 < \hbar\omega$.

Assuming that the states do not couple to themselves but only to each other, linear coupling of the states in the co-ordinate Q, $\hat{c}Q$, can then be described by the following integrals:

$$\begin{aligned} \int dr\phi_1^*(r)\,\hat{c}\phi_2(r) &= c \neq 0 \\ \int dr\phi_1^*(r)\,\hat{c}\phi_1(r) &= \int dr\phi_2^*(r)\,\hat{c}\phi_2(r) = 0 \end{aligned} \tag{2.26}$$

where c represents the strength of the coupling. Further, because the coupling is linear, states with n vibrational quanta will only be coupled to states with $p = n \pm 1$ vibrational quanta, Figure 2.7. This is because the progression of vibrational states goes as: even function, odd function, even function, odd function and so on, while c is an odd function and the product $\chi_n c\chi_p$ must be an even function for $\int \chi_n c\chi_p$ to be non-zero. The coupling is then:

$$\begin{aligned} \int drdQ\chi_n^*(Q)\,\phi_1^*(r)\,\{\hat{c}Q\}\chi_p(Q)\,\phi_2(r) &= c\sqrt{\frac{\hbar}{m\omega}}\sqrt{\frac{n+1}{2}} \text{ for p = n+1} \\ &= c\sqrt{\frac{\hbar}{m\omega}}\sqrt{\frac{n}{2}} \text{ for p = n-1} \\ &= 0 \text{ for all other p, n} \end{aligned} \tag{2.27}$$

The coupling between the vibronic progressions of the electronic states can now readily be written out in matrix form, with the diagonal terms determined by Eqns 2.24 and 2.25 and the off-diagonal terms determined by Eqn. 2.27:

	$\phi_1\chi_0$	$\phi_2\chi_0$	$\phi_1\chi_1$	$\phi_2\chi_1$	$\phi_1\chi_2$	$\cdots$
$\phi_1\chi_0$	$(0+1/2)\,\hbar\omega$	0	0	$c\sqrt{\frac{\hbar}{m\omega}}\sqrt{\frac{1}{2}}$	0	$\cdots$
$\phi_2\chi_0$	0	E_0 $+(0+1/2)\,\hbar\omega$	$c\sqrt{\frac{\hbar}{m\omega}}\sqrt{\frac{1}{2}}$	0	0	$\cdots$
$\phi_1\chi_1$	0	$c\sqrt{\frac{\hbar}{m\omega}}\sqrt{\frac{1}{2}}$	$(1+1/2)\,\hbar\omega$	0	0	$\cdots$
$\phi_2\chi_1$	$c\sqrt{\frac{\hbar}{m\omega}}\sqrt{\frac{1}{2}}$	0	0	E_0 $+(1+1/2)\,\hbar\omega$	$c\sqrt{\frac{\hbar}{m\omega}}\sqrt{\frac{2}{2}}$	$\cdots$
$\phi_1\chi_2$	0	0	0	$c\sqrt{\frac{\hbar}{m\omega}}\sqrt{\frac{2}{2}}$	$(2+1/2)\,\hbar\omega$	$\cdots$
$\vdots$	$\vdots$	$\vdots$	$\vdots$	$\vdots$	$\vdots$	$\ddots$

Table 2.14: Vibronic Coupling Matrix

To an infinite number of phonons.

Solving this matrix for the energy eigenvalues by diagonalising, allows the energies of the coupled states to be calculated, this is the same as finding E_+ and E_- in the previous section only for more states and with a bigger matrix.

The eigenvectors of the matrix can then be found and written as:

	$\phi_1\chi_0$	$\phi_2\chi_0$	$\phi_1\chi_1$	$\phi_2\chi_1$	$\phi_1\chi_2$	$\cdots$
a	a_{10}	a_{20}	a_{11}	a_{21}	a_{12}	$\cdots$
b	b_{10}	b_{20}	b_{11}	b_{21}	b_{12}	$\cdots$
c	c_{10}	c_{20}	c_{11}	c_{21}	c_{12}	$\cdots$
d	d_{10}	d_{20}	d_{11}	d_{21}	d_{12}	$\cdots$
e	e_{10}	e_{20}	e_{11}	e_{21}	e_{12}	$\cdots$
$\vdots$	$\vdots$	$\vdots$	$\vdots$	$\vdots$	$\vdots$	$\ddots$

Table 2.15: Vibronically coupled eigenvector matrix.

In the coupled configuration the energy states are made up of varying amounts of each of the uncoupled states $\phi_m\chi_n$. The eigenvectors of the matrix give the make-up of the new states in terms of the old states: $\phi_1\chi_n$ and $\phi_2\chi_p$. The amounts of each

of the old uncoupled, states $\phi_m\chi_n$ contained in each of the new, coupled, states a, b, c... are given by the constants a_{mn}, b_{mn}, c_{mn} ... listed in Table 2.15. They are the coefficients of $|\phi_m\chi_n\rangle$, where m = 1 or 2 and n = 0, 1, 2, 3... . These constants can be used to calculate the relative probabilities of transitions involving the new, vibronic states, from the proportion now contained in them of old, electronic states, involved in quantum mechanically allowed electronic transitions.

The separation of the observed states may differ considerably from the separation of the uncoupled states, this may be understood as follows:

State $\phi_1\chi_0$ couples to state $\phi_2\chi_1$ and they repel quadratically in c (the coupling strength) as they are mixed (as for two states coupled by a static perturbation, Section 2.2.4). (Fig. 2.8)

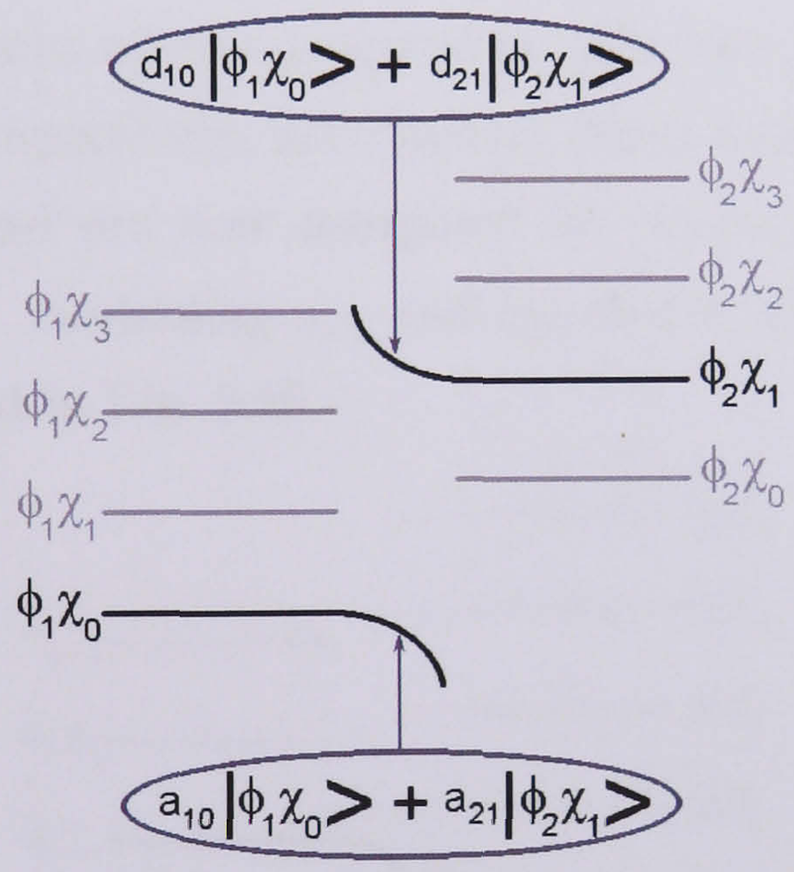

Figure 2.8: $\phi_1\chi_0$ couples to $\phi_2\chi_1$. Shown for $E_0 < \hbar\omega$.

Also $\phi_1\chi_1$ couples $\phi_2\chi_0$ and they are mixed and repel (Fig. 2.9).

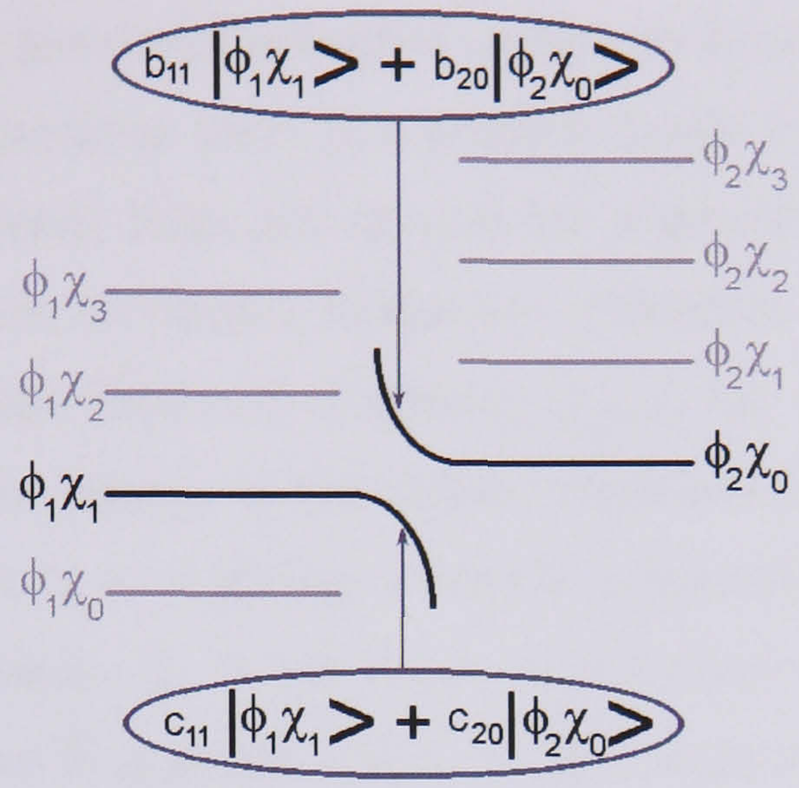

Figure 2.9: $\phi_1\chi_1$ couples to $\phi_2\chi_0$. Shown for $E_0 < \hbar\omega$.

The coupling propagates up the progression. The two lowest energy states containing $\phi_1\chi_0$ and $\phi_2\chi_0$ respectively, have moved closer together than the uncoupled states $\phi_1\chi_0$ and $\phi_2\chi_0$ and are now composed of: $a_{10}|\phi_1\chi_0\rangle + a_{21}|\phi_2\chi_1\rangle$+... and $c_{11}|\phi_1\chi_1\rangle + c_{20}|\phi_2\chi_0\rangle$+... containing a_{10} and c_{20} of the original zero-phonon states respectively, as illustrated in Fig. 2.10.

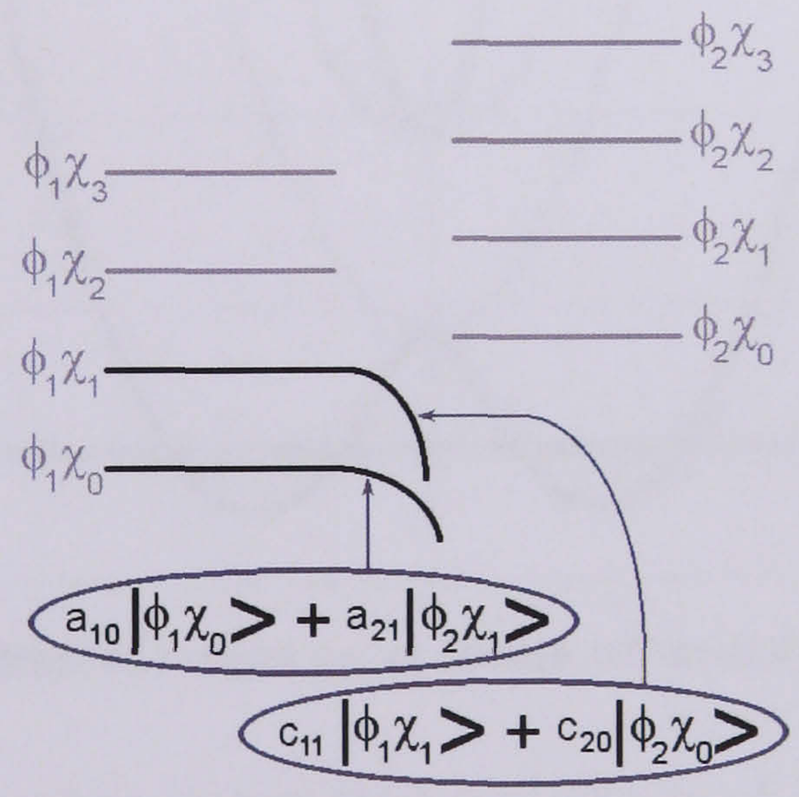

Figure 2.10: New separation of the two lowest energy coupled states. Shown for $E_0 < \hbar\omega$.

Physically the vibration distorts the defect. Harmonic vibrations at the uncoupled

states of the defect have a parabolic potential surface as a function of displacement, Q, in the vibration. This is because there is a greater elastic restoring force (that varies as the displacement squared) from the crystal for a greater amplitude of vibration, Fig. 2.11. By coupling the electronic states the vibration lowers the energy of the states, so that for some amplitude of vibration $|Q_{min}|$, the potential V is lower than for zero displacement. The energy of the defect, coupled by a vibration in Q, is then lower at $\pm|Q_{min}|$ than at Q = 0 giving a double minimum in the potential surface as a function of displacement, Q, in the mode of vibration of the defect (Eqn. 2.28). At Q = 0 therefore, there is a saddle point at the minimum energy the uncoupled configuration, while for $|Q| > |Q_{min}|$ the potential rises again as the elastic restoring forces of the crystal resist the motion and the energy gained by the distortion is offset.

$$\begin{vmatrix} \frac{1}{2}m\omega^2Q^2 - V & cQ \\ cQ & E_0 + \frac{1}{2}m\omega^2Q^2 - V \end{vmatrix} = 0 \qquad (2.28)$$

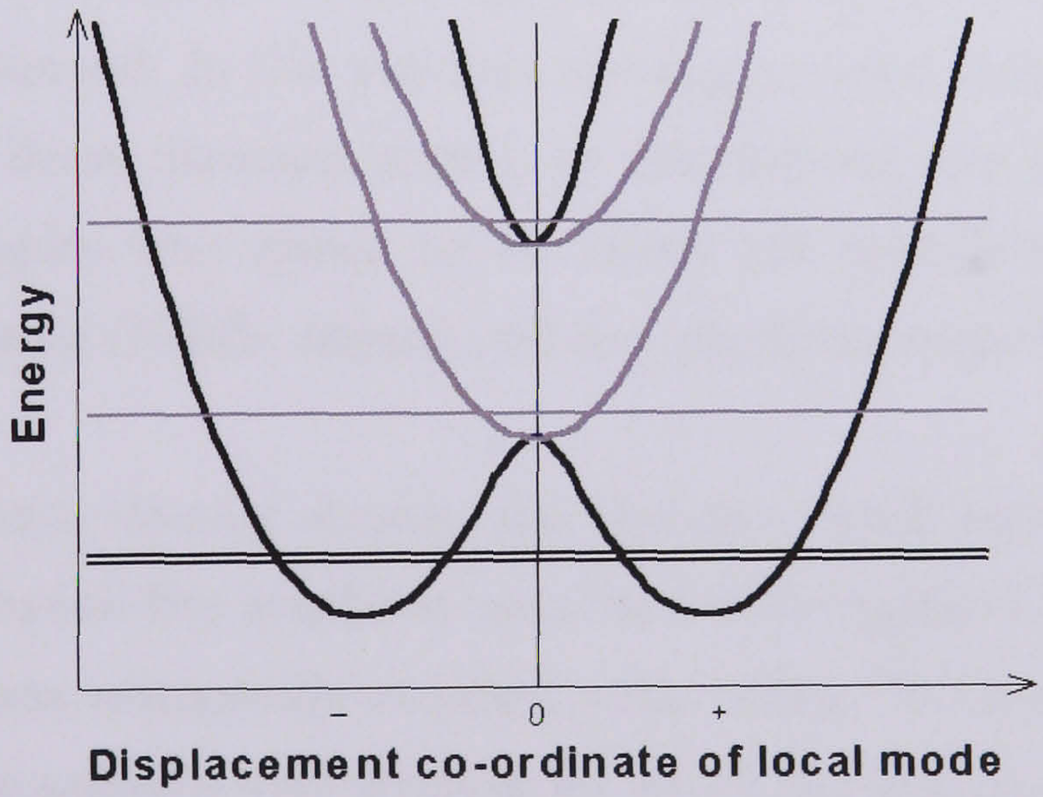

Figure 2.11: Potential surface at two electronic states of a mode of vibration at an undistorted defect (grey) and when the states are coupled by the vibration (black) plotted from Eqn. 2.28 where Q is the displacement co-ordinate. Lowest two energy eigenvalues shown by horizontal lines.

Chapter 3

Experimental Details

3.1 Diamond Synthesis and Isotopic Control

All the samples used in this thesis were grown from fine diamond powder on a diamond seed in the presence of a metal solvent/catalyst (e.g. iron, cobalt) under high pressures at high temperatures (HPHT). Nitrogen getters were used to reduce the incorporation of nitrogen in the diamond. In this way type IIa single crystal diamonds are produced. For a review of De Beers diamond growth by this process, see Burns et al [5]. The majority of the samples were grown by De Beers, the isotopically enriched sample was grown by H. Kanda (NIMS, Japan) and the remainder came from T. R. Anthony (GE, USA).

To ensure minimum internal strains, and therefore small optical line widths, the stress work used inclusion-free synthetic diamonds with negligible nitrogen concentrations. One sample was isotopically enriched with ~99% ^{13}C. Diamond was the first semiconductor where samples were studied, for which the isotope of the host material had been totally changed [31]. Changing the isotope of all of the host atoms from ^{12}C to ^{13}C changes the vibrational frequencies, of all modes involving the motion of only carbon atoms, in the approximate ratio $\sqrt{(12/13)}$ [31]. This allows the identification of local modes and any impurity content (involved in the vibration) of the defect from which they arise.

Eight other samples with a range of nitrogen concentrations were used. These contained only dispersed, single substitutional nitrogen. Since nitrogen is known to be taken up differently by different sectors during growth [5], these samples were cut from single sectors where possible.

3.2 Sample Preparation

The samples used for stress were X-ray oriented, laser cut and mechanically polished so that uniaxial stresses could be applied along the ⟨001⟩, ⟨111⟩, ⟨110⟩ and ⟨112⟩ crystallographic directions. They were variously irradiated at room temperature with 10^{17} to 2 x 10^{17} cm^{-2} electrons of energy 1.5 or 2 MeV, generating between 10^{16} and 2 x 10^{17} cm^{-3} of $\mathbf{I}^0_{\langle 001 \rangle}$. All samples were cleaned thoroughly with acetone before being mounted for use.

The remaining samples were simply polished to provide parallel faces (approximately 3x3mm) for spectroscopy through about 1mm thickness. After initial measurements these samples were mounted in indium, (for good thermal contact) on a water cooled copper block and irradiated 'side by side' so that they received the same treatment.

3.3 Defect Observation

3.3.1 Absorption Spectroscopy

Light passing through a diamond is absorbed when it is at the right wavelength to induce transitions between vibrational or electronic states of point defects, such as those studied here. In absorption spectroscopy the spectrum of this absorbed light is recorded, identifying the wavelengths at which the defects are absorbing and so the energies of the transitions. Spectra provide information about the transitions and their probabilities, so this is a quantitative technique from which much can be learned about optical defects and their concentrations in diamond. Background spectra are

recorded under the same conditions without a sample present and 'factored out' (See Eqn. 3.1 [38]) of the sample spectra to determine the energy dependence of absorption by the sample only and eliminate the wavelength dependence of the source, detector and polariser.

$$\text{absorption coefficient} = \frac{1}{t} \ln \left(\frac{I_0}{I_t} \right) [38] \tag{3.1}$$

where t is the sample thickness in cm, I_0 is the incident intensity (or background) and I_t is the intensity transmitted through the sample.

Dispersive Spectroscopy

Some of the earlier temperature dependence measurements and measurements of ^{13}C diamond were recorded using a Grating Monochromator spectrometer. Light passed through the sample then through a slit into the spectrometer, before being focused as a parallel beam onto a grating inside the spectrometer. The dispersed light from the grating is refocused and the wavelengths are then scanned over by the detector.

Fourier Transform Spectroscopy

Most spectra in this thesis were recorded using a Bruker IFS66 Fourier Transform spectrometer, in the near IR, using a tungsten halogen lamp source and Si diode detector. The inside of a Fourier Transform (FT) spectrometer, shown in Fig. 3.1, is effectively a Michelson Interferometer. A beam splitter is used to send some of the light to a fixed mirror and some to an oscillating mirror (controlled by the computer). These beams then recombine and interfere, one having been phase-shifted with respect to the other. A HeNe laser is used inside the spectrometer to calibrate the path length of the beam. The beam then passes through the sample and absorption occurs at wavelengths characteristic of the sample's electronic structure. It is the interference pattern of the two beams which is then recorded by the detector. The signal is inverse Fourier transformed to produce the spectrum. This technique has the advantage that [53] the wavelengths are determined very accurately and all wavelengths can be

recorded instantaneously, rather than having to scan through them individually as with the monochromator. This means that with the entire spectrum (from 1 to about 3 eV using the near IR setup) recorded with each measurement, nothing is missed and many things may be studied under the same conditions. Faster data acquisition means that scans can be repeated many times over a short period to reduce noise; this is particularly helpful for weak features.

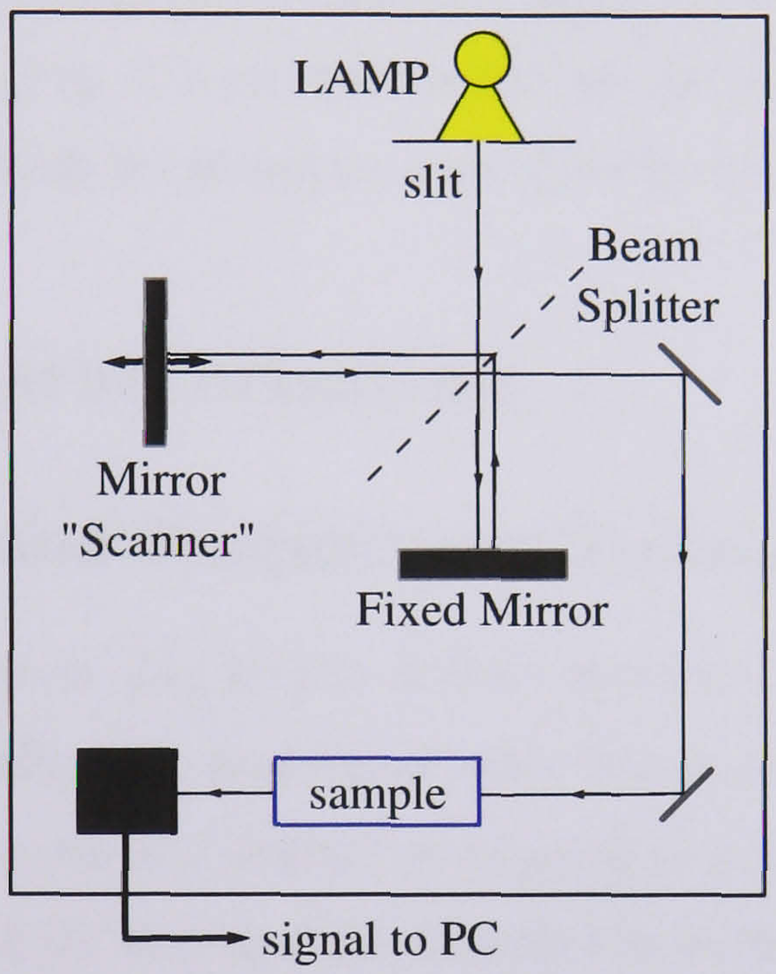

Figure 3.1: Inside an FT spectrometer, see text for further details.

For determining the concentration of dispersed nitrogen and the types and concentrations of nitrogen aggregates present in a sample (see Chapter 7) spectra were recorded in the mid IR region using a Nicolet FTIR spectrometer.

3.3.2 EPR

The application of a magnetic field to an atom or molecule with an unpaired electron, causes the spin of the electron to either line up parallel or anti-parallel to the magnetic field. Electrons have different energies in these two alignments, so the degeneracy

of the $\pm 1/2$ spins of the electron is lifted by the field. In Electron-Paramagnetic-Resonance (epr) spectroscopy, sometimes referred to as Electron-Spin-Resonance (esr) spectroscopy, the microwave absorption spectrum of such unpaired electrons in a strong magnetic field is measured. For a review of epr in diamond see [27].

Carbon atoms in diamond do not have unpaired electrons, so it is point defects within the lattice, with unpaired electrons, which show up in epr. Nitrogen, for example, with its anti-bonding extra electron, gives a strong epr signal [54]. The two p_π orbitals shown in Fig. 2.3 are the source of the epr signal arising from the self-interstitial through which its structure was identified [28].

3.4 Defect Characterisation

3.4.1 Cryogenics and Temperature Variation and Calibration

Resolving absorption features due to the defects studied in this thesis requires low sample temperatures, ideally 77K and below since the lines broaden with increasing temperature. Liquids nitrogen and helium were used to achieve this. Three different cryostats were used. The first was used for sample characterisation and temperature dependence measurements. The sample cavity was pumped to a vacuum better than 10^{-6}mBar to insulate the sample chamber and prevent condensation on the windows which were at room temperature. Calcium fluoride windows were used since these are optically transparent in the region of interest. The sample was fixed in a copper mount with indium, a soft and workable metal, putting it in good thermal contact with the copper. The copper was in turn in thermal contact with a reservoir that could either be filled with liquid nitrogen or connected to a syphon providing a helium vapour flow with the aid of a pump. The former was used to achieve a stable sample temperature of 77K while the latter was required for temperatures below this, down to a minimum of approximately 4K. An Oxford Instruments heating element was placed just above the copper mount in thermal contact with the copper base of the reservoir. Varying the power supplied to the heater together with adjustments to the

helium flow valves into the syphon and the pump allowed the sample to be held at stable temperatures from 4K up to and above room temperature, for the duration of a spectral measurement (and longer). The sample temperature was monitored and controlled by an Oxford instruments ITC503 Intelligent Temperature Controller connected to the heater.

The second cryostat was used with liquid nitrogen only. Again the outermost cavity was pumped and held at vacuum and the sample was in thermal contact with the cryogenic liquid. This setup was used for preliminary stress measurements until it was realised that lower temperatures were required. The third cryostat Figs. 3.2 and 3.3 was used for stress measurements at liquid helium temperature and above - up to about 40K. This cryostat has Spectrosil-B quartz windows. Here the sample was held in a cavity containing low pressure helium gas as an exchange gas. This cavity was in thermal contact with a surrounding cavity through which helium vapour flowed. This cavity in turn was insulated by a surrounding vacuum cavity which was continuously pumped. The sample temperature was controlled in the same way as in the first cryostat. Silicon diode thermometers were placed in suitable locations in each of the cryostats so that with the system in equilibrium the sample temperature could be measured accurately. The temperature scale was calibrated using a standard diode calibration curve, supplied by Oxford Instruments, fitted to 3 reference points at liquid helium, liquid nitrogen and ice melt temperatures.

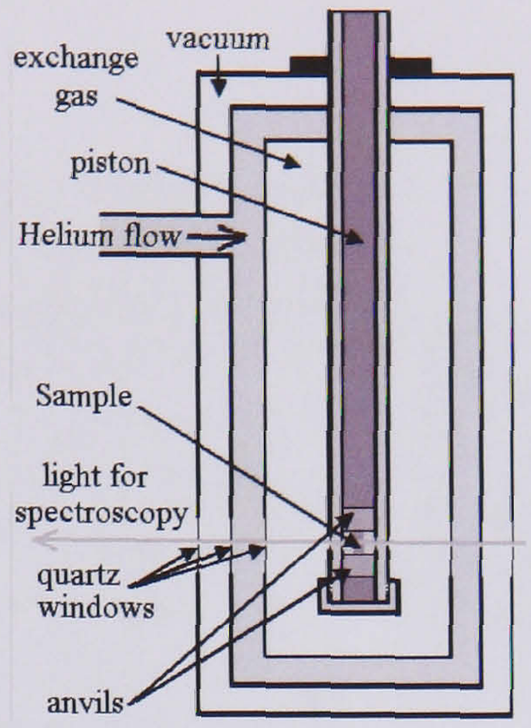

Figure 3.2: Schematic of Helium flow dewar.

A sheet of polaroid was fixed over the window of the dewar, polarising the light either parallel or perpendicular to the stress axis to select out differently orientated defect absorption.

3.4.2 Uniaxial Stress

Gaskets were cut from foil and attached to hardened steel anvils using a thin layer of GE varnish. This was done carefully to ensure a flat and even, clean surface to avoid uneven pressure which may initiate a crack in the sample that would propagate rapidly under pressure. Visual examination of indentation of these gaskets after an experiment gave an indication of how even the applied stress was across the sample. Foil 'wings' were painstakingly attached to the sides of the sample using GE varnish to block all light from going past the sample between the anvils in the spectrometer. Great care was taken to ensure these 'wings' did not exceed the dimensions of the samples and get in between the sample and the anvils, but that they left no gaps. The remaining faces of the sample were cleaned thoroughly to remove any grease or varnish that may be in the way of the beam in the spectrometer and any dust or lumps of varnish that may get in between the sample and the gasket and affect the applied stress.

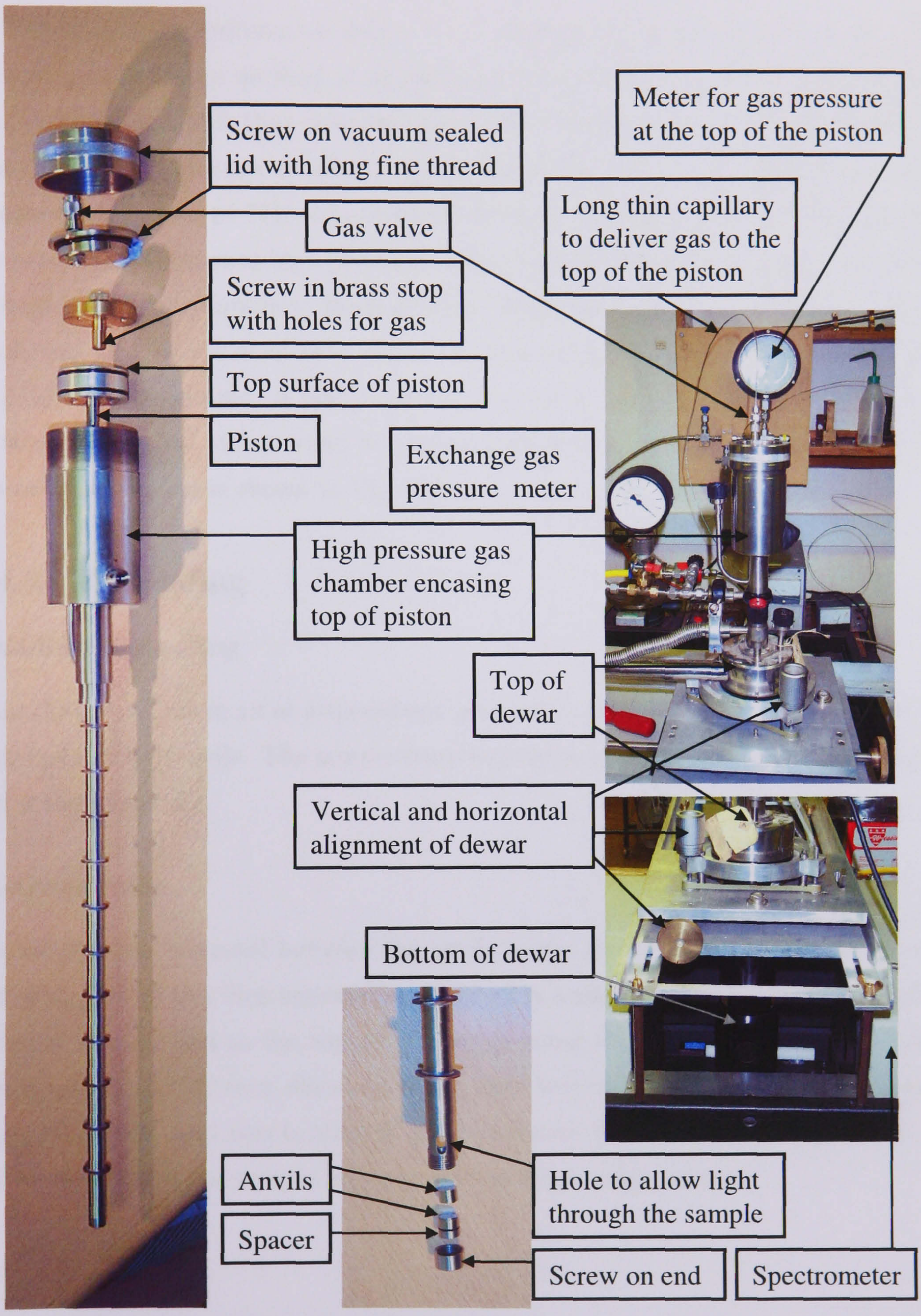

Figure 3.3: Uniaxial stress equipment setup.

Two different experimental setups were used for applying uniaxial stress. They differed mainly in the method of applying pressure to the top of the piston and the temperatures at which they could be used. The sample was mounted in exactly the same way in both setups as shown by the schematic in Fig. 3.2. Preliminary stress measurements, done at 77K, employed an oil based hydraulic system, while the lower temperature system used high pressure nitrogen gas delivered to the top of the piston through a long thin capillary. Both provided high stable pressures. This applied to a small area (the size of most faces of the samples used), easily enabled pressures of up to 2 GPa on the sample. A finely calibrated pressure gauge was used in both setups so that the applied stress could be varied accurately, finely and continuously. The gas pressure system is shown in Fig. 3.3.

3.4.3 Annealing

Standard Annealing

Annealing was done in air at atmospheric pressure in the centre of a long electrical furnace open at both ends. The temperature was checked using a mercury thermometer and a thermocouple.

Re-Orientation

The sample was mounted between the anvils in the stress cell as normal, the sample end of the piston was then emersed in motor oil in a glass beaker placed on a hotplate. Pressure was applied to the top of the piston using the hydraulic setup and the oil was heated to 300°C over about an hour, then held at this temperature for several hours before the heat was turned off and the system was left to cool. The stress was not removed until the sample had returned to room temperature.

3.4.4 Data Analysis

Section 2.2 explains the information that the change in the energies and intensities of the stress split components of transitions can give us about defects, but before this analysis can be done these absorption line energies and intensities need to be determined from the spectra. Unfortunately this is not straightforward for the lines arising from $\mathbf{I}^0_{\langle 001\rangle}$. The 1685 meV line is a weak feature sitting on a steep background due to the GR1 and the 1859 meV line is asymmetric and in amongst the phonon sideband structure of the GR1, Fig. 2.2. It is not known how to produce $\mathbf{I}^0_{\langle 001\rangle}$ in pure diamond without the presence of $\mathbf{V}^0$ in the spectrum.

To determine the area of a peak (and to a lesser extent its peak energy) accurately, requires sensible and consistent baselines to be fitted to the data that can be subtracted away leaving only and all the absorption due to $\mathbf{I}^0_{\langle 001\rangle}$. The baseline needs to be adaptable to the changing background as the vacancy is perturbed.

A number of methods were tried, for the 1685 meV region the most sensible baseline seemed to be a quadratic. A program was written to fit this objectively and consistently. The baseline is fitted as follows: the user visually selects two continuous regions either side of the peak. An equal number of points (x_i,y_i) from each of these two regions, is then selected by the program, a minimum of two times the line width away from the centre of the line. The discrepancy between the fitted quadratic curve y(x) and the chosen data points (numbered 1 to n) may be described by Eqn 3.2.

$$\sum_{i=1}^{n} (y_i - y)^2 = \sum_{i=1}^{n} \left(y_i - ax^2 - bx - c\right)^2 = Q \tag{3.2}$$

where a, b and c are the parameters of the quadratic. The discrepancy is minimised using Eqn 3.3:

$$\frac{\delta Q}{\delta a} = \frac{\delta Q}{\delta b} = \frac{\delta Q}{\delta c} = 0 \tag{3.3}$$

This gives three equations in three unknowns. These three equations may be written in matrix form and solved for a, b and c using row reduction, so the best fit is

determined analytically; the result is shown in Eqns 3.4, 3.5 and 3.6.

$$c = \frac{\frac{\left(\frac{\sum y_i \sum x_i^4}{\sum x_i^2} - \sum y_i x_i^2\right)\left(\frac{\sum x_i^2 \sum x_i^4}{\sum x_i^3} - \sum x_i^3\right)}{\left(\frac{\sum x_i \sum x_i^4}{\sum x_i^2} - \sum x_i^3\right)} - \frac{\sum y_i x_i + \sum x_i^4}{\sum x_i^3} + \sum y_i x_i^2}{\frac{\left(\frac{n \sum x_i^4}{\sum x_i^2} - \sum x_i^2\right)\left(\frac{\sum x_i^2 \sum x_i^4}{\sum x_i^3} - \sum x_i^3\right)}{\left(\frac{\sum x_i \sum x_i^4}{\sum x_i^2} - \sum x_i^3\right)} - \frac{\sum x_i \sum x_i^4}{\sum x_i^3} + \sum x_i^2} \tag{3.4}$$

$$b = \frac{\left(\frac{\sum y_i x_i \sum x_i^4}{\sum x_i^3} - \sum y_i x_i^2\right) + c\left(\sum x_i^2 - \frac{\sum x_i \sum x_i^4}{\sum x_i^3}\right)}{\frac{\sum x_i^2 \sum x_i^4}{\sum x_i^3} - \sum x_i^3} \tag{3.5}$$

$$a = \frac{\sum y_i x_i^2 - c \sum x_i^2 - b \sum x_i^3}{\sum x_i^4} \tag{3.6}$$

These sums, a, b and c, are easily computed within the program and the curve simulated. This provides a robust fit, provided the assignment of a quadratic to the data is reasonable.

A lorentzian function was then least squares fitted to the peak. The peak position and area of this lorentzian were taken as the energy and intensity of the line respectively. See Fig. 3.4 for an example output of the program. This program proved robust and provided excellent fits to most spectra, the biggest difficulty came when the GR1 moved very close to the 1685 meV line, this is discussed in the next section.

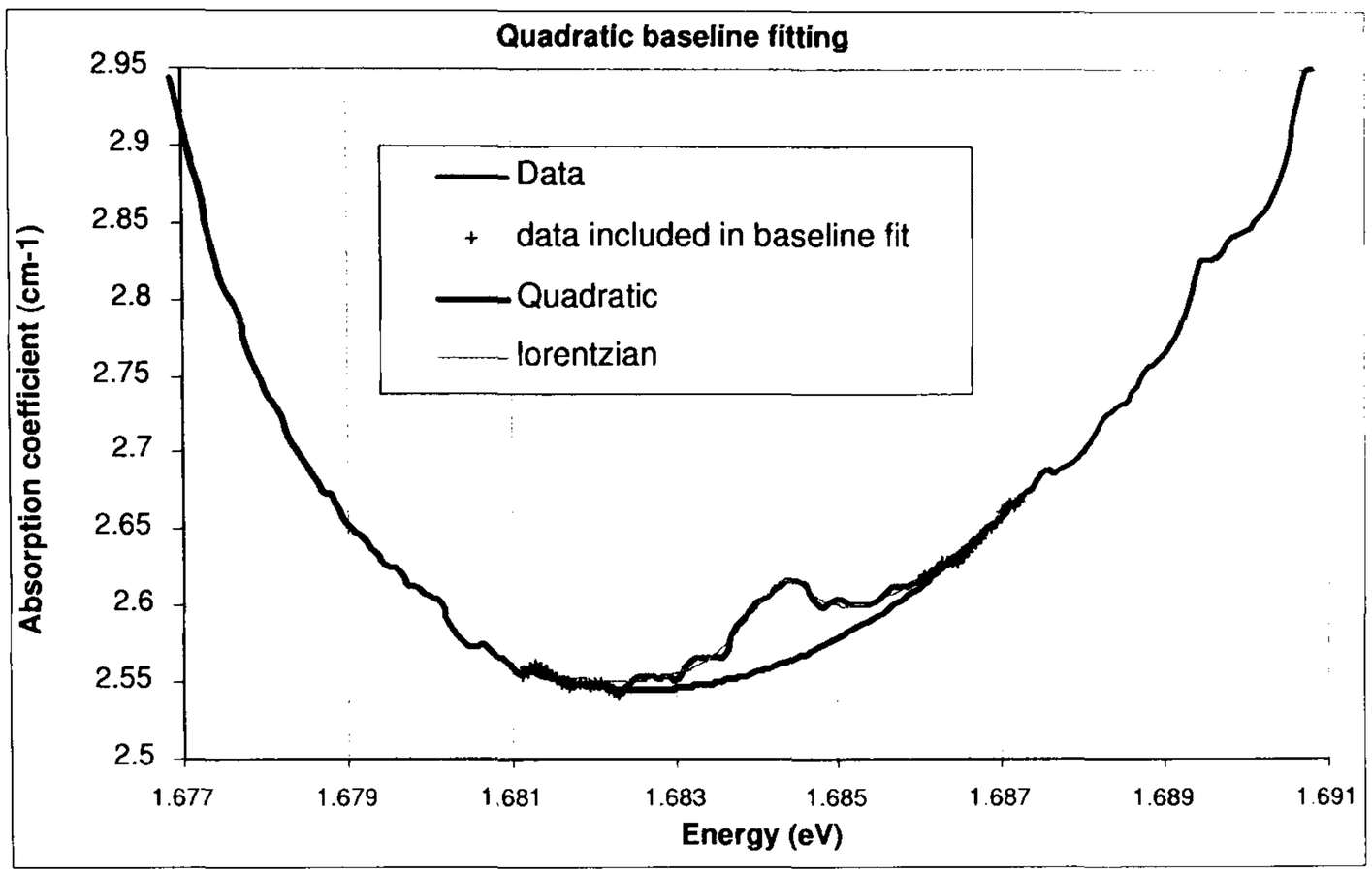

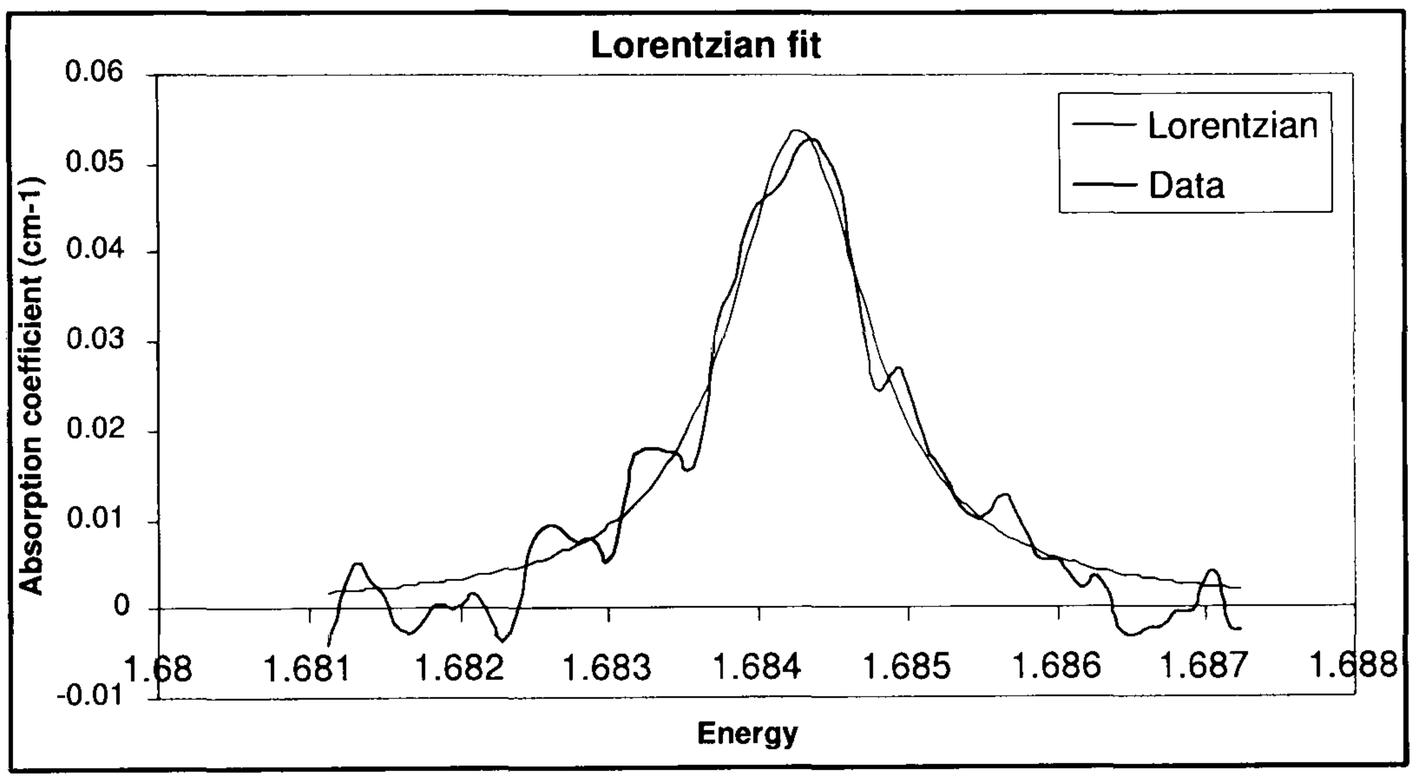

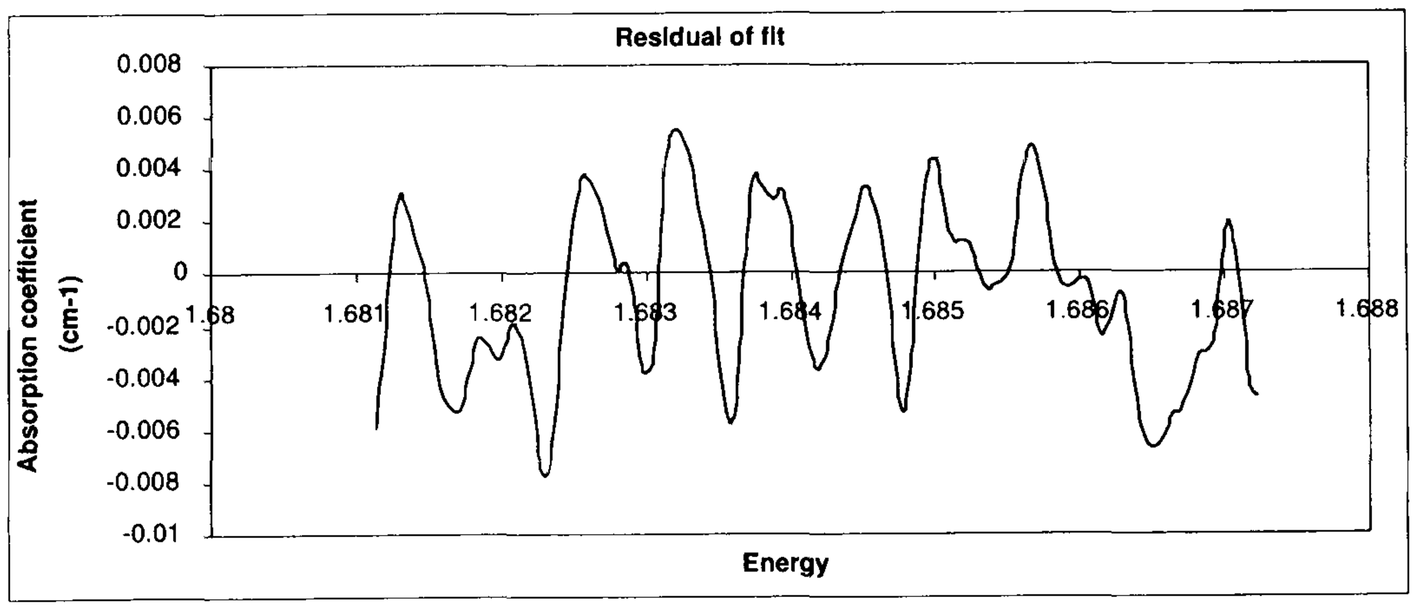

Figure 3.4: Example output of a program, written in Excel using Visual Basic, to fit a quadratic baseline to the GR1 absorption and then a lorentzian to the 1685 meV line (or the 1692 meV stress induced line). This was used to analyse some of the data presented in Chapter 5.

Two different fitting methods were used for the 1859 meV line, one was to apply a straight line baseline by eye, including the asymmetry and find the area under the data, the other was to fit a straight line baseline to the background on the right hand side of the line and then to fit a gaussian function to the data, excluding the asymmetric part from the fit, Fig. 3.5. As the line and its background broaden and move as a function of stress, neither of these approaches proved consistent and both require some human judgement. The resulting accuracy is discussed in the next section.

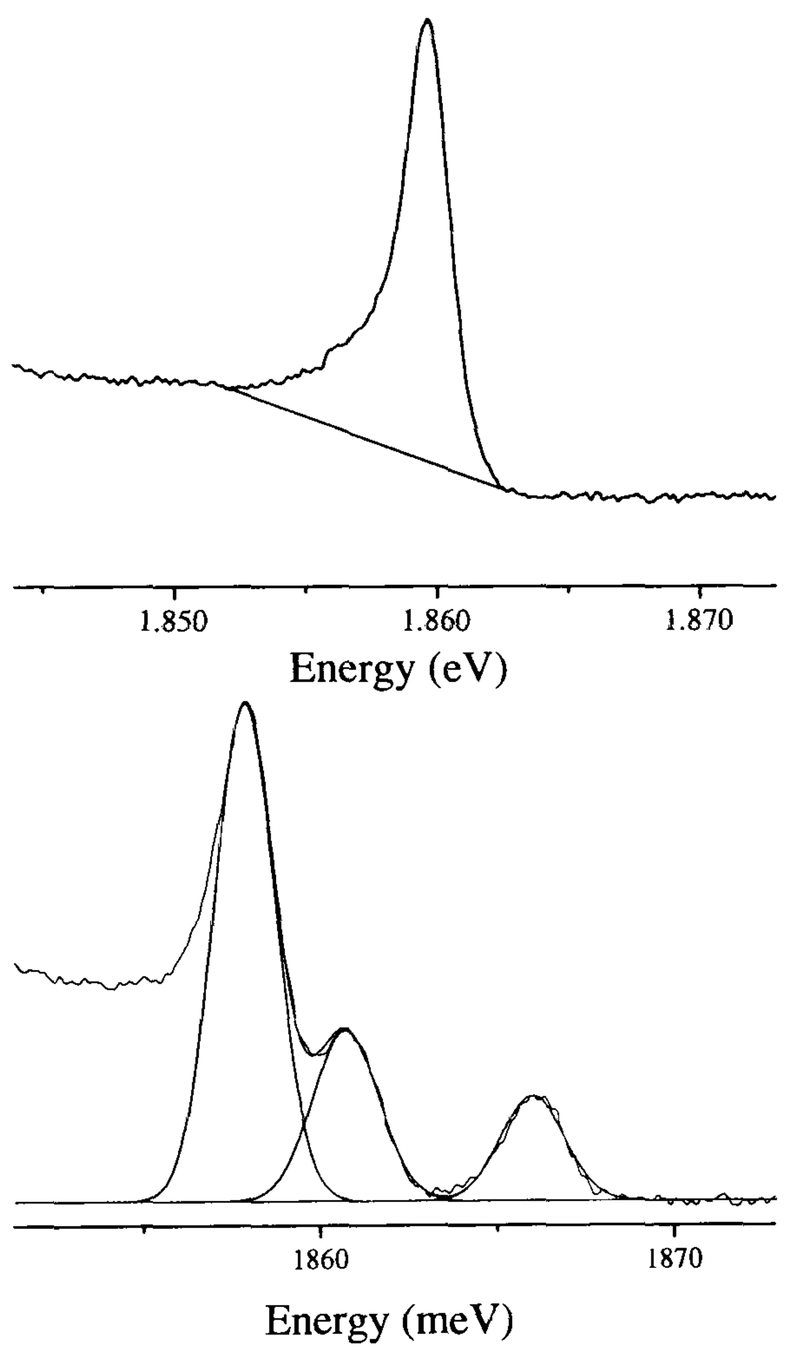

Figure 3.5: Two different methods of determining the intensity of the 1859 meV line (and any stress split components).

Once all data were recorded and plotted as a function of stress, the perturbation parameters (derived from group theory, Section 2.2) were fitted to the plots using least squares fitting in excel.

3.4.5 Errors and Difficulties

Distinguishing Perturbed Lines

Four lines appear in the spectra between 1690 and 1692 meV each separated by less than 1 meV. Fortunately, although weak, these lines are sharp enough to be resolved at low stress. Some are due to $\mathbf{I}^0_{\langle 001 \rangle}$, some are not and the energies and intensities of each of them need to be tracked as a function of stress; telling them apart when they are split, shifted and have grown or faded in intensity requires careful measurement at low stress to track them. Measurement at different temperatures enables exploitation of their differing temperature dependencies to aid in this process. The lines were sensibly separable at low temperature (<40K) since this is where they are sharpest.

Optimising the Temperature

All the lines in the spectra were much sharper at 4K than at 77K. Recording spectra at low temperature therefore increases the accuracy of determining the peak energy of a line, (see Fig. 3.6 for an illustration) and improves the chances of resolving splittings. Some lines could only be distinguished at very low temperature.

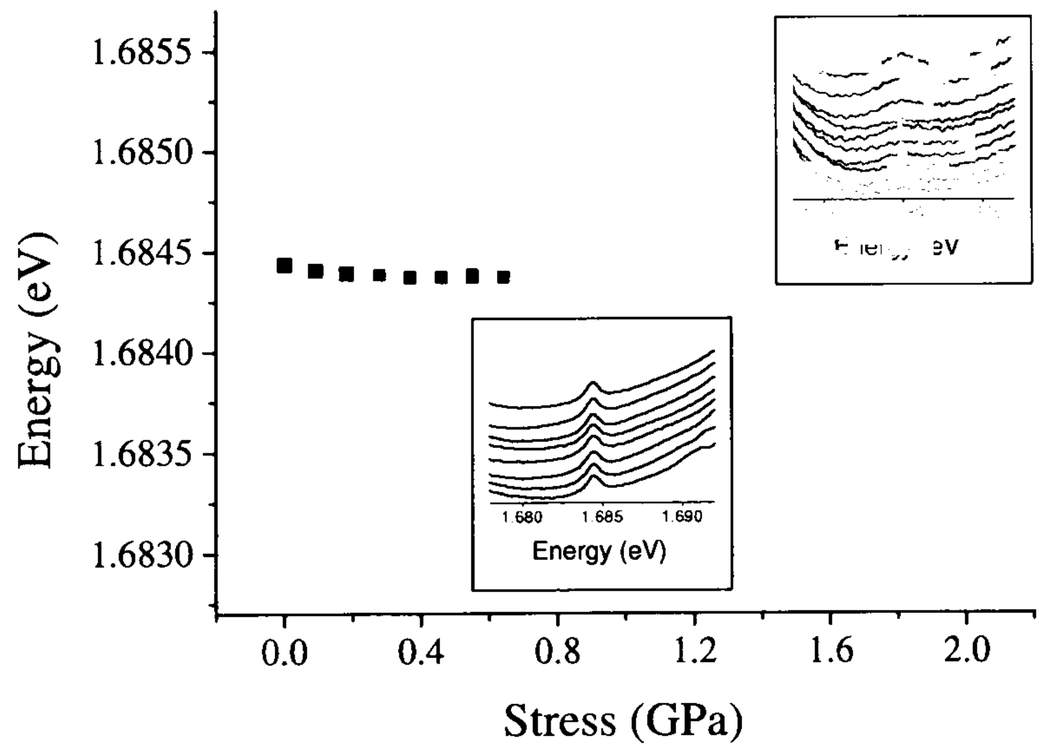

Figure 3.6: The effect of temperature on the accuracy of line position measurement. Spectra inset. Grey points measured at 77K, black at 40K. The energy displacement is genuine, the increased scatter is a result of increased line widths.

However, some lines are thermally populated and so require higher temperatures to observe them, especially if the state from which they originate is rising in energy with the applied stress relative to the ground state. The higher the temperature the broader the line, so for weak features such as the 1685 meV there is a trade-off between resolution and intensity.

The background may also be easier to deal with at low temperature. The optimum temperature for measurements was 4K for all transitions originating from the ground state and 20 or 40 K for all others depending on the line and stress direction and the information required from it. Of course it is important that the temperature does not change during the experiment so that the results are consistent. The equipment was always allowed to stabilise in temperature so that two identical spectra could be recorded half an hour apart, before experimentation properly began. The lines themselves act as the best thermometers, particularly at the GR1 whose temperature dependence is well documented.

Baselines - Error in Determining the 1685 meV Line Energy

A sensible baseline is critical since 28% of the area of a lorentzian is below 10% of the height [38]. The 1685 meV line is very weak and is sitting just to higher energy of the intense 1673 meV GR1 line, with the best baseline fitting methods in the world, measurements of its position are going to be subject to error. These errors can be clearly seen in the data recorded for the same stress experiment at different temperatures. At higher temperatures the 1685 meV line is broader and although it is more intense most of this is spread out across the steep background, the GR1 is also broader so the background is steeper. The lowest temperature at which the line may be observed before it disappears, seems to be the most accurate at which to record its position. The catch is that in some stress directions this temperature rises with stress as the initial state of the transition rises in energy. All this is illustrated in Fig. 3.7.

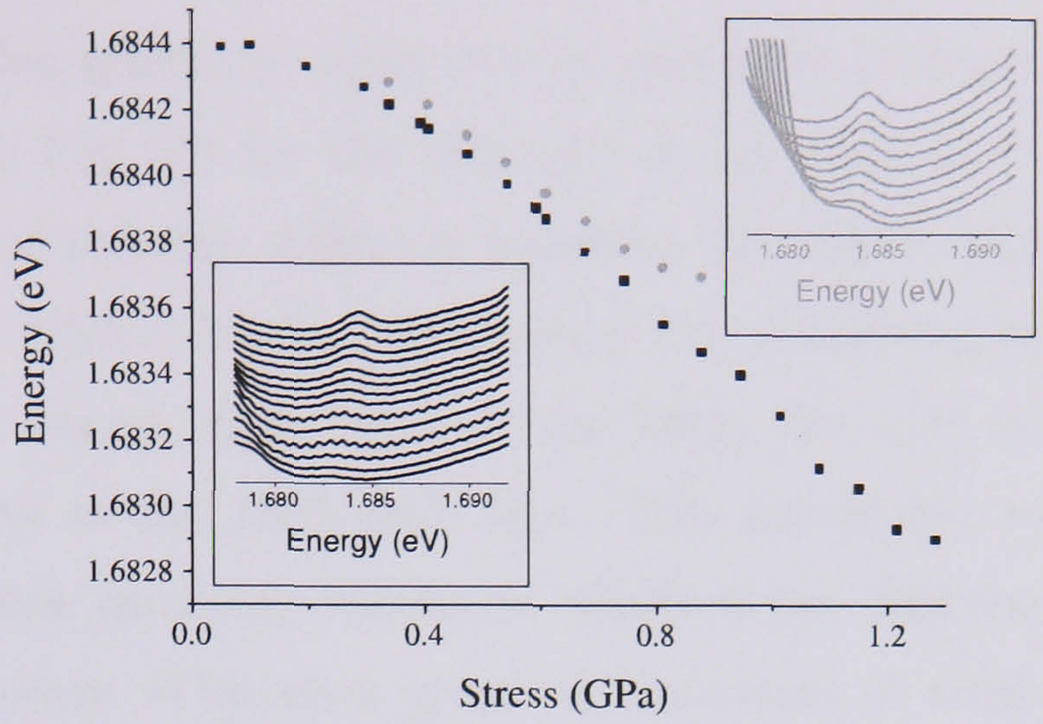

Figure 3.7: The effect of the proximity of the GR1 on measurement of the energy of the 1685 meV line. Spectra inset. The shift of the 1685 meV line with stress should be the same in both examples while the shift of the GR1 is different.

Baselines - Error in Determining the 1859 meV Line Intensity

Long experience of fitting baselines to this awkward line has taught me that it's remarkable that we can ever learn anything quantitative from measuring its intensity variations. Trying to include the apparent asymmetry makes the fit highly subjective and probably an overestimate that may suffer as the line broadens. Fitting a gaussian to the higher energy side looks convincing and seems repeatable but is most likely an underestimate and will be less so as the line (and so the gaussian) broadens. The truth may lie somewhere between the two.

The effects of these errors on measuring the change in intensity of the 1859 meV line, as its transition probability falls and it shifts and broadens with stress, is illustrated in Fig. 3.8. A transition is induced by stress to higher energy producing absorption where the baseline is clear, so that the intensity may be measured objectively. As we will see in Section 5.3.5 of Chapter 5, the rate of rise in the intensity of this line should be matched by the rate of fall in the 1859 meV line and its intensity related to the initial intensity of the 1859 meV line in a well determined way. Fitting the theory to the behaviour of this induced line should therefore enable us to predict

how the 1859 meV line intensity ought to vary and what it should start out as. Data points are plotted in Fig. 3.8 for the intensity of the 1859 meV line determined by correcting for each of the two different baselines described above. A curve is also plotted from theory where, having determined the remaining parameters relatively accurately from the energy shift rates of the lines, the only adjustable parameter is the initial intensity of the 1859 meV line. This parameter was determined from fitting the induced line intensity variation, which is (as discussed above) much less subject to baseline error. This then gives an indication of what the 1859 meV line area should be as a function of stress. Clearly the average of the 1859 meV line areas as determined by the two different methods gives a sensible measure; this is the result used in Chapter 5.

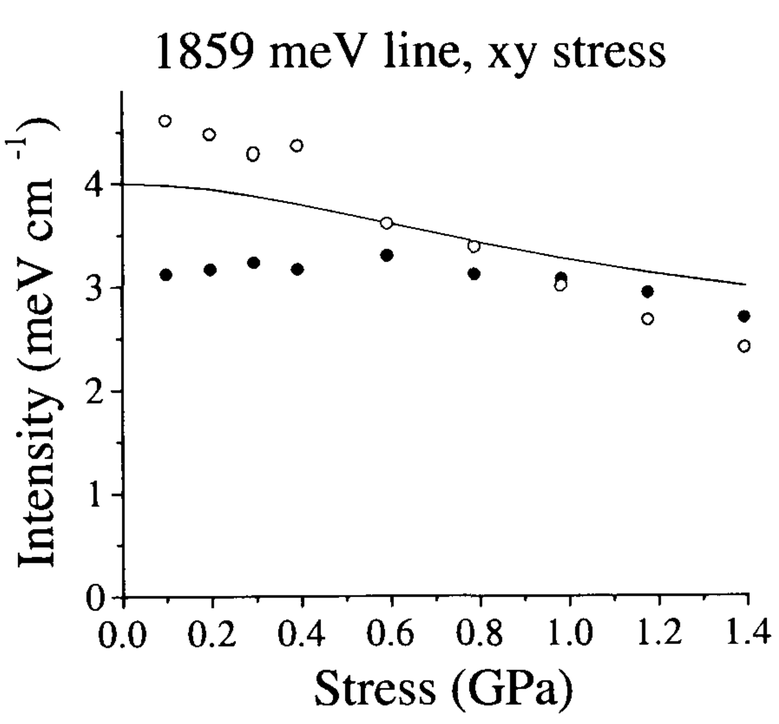

Figure 3.8: Open circles represent the 1859 meV line intensity found by fitting a straight line baseline by eye to include the asymmetry of the line, whilst the closed circles represent the 1859 meV line intensity found by fitting a gaussian to the right hand side of the line and excluding the asymmetry. For a discussion of the relative merits of the two methods see text. Setting the unperturbed intensity of the line to near 4, produces a good fit of the theory to both this 1859 and the more readily measured 1864 meV line (not asymmetric, flat baseline) intensity data.

Chapter 4

GR1

This thesis is predominantly concerned with the perturbation of and absorption by self-interstitials, however, vacancies are present in all our diamonds, absorb very strongly and may also be perturbed; so it is necessary to understand how absorption by vacancies behaves as a function of stress and temperature. The vacancy has been extensively studied, but it is easy in this instance (since the data is recorded anyway) to revisit old work using modern samples and equipment and since the interstitial results are complicated, it is useful to work on the vacancy as a check of the experiment.

4.1 Literature

4.1.1 Vacancies in Diamond

Isolated vacancies have been identified in diamond in the neutral ($\mathbf{V}^0$) and negative ($\mathbf{V}^-$) charge states; both can be seen in optical absorption [51] and epr spectroscopies [55, 56] as well as through positron annihilation experiments [57]. In optical absorption neutral and negatively charged vacancies are observed as the GR1 (1.673 eV) to GR8 and ND1 (3.154 eV) lines respectively.

In epr $\mathbf{V}^-$ gives rise to the S1 signal owing to its S=3/2, $^4A_2$ ground state [56].

Although its ground state is diamagnetic $\mathbf{V}^0$ may also be observed in epr, this time through an S=2, $^5A_2$ excited state. The signal is observed when excited neutral vacancies are created through the ionisation of negatively charged vacancies by UV light [55]. Both $\mathbf{V}^0$ and $\mathbf{V}^-$ have tetrahedral symmetry in their epr states.

The epr measurements also show that in both charge states the unpaired electron probability is predominantly localised in the dangling orbitals within the vacancy and that the nearest neighbours relax outwards. Thanks to these identifications in epr the intensities of the optical signals from $\mathbf{V}^0$ and $\mathbf{V}^-$ have been calibrated in terms of their concentrations [58].

Vacancies migrate in the neutral charge state (negative vacancies undergo reversible charge transfer to $\mathbf{V}^0$ to migrate) with an activation of 2.3±0.3 eV so they are stable up to annealing temperatures of about 800°C [59].

4.1.2 The Neutral Vacancy

The GR1 (General Radiation 1) damage centre in diamond was identified as the isolated neutral vacancy by Clark and Walker in 1973 [37]. In optical absorption the centre produces two zero-phonon lines at 1665 and 1673 meV and considerable vibronic structure to higher energy (Figure 2.2) as well as lines GR2-8 between 2.8 and 3.1 meV [60]. The temperature dependence of the GR1 lines showed that there are states separated by 8 meV in the ground state of the defect. This, in conjunction with the uniaxial stress splitting of these two lines, was used to identify the symmetry of the centre as tetrahedral (T_d) [37]. Owing to its production in all types of diamond by all types of irradiation the GR1 was already considered to be an intrinsic defect. This led Clark and Walker to consider just two possible candidates with tetrahedral symmetry, a vacancy or a self-interstitial. The expectation from numerous theoretical predictions was that the interstitial would not be stable at a tetrahedral site and since it was (in 1973) thought likely to be mobile below room temperature, (as in silicon) the vacancy was the preferred candidate. Further temperature and uniaxial stress dependence studies on GR2-8 [60] identified them with the same defect.

Clark and Walker stated in their conclusions [37] that there is a great deal of mixing of the states under stress, clearly shown by the quadratic shift rates and variation of component intensities. They could not provide a full interpretation of the data. This was provided in 1974 by Davies and Penchina who repeated the experiment and diagonalised the perturbed hamiltonian for the centre, showing that the E and A ground states are strongly coupled, producing new eigenstates that account for the intensity variation of the lines. Clark and Walker's data suffered anomalous splittings in the ⟨111⟩ direction that were not encountered in 1974 by Davies and Penchina [1] who presented a complete and self consistent analysis which will be made use of here.

4.2 Results: Uniaxial Stress on the GR1 Lines

The majority of the results presented in this thesis are concerned with changes observed in the absorption spectrum of diamond under uniaxial stress. Absorption is recorded simultaneously at all wavelengths within the set range by the FT spectrometer used in all the uniaxial stress experiments presented in this thesis. Each spectrum, therefore, records the behaviour of a number of absorption features all under the same conditions of temperature, stress and polarisation. The lines due to the interstitial are the major interest in this thesis. Where these lines are present the GR1 is also present. Since the GR1 stress splitting is well established, both quantitatively and qualitatively, comparison of new results with the published data serves as a check, helping to ensure that the orientation of the sample and of the polariser is as it is supposed to be and that the magnitude of the shifts under the applied stress corresponds to the magnitude of stress being applied. Analysis of the GR1 lines can therefore authenticate and be used to standardise all the stress data presented in this thesis. For simplicity and since they do not appear in the low temperature spectra anyway, the 1665 meV line and its components have been omitted from the analysis. The well known temperature dependence of the GR1 doublet is also a useful tool for qualitative checks and if necessary quantitative calibration.

⟨001⟩ Stress

In this stress direction the degeneracy of the ground, E state, is lifted and splits into an A and B state, while the triply degenerate excited state splits into a doubly degenerate E state and a non-degenerate state. The A_1 states then mix, Fig. 4.1.

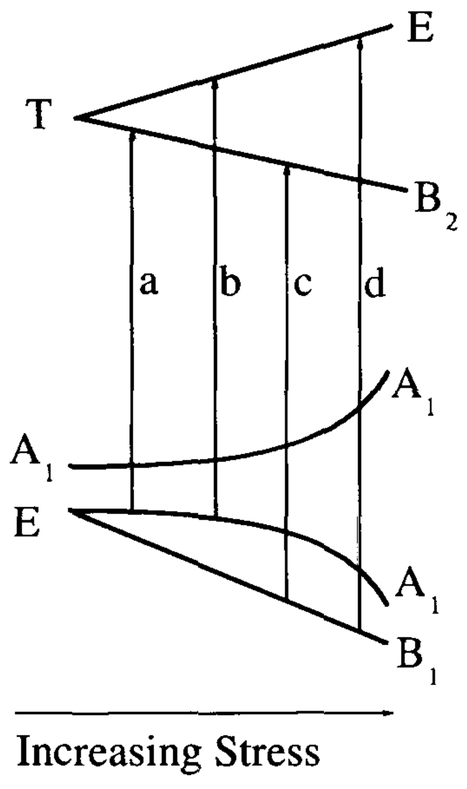

Figure 4.1: Schematic representation of the effect of an applied ⟨001⟩ stress on the energy levels of the vacancy. Transitions shown are those observed under stress from the ground state. This figure is not to scale.

As a result of the coupling the lines originating from these states then shift quadratically with stress, Figure 4.3. The lines on this figure are plotted using the parameters of Davies and Penchina and adopting their notation (itself an amalgamation of Clark and Walker's notation). Transitions b and d are allowed in the ⊥ (perpendicular) polarisation, while a is allowed for E ∥ (parallel) to the stress. Transition c is not dipole allowed in any polarisation but has been observed with E ∥ to the stress by Davies and Penchina [1] and in both polarisations by Clark and Walker [37]. It is seen again in the current work in both polarisations more or less equally. Transition a is observed clearly with E ∥ to the stress and shows through a little in the ⊥ polarisation. Line b is observed equally in both polarisations although extremely weakly and only at low temperature where it is sharp enough to resolve, albeit thermally

depopulated. Clark and Walker also observed this in both polarisations. All these lines are very weak although readily resolved, Fig. 4.2, the only intensely allowed transition in this direction is d, dwarfing the other lines in the $\perp$ polarisation and showing through weakly with E $\parallel$ to the stress (unsurprisingly when it has such an intensity in the other polarisation).

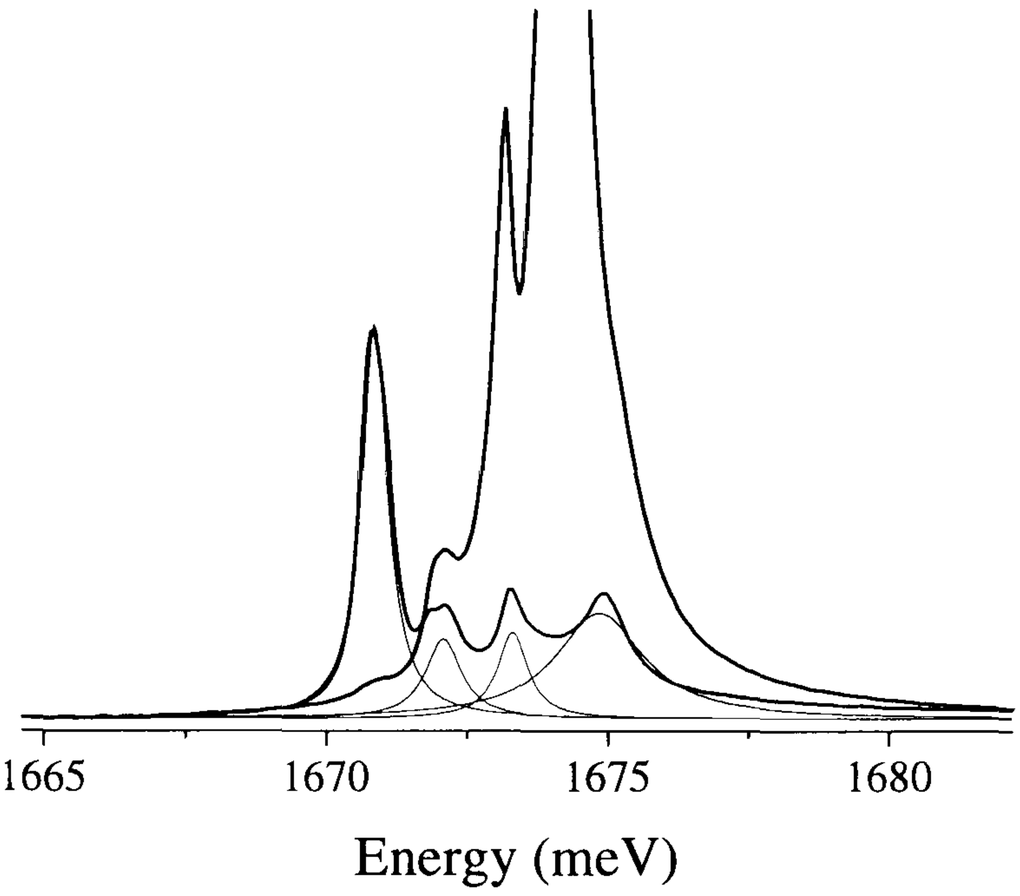

Figure 4.2: Spectrum showing the stress split components of the 1673 meV(GR1) line under $\langle 001 \rangle$ stress, polarisation $\perp$ to stress (black line) and $\parallel$ to stress (grey line). Four distinct components are resolved in both polarisations and are shown deconvolved for the polarisation $\parallel$ to stress case.

Data was recorded for this direction in 3 different experimental runs, one at 77K where only a and d were resolvable and two at lower temperatures. Data from one of the latter runs is shown in Fig. 4.3. Most of the data was in good agreement with Davies and Penchina [1]. The few data points which were not were discarded or calibrated in stress with respect to the published shift rates [1]. This data then proved consistent within the analysis of the stress response of other centres presented later in this thesis.

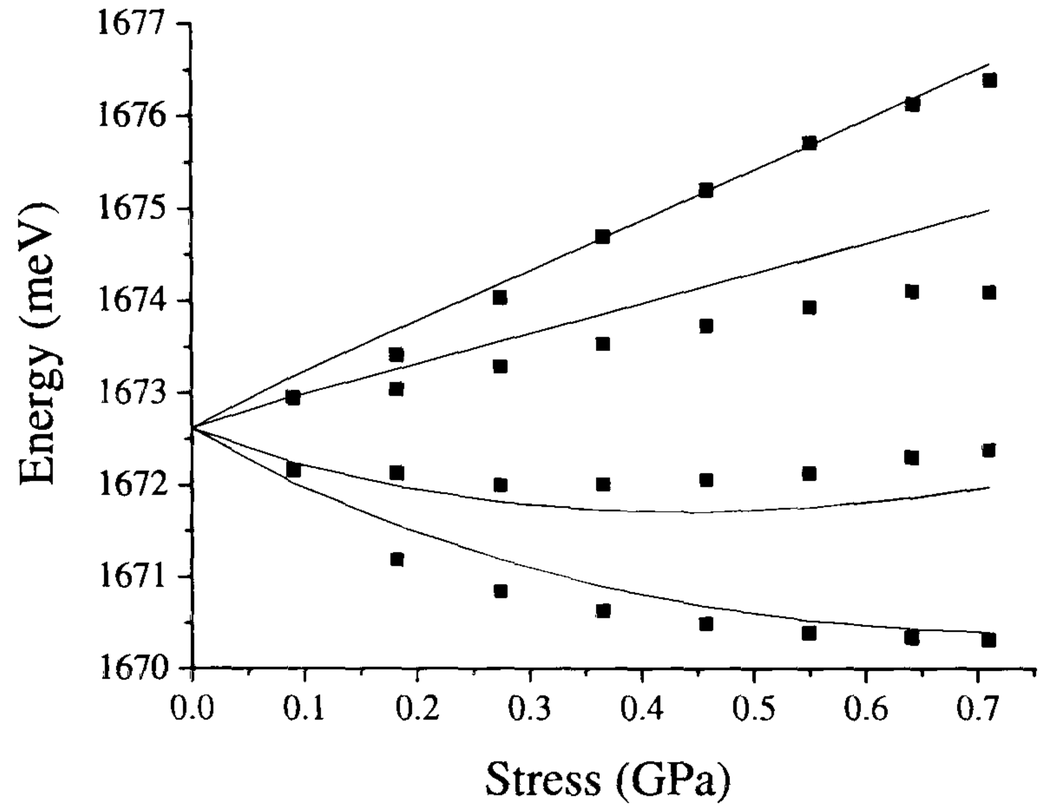

Figure 4.3: Energies of the components of the ⟨001⟩ stress split GR1 as a function of stress. Starting from lowest energy these are labelled a, b, c and d respectivcly. Points show current results, for polarisation see text. Lines are plotted using the theory and parameters of Davies and Penchina [1].

[110] Stress

In this stress direction the degeneracy in the ground and excited states is again lifted by the stress this time into A_1 and A_2 states in the ground state and into A_1, B_1 and B_2 states in the excited state. Again the A_1 states mix Fig. 4.4.

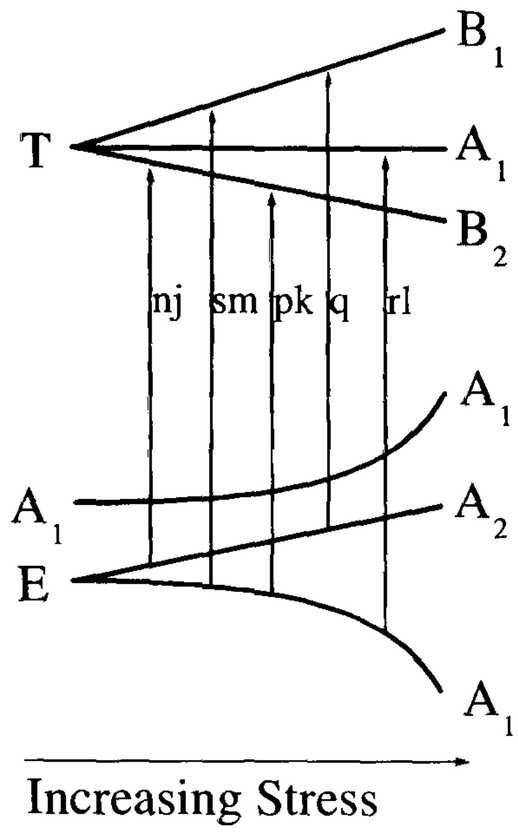

Figure 4.4: Schematic representation of the effect of an applied ⟨110⟩ stress on the energy levels of the vacancy. Transitions shown are those observed under stress from the ground state. This figure is not to scale.

Transitions nj and sm are dipole allowed with E ∥ to the stress; pk, q and rl are allowed with $[1\bar{1}0]$ polarisation and rl is also allowed with [001] polarisation. With E ∥ to the stress transitions nj and sm were both observed with nj absent only at very low temperatures as expected. In some experiments at low stresses, the intense rl line 'showed through' a little in the wrong polarisation and visibly distorted the sm line, whose energy is then only clearly resolved at high stresses; this is apparent in the data points of Fig. 4.5. With $[1\bar{1}0]$ polarisation pk and rl were observed, q is most likely obscured by pk as encountered by Davies and Penchina. The curvature in the shift rate identifies it as pk rather than q. Transition pk was also resolved weakly in the [001] polarisation at low temperature, this is not surprising since it is intense with $[1\bar{1}0]$ polarisation and would be expected to 'show through' a little if the viewing direction is not exactly $[1\bar{1}0]$. The fraction of the forbidden line showing through is tiny.

Six experimental runs were conducted with [110] stress, one run displayed clear hysteresis in the energy shifts, the energy shifts in two other runs were all a little higher than expected, but the remaining data sets were in good agreement with the

published splittings. Where necessary the data was calibrated in stress using the parameters of Davies and Penchina, the data set would be taken as a whole and a set adjustment made to all the stress values to provide the best least squares fit of the GR1 data. Where there was hysteresis two values were used - one for the way up and another for the way down, the fit was then excellent. Adjusting the data set as a whole (or half - up/down) is more accurate than making adjustments point by point, since it averages away the errors in determining the peak positions of the GR1 stress split components. The calibrations used resulted in excellent consistency of data presented later in this thesis for the other centres observed in the same spectra.

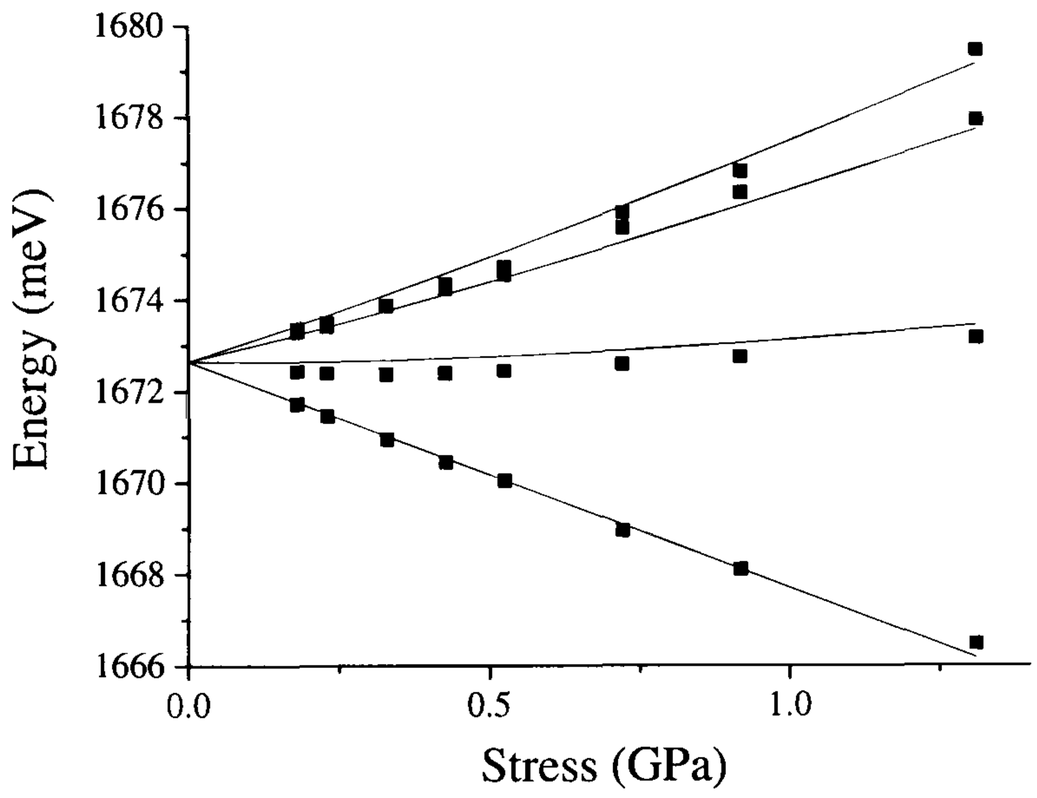

Figure 4.5: Energies of the components of the ⟨110⟩ stress split GR1 as a function of stress. Starting from lowest energy these are labelled nj, pk, rl and sm respectively. Points show current results, for polarisation see text. Lines are plotted using the theory and parameters of Davies and Penchina [1].

⟨111⟩ Stress

In this stress direction the degeneracy in the ground state is preserved while the excited state splits into A_1 and E states Fig. 4.6. There is therefore no mixing of states and no quadratic term in the shift rates of the stress split components Fig. 4.7.

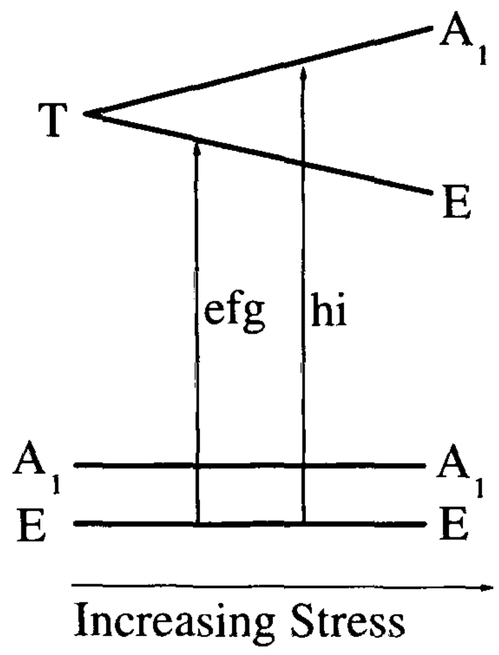

Figure 4.6: Schematic representation of the effect of an applied ⟨111⟩ stress on the energy levels of the vacancy. Transitions shown are those observed under stress from the ground state. This picture is not to scale.

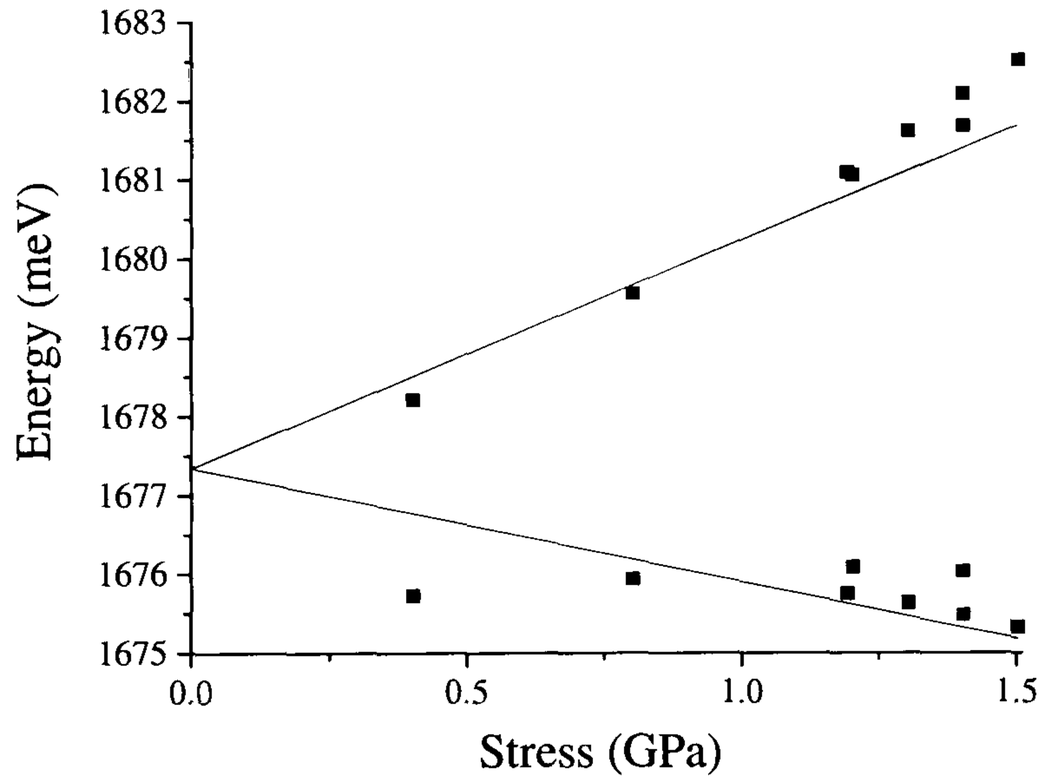

Figure 4.7: Energies of the components of the ⟨111⟩ stress split GR1 in ^{13}C diamond as a function of stress. Starting from lowest energy these are labelled e, f, g and hi respectively. Points show current results, for polarisation see text. Lines are plotted using the theory and parameters of Davies and Penchina [1].

The transition efg Fig. 4.6 is dipole allowed in both polarisations while hi is allowed for E $\perp$ to the stress. Both these transitions are duly observed and in the correct polarisations. One appears to contain many unresolved components to which a single

gaussian has been fitted. Generally in uniaxial stress experiments natural ⟨111⟩ faces are used in preference to polished faces, since it is exceedingly difficult to polish a ⟨111⟩ face on a diamond [61]. The sample used here was synthetic and so its faces were polished and may be a fraction of a degree off ⟨111⟩ giving spurious splitting. During this experiment it was clear that the piston was sticking so the data is calibrated in stress using the GR1. For the interstitial in the following section the calibrated data for this ⟨111⟩ stress is consistent with expectation formed from the results of other directions, suggesting that the calibration is reasonable.

4.3 Summary

The data recorded here is broadly and quantitatively consistent with the work of Davies and Penchina [1] showing that the setup and polarisers are working as they should. Where there was a known experimental problem with the recorded stress values in a given experimental run, the GR1 has proved useful for providing a sensible and self-consistent calibration of the stress, so that use may be made of the data studying the other centres present in those spectra. Many 'forbidden' components were observed in the spectra, all of these were weak and resolvable only at low temperatures (4-40K). The work of Davies and Penchina [1] was conducted at 80K, whilst the work of Clark and Walker [37] was carried out between 20-80K. The appearance of lines at 77K here is in agreement with that of Davies and Penchina. Lines sharpen considerably below this temperature improving resolution. Weakly allowed transitions and spurious effects arising from uneven or misaligned stress or slightly misaligned viewing/polarisation can then become apparent and may need to be considered with skepticism. Consistency of the data as a whole is important and, with this much carefully calibrated data, should be achievable in the analysis.

Chapter 5

The ⟨001⟩-Split Self-Interstitial

5.1 Literature

5.1.1 Calculations in the Literature

In 1973 'Linear-Combination-of-Atomic-Orbitals-molecular-orbitals cluster calculations using the extended Huckel theory' [62], were used to predict that the ⟨100⟩-Split structure was the most stable configuration for a self-interstitial in diamond, with a bond centred structure being the next most stable. These calculations predicted that the minimum energy configuration changes with charge state, so the authors suggested that the Bourgoin-Corbett mechanism of athermal migration [63] may apply to the self-interstitial in diamond in the presence of ionising radiation. Where the minimum energy configuration and so equilibrium position, of an interstitial varies with charge state, Bourgoin and Corbett proposed a mechanism [63] for its athermal migration through the lattice, via a succession of changes of charge state. This may occur, in the presence of ionising radiation, if due to repeated changes in charge state dynamically affecting its configurational potential surface, an interstitial is able to translate to a new lattice site through movement to a new equilibrium position and back again, with respect to its repeating lattice environment. In 1978 calculations showed the ⟨001⟩-split structure to be the most stable (or nearly) in all charge states,

suggesting this mechanism might not occur [64].

Recent calculations using Local-density-functional pseudopotential theory [65] showed that the only truly stable structure for an interstitial atom is the ⟨100⟩-Split structure in the neutral, -1, +1 and +2 charge states. The ground state of the defect was found to have $^1B_1$ symmetry. An upper bound for the energy barrier to the motion of the ⟨100⟩-split interstitial was found to be 1.7eV.

Other recent calculations using supercells with plane waves and soft Troullier-Martins pseudopotentials [66] agreed that a split-⟨001⟩ form of the interstitial is the most likely configuration for the defect.

Defect formation through carbon atom displacement by ion impact has also been studied by molecular dynamics simulations with the Tersoff potential [67]. Again, the most stable defect was found to be an ⟨100⟩-split interstitial, with a bonding configuration described by the authors as resembling graphite. They found that the disrupted region around it, predicted to extend several nanometers, is rich in sp^2 like (graphitic) bonds and proposed that this is the elementary electrically conductive cell found experimentally in radiation-damaged diamond.

First principles calculations using AIMPRO [68, 69] predict a minimum in the energy of the ⟨001⟩-split interstitial (in its ground state) when it has a distorted structure with D_2 symmetry, a distortion that transforms as B_1 in the ideal D_{2d} symmetry [69]. There are two equivalent distortions involving a clockwise or counter clockwise twist of the defect around the principal axis giving two equivalent minima.

5.1.2 Experimental Results in the Literature

The epr centre R2 was identified as the isolated neutral ⟨100⟩-split self-interstitial in diamond ($\mathbf{I}^0_{\langle 001\rangle}$) [28] through measurement of the angular variation of the line width, ^{13}C hyperfine structure and epr of samples annealed under uniaxial stress showing re-orientation of the defect (since this shows the alternative compressed vacancy model for R2 is highly unlikely). The epr signal arises from an excited S=1 state 50meV above an S=0 ground state of the neutral carbon interstitial, indicating that two

unpaired electrons are responsible for the epr. The ground state is non-paramagnetic. Through analysis of the angular variation of the ^{13}C line broadening, this unpaired electron probability density was localised in the two non-bonding p_π orbitals on the two principal C atoms of the ⟨001⟩-split self-interstitial, as depicted in Fig. 2.3, R2 has D_{2d} symmetry in this paramagnetic excited state with S=1, 50 meV above the ground state (S=0) which cannot be observed using epr.

The intensities of lines observed in optical absorption at 1685 and 1859 meV correlate with the concentration of R2 observed in epr [28, 29]. The lines also show the same annealing behaviour as R2 [28, 29] identifying them with the self-interstitial.

The isothermal annealing of the 1859 meV line at 460K shows that it anneals out following first order kinetics with an activation energy of 1.68 ± 0.15 eV [70]. For the first time this was correlated with rapid annealing of a proportion of the GR1 and attributed to the migration of interstitials to vacancies followed by mutual annihilation, although at this time the 1859 meV line was thought only to be interstitial related, it was not known that it was the interstitial. More recent isochronal anneals yielded a value of 1.6 eV [71, 72]. These values do not challenge the upper bound for the energy barrier to the motion of the ⟨100⟩-split interstitial of 1.7 eV calculated previously from theory [65].

The 1685 meV line was originally thought to be a transition at the GR1 centre [73] but later work showed that it was not [37, 1]. The 1859 meV line, reported in Gordon Davies thesis [74], was also incorrectly attributed to the GR1 centre until Walker [29] showed that the 1685 and 1859 meV lines were due to the same defect by establishing that they correlate in intensity, display complementary thermal behaviour and anneal at the same time at lower temperatures than the GR1. He referred to both as zero-phonon lines. He also linked the defect to R2, now known to be the self-interstitial. The activation energy of the decrease in intensity of the 1685 meV with decreasing temperature was measured as 6 ± 2meV [73, 37]. Using this value and Boltzmann statistics to fit the 1859 intensity variation with temperature Walker [29] established an energy scheme involving singlet states 6, 1692 and 1859 meV above the ground

state, where transitions of 1685 and 1859 meV, from the 6 meV and ground states respectively, are the only allowed transitions. As a result of his studies of the dose dependence of the production of R2 Walker believed that the defect must involve an impurity and so ruled out the ⟨100⟩-split interstitial, although he did believe the centre was basically an interstitial complex.

Walker later published uniaxial stress data on the 1685 and 1859 meV lines, that he referred to as 'the tetragonal defect' as part of a review on defects in diamond [51]. The data were described as 'indicating this (tetragonal) symmetry for the optical lines'. A full analysis of the data was not included, so the conclusions were qualitative.

Recent studies of these optical lines in ^{13}C diamond [47] presented later in this chapter, show a negative isotope shift in the 1859 meV line indicating that the transition involves a local mode of vibration of $\mathbf{I}^0_{\langle 001\rangle}$ with quantum 168.6(1) meV. The temperature dependence measurements were repeated and confirmed that the 1859 meV transition originates from the ground state of the defect while the 1685 meV transition originates from a state 6.2(5) meV above the ground state. All energies correspond to ^{12}C diamond unless otherwise stated.

Equal concentrations of vacancies and interstitials are produced by irradiation at temperatures below about 100K. Above this temperature, recombination-enhanced diffusion of self-interstitials occurs under the conditions of electron irradiation and the resulting interstitial concentration is 1/3 of the vacancy concentration [71].

5.1.3 Interpretations in the Literature

With respect to the mobility of the interstitial during irradiation, the authors who reported it [71] propose that the fall in interstitial concentration to 1/3 of the vacancy concentration for irradiation above 100K is due to the creation of a highly mobile interstitial, I^*, (possibly a T_d interstitial) by electronic excitation and/or charge transfer, with migration energy 0.3eV. A conclusion that there is a significant barrier to vacancy-interstitial recombination in diamond arose from the same data.

The results of isotopic substitution and temperature dependence studies on the

1859 meV line have been used to show the transition originates in a dipole-forbidden electronic transition that is made allowed by mixing with the 1685 meV transition through a vibrational mode [47]. These data and the unusually small splitting in the ground state were explained as the result of a dynamic distortion, as vibrations of the centre mix the vibronic progressions of the two states [47] reducing their separation by orders of magnitude and lowering their energy below that of the epr state. Without this interaction the epr active state might be expected to be the ground state of the defect. The distortion results in a potential surface with two equal minima for the positive and negative distortion and a saddle point at zero displacement. Although the symmetry of the deformation was not determined the minimum energy positions are in close agreement with those later predicted by Goss et al [69] for a B_1 distortion.

First principles calculations using AIMPRO have been used [68, 69] to confirm the assignment of R2 and to model the optical properties, proposing an inversion-doubling process to give rise to the 6 meV splitting in the ground state so that the 1685 and 1859 meV transitions can be understood as being transitions between states made up from the p-orbitals on the two principal carbon atoms of $\mathbf{I}^0_{\langle 001\rangle}$. These calculations predict a minimum in the energy of I_0 (in its ground state) when it has a distorted structure with D_2 symmetry, a distortion that transforms as B_1 in the ideal D_{2d} symmetry [69]. There are two equivalent distortions involving a clockwise or counter clockwise twist of the defect around the principal axis giving two equivalent minima (the inversion doubling giving rise to the 6 meV splitting exists because the centre can distort equally in two directions in this way). States corresponding to the two minima would be coupled and split by tunnelling. This, it was supposed, is the 6 meV splitting observed in the ground state of the defect [69].

5.1.4 Related Centres in Other Materials

The structure of $\mathbf{I}^0_{\langle 001\rangle}$ in diamond is similar to that of the carbon interstitial in silicon [75] where the change of species lowers the symmetry to C_{2v} and for split carbon interstitial - group V substitutional atom defects identified in silicon [76].

5.2 Isotopic and Temperature Dependence of Absorption at the Interstitial

5.2.1 Temperature Dependence

The intensity of the 1859 meV absorption line increases with decreasing temperature, saturating below about 20K, while the intensity of the 1685 meV absorption line falls until the line disappears below 20K. Their behaviour is complementary, Fig. 5.1. Qualitatively this shows that the 1859 meV transition originates from the ground state of the defect, which will be fully populated at low temperatures, while the 1685 meV transition originates from an excited state which is thermally populated as the temperature is raised. The data can be quantitatively fitted in terms of a Boltzmann distribution in the population of the respective non-degenerate ground states of these two transitions. The fit is a function of the separation of the ground states, E_g, and the temperature T, and is related to the intensities of the transitions by their probabilities measured from their intensities when fully populated, I_0^{1685} and I_0^{1859}. The functions are as follows:

$$\begin{aligned} I^{1859}(T) &= \frac{(I_0^{1859})}{1+e^{-E_g/kT}} \\ I^{1685}(T) &= \frac{(I_0^{1685})\,e^{-E_g/kT}}{1+e^{-E_g/kT}} \end{aligned} \tag{5.1}$$

The best fit to the data gives $E_g = 6.2 \pm 0.5$ meV on average over the temperature range 2 to 180 K and I_0^{1685} / $I_0^{1859} = 0.45 \pm 0.05$ meV [47]. The data demonstrates the closely spaced doublet nature of the ground state.

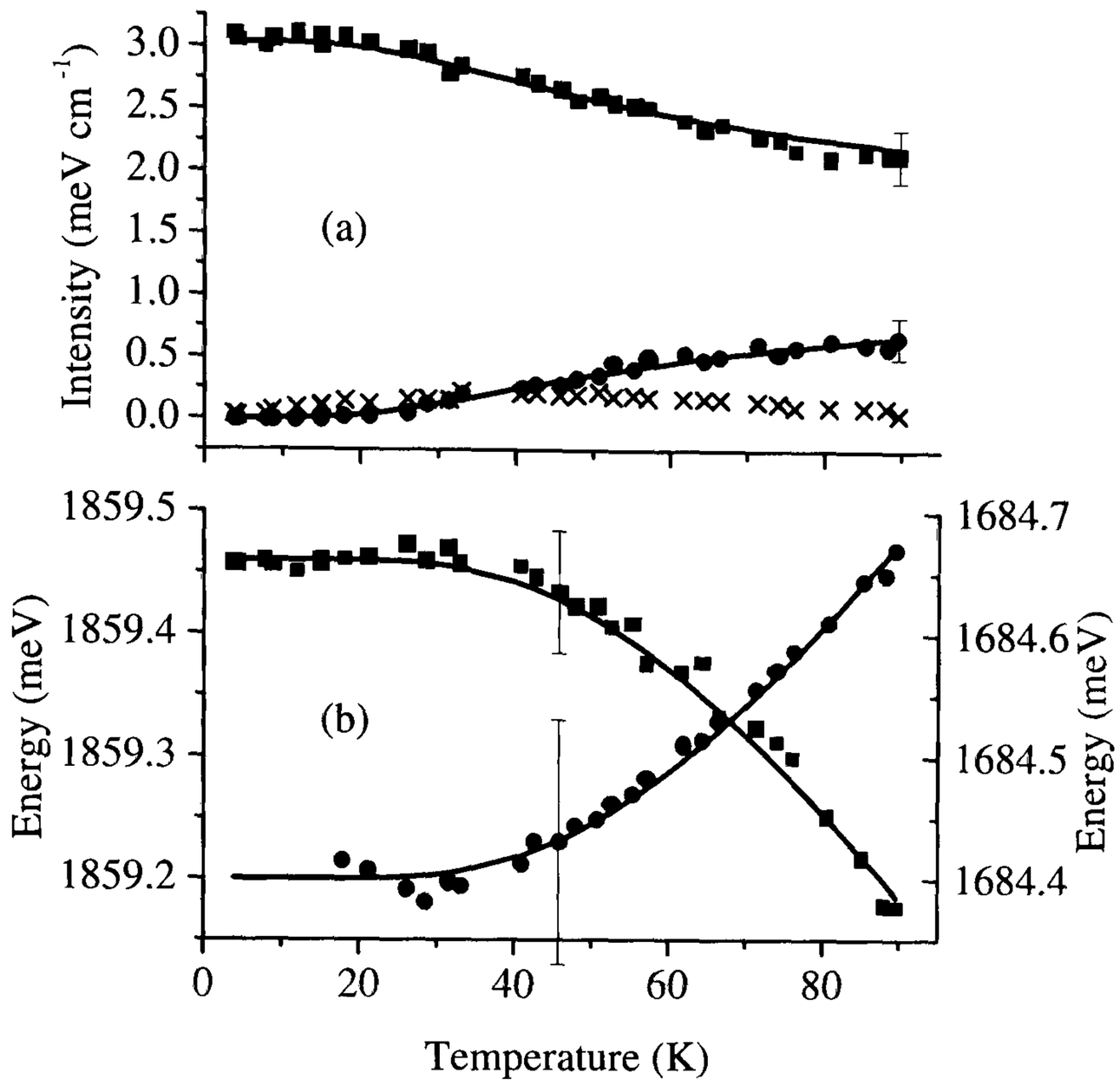

Figure 5.1: (a) Intensity of the 1859 (squares) 1685 (circles) and 1691 meV lines (crosses) as a function of temperature. (b) Energies of the 1685 and 1859 meV lines as a function of temperature. Lines are plotted using the best fit of Eqn. 5.2 to the data given by the parameters in the text.

Walker [29] first showed that the 1685 and 1859 meV lines have complementary thermal behaviour. In agreement with the new measurements presented above the activation energy of the decrease in intensity of the 1685 with decreasing temperature was quoted as 6 $\pm$ 2 meV [73]. Using this value and Boltzmann statistics to fit the 1859 intensity variation with temperature Walker established an energy scheme involving singlet states 6, 1692 and 1859 meV above the ground state, where the 1685 and 1859 meV transitions from the 6 meV and ground states respectively are the only allowed transitions, both referred to as ZPL's. This scheme is broadly confirmed by the new data, although it will be shown in the next section that the 1859 meV line is not a ZPL, a discovery that will lead to an exploration of the ground state splitting.

In addition, the new measurements presented in this thesis show that the energies of the transitions also change with temperature. The 1859 meV line shifts to lower energy with increasing temperature, while the 1685 meV line shifts to higher energy at a complementary rate, Fig. 5.1. This reduction in the ground state splitting as the temperature is raised, may be interpreted as resulting from a resonant interaction of diamond band modes with the small splitting energy, arising from the closely spaced doublet nature of the ground state. Thus the effect may be readily parameterised; the lines fitted to the data of Figure 5.1 are plotted from:

$$E\left(T\right) = E\left(0\right) \pm \frac{a}{e^{(b/kT)} - 1} \tag{5.2}$$

where the best fit to the data gives the energies of the transitions in the limit of low temperature, $E(0) = 1859.5$ and 1684.4 meV respectively, $a = 2.05$ meV and b (the quantum of the effective vibrational mode) $= 16.5$ meV.

The interaction increases with temperature as the modes are populated, parameterised by the Bose-Einstein phonon distribution:

$$n\left(\omega, T\right) = \frac{1}{e^{\hbar\omega/kT} - 1} \tag{5.3}$$

for phonons of frequency ω at temperature T. This part of Eqn. 5.2 is therefore effectively a phonon occupation factor. The parameter b of Eqn. 5.2 is then an estimate of the energy of the effective vibrational modes that are interacting with the split ground state and the parameter a is a coupling coefficient that parameterises the effectiveness of these phonons at driving the coupling of these states.

5.2.2 Absorption Spectrum of ^{13}C Diamond

The effect of Carbon isotope doping on the 1685 and 1859 meV lines has been measured, spectra are shown in Fig. 5.2 in the 1859 meV region. On changing from natural abundance to ^{13}C diamond the 1685 meV line shifts by $+1.7 \pm 0.2$ meV, while the 1859 meV line shifts by -5.35 ± 0.25 meV, [47]. Large negative isotope shifts are unexpected for zero-phonon lines produced by radiation damage in diamond [30].

while local vibrational modes are likely to produce a negative shift since vibrational frequencies are reduced in the ratio $\sqrt{12/13}$ on changing from ^{12}C to ^{13}C. From this data it is concluded that the 1859 meV line is a phonon side-band and not a zero-phonon line [47].

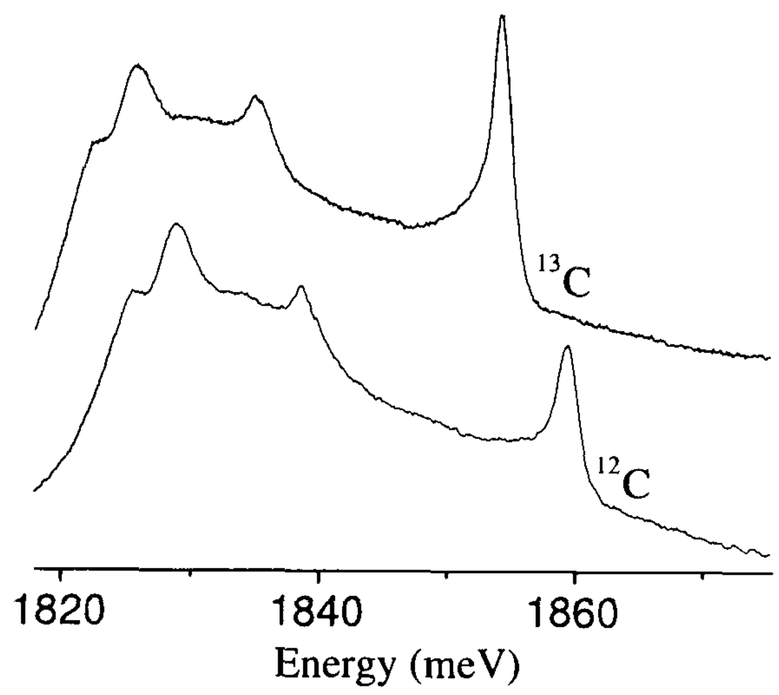

Figure 5.2: Isotope shift of the 1859 meV line, bumps to lower energy are the optic modes of $\mathbf{V}^0$.

From the energies of the 1685 and 1859 meV transitions and the ground state splitting, E_g, determined in the last section, the quantum of the phonon involved in the 1859 meV transition can be determined as $\hbar\omega = 168.6 \pm 0.9$ meV [47] [1].

The maximum vibrational quantum in the diamond molecule is about 166 meV at room temperature [77], so the vibration associated with the 1859 meV transition is not in the phonon continuum of diamond, it's a local mode; but only just. This is reflected both in the sharp nature of the line (characteristic of local modes) and the only slightly broadened, structureless nature of the line in a sample with mixed isotopes [47] that is characteristic of shallow (extended) local modes [78]. This proximity to the diamond phonon continuum later led Davies et al [79] in a separate piece of work,

[1] using the value for E_g determined from the temperature dependence in the last section - this was some average over the temperature range 2 to 180 K. However, it was also shown in the last section that the 1685 and 1859 meV transitions vary in energy with temperature. This means that E_g varies with temperature, so to find an accurate value for $\hbar\omega$ requires measurement of E_g and the energy of the 1859 meV transition at the same temperature. This will be done spectroscopically at low temperature later in Section 5.3.3

to fit the apparent asymmetry of the line to low energy, in terms of coupling into the continuum; the fit was qualitative and so assumed the strength of the coupling is sufficient to produce the observed asymmetry.

The temperature dependence of this phonon assisted transition has shown that it originates from the ground state of $I^0_{\langle 001\rangle}$. The corresponding zero-phonon line is generally not observed (this will be re-visited later under stress) and has been assumed in the analysis of [47], (described below and extended later in this thesis) to be a forbidden transition that is made allowed by mixing with a phonon resulting in the 1859 meV line. The electronic excited state of the 1685 meV zero-phonon transition is the excited state of this forbidden ZPL and so is the electronic component of the 1859 meV vibronic excited state (see Fig. 5.3). There are no higher order phonon-sidebands than the 1859 meV one phonon transition observed.

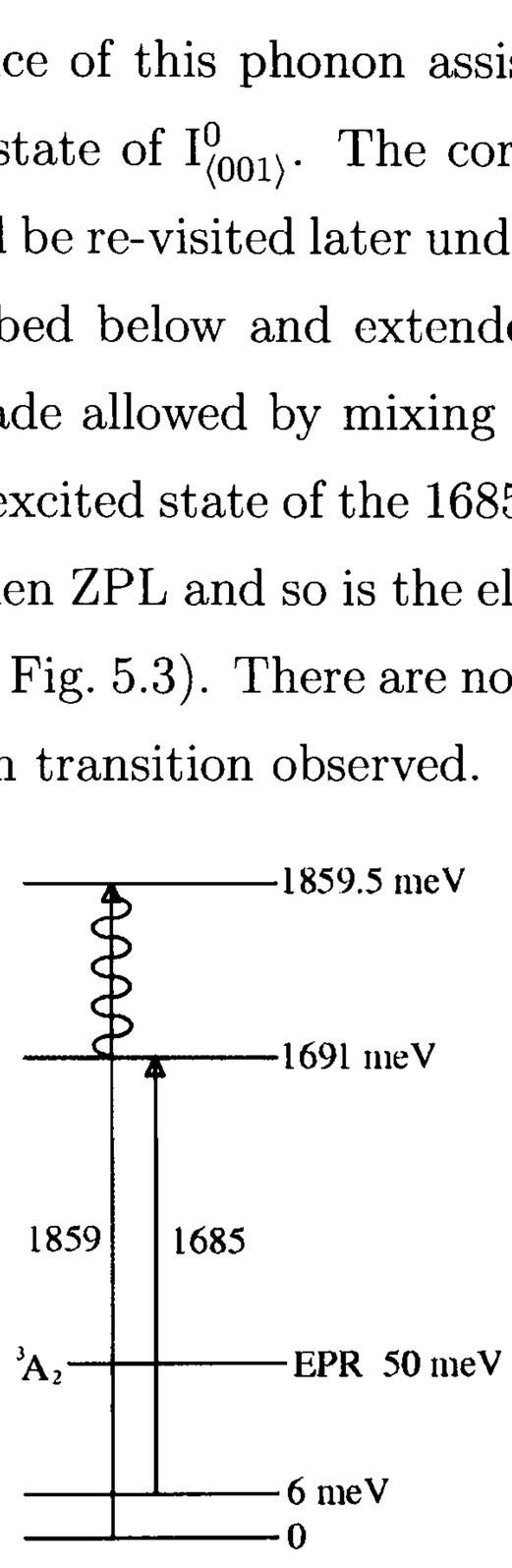

Figure 5.3: Energy levels of $\mathbf{I}^0_{\langle 001\rangle}$. Wavy line represents a phonon, allowed optical absorption transitions are shown as vertical arrows.

A vibronic coupling model is therefore proposed and developed [47] consistent with the magnitude of isotope shift and allowed transitions, using the basic theory explained at the end of the Theory Chapter in the vibrational coupling section (2.3).

Setting $\hbar\omega = 1$, Fig. 5.4, the matrix (Table 2.14) may be diagonalised[2] in units of

[2]Of course the calculation must be done for a finite number of phonons, in this case 34 is just

$\hbar\omega$. The diagonal elements (Fig. 5.5) then give the energy eigenvalues of the coupled system so that the difference in energy of the lowest two is the observed energy separation, E_g, of the split ground state. The corresponding eigenvectors may also be calculated, Fig. 5.6. Note the vectors are given by the program in columns rather than rows as depicted in Table 2.15.

	A0	B0	A1	B1	A2	B2	A3	B3	A4	B4	A5	B5	A6	B6
A0	0.5	0	0	1.365	0	0	0	0	0	0	0	0	0	0
B0	0	1.85	1.365	0	0	0	0	0	0	0	0	0	0	0
A1	0	1.365	1.5	0	0	1.93	0	0	0	0	0	0	0	0
B1	1.365	0	0	2.85	1.93	0	0	0	0	0	0	0	0	0
A2	0	0	0	1.93	2.5	0	0	2.364	0	0	0	0	0	0
B2	0	0	1.93	0	0	3.85	2.364	0	0	0	0	0	0	0
A3	0	0	0	0	0	2.364	3.5	0	0	2.729	0	0	0	0
B3	0	0	0	0	2.364	0	0	4.85	2.729	0	0	0	0	0
A4	0	0	0	0	0	0	0	2.729	4.5	0	0	3.052	0	0
B4	0	0	0	0	0	0	2.729	0	0	5.85	3.052	0	0	0
A5	0	0	0	0	0	0	0	0	0	3.052	5.5	0	0	3.343
B5	0	0	0	0	0	0	0	0	3.052	0	0	6.85	3.343	0
A6	0	0	0	0	0	0	0	0	0	0	0	3.343	6.5	0
B6	0	0	0	0	0	0	0	0	0	0	3.343	0	0	7.85

Figure 5.4: Partial vibronic coupling matrix, calculated using the theory of Section 2.3, Table 2.14, with $\hbar\omega$=1, $E_0 = 1.35\hbar\omega$ and $c\sqrt{\frac{\hbar}{m\omega}} = 1.93$.

about the limit of the programme (a 70 x 70 matrix), repeating the calculation for successively increasing numbers of phonons, up to this limit, shows that the energies and eigenvectors converge to the required accuracy. Also, it is clear from the eigenvector matrix that there is an insignificant proportion of the highest phonon states mixed into the states of interest. Unsurprisingly the proportion falls with increasing phonon number.

	a	b	c	d	e	f	g	h	i	j	k	l	m	n
A0	0.106	0	0	3E-11	3E-12	0	0	0	9E-10	0	0	8E-12	9E-13	0
B0	0	2.478	-0	0	0	3E-09	-0	0	0	7E-12	-0	0	0	-0
A1	0	-0	-0.74	0	0	2E-14	-0	0	0	-0	2E-08	0	0	-0
B1	3E-11	0	0	4.391	6E-08	0	0	2E-14	-0	0	0	-0	-0	0
A2	3E-12	0	0	6E-08	-0.78	0	0	-0	7E-11	0	0	7E-10	-0	0
B2	0	3E-09	2E-14	0	0	6.238	1E-07	0	0	2E-12	2E-14	0	0	-0
A3	0	-0	-0	0	0	1E-07	0.315	0	0	3E-10	-0	0	0	-0
B3	2E-17	0	0	2E-14	-0	0	0	7.391	5E-13	0	0	2E-16	1E-08	0
A4	9E-10	0	0	-0	7E-11	0	0	5E-13	1.058	0	0	3E-07	-0	0
B4	0	7E-12	-0	0	0	2E-12	3E-10	0	0	8.448	-0	0	0	-0
A5	0	-0	2E-08	0	0	3E-14	-0	0	0	-0	1.448	0	0	3E-08
B5	8E-12	0	0	-0	7E-10	0	0	5E-18	3E-07	0	0	10.32	-0	0
A6	9E-13	0	0	-0	-0	0	0	1E-08	-0	0	0	-0	5.159	0
B6	0	-0	-0	0	0	-0	-0	0	0	-0	3E-08	0	0	11.41

Figure 5.5: Partial vibronic coupling matrix diagonalised to give energy eigenvalues. Lowest energy states are c and e. E_0=1.35 and $c\sqrt{\frac{\hbar}{m\omega}}$=1.93.

	a	b	c	d	e	f	g	h	i	j	k	l	m	n
A0	0.65	0	0	0.204	0.508	0	0	0.027	0.428	0	0	0.002	0.096	0
B0	0	0.595	-0.32	0	0	0.072	0.39	0	0	0.01	-0.41	0	0	8E-04
A1	0	0.273	0.607	0	0	0.231	-0.44	0	0	0.05	0.122	0	0	0.006
B1	-0.19	0	0	0.581	-0.48	0	0	0.137	0.175	0	0	0.017	0.327	0
A2	-0.19	0	0	0.32	0.536	0	0	0.303	-0.47	0	0	0.064	0.324	0
B2	0	-0.28	-0.48	0	0	0.517	-0.01	0	0	0.172	0.29	0	0	0.029
A3	0	-0.06	0.435	0	0	0.333	0.368	0	0	0.294	-0.39	0	0	0.089
B3	0.349	0	0	-0.22	-0.35	0	0	0.515	0.141	0	0	0.197	0.097	0
A4	-0.44	0	0	-0.24	0.267	0	0	0.217	0.207	0	0	0.34	-0.27	0
B4	0	0.266	-0.26	0	0	-0.11	-0.42	0	0	0.384	0.045	0	0	0.233
A5	0	-0.24	0.176	0	0	-0.31	0.439	0	0	0.064	0.287	0	0	0.345
B5	0.32	0	0	0.204	-0.14	0	0	-0.25	-0.36	0	0	0.472	-0.15	0
A6	-0.25	0	0	0.069	0.087	0	0	-0.24	0.434	0	0	0.18	0.319	0
B6	0	-0.03	-0.09	0	0	0.034	-0.29	0	0	-0.29	-0.39	0	0	0.398

Figure 5.6: Partial eigenvectors for coupled states, calculated using the theory of Section 2.3, Table 2.15. E_0=1.35 and $c\sqrt{\frac{\hbar}{m\omega}}$=1.93. The eigenvectors are not normalised, although, since only the ratio of two of the coefficients is of interest, this does not matter. Lowest energy states are c and e, see Figure 5.5.

At an undistorted defect where the minimum mode in the potential surface for the vibration is at the same value of Q in the ground and excited states, $Q_{min}^{ground} = Q_{min}^{excited}$ transitions are only allowed for $\phi_g\chi_a$ to $\phi_e\chi_b$ for $a = b$. This breaks down when Q_{min} is one of the states involved is moved by a distortion, so that $Q_{min}^{ground} \neq Q_{min}^{excited}$. The observation of a transition such as the 1859 from the ground to a one-phonon state is an indication that the vibration is interacting with one of the states in some way. In this case a dynamic distortion in the ground state.

Using the labels A and B for interacting ground states (used in the figures) the undistorted defect transitions are allowed from B to a state much higher energy E

and are forbidden from A. They are therefore allowed from B00 to E00 and from B01 to E01 and so on.

Experimentally the 1859 meV one phonon transition is observed from the lowest energy coupled state, (whose energy and eigenvector is given in column e Figs 5.5 and 5.6) to the one phonon state E01. Since transitions to this E01 state are only quantum mechanically allowed from B01 in the uncoupled configuration, the coefficient of this state in the makeup of eigenvector e (row B01, column e Fig. 5.6) gives the effect of the coupling on the transition probability of the 1859 (raises it from zero). The negative sign is of no consequence since the transition probability is proportional to the square of the eigenvector. Likewise, experimentally the 1685 meV zero phonon transition is observed from the second lowest energy state (whose eigenvector is given in column c Figs 5.5 and 5.6) to the zero phonon state E00. Since transitions to this E00 state are only allowed from B00 in the uncoupled configuration, the co-efficient of this state in the makeup of eigenvector c (row B00, column c, Fig. 5.6) gives the effect of the coupling on the transition probability of the 1685 (lowers it from 1). The ratio of these two numbers squared can then be compared to the experimental ratio of the intensities of these two lines.

There are then two unknowns E_0 and c (as defined in Section 2.3) to be fitted with two measured values E_g and the intensity ratio.

The ratio of the intensities of the 1685 and 1859 meV lines (0.45 ± 0.05 meV) and the measured separation of the coupled states ($E_g = 6.2 \pm 0.5$ meV) can be fitted with a separation of the uncoupled states at the undistorted configuration of $E_0 = 230 \pm 50$ meV and a coupling strength of $c\sqrt{\frac{\hbar}{m\omega}} = (1.93 \pm 0.009)\,\hbar\omega$.

The energies (relative to the uncoupled energy of which state A, which forms the origin) of the states are plotted in Fig. 5.7 for $E_0 = 230 \pm 50$ meV as a function of the coupling strength. The reason the energy separation of the two lowest observed states can be lowered by the distortion so dramatically (two orders of magnitude) was described in Section 2.3 and the shift of the two lowest states as a function of c in Fig. 5.7 qualitatively matches that shown in Fig. 2.10 of that section. The behaviour

of the higher energy states with increasing distortion is more chaotic than for the lower two states, since they are interacting with states both from above and from below, Fig. 2.7.

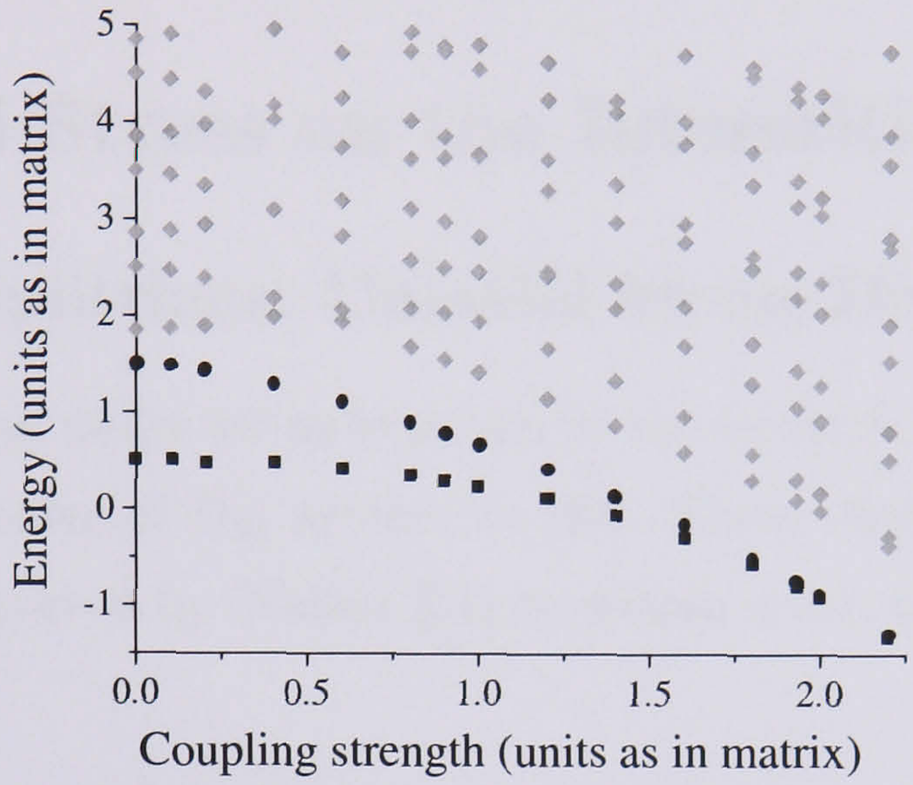

Figure 5.7: Energy eigenvalues as a function of increasing coupling strength, lowest two energies shown in black.

This model will be revisited and extended later in Section 5.3.10.

5.2.3 Progress in this Section

The energy level scheme for $\mathbf{I}^0_{\langle 001 \rangle}$ takes the form shown in Fig. 5.3 with a ground state splitting of 6.2 ± 0.5 meV on average between 2 and 180K. The 1859 meV absorption line displays a negative isotope shift, indicating that the transition involves a phonon, of quantum determined to be about 168 meV; a shallow local mode.

The energies of the two allowed transitions change subtly with temperature in a well defined manner corresponding to a reduction in the ground state splitting with increasing temperature which has been parameterised.

A vibronic coupling model is proposed that is consistent with the data, this produces a dynamic distortion of the centre and lowers the energies of two spin 0 states below that of the spin 1 epr state resulting in a non-paramagnetic ground state for

$\mathbf{I}^0_{\langle 001\rangle}$.

The symmetry of the ground state, vibration and dynamic distortion have not been determined.

5.3 Uniaxial Stress on the Interstitial

5.3.1 Energy Splittings: Uniaxial Stress Data

The appearance of lines under stress is shown in the example spectra in Fig. 5.8 and is consistent with a centre of D_{2d} symmetry [40]. These data are essentially consistent with the data reported by Walker [51] to within error, but with two significant differences;

1. For $\langle 110\rangle$ stress with the polariser parallel to the stress the shift rates for both lines should be the same whatever the viewing direction. For the 1685 meV line in Walker's data they don't appear to be (they may be plotted on different scales although they are not labelled as such).

2. Walker did not report observing the 1692 or 1864 meV lines induced by stress. There are three reasons why this might be. First, Walker's experiment was done using a dispersive spectrometer, so he may not have recorded spectra up to a high enough energy above the lines of interest under stress. Secondly, both transitions originate from the ground state, for measurements recorded at about 80K their intensities may be too small to observe at low stresses. Thirdly, there are lines at 1691 and 1693 meV (in our samples, the latter is also reported by Clark and Walker [73]) at zero stress due to some other defect, if this appeared in his samples then without careful measurement at very low stress, the 1692 meV induced line may be assumed to originate at either energy and so may have been discounted.

This is easy to believe: in the current work, from preliminary data recorded at 77K, the rapidly shifting 1692 meV stress induced line (+4 meV in the first GPa) was

initially traced back to the 1691 meV line at zero stress in the absence of intermediate spectra, that show the latter disappearing under very little stress whilst the former grows up starting just 1 meV to higher energy. This induced line was also only clearly visible above the noise in one stress direction at this temperature.

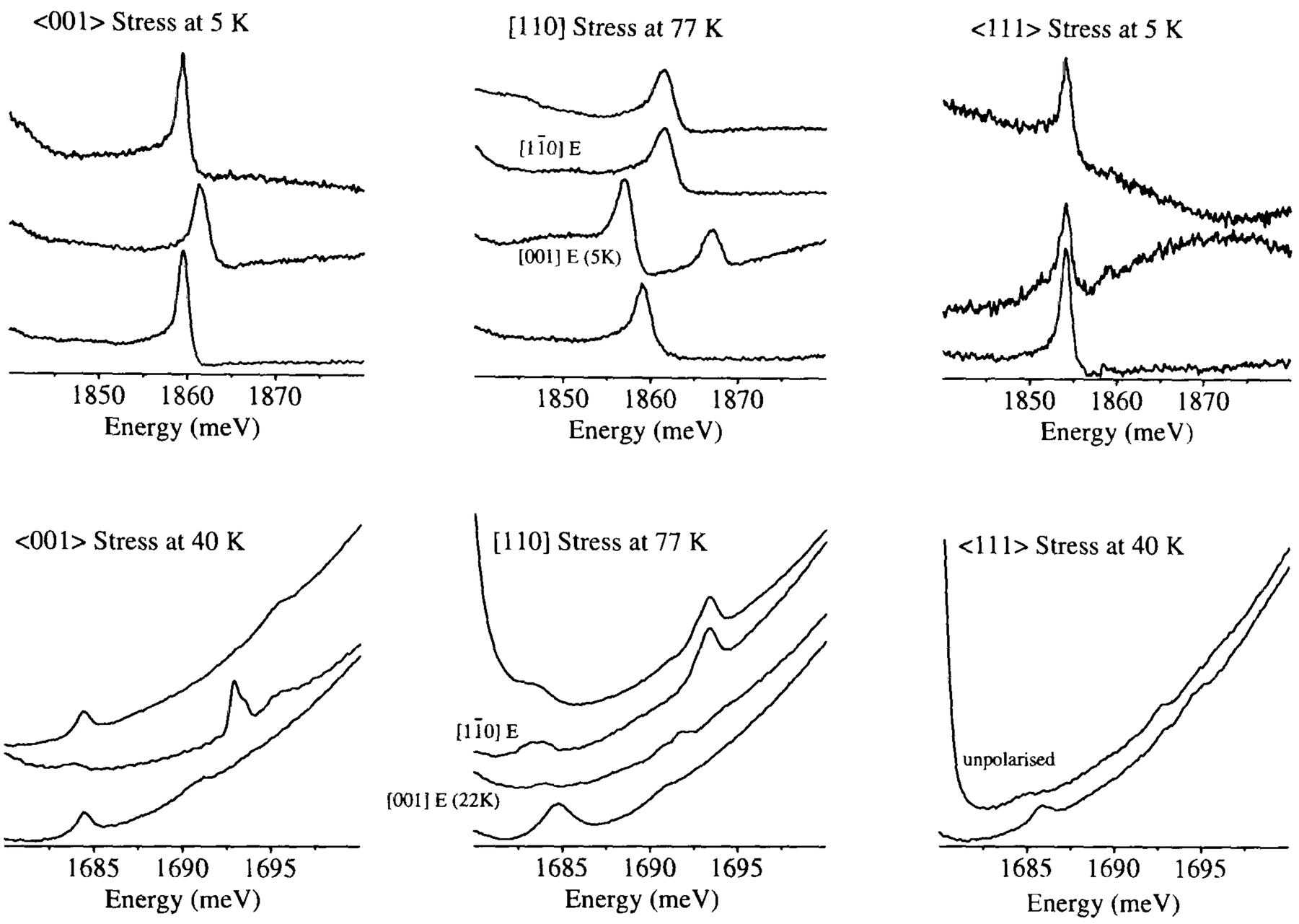

Figure 5.8: The effects of stress on the absorption spectra near 1685 meV (bottom row) and 1859 meV (top row), for uniaxial stresses applied as indicated. In each diagram the lowest spectrum is at zero stress, and the top spectrum was recorded with an applied stress and with electric vector **E** parallel to the stress axis. The middle spectrum was recorded under the same stress and with **E** perpendicular to the stress axis, with the specific directions shown for [110] stress. For ⟨111⟩ stress, the spectra were measured in a small ^{13}C sample, and to increase the signal-to-noise ratio the stressed spectrum for the 1685 meV region is shown unpolarised. To optimise the signals, the spectra were measured at the temperatures indicated.

The change in energy as a function of increasing applied uniaxial stress of the 1685 and 1859 meV absorption lines in the spectra of polarised light is shown in Fig. 5.9 for stress applied along the ⟨001⟩, ⟨110⟩ and ⟨111⟩ crystallographic directions. The applied strain is much less than the strain (or displacement) associated with typical zero point oscillations of an atom. Note that the data for ⟨111⟩ stress were taken using a ^{13}C sample; this produces a shift in the zero stress position of the lines (this has been taken into account during the analysis) but should not affect the shift rates, since the elastic constants of diamond are little affected by the change of isotope [80]. Data were also taken at different temperatures to optimise the intensity of the various transitions while maintaining a narrow line width. Where stress data have been recorded at different temperatures, the effect of the small shift in energy with temperature (Section 5.2.1) has been taken into account.

The first thing to note from the data of Fig. 5.9 is that the linear component of the shift rates is negligible in all the perturbations. In fact, the shift rates can be reasonably fitted entirely using terms quadratic in the stress. This indicates that the dominant perturbations are interactions between the states as described in the Theory Chapter, Section 2.2.4.

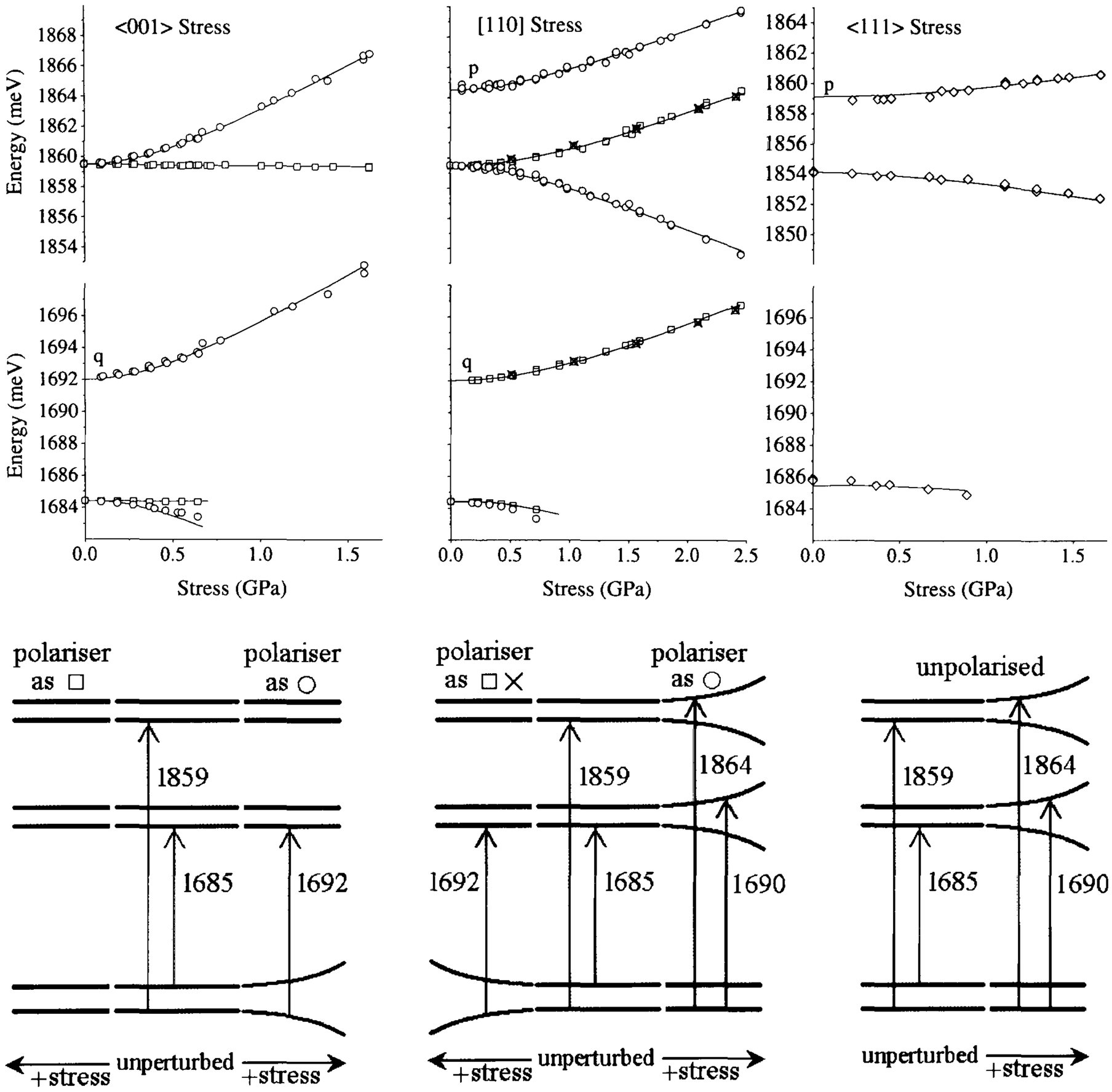

Figure 5.9: The energies of the optical transitions as functions of stress applied along the ⟨001⟩, ⟨110⟩ and ⟨111⟩ axes. Data recorded with light polarised parallel to the stress axis are shown by squares, and with perpendicular polarisation by circles. For [110] stress, the circles show specifically the perpendicular polarisation with electric vector $\mathbf{E} \parallel [001]$ and the crosses show $\mathbf{E} \parallel [1\bar{1}0]$. The ⟨111⟩ data were taken using a small ^{13}C sample, and to increase the signal/noise ratio they were recorded with unpolarised light. The lines are calculated as in Section 5.3.5, with the assumption that the shift rates are independent of the isotope. Energy level schemes are shown to aid interpretation, but are not to scale.

5.3.2 Annealing of Stress Induced Lines

In the limit of low stress, under varying conditions, four distinct lines can be identified at 1690, 1691, 1692 and 1693 meV. All these lines may shift, split and sometimes grow or disappear with stress. Under an applied stress the lines and their components can just be distinguished through careful tracking of their movements at low stresses and knowledge of their temperature dependence. However this does not identify the defect origin of the transitions. The role of annealing in identifying transitions that belong to the same defect was highlighted at the end of Section 2.1.

To establish which of these transitions originate at $\mathbf{I}^0_{\langle 001\rangle}$ the intensities of the 1691, 1692 and 1693 meV lines have been investigated as a function of isochronal annealing. The sample was annealed at 550, 600, 675, 725 and 775K each for one hour. To observe the 1692 meV line with an appreciable intensity requires the application of stress, so spectra were recorded with an applied stress after each anneal. After the 550 and 600K anneals there was no appreciable change in the intensity of any of the lines. After the anneals at 675, 725 and 775 K the intensity of the 1859 meV line, known to be due to $\mathbf{I}^0_{\langle 001\rangle}$, had fallen to approximately 95%, 2/3 and 1/5 of its original intensity respectively, Fig. 5.10a. The intensity of the 1692, shown unannealed and after the 775K anneal at two different values of applied stress, Fig. 5.10c, fell by approximately the same proportion each time, identifying it with $\mathbf{I}^0_{\langle 001\rangle}$. While the intensities of the 1691 and 1693 lines, shown at zero stress in Fig. 5.10b fell by far less (if at all), showing that they must originate at another unrelated defect and should not be included in the analysis for $\mathbf{I}^0_{\langle 001\rangle}$.

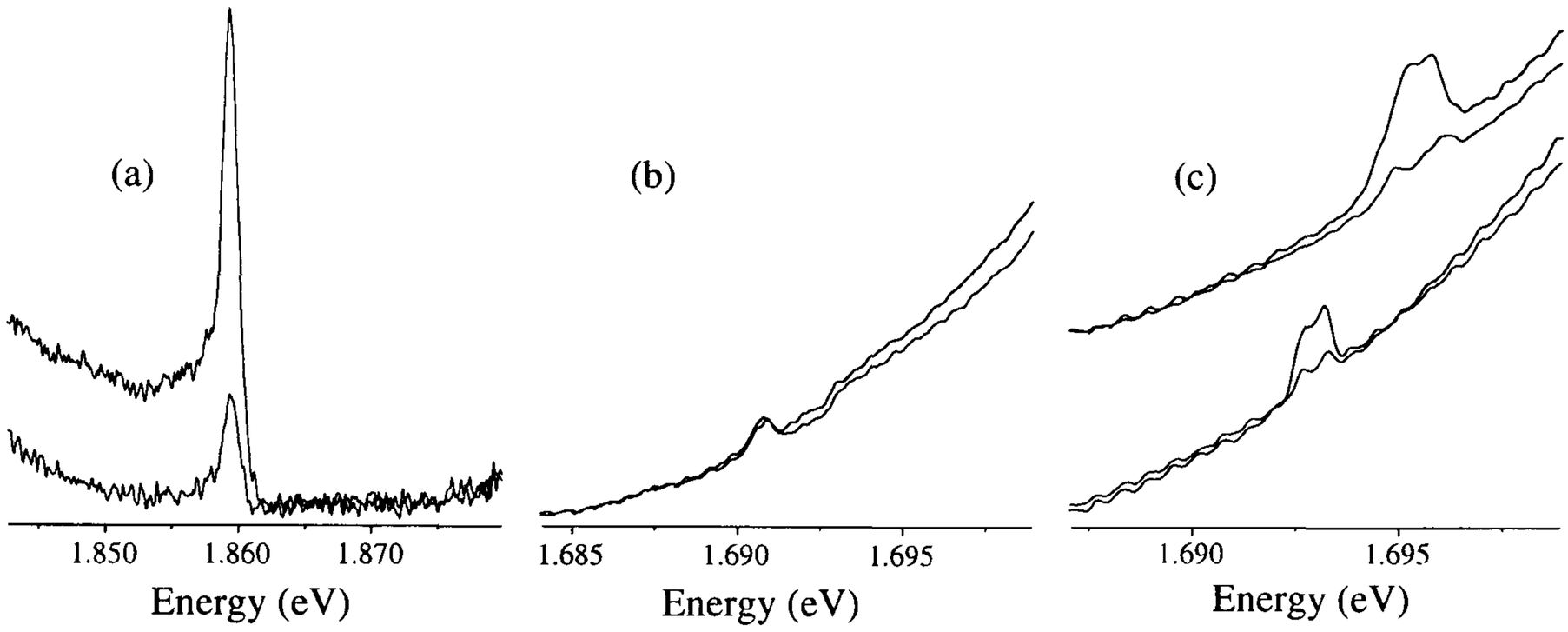

Figure 5.10: Spectra before annealing (black) and after a 775K anneal (blue) for (a) the 1859 meV line, (b) the 1691 and 1693 meV lines without an applied stress and (c) for the 1692 meV line under two different values of applied stress

5.3.3 Fitting the Theory to the Data for D_{2d} Symmetry

In Table 5.1 the stress tensor components are calculated for each of the 3 inequivalent orientations of D_{2d} defects, given in Table 2.6, relative to the direction of the applied stress using Equations 2.1 and 2.2 given in Section 2.2.3. These are shown in the stress tensor components columns for each direction of applied stress[3]. It is then straightforward to write down the transformations within the D_{2d} point group that each orientation of defect undergoes, under the applied stress, from the electronic operators associated with the non-zero stress tensor components in Equation 2.4 given in Section 2.2.3. This is done in column 'transformations'.

The electric dipole induced in diamond at a defect of D_{2d} symmetry transforms as z, so the orientation of the z axis can be used to identify which of the 3 defect orientations is observed in a given polarisation. Absorption at a defect will be observed

[3]Note that the $\langle 110 \rangle$ stress direction contains no new stress tensor components compared to the $\langle 001 \rangle$ and $\langle 111 \rangle$ stresses and so provides no new perturbations. This can serve as a consistency check for the data (the data here for $\mathbf{I}^0_{\langle 001 \rangle}$ is self-consistent) and through polarised spectra can give information about the orientation of the dipole at the defect

in the spectrum only if the dot product of its dipole orientation with the orientation of the E vector of the polarised light is non-zero. Re-orientation of $\mathbf{I}^0_{\langle 001\rangle}$ does not occur under stress at the temperature of these measurements [28], so the three orientations are expected to be equally populated. The transformations under stress at the defects being observed in each polarisation can then be compared with the experimental effects on the spectrum to determine which transformations result in the observed interactions of the states.

An induced transition is observed strongly at 1692 meV (in the limit of low stress) under $\langle 001\rangle$ stress with a polariser perpendicular to the stress and under $\langle 110\rangle$ stress with a polariser parallel to the stress or to $\langle 110\rangle$, Fig. 5.8, 5.9 (Table 5.1 column 'transition induced' defects with orientations 2 and 3). This induced line is observed only when the stress tensor component $s_{xx} - s_{yy}$ (which transforms as B_1, Eqn. 2.4) is non-zero and shifts at a rate related to its magnitude Table 5.1, Fig. 5.9. The shift rate is fitted quantitatively in the a later section.

The intensity of this induced transition is at a maximum at low temperature indicating that it is a transition from the ground state 'a' of the interstitial. It therefore shares an excited state with the 1685 meV transition and so is made allowed by a transfer of transition probability from the 1685 meV transition under a B_1 transformation. This arises from mixing between the states 'a' and 'b' Fig. 5.9 under this perturbation. This transition is the forbidden zero-phonon component of the 1859 meV local mode referred to in Section 5.2.2. Once the symmetry of the ground state 'a' is assigned, the symmetry of state 'b' is then known explicitly from the product of the symmetry of 'a' with (B_1 the transformation that mixes them) Table 2.11, e.g. if 'a' is a B_1 state then 'b' must be an A_1 state.

The difference between the energy of the 1685 meV line and this induced transition in the limit of low stress then gives a spectroscopic measure of the ground state splitting, E_g. The 1692 meV line is observed very weakly below 20K without an applied stress at 1692.0±0.1 meV and the 1685 meV line is at an energy of 1684.40±0.05 meV in the limit of low temperature, Fig. 5.1. Therefore $E_g = 7.6 \pm 0.1$ meV in the limit of

low temperature. This value will decrease with increasing temperature as discussed in Section 5.2.1. The 1859 meV line is at an energy of 1859.45 ± 0.05 meV in the limit of low temperature and is a one-phonon replica of the 1692 meV transition that is now known spectroscopically to be at 1692.0 ± 0.1 meV at the same temperature; this gives a new value for the phonon energy of $1859.45 - 1692.0 = 167.5 \pm 0.1$ meV. This is about a meV less than the value estimated from the temperature dependence data and is nearer still to the diamond phonon cutoff at about 166 meV, this is indeed a shallow local mode.

Another induced transition is observed strongly at 1864 meV, this time under $\langle 110 \rangle$ stress with a polariser perpendicular to the stress and parallel to $\langle 001 \rangle$ (defect orientation 1 Table 5.1) and under $\langle 111 \rangle$ stress in both polarisations (all defect orientations), Fig. 5.8, 5.9. This induced line is observed only when the stress tensor component s_{xy} (which transforms as B_2, (Eqn. 2.4) is non-zero and shifts at a rate related to its magnitude, Table 5.1, Fig. 5.9. The shift rate is fitted quantitatively in a later section. The intensity of this induced transition is at a maximum at low temperatures indicating that like the 1859 meV line it is a transition from the ground state 'a', to a state 'f' that must be $1864.5 - 1859.5 = 5.0 \pm 0.1$ meV above the 1859 meV excited state 'e'. The existence of this state was not known before these experiments. This induced transition is made allowed by a transfer of transition probability from the 1859 meV transition under a B_2 transformation. This arises from mixing between the excited state 'e' and the previously unseen state 'f', Fig. 5.9, under this perturbation.

In D_{2d} symmetry, z dipole-allowed transitions transform as B_2, Table 2.2. The 1859 meV transition from 'a' to 'e' is allowed without an applied stress. So, once the symmetry of the ground state 'a' is assigned, the symmetry of state 'e' is known from the product of the symmetry of 'a' with the B_2 symmetry of the dipole transformation using Table 2.11. The symmetry of the state 'f' can then be identified from the product of the symmetry of 'e' with the B_2 transformation that mixes 'e' into 'f' under stress.

The 1859 meV transition is known to be a local mode of vibration (Section 5.2.2) arising from the interaction of a phonon with the electronic excited state of the 1685 meV transition, 'c'. The symmetry of this vibration can now be identified uniquely from the product of the symmetries of the states 'c' and 'e'. While the symmetries of these states may change with the choice of ground state symmetry, their product does not. The phonon mediating the 1859 meV transition is therefore a mode of vibration of the interstitial with B_1 symmetry.

State 'e' is a vibronic energy state of the interstitial and states 'a', 'b' and 'c' are electronic in nature. The nature of the state 'f' can not easily be determined by the stress measurements alone, so further experimentation is required this is reported and studied in the next section.

5.3.4 Isotopic Substitution and Stress Induced Transitions - Understanding the Interactions of the States

Uniaxial stress was applied along the $\langle 111 \rangle$ axis of the ^{13}C sample used originally to measure the isotope shift of the 1859 meV line (Section 5.2.2). The energy of the line induced by stress at 1864.5 meV in ^{12}C diamond in the limit of low stress, shifted down to 1858.9 meV in the ^{13}C sample. This is very similar to the isotope shift of the 1859 meV line, identified by its isotope shift as a local mode and shows that the induced line is also a vibronic transition. The newly identified state 'f', therefore, is a vibronic energy state of $\mathbf{I}^0_{\langle 001 \rangle}$. The question then is whether the mixing between states 'e' and 'f' is mediated via the vibrational or electronic components defined as χ and ψ respectively in Section 2.3.

For the mixing to be mediated by the electronic components of the two transitions they must be different and nearly degenerate, so there must be an electronic state 'd' that mediates the 1864 meV vibronic transition near to the electronic state 'c' that mediates the 1859 meV vibronic transition (shown in Section 5.2.2). These states 'c' and 'd' must then interact under the same B_2 transformation that mixes the states 'e' and 'f'. This leads us to seek direct evidence of this postulated state 'd'.

Stress	Polarisation	Local Axis Orientation				Stress Tensor Components							Transformations	Transition induced	
		Defect	x	y	z	s_{xx}	s_{yy}	s_{zz}	s_{xy}	s_{xz}	s_{yz}	$\lvert s_{xx} - s_{yy} \rvert$	D_{2d}	1692 meV	1864 meV
[110]	[001]	1	100	010	001	s/2	s/2	-	s/2	-	-	-	a_1', b_2'	No	Yes
	[110] or	2	010	001	100	s/2	-	s/2	-	s/2	-	s/2	a_1', a_1, b_1, e_y	Yes	No
	$[1\bar{1}0]$	3	001	100	010	-	s/2	s/2	-	-	s/2	s/2	a_1', a_1, b_1, e_x	Yes	No
⟨001⟩	∥ to stress	1	100	010	001	-	-	s	-	-	-	-	a_1	No	No
		2	010	001	100	-	s	-	-	-	-	s	a_1', b_1	Yes	No
	⊥ to stress	3	001	100	010	s	-	-	-	-	-	s	a_1', b_1, e_x	Yes	No
⟨111⟩	Spectra	1	100	010	001	s/3	s/3	s/3	s/3	s/3	s/3	-	a_1', a_1, b_2, e_x, ey	No	Yes
	not pol.	2	010	001	100	s/3	s/3	s/3	s/3	s/3	s/3	-	a_1', a_1, b_2, e_x, e_y	No	Yes
	dependent	3	001	100	010	s/3	s/3	s/3	s/3	s/3	s/3	-	a_1', a_1, b_2, e_x, e_y	No	Yes

Table 5.1: Comparison of observed effects with expected perturbations in D_{2d} the point group

Transitions from 'b' to 'c' are dipole allowed (this is the 1685 meV line) so under a B_2 perturbation, when state 'c' is expected to be mixed into state 'd' if it exists, transitions from 'b' to 'd' should be induced. To observe and identify this weak transition requires a thermal population in state 'b' but also low thermal line broadening. Under a small applied $\langle 110 \rangle$ stress in an $\langle 001 \rangle$ polarised spectrum recorded at 22K a weak line was observed at 1689.7 ± 0.3 meV in the limit of low stress, Fig. 5.11. A combination of the temperature and stress dependence of the lines at 1691, 1692 and 1693 meV precludes them from appearing at this energy with this intensity under this amount of stress, in this direction and polarisation, at this temperature. This line is not observed in any other spectra. State 'd' is therefore identified as a previously unidentified electronic excited state of $\mathbf{I}^0_{\langle 001 \rangle}$.

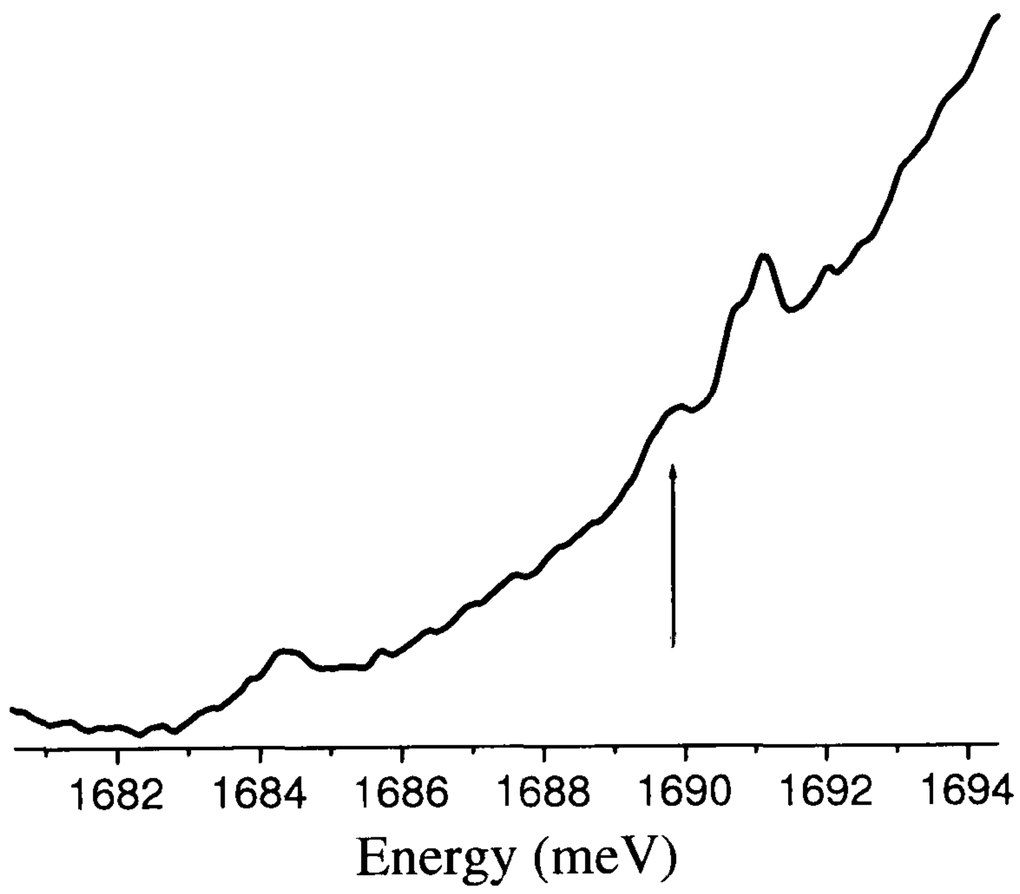

Figure 5.11: Spectrum showing the 1690 meV induced transition. The 1685, 1691, 1692 and 1693 meV lines are also discernable. The 1691 meV line is starting to split into two.

Likewise, since transitions from 'a' to 'e' are dipole allowed (this is the 1859 meV line) under a B_1 perturbation, when state 'a' is expected to be mixed into state 'b', transitions from 'b' to 'e' should be induced. Again, to observe and identify this weak transition requires a thermal population in state 'b' but also low thermal line

broadening. The line should appear at 1851.4 meV and move to lower energy with increasing stress. There is higher noise in this region of the spectrum due to a fall off in the sensitivity of the detector and there is also structure due to the GR1. Increasing the stress increases the transition probability, but also increases the separation of the ground states quadratically, the thermal population in state 'b' falls exponentially with increasing separation from the ground states. Not surprisingly, this induced line is not observed.

Following the identification of state 'd' the rate of shift in energy of the states of $\mathbf{I}^0_{\langle 001\rangle}$ with stress can now be understood and formalised, this is done in the following section. Without the isotope results the analysis of the next section would not have been possible.

5.3.5 Quantifying the Interactions of the States Under Symmetry Lowering Perturbations

There are three closely spaced doublets 'a' 'b', 'c' 'd' and 'e' 'f'. These are sufficiently far apart that no appreciable interactions occur between them, while strong interactions may be expected and are observed between their components. The perturbations of these states can then be written down in three 2x2 matrices using Eqn. 2.4.

For state ψ_1 of symmetry Γ_1 to interact with a state ψ_2 with symmetry Γ_2 under a perturbation of symmetry Γ_3 their product $\langle\Gamma_1|\Gamma_3|\Gamma_2\rangle$ must transform as A_1 using the rules laid out in Table 2.11. For non-degenerate states, $\langle\Gamma_1|\hat{a_1}|\Gamma_2\rangle$ always transforms as A_1 for $\Gamma_1 = \Gamma_2$ and never transforms as A_1 for $\Gamma_1 \neq \Gamma_2$. This is true for any choice of Γ_1 and Γ_2. States can therefore interact with themselves (this does not happen at $\mathbf{I}^0_{\langle 001\rangle}$) under $\hat{a_1}$ operations (on-diagonal-terms, negligible for $\mathbf{I}^0_{\langle 001\rangle}$) and at $\mathbf{I}^0_{\langle 001\rangle}$, it has been shown experimentally that they interact with each other (off-diagonal-terms) under $\hat{b_1}$ operations in the ground states (g) and under $\hat{b_2}$ operations in the middle excited (m) and excited (e) states, Section 5.3.3. The interaction of states described by Eqn. 2.8 in Section 2.2.4 can then be written out for the ground, middle and excited states as follows:

	ψ_a	ψ_b
ψ_a	$\langle\psi_a\|\hat{a_1}\|\psi_a\rangle s_{zz} + \langle\psi_a\|\hat{a_1'}\|\psi_a\rangle(s_{xx}+s_{yy})$	$\langle\psi_b\|\hat{b_1}\|\psi_a\rangle(s_{xx}-s_{yy})$
ψ_b	$\langle\psi_a\|\hat{b_1}\|\psi_b\rangle(s_{xx}-s_{yy})$	$\langle\psi_b\|\hat{a_1}\|\psi_b\rangle s_{zz} + \langle\psi_b\|\hat{a_1'}\|\psi_b\rangle(s_{xx}+s_{yy})$ $+E_g$

Table 5.2: Ground state doublet perturbation matrix.

	ψ_c	ψ_d
ψ_c	$\langle\psi_c\|\hat{a_1}\|\psi_c\rangle s_{zz} + \langle\psi_c\|\hat{a_1'}\|\psi_c\rangle(s_{xx}+s_{yy})$	$\langle\psi_d\|\hat{b_2}\|\psi_c\rangle s_{xy}$
ψ_d	$\langle\psi_c\|\hat{b_2}\|\psi_d\rangle s_{xy}$	$\langle\psi_d\|\hat{a_1}\|\psi_d\rangle s_{zz} + \langle\psi_d\|\hat{a_1'}\|\psi_d\rangle(s_{xx}+s_{yy})$ $+E_m$

Table 5.3: Excited electronic state doublet perturbation matrix.

	ψ_e	ψ_f
ψ_e	$\langle\psi_e\|\hat{a_1}\|\psi_e\rangle s_{zz} + \langle\psi_e\|\hat{a_1'}\|\psi_e\rangle(s_{xx}+s_{yy})$	$\langle\psi_f\|\hat{b_2}\|\psi_e\rangle s_{xy}$
ψ_f	$\langle\psi_e\|\hat{b_2}\|\psi_f\rangle s_{xy}$	$\langle\psi_f\|\hat{a_1}\|\psi_f\rangle s_{zz} + \langle\psi_f\|\hat{a_1'}\|\psi_f\rangle(s_{xx}+s_{yy})$ $+E_e$

Table 5.4: Excited one-phonon replica doublet perturbation matrix.

Since the wave-functions are real and hermitian, $\langle\psi_1|\hat{\Gamma}|\psi_2\rangle = \langle\psi_2|\hat{\Gamma}|\psi_1\rangle$. The perturbed energy eigenvalues $E_{+/-}$, for the upper and lower energy components of each doublet, are then found from a determinant of the form:

$$\begin{vmatrix} \alpha - E & \gamma \\ \gamma & \beta + \Delta E - E \end{vmatrix} = 0 \tag{5.4}$$

where $\Delta E = E_{g/m/e}$ and α, β and γ are stress dependent. So that:

$$E_{\pm} = \frac{1}{2}(\alpha + \beta + \Delta E) \pm \frac{1}{2}\sqrt{(\beta + \Delta E - \alpha)^2 + 4\gamma^2} \tag{5.5}$$

The states repel as they interact so the positive solution gives the change in energy of the upper state and the negative solution gives the change energy of the lower state, both values are relative to the initial energy of the lower of the two states. The change in energy of the transitions is then the difference in the change in energy of their initial and final states.

Since the mixing of states 'e' and 'f' is mediated by their electronic components 'c' and 'd', $\gamma_m = \gamma_e$. Additionally since the measurement is always of the difference in energy, the components of the linear terms α_g, β_g and α_m, β_m and α_e, β_e are reduced to three distinct differences $(\alpha_m - \alpha_g)$, $(\alpha_m - \beta_g)$ and $(\beta_m - \alpha_g)$, see Table 5.5.

Transition	Initial State	Final State	Linear Shift
1859	a	e	$\alpha_e - \alpha_g = (\alpha_m - \alpha_g)$
1685	b	c	$(\alpha_m - \beta_g)$
1864	a	f	$\beta_e - \alpha_g = (\beta_m - \alpha_g)$
1692	a	c	$(\alpha_m - \alpha_g)$
1690	b	d	$\beta_m - \beta_g = (\beta_m - \alpha_g) - (\alpha_m - \alpha_g) + (\alpha_m - \beta_g)$

Table 5.5: Linear parameters

In the ground / middle / excited states:

$$\alpha_{g/m/e} = \langle \phi_{a/c/e} | \hat{c_1} | \phi_{a/c/e} \rangle s_{zz} + \langle \phi_{a/c/e} | \hat{a'_a} | \phi_{a/c/e} \rangle (s_{xx} + s_{yy})$$
$$\beta_{g/m/e} = \langle \phi_{b/d/f} | \hat{a_1} | \phi_{b/d/f} \rangle s_{zz} + \langle \phi_{b/d/f} | \hat{a'_1} | \phi_{b/d/f} \rangle (s_{xx} + s_{yy}) \quad (5.6)$$

The differences are then:

$$(\alpha_m - \alpha_g) = a_{ca} (s_{zz}) + a'_{ca} (s_{xx} + s_{yy})$$
$$(\alpha_m - \beta_g) = a_{cb} (s_{zz}) + a'_{cb} (s_{xx} + s_{yy})$$
$$(\beta_m - \alpha_g) = a_{da} (s_{zz}) + a'_{da} (s_{xx} + s_{yy}) \quad (5.7)$$

where $a_{ca} = \langle \psi_c | \hat{a_1} | \psi_c \rangle - \langle \psi_a | \hat{a_1} | \psi_a \rangle$ and $a'_{ca} = \langle \psi_c | \hat{a'_1} | \psi_c \rangle - \langle \psi_a | \hat{a'_1} | \psi_a \rangle$ and so on. There are then 6 linear parameters required to fit the data a_{ca}, a'_{ca}, a_{cb}, a'_{cb}, a_{da}

and a'_{da} and two quadratic parameters b_{cd} and b_{ab}. These are fitted to the data in Fig. 5.9 using Eqns 5.4 and 5.5. When there is no x or y component in the stress, there is no interaction between the states and the shift is simply determined by the linear perturbations associated with the relevant states, i.e. α for the lower state and $\beta + \Delta E$ for the upper state of each doublet. The change in energy of the transition is given by:

$$E_{shift}(s) = E_{final} - E_{initial}$$

So when there is no interaction of the states:

$$E^{1859}_{shift}(s) = E^{e}_{-} - E^{g}_{-} = \alpha_m - (\beta_g + E_g) = a_{cb} s_{zz} - E_g \tag{5.8}$$

$$E^{1685}_{shift}(s) = E^{m}_{-} - E^{g}_{-} = \alpha_m - \alpha_g = a_{ca} s_{zz} \tag{5.9}$$

where s_{zz} is some multiple of the applied stress, s, as given in Table 5.1, column 'stress tensor-components'.

When there is an interaction between the components of one of the doublets involved in the transition $E_{shift}(s)$ is a more complicated function. For an interaction in the ground state doublet, (when $(s_{xx} - s_{yy})$ is non zero):

$$\begin{aligned} E^{1859}_{shift}(s) &= \frac{1}{2}[(\alpha_m - \alpha_g) + (\alpha_m - \beta_g) - E_g] \\ &\quad + \frac{1}{2}\sqrt{[(\beta_g - \alpha_m) + E_g - (\alpha_g - \alpha_m)]^2 + 4\gamma_g^2} \\ &= \frac{1}{2}[(a_{ca} + a_{cb})\, s_{zz} + (a'_{ca} + a'_{cb})\,(s_{xx} + s_{yy}) - E_g] \\ &\quad + \frac{1}{2}\sqrt{[(a_{ca} - a_{cb})\, s_{zz} + (a'_{ca} - a'_{cb})\,(s_{xx} + s_{yy}) + E_g]^2} \\ &\quad + \frac{1}{2}\sqrt{4[b_{ab}\,(s_{xx} - s_{yy})]^2} \end{aligned} \tag{5.10}$$

The 1692 meV transition is induced by this interaction and will shift at the same rate since:

$$E^{1692}_{shift}(s) = E^{m}_{-} - E^{g}_{-} = E^{e}_{-} - E^{g}_{-} = E^{1859}_{shift}(s) \tag{5.11}$$

For the 1685 meV transition:

$$E^{1685}_{shift}(s) = E^{m}_{-} - E^{g}_{+} \tag{5.12}$$

the shift is then the same as $E^{1859}_{shift}(s)$ but with a minus sign before the square root. For an interaction in the excited state doublets, (when s_{xy} is non-zero):

$$\begin{aligned} E^{1859}_{shift}(s) &= (E_-)_m - (E_-)_g \\ &= \frac{1}{2}[(\alpha_m - \alpha_g) + (\beta_m - \alpha_g) + E_m] \\ &\quad -\frac{1}{2}\sqrt{[(\beta_m - \alpha_g) + E_m - (\alpha_m - \alpha_g)]^2 + 4\gamma_m^2} \\ &= \frac{1}{2}[(a_{ca} + a_{da})\, s_{zz} + (a'_{ca} + a'_{da})\,(s_{xx} + s_{yy}) + E_m] \\ &\quad -\frac{1}{2}\sqrt{[(a_{da} - a_{ca})\, s_{zz} + (a'_{da} - a'_{ca})\,(s_{xx} + s_{yy}) + E_m]^2} \\ &\quad +\frac{1}{2}\sqrt{4\,(b_{cd}s_{xy})^2} \end{aligned} \tag{5.13}$$

The 1864 meV transition is induced by this interaction and will shift at the same rate but with a plus sign before the square root. For the 1685 meV line:

$$E^{1685}_{shift}(s) = (E_-)_m - (E_+)_g \tag{5.14}$$

this is Eqn. 5.13 with α_g replaced by $\beta_g + E_g$. So,

$$\begin{aligned} E^{1685}_{shift}(s) = \frac{1}{2}[(2a_{cb} + a_{da} - a_{ca})\, s_{zz} + (2a'_{cb} + a'_{da} - a'_{ca})\,(s_{xx} + s_{yy}) - 2E_g + E_m] \\ -\frac{1}{2}\sqrt{[(a_{da} - a_{ca})\, s_{zz} + (a'_{da} - a'_{ca})\,(s_{xx} + s_{yy}) + E_m]^2 + 4\,(b_{cd}s_{xy})^2} \end{aligned} \tag{5.15}$$

The 1690 meV transition is induced by this interaction and will shift at the same rate but with a plus sign before the square root. Fitting these Eqns to the data (Fig. 5.9) gives:

$$\begin{aligned} a_{ca} &= -0.09 \pm 0.1 \text{ meV/GPa} \\ a'_{ca} &= 0.2 \pm 0.1 \text{ meV/GPa} & b_{ab} &= 6.1 \pm 0.1 \text{ meV/GPa} \\ a_{cb} &= -0.03 \pm 0.3 \text{ meV/GPa} & b_{cd} &= 6.4 \pm 0.1 \text{ meV/GPa} \\ a'_{cb} &= 0.5 \pm 0.2 \text{ meV/GPa} \\ a_{da} &= 0.2 \pm 0.6 \text{ meV/GPa} & E_g &= 7.6 \pm 0.1 \text{ meV} \\ a'_{da} &= -0.3 \pm 0.1 \text{ meV/GPa} & E_m = E_e &= 5.0 \pm 0.1 \text{ meV} \end{aligned} \tag{5.16}$$

The errors shown indicate the amount by which the best fit can be changed to produce an increase of 10% in the sum of squares. Some of the hazards of measuring the energies and intensities of the lines at the interstitial and their components were discussed in Section 3.4.5. To minimise the influence of these errors on the parameters obtained above, the values were taken from the best fit of the theory to all of the available data, with the result that not one parameter depends solely on the result of one experiment - there is plenty of cross-referencing. This reduces the impact of any isolated systematic error from one experiment (already reduced via detailed checking of the data against the known behaviour of the GR1). Random errors due to choice of baseline and line fitting were reduced through the use of fitting programs and consistent fitting procedures, although these are necessarily subjective so a small systematic error may remain.

As the states are mixed into each other with stress the relative probabilities of transitions to/from them changes according to the theory laid out in Section 2.2.4. This is related to the intensity of the lines at $\mathbf{I}^0_{\langle 001\rangle}$ by $\cos^2\theta\,(s)$, Eqn. 2.20 and the stress dependent ground state splitting $\Delta E\,(s)$ in Table 5.6

Transition	States	Mixing in ground states,g	Mixing in excited states,m&e
1685	$g^+ \rightarrow m^-$	$(1-\cos^2\theta)\,\frac{I^{1685}_{s=0}e^{-\Delta E/kT}}{1+e^{-\Delta E/kT}}$	$(1-\cos^2\theta)\,I^{1685}_{s=0}$
1690	$g^+ \rightarrow m^+$	0	$(\cos^2\theta)\,I^{1685}_{s=0}$
1692	$g^- \rightarrow m^-$	$(\cos^2\theta)\,\frac{I^{1685}_{s=0}}{\left(1+e^{-\Delta E/kT}\right)}$	0
1859	$g^- \rightarrow e^-$	$(1-\cos^2\theta)\,\frac{I^{1685}_{s=0}}{\left(1+e^{-\Delta E/kT}\right)}$	$(1-\cos^2\theta)\,I^{1859}_{s=0}$
1864	$g^- \rightarrow e^+$	0	$(\cos^2\theta)\,I^{1859}_{s=0}$

Table 5.6: Line intensity variations with stress, where $\cos^2\theta$ is a stress dependent parameter given by Eqn. 2.20 and ΔE is also stress dependent.

Note the intensity is affected by the population in the ground state of the transition as well as by its probability. This is a function of the separation of the ground states which is highly stress dependent when there is mixing in the ground state

and unchanged otherwise. The functions in Table 5.7 are plotted in Figures 5.12 and 5.13, using the parameters in (5.16) and fits well to the data. The only adjustable parameter is the prefactor which corresponds to the initial intensity of the 1859 meV line before stress is applied, so the fit is essentially without adjustable parameters. All thermalisation effects are accounted for and there is no unexpected degeneracy of the ground state.

The prefactor of the curve fitted to the 1859 meV line intensity was determined from the best fit to the 1864 meV line intensity, since this is more objectively baseline corrected than the awkward 1859 meV line, see Section 3.4.5. The fit is remarkably believable when compared to the data, considering the difficulty making accurate intensity measurements (Section 3.4.5).

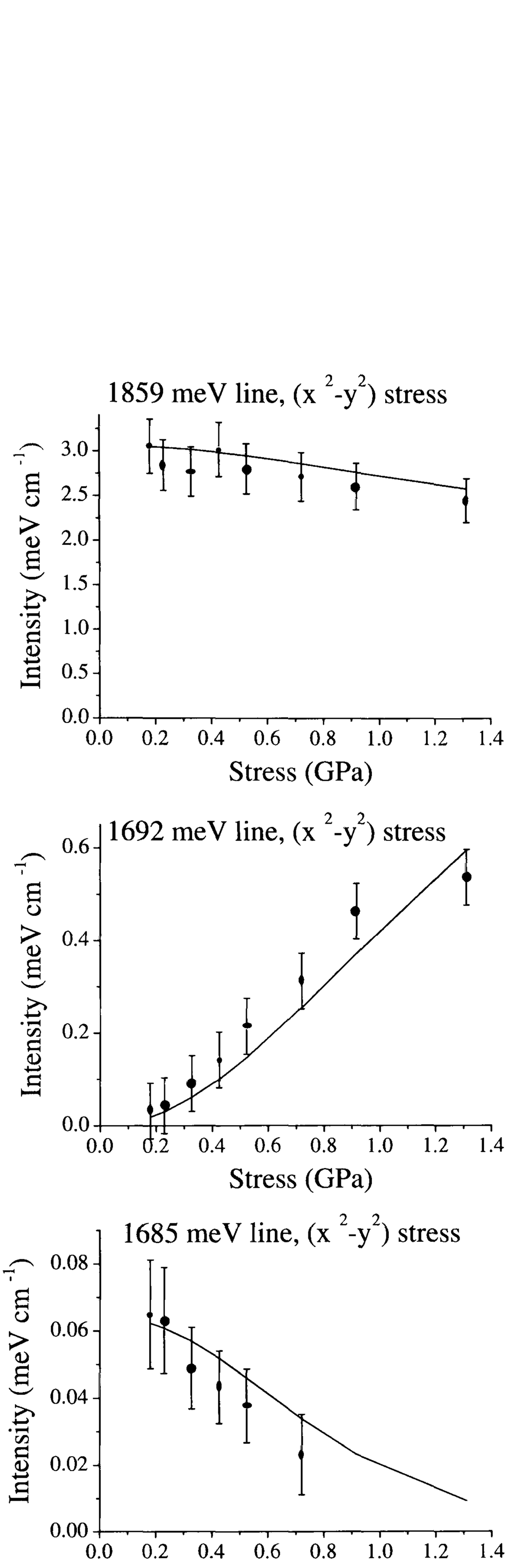

Figure 5.12: The effect of mixing in the ground states on the intensities of the transitions. Points are data, line is theory fitted without adjustable parameters. See Table 5.7, where $\cos^2\theta$ is calculated using the parameters of (5.16).

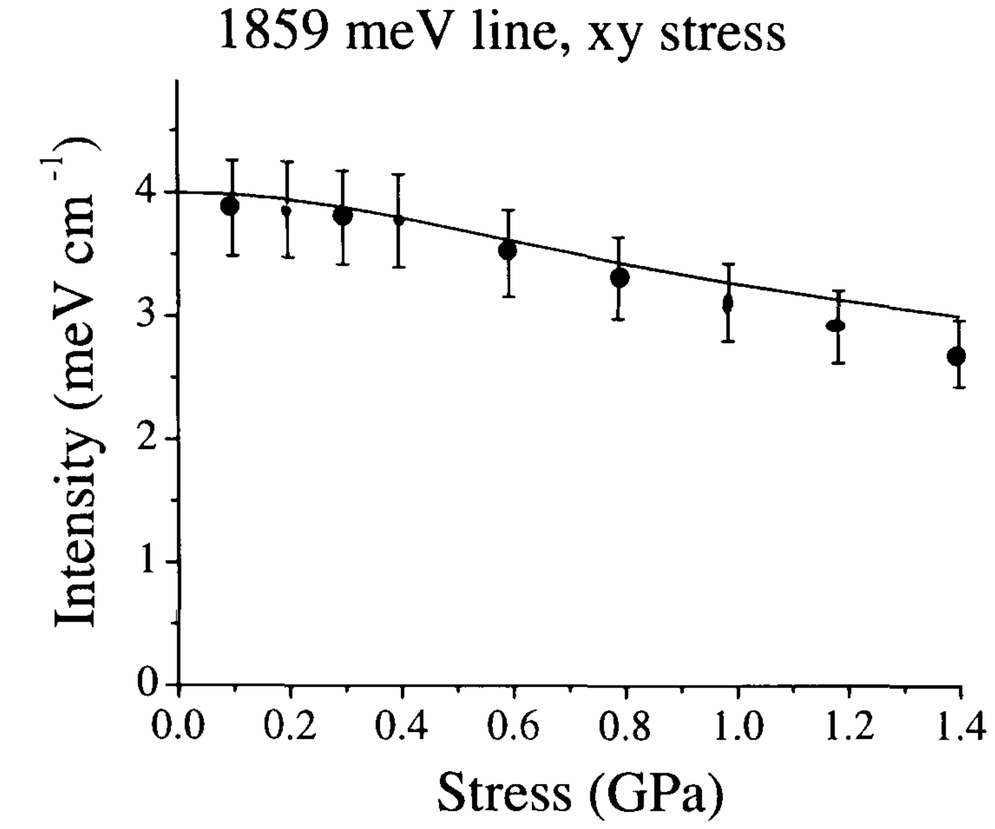

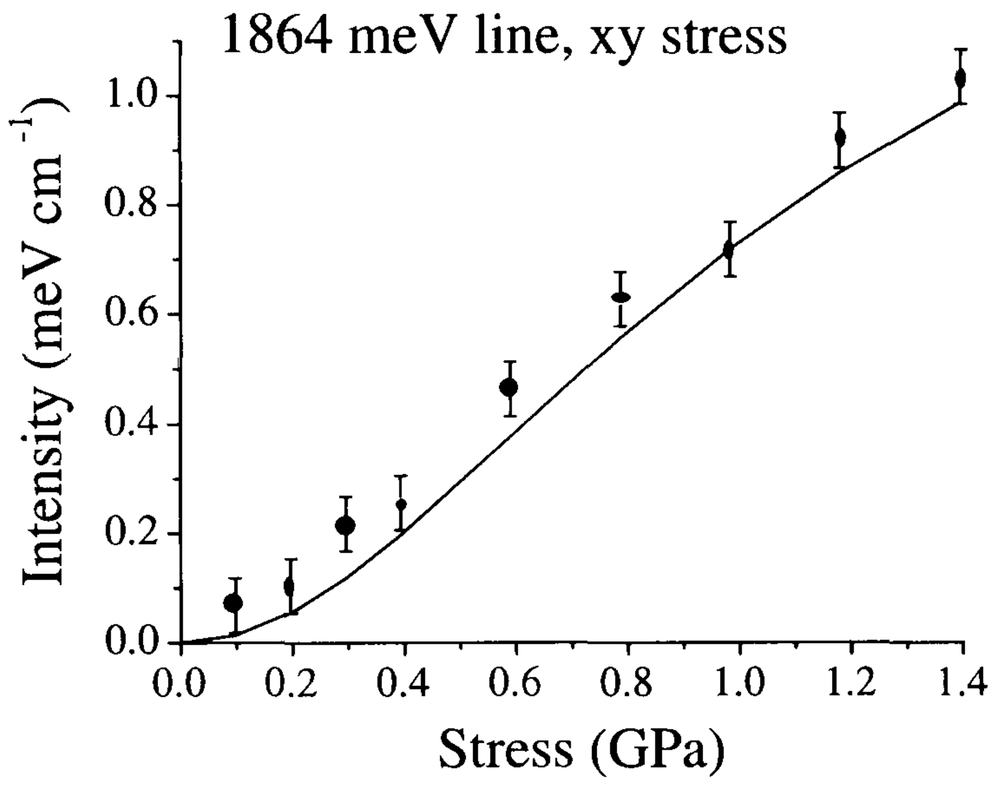

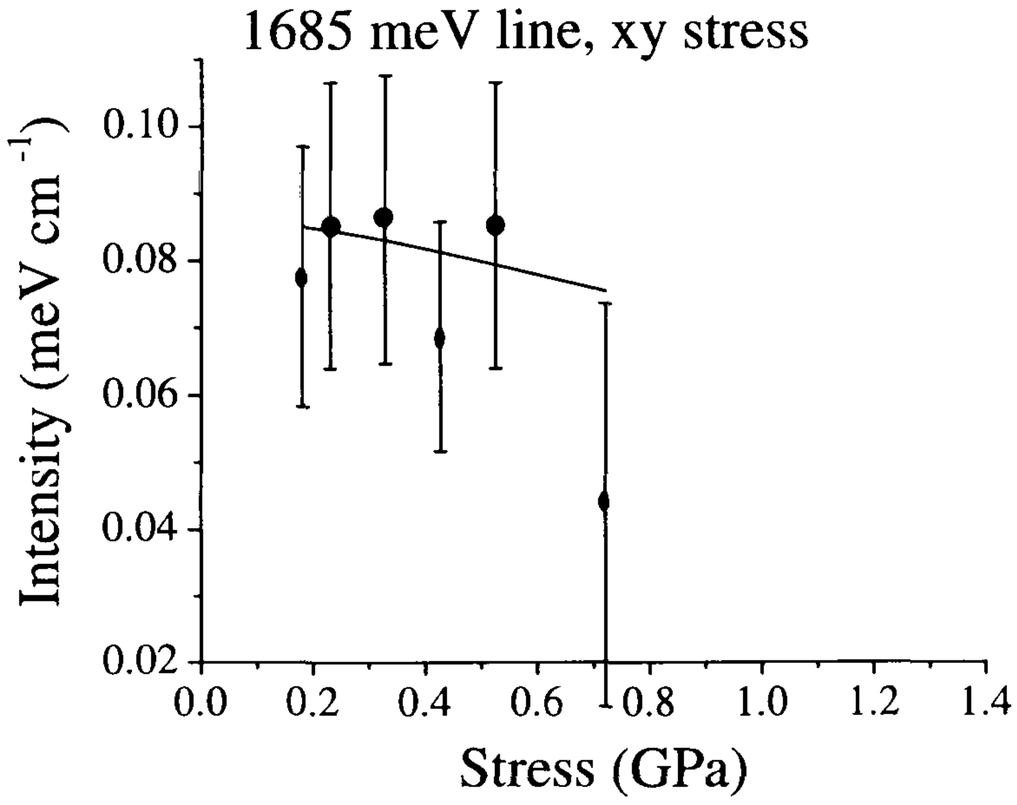

Figure 5.13: The effect of mixing in the excited states on the intensities of the transitions. Points are data, line is theory fitted without adjustable parameters. See Table 5.7, where $\cos^2\theta$ is calculated using the parameters of (5.16).

5.3.6 Internal Strain

Transitions can be induced at $\mathbf{I}^0_{\langle 001 \rangle}$ under an applied stress with energies 1864 and 1692 meV. In the absence of an applied stress a line has not been observed at 1864 meV, although in this region of the spectrum it would be hard to identify a small intensity. However, the 1692 meV induced line is observed weakly, as a sharp feature, at temperatures below 20K Fig. 5.14 without an applied external stress, with an intensity of about 1% of that of the 1859 meV line. The parameters determined in the last section show that to induce this line to this extent requires a difference in the components of the stress, resolved along the x and y local axes of the defect, Eqn. 2.4, of 0.1 GPa on average across the population of interstitials. Note that a spherically symmetric strain would not produce the observed line and any stresses greater than about 0.2 GPa, resolved along the required direction, would shift the energy of the transition by more than the observed line width so this is not an average with a high standard deviation. This gives a measure of internal stresses.

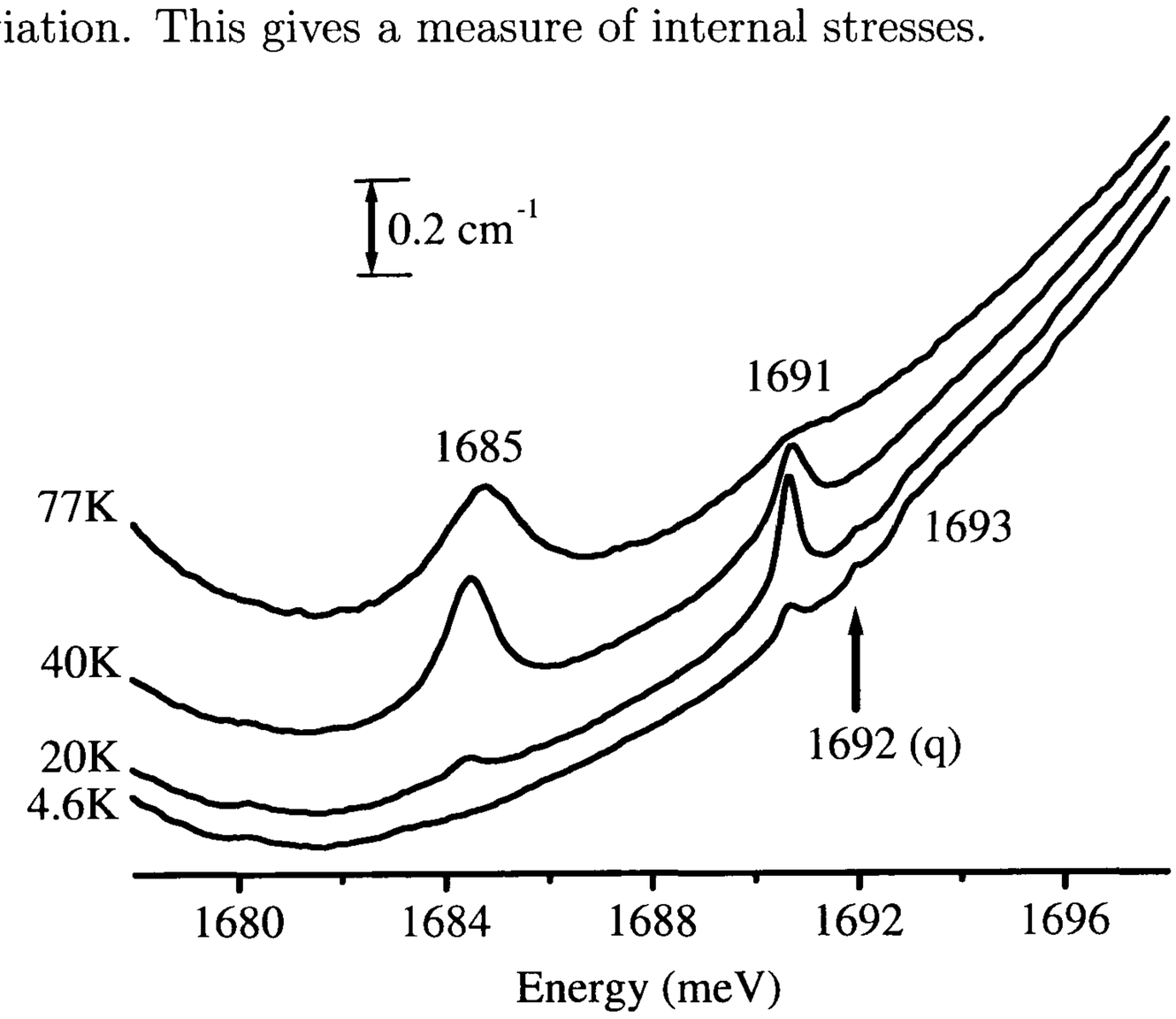

Figure 5.14: Lines in the 1685 meV region at various temperatures without an applied stress

5.3.7 Annealing Under Stress

One sample was annealed to approximately 300°C (573K) under 1.6 GPa of uniaxial stress, applied along the ⟨110⟩ direction for several hours. Unfortunately the sample broke into two pieces in the process, cleaving cleanly along a ⟨111⟩ plane (the dominant cleavage plane in diamond [61]) parallel to the stress. This is likely to have been due to some small impurity or fault causing a small raised area between the anvils and the sample which would have placed part of the sample under excess pressure, starting a crack that could easily propagate under the applied stress.

With the stress applied along this direction the effect of any thermal re-orientation would be an increased number of defects oriented as 1 in Table 5.1 and fewer oriented as 2 and 3. The effect of this on the spectrum under ⟨110⟩ stress would be an increased intensity of the 1864 meV line induced by this perturbation at interstitials oriented as 1, Table 5.1, and decreased intensity of the 1692 meV line induced at interstitials oriented as 2 and 3. The two halves of the broken sample were both measured under stress after being cut and polished to give two sets of parallel faces one for stress along the original direction and the other for spectroscopy, (viewing along [001] in one half and $[1\bar{1}0]$ in the other). There was no measurable change in the intensities of the induced lines as a function of stress compared to data taken before the annealing.

A significant proportion of interstitials might be expected to re-orient under these conditions [28] should the sample have remained intact, so it seems the broken sample was not under sufficient stress. Since it did break the actual stress cannot be known. Alternatively the samples may have been heated sufficiently during polishing to re-distribute the orientations.

5.3.8 Fitting the Theory to the Data for D_2 Symmetry

Since the data may be fitted reasonably with all linear terms set to zero, the results can be explained in terms of a centre with static, D_2 symmetry as well as the higher symmetry, D_{2d}, fitted in Section 5.3.3; the data are fitted using the same method as before but for the D_2 point group, Eqn. 2.5 Table 5.7.

The consequences of this are as follows; The 1692 meV line is induced when the $\hat{a_1'}$ or $\hat{a_1''}$ terms are present in the perturbation (Table 5.7). This means that the ground states 'a' and 'b' are mixed by an A_1 transformation and so must have the same symmetry according to the product rules of Table 2.12. As a result and since transitions from 'b' to 'c' and from 'a' to 'e' are dipole allowed (observed as the 1685 and 1859 meV lines respectively) the 1692 meV transition induced by stress from 'a' to 'c' and a transition at 1851 meV (not observed with or without stress) from 'b' to 'e' must also be dipole allowed transitions. To explain the data in terms of this point group therefore requires that the 1692 and 1851 meV transitions are allowed but have near zero probability.

Fitting the data in this point group also requires that the 1692 meV line must be induced when the $\hat{a_1'}$ or $\hat{a_1''}$ terms are present in the perturbation, but not when they are present together in equal amounts at the same defect (Table 5.7). This indicates that $\hat{a_1'} = -\hat{a_1''}$. The negative sign will not affect the shift rates since they are quadratic and this parameter is the γ mixing term (Eqn. 5.5) and is squared. In the absence of any linear shifts, setting the parameters $\hat{a_1'}$ and $\hat{a_1''}$ opposite and equal in this way effectively raises the symmetry they parameterise, to D_{2d}, by restoring the reflection planes and consequently the S_4 improper rotation.

In this higher symmetry D_{2d} point group $\hat{a_1'}s_{xx} + \hat{a_1''}s_{yy}$ becomes $\hat{b_1}(s_{xx} - s_{yy})$, Eqns 2.4 and 2.5, which is reasonable if these terms are exactly equal and opposite. If they are not, the effect on the data will be first: that the 1692 meV line will be induced with a small intensity under [110] stress [001] polarisation and under $\langle 111 \rangle$ stress, because the terms will not completely cancel. The $\hat{a_1'}$ and $\hat{a_1''}$ terms can differ in magnitude by up to 6% before this would be observable above the noise at the highest stress we have measured. The second effect will be that the 1692 meV line will split into two components under [110] stress, [110] and $[1\bar{1}0]$ polarisation and under $\langle 001 \rangle$ stress $\perp$ polarisation. The splitting must be greater than about 0.5 meV at the highest stress to be resolvable which corresponds to a difference in $|\hat{a_1'}|$ and $|\hat{a_1''}|$ of 20%. Splittings in this line are observed in some spectra, although these are inconsistent

with static D_2 symmetry and are almost certainly spurious since a difference in the magnitude of the parameters, big enough to cause the observed splitting, would induce a considerable intensity under [110] stress [001] polarisation and under [111] stress, where none is observed, this is discussed further in Section 5.3.11. An upper limit is therefore fixed for the difference between $|\hat{a_1'}|$ and $|\hat{a_1''}|$ at 6%.

5.3.9 Fitting the Theory to the Data for C_{2v} Symmetry

The data may also be explained in terms of a centre with static C_{2v} symmetry for the same reasons as for D_2 and with similar consequences. The theory here comes from Table 2.4, Eqn. 2.6 fitted to the data in Table 5.8 where the local axes x and y are now along $\langle 110 \rangle$ type directions instead of the cube axes, Table 2.8. This time the 1864 meV line is induced when the $\hat{a_1'}$ and $\hat{a_1''}$ terms are present in the perturbation. This means that in C_{2v} symmetry the excited states 'c' and 'd' are mixed by an A_1 transformation, as are 'e' and 'f'. Therefore the states 'c' and 'd' must have the same symmetry, as must 'e' and 'f'. Since transitions from 'a' to 'e' and from 'b' to 'c' are dipole allowed, the 1864 meV transition induced by stress from 'a' to 'f' and the 1690 meV transition induced by stress from 'b' to 'd', must also be dipole allowed transitions in C_{2v} symmetry, but happen to have near zero probability without an applied stress. Again, although the 1864 meV transition is induced when the $\hat{a_1'}$ or $\hat{a_1''}$ terms are present it is not induced when they are present, together in equal amounts at the same defect, so that $\hat{a_1'} = -\hat{a_1''}$.

As before, setting these parameters equal and opposite effectively raises the symmetry to D_{2d}, this time by restoring the x and y C_2 rotation axes and consequently the S_4 improper rotation axis.

If these terms are not exactly equal and opposite the effect on the data will be first that the 1864 meV line will be induced with a small intensity under [110] stress, [110] and $[1\bar{1}0]$ polarisations and under $\langle 001 \rangle$ stress $\perp$ polarisation because the terms will not completely cancel. The $\hat{a_1'}$ and $\hat{a_1''}$ terms can differ in magnitude by up to approximately 10% before this would be observable above the noise at the highest

Stress	Polarisation	Local Axis Orientation				Stress Tensor Components						Transformations	Effect on spectrum transition induced	
		Defect	x	y	z	s_{xx}	s_{yy}	s_{zz}	s_{xy}	s_{xz}	s_{yz}	D_2	1692 meV	1864 meV
110	[001]	1	100	010	001	s/2	s/2	0	s/2	0	0	$a1\prime, a1'', b1$	No	Yes
		2	010	100	00$\bar{1}$	s/2	s/2	0	s/2	0	0	$a1', a1'', b1$	No	Yes
	[110] or	3	010	001	100	s/2	0	s/2	0	s/2	0	$a1, a1', b2$	Yes	No
		4	001	010	$\bar{1}$00	0	s/2	s/2	0	0	-s/2	$a1, a1'', b3$	Yes	No
		5	001	100	010	0	s/2	s/2	0	0	s/2	$a1, a1'', b3$	Yes	No
	[1$\bar{1}$0]	6	100	001	0$\bar{1}$0	s/2	0	s/2	0	-s/2	0	$a1, a1', b2$	Yes	No
001	to stress$\parallel$	1	100	010	001	0	0	s	0	0	0	$a1$	No	No
		2	010	100	00$\bar{1}$	0	0	s	0	0	0	$a1$	No	No
		3	010	001	100	0	s	0	0	0	0	$a1''$	Yes	No
	$\perp$	4	001	010	$\bar{1}$00	s	0	0	0	0	0	$a1'$	No	No
	to stress	5	001	100	010	s	0	0	0	0	0	$a1'$	Yes	No
		6	100	001	0$\bar{1}$0	0	s	0	0	0	0	$a1''$	Yes	No
111	Spectra not pol. dependent	1	100	010	001	s/3	s/3	s/3	s/3	s/3	s/3	$a1, a1', a1'', b1, b2, b3$	No	Yes
		2	010	100	00$\bar{1}$	s/3	s/3	s/3	s/3	-s/3	-s/3	$a1, a1', a1'', b1, b2, b3$	No	Yes
		3	010	001	100	s/3	s/3	s/3	s/3	s/3	s/3	$a1, a1', a1'', b1, b2, b3$	No	Yes
		4	001	010	$\bar{1}$00	s/3	s/3	s/3	s/3	-s/3	-s/3	$a1, a1', a1'', b1, b2, b3$	No	Yes
		5	001	100	010	s/3	s/3	s/3	s/3	s/3	s/3	$a1, a1', a1'', b1, b2, b3$	No	Yes
		6	100	001	0$\bar{1}$0	s/3	s/3	s/3	s/3	-s/3	-s/3	$a1, a1', a1'', b1, b2, b3$	No	Yes

Table 5.7: Comparison of observed effects with expected perturbations in the D_2 point group

stress measured. This is estimated using the smallest intensity with which the line is observed when it is known to be induced and is higher than for the 1692 meV line because of baseline issues (described in Section 3.4.5) and because the detector sensitivity is falling off in that part of the spectrum, so there is greater noise. As before the second effect will be that the 1864 meV induced line will split into 2 components this time under [110] stress [001] polarisation and under ⟨111⟩ stress. The splitting must be greater than 1 meV to be resolvable, again more than for the 1692 meV line because this line is broader. This corresponds to a difference in $|\hat{a}_1'|$ and $|\hat{a}_1''|$ of 50%, so this effect is less likely to be noticed.

As a crude interpretation this sets an upper limit to the static variation of the defects from the ideal D_{2d} symmetry at about 10%. The extent of deformation expected from the vibrational model parameterised in Section 5.2.2 and in the next section is about 5% of a bond length, although this effect is dynamic.

The angular variation of the line width in epr was found not to fit a modified spin hamiltonian with an additional rhombic term $\delta E(s_x^2 - s_y^2)$ choosing x and y to be along either ⟨001⟩ or ⟨110⟩ (corresponding to D_2 and C_{2v} interstitials respectively)[72]. This, of course, applies to the (excited) epr state and cannot necessarily be expected to hold in the ground state.

5.3.10 Vibronic Model

The temperature dependence data of Section 5.2.1 shows that there are two closely spaced electronic energy levels in the ground state of $\mathbf{I}^0_{\langle 001\rangle}$, which has long been established [29]. This small splitting arises from a dynamic distortion as vibrations of $\mathbf{I}^0_{\langle 001\rangle}$ mix the vibronic progressions of the two parent electronic states reducing their separation by orders of magnitude, Section 5.2.2 [47]. A vibration can be considered as being a dynamic strain resulting in a dynamic distortion of $\mathbf{I}^0_{\langle 001\rangle}$, represented by the potential surface of Fig. 5.15, parameterised in Section 5.2.2 and re-parameterised this section. The minima have a depth of more than 200 meV. This is far greater than the distortion of a few meV at most, discussed under static strain, since the instantaneous

Stress	Polarisation	Local Axis Orientation				Stress Tensor Components						Transformations	Effect on spectrum transition induced	
		Defect	x	y	z	s_{xx}	s_{yy}	s_{zz}	s_{xy}	s_{xz}	s_{yz}	D_2	1692 meV	1864 meV
		1	$11\bar{0}$	$\bar{1}10$	001	s	0	0	0	0	0	$a1'$	No	Yes
	$\perp$ 001	2	$\bar{1}10$	$11\bar{0}$	$00\bar{1}$	0	s	0	0	0	0	$a1''$	No	Yes
110	$\parallel$	3	$01\bar{1}$	$0\bar{1}1$	100	s/4	s/4	s/2	-s/4	$s/(2\sqrt{2})$	$-s/(2\sqrt{2})$	$a1', a1'', a1, a2, b1, b3$	Yes	No
	$\perp$	4	$01\bar{1}$	$0\bar{1}\bar{1}$	$\bar{1}00$	s/4	s/4	s/2	-s/4	$-s/(2\sqrt{2})$	$s/(2\sqrt{2})$	$a1', a1'', a1, a2, b1, b3$	Yes	No
		5	101	$10\bar{1}$	010	s/4	s/4	s/2	s/4	$s/(2\sqrt{2})$	$s/(2\sqrt{2})$	$a1', a1'', a1, a2, b1, b3$	Yes	No
	$1\bar{1}0$	6	$\bar{1}01$	$\bar{1}0\bar{1}$	$0\bar{1}0$	s/4	s/4	s/2	s/4	$s/(2\sqrt{2})$	$s/(2\sqrt{2})$	$a1', a1'', a1, a2, b1, b3$	Yes	No
		1	$11\bar{0}$	$\bar{1}10$	001	0	0	s	0	0	0	$a1$	No	No
	$\parallel$	2	$\bar{1}10$	$11\bar{0}$	$00\bar{1}$	0	0	s	0	0	0	$a1$	No	No
001	$\perp$	3	$01\bar{1}$	$0\bar{1}1$	100	s/2	s/2	0	-s/2	0	0	$a1', a1'', a2$	Yes	No
	$\perp$	4	$01\bar{1}$	$0\bar{1}\bar{1}$	$\bar{1}00$	s/2	s/2	0	-s/2	0	0	$a1', a1'', a2$	Yes	No
		5	101	$10\bar{1}$	010	s/2	s/2	0	s/2	0	0	$a1', a1'', a2$	Yes	No
	$1\bar{1}0$	6	$\bar{1}01$	$\bar{1}0\bar{1}$	$0\bar{1}0$	s/2	s/2	0	s/2	0	0	$a1', a1'', a2$	Yes	No
	Spectra	1	110	$\bar{1}10$	001	2s/3	0	s/3	0	$(\sqrt{2})s/3$	0	$a1', a1, b1$	No	Yes
	not	2	$\bar{1}10$	110	$00\bar{1}$	0	2s/3	s/3	0	0	$-(\sqrt{2})s/3$	$a1'', a1, b3$	No	Yes
111	pol.	3	011	$0\bar{1}1$	100	2s/3	0	s/3	0	$(\sqrt{2})s/3$	0	$a1', a1, b2$	No	Yes
	dependent	4	$01\bar{1}$	$0\bar{1}\bar{1}$	$\bar{1}00$	0	2s/3	s/3	0	0	$(\sqrt{2})s/3$	$a1'', a1, b3$	No	Yes
		5	101	$10\bar{1}$	010	2s/3	0	s/3	0	$(\sqrt{2})s/3$	0	$a1', a1, b1$	No	Yes
	$1\bar{1}0$	6	$\bar{1}01$	$\bar{1}0\bar{1}$	$0\bar{1}0$	0	2s/3	s/3	0	0	$(\sqrt{2})s/3$	$a1'', a1, b3$	No	Yes

Table 5.8: Comparison of observed effects with expected perturbations in the C_{2v} point group

strain induced by a vibration is far greater than can be applied statically during a uniaxial stress experiment.

The minima represent equivalent distortions of $\mathbf{I}^0_{\langle 001\rangle}$ in opposite senses to either side of the mean undistorted configuration, represented by the saddle point at zero displacement in the mode. The mode of vibration was identified as that involved in the 1859 meV transition, which is made allowed by the vibration, (Section 5.2.2[47]). The symmetry of the mode and of the deformation can not be identified from the isotopic and temperature dependence experiments alone. However the uniaxial stress data have shown that the optically observed symmetry of $\mathbf{I}^0_{\langle 001\rangle}$ is D_{2d} and that the ground states are coupled by perturbations that transform as B_1 in that point group, Section 5.3.3.

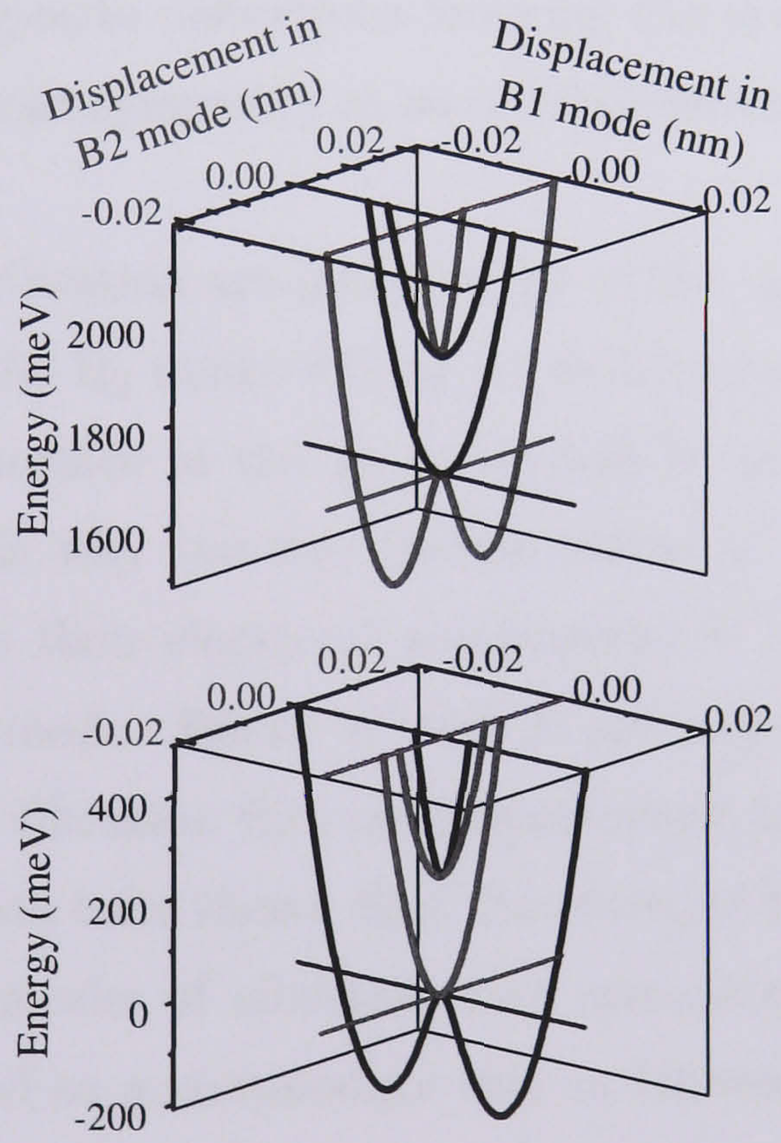

Figure 5.15: Potential surfaces of the interstitial in the B_1 and B_2 modes calculated using the theory of Section 2.3, Eqn. 2.28 from the parameters determined in this section.

This is an $x^2 - y^2$ perturbation and lowers the symmetry to D_2, Section 2.2.2,

Fig. 2.5. The minima in the potential surface can therefore be identified with distortions of $\mathbf{I}^0_{\langle 001\rangle}$ to D_2 symmetry through clockwise and counterclockwise displacements within a B_1 mode of vibration Figs 2.5, 2.4, 5.15, consistent with the predictions of Goss et al [69, 68].

The stress data has also revealed a previously unidentified electronic state 'd' and one phonon replica 'e' split by a few meV from the known electronic state 'c' and its one phonon replica 'f' respectively, in the first excited states of $\mathbf{I}^0_{\langle 001\rangle}$. These states have been shown to couple through B_2, (xy) perturbations that lower the symmetry to C_{2v} Section 2.2.2, Fig. 2.6. By analogy with the ground states this small splitting can be explained as arising from a dynamic distortion of $\mathbf{I}^0_{\langle 001\rangle}$, this time in a B_2 mode, resulting in a double minimum potential surface in that mode in the excited state. The minima correspond to opposite distortions lowering the symmetry to equivalent C_{2v} configurations and the mean symmetry at zero displacement is still D_{2d}, Figs 2.6, 2.5 and 5.15.

B_1 and B_2 modes of vibration are independent in the harmonic approximation so the potential surface in the B_2 mode will be an undistorted parabola in the ground state and the potential surface in the B_1 mode will be an undistorted parabola in the excited state. This is why the one phonon states 'e' and 'f' display the same behaviour under stress as their electronic components 'c' and 'd'; they are all zero-phonon states in the B_2 mode. States 'e' and 'f' are only one phonon states in the B_1 mode, a symmetry of vibration they are unperturbed by.

The uniaxial stress data have shown that the states of the defect may be coupled by either of two distinct modes of vibration with symmetry B_1 or B_2. The vibronic model is readily expanded to accommodate this as follows: The vibronic states are now products of ϕ, χ^1 and χ^2, where χ^1 and χ^2 are vibrations in B_1 and B_2 modes respectively. Equations 2.24 and 2.25 become:

$$\begin{aligned} E_{n,N} &= (n+1/2)\,\hbar\omega_1 + (N+1/2)\,\hbar\omega_2 \\ \text{and} \quad E_{p,P} &= E_0 + (p+1/2)\,\hbar\omega_1 + (P+1/2)\,\hbar\omega_2 \end{aligned} \tag{5.17}$$

where $\hbar\omega_1$ and $\hbar\omega_2$ are the vibrational quanta (phonon energies) in the B_1 and B_2

modes respectively. Now:

$$\phi_1 \chi_n^1 \chi_N^2 \left(\hat{c}Q\right) \phi_2 \chi_{n\pm1}^1 \chi_N^2 = c \left(\chi_n^1 Q_1 \chi_{n\pm1}^1\right) \left(\chi_N^2 \chi_N^2\right) \tag{5.18}$$

where $\int \left(\chi_N^2 \chi_N^2\right) dQ = 1$. Since $\int \chi_N^2 \chi_M^2 dQ = 0$ for N≠M, if the number, N, of B_2 phonons is not the same for two states they will not interact, (because they are orthogonal since they have different energies and there is no distortion in this mode) and the coupling term will be zero. So Eqn. 2.27 stands for N=M.

The matrix then becomes: (see Table 5.9)

	A00	B00	A10	A01	B10	B01
A00	$\frac{\hbar\omega_1+\hbar\omega_2}{2}$	0	0	0	$c\sqrt{\frac{\hbar}{2m\omega_1}}$	0
B00	0	$E_0+\frac{\hbar\omega_1+\hbar\omega_2}{2}$	$c\sqrt{\frac{\hbar}{2m\omega_1}}$	0	0	0
A10	0	$c\sqrt{\frac{\hbar}{2m\omega_1}}$	$\frac{3\hbar\omega_1+\hbar\omega_2}{2}$	0	0	0
A01	0	0	0	$\frac{\hbar\omega_1+3\hbar\omega_2}{2}$	0	0
B10	$c\sqrt{\frac{\hbar}{2m\omega_1}}$	0	0	0	$E_0+\frac{3\hbar\omega_1+\hbar\omega_2}{2}$	0
B01	0	0	0	0	0	$E_0+\frac{\hbar\omega_1+3\hbar\omega_2}{2}$

Table 5.9: Vibronic coupling matrix extended to two independent modes of vibration

Setting $\hbar\omega = 1$ (Fig. 5.16) the matrix (Table 5.9) may be diagonalised[4] in units of $\hbar\omega$, Fig. 5.17. As before the diagonal elements then give the energy eigenvalues of the coupled system so that the difference in energy of the lowest two is the observed energy separation, E_g, of the split ground state.

[4]Again, the calculation must be done for a finite number of phonons, in this case 7 is just about the limit of the programme (a 72 x 72 matrix).

	A00	B00	A10	A01	B10	B01	A20	A11	A02	B20	B11	B02	A30
A00	1	0	0	0	1.351	0	0	0	0	0	0	0	0
B00	0	2.47	1.351	0	0	0	0	0	0	0	0	0	0
A10	0	1.351	2	0	0	0	0	0	0	1.91	0	0	0
A01	0	0	0	2	0	0	0	0	0	0	1.351	0	0
B10	1.351	0	0	0	3.47	0	1.91	0	0	0	0	0	0
B01	0	0	0	0	0	3.47	0	1.351	0	0	0	0	0
A20	0	0	0	0	1.91	0	3	0	0	0	0	0	0
A11	0	0	0	0	0	1.351	0	3	0	0	0	0	0
A02	0	0	0	0	0	0	0	0	3	0	0	0	0
B20	0	0	1.91	0	0	0	0	0	0	4.47	0	0	2.339
B11	0	0	0	1.351	0	0	0	0	0	0	4.47	0	0
B02	0	0	0	0	0	0	0	0	0	0	0	4.47	0
A30	0	0	0	0	0	0	0	0	0	2.339	0	0	4

Figure 5.16: Partial vibronic coupling matrix for B_1 and B_2 modes with $\hbar\omega$=1 , E_0=1.47 and $c\sqrt{\frac{\hbar}{m\omega}}$=1.91. Only the B_1 mode couples the ground states, for B_2 c=0, vice versa in the excited state.

The corresponding eigenvectors may also be calculated. Note the vectors are still given by the program in columns rather than rows as depicted in Table 2.15. Now B10 represents state B with one phonon in the B1 mode and none in the B2 mode. At the undistorted defect transitions are allowed from B to a state E and are forbidden from A. They are therefore allowed from B00 to E00 and from B10 to E10 and so on.

	a	b	c	d	e	f	g	h	i	j	k	l	m	n
A00	0.694	0	0	0	-0	0	-0	0	0	0	0	0	0	0
B00	0	3.473	-0	0	0	0	0	0	0	1E-16	0	0	-0	0
A10	0	-0	-0.15	0	0	0	0	0	0	4E-17	0	0	5E-16	0
A01	0	0	0	1.735	0	0	0	0	0	0	-0	0	0	3E-20
B10	1E-16	0	0	0	5.179	0	-0	0	0	0	0	0	0	0
B01	0	0	0	0	0	4.699	0	-0	0	0	0	0	0	0
A20	-0	0	0	0	1E-28	0	-0.2	0	0	0	0	0	0	0
A11	0	0	0	0	0	2E-23	0	0.854	0	0	0	0	0	0
A02	0	0	0	0	0	0	0	0	2.82	0	0	0	0	0
B20	0	2E-26	1E-21	0	0	0	0	0	0	7.026	0	0	-0	0
B11	0	0	0	5E-17	0	0	0	0	0	0	6.645	0	0	-0
B02	0	0	0	0	0	0	0	0	0	0	0	5.042	0	0
A30	0	-0	5E-16	0	0	0	0	0	0	-0	0	0	0.96	0
A21	0	0	0	-0	0	0	0	0	0	0	-0	0	0	0.808

Figure 5.17: Partial diagonalised vibronic coupling matrix for B_1 and B_2 modes with $\hbar\omega$=1 , E_0=1.47 and $c\sqrt{\frac{\hbar}{m\omega}}$=1.91. Only the B_1 mode couples the ground states, for B_2 c=0, vice versa in the excited state.

Experimentally the 1859 meV one phonon transition is observed from the lowest energy coupled state, (whose energy and eigenvector is now given in column g Figs. 5.17 and 5.18 respectively) to the one phonon state E01. Since transitions to this E10 state are only quantum mechanically allowed from B10 in the uncoupled configuration, the coefficient of this B10 state (row B10, column g) gives the effect of the coupling on the transition probability of the 1859 (raises it from zero). Likewise, experimentally the 1685meV zero phonon transition is observed from the second lowest energy coupled state (whose eigenvector is now given in column c Figs. 5.17 and 5.18 respectively) to the zero phonon state E00. Since transitions to this E00 state are only allowed from B00 in the uncoupled configuration, the co-efficient of this B00 state (row B00, column c) gives the effect of the coupling on the transition probability of the 1685 (lowers it from 1). The ratio of these two numbers squared

and the separation of the two lowest states are unchanged (from their values in Section 5.2.2) by the presence of the second mode, as may be expected since the two modes are independent.

	a	b	c	d	e	f	g	h	i	j	k	l	m	n
A00	0.669	0	0	0	0.218	0	0.535	0	0	0	0	0	0	0
B00	0	0.664	-0.32	0	0	0	0	0	0	0.074	0	0	0.4	0
A10	0	0.493	0.623	0	0	0	0	0	0	0.249	0	0	-0.45	0
A01	0	0	0	0.683	0	0	0	0	0	0	0.152	0	0	0.542
B10	-0.15	0	0	0	0.674	0	-0.47	0	0	0	0	0	0	0
B01	0	0	0	0	0	0.563	0	-0.33	0	0	0	0	0	0
A20	-0.25	0	0	0	0.449	0	0.533	0	0	0	0	0	0	0
A11	0	0	0	0	0	0.512	0	0.63	0	0	0	0	0	0
A02	0	0	0	0	0	0	0	0	0.7	0	0	0	0	0
B20	0	-0.09	-0.48	0	0	0	0	0	0	0.602	0	0	-0.04	0
B11	0	0	0	-0.13	0	0	0	0	0	0	0.523	0	0	-0.48
B02	0	0	0	0	0	0	0	0	0	0	0	0.747	0	0
A30	0	-0.36	0.431	0	0	0	0	0	0	0.455	0	0	0.424	0
A21	0	0	0	-0.29	0	0	0	0	0	0	0.488	0	0	0.534

Figure 5.18: Partial eigenvector matrix for B_1 and B_2 modes with $\hbar\omega$=1 , E_0=1.47 and $c\sqrt{\frac{\hbar}{m\omega}}$=1.91. Only the B_1 mode couples the ground states, for B_2 c=0, vice versa in the excited state.

The stress experiments have provided a new measure of the separation of the coupled states E_g = 7.6 meV. Fitting the two unknowns E_0 and c with the two measured values E_g and the intensity ratio, of which the first is now revised, gives $E_0 = 250 \pm 50$ meV and a coupling strength of $c\sqrt{\frac{\hbar}{m\omega}} = (1.91 \pm 0.01)\,\hbar\omega$, only a slight change from before. This fitting can be done for the two mode case (Figs. 5.16, 5.17 and 5.18), but since the presence of the second mode does not affect the result, it is more accurate to do the calculation using the one mode matrix where a much greater number of phonons may be used for the same size of matrix (Figs.5.19, 5.20 and 5.21).

	A0	B0	A1	B1	A2	B2	A3	B3	A4	B4	A5	B5	A6	B6
A0	0.5	0	0	1.351	0	0	0	0	0	0	0	0	0	0
B0	0	1.97	1.351	0	0	0	0	0	0	0	0	0	0	0
A1	0	1.351	1.5	0	0	1.91	0	0	0	0	0	0	0	0
B1	1.351	0	0	2.97	1.91	0	0	0	0	0	0	0	0	0
A2	0	0	0	1.91	2.5	0	0	2.339	0	0	0	0	0	0
B2	0	0	1.91	0	0	3.97	2.339	0	0	0	0	0	0	0
A3	0	0	0	0	0	2.339	3.5	0	0	2.701	0	0	0	0
B3	0	0	0	0	2.339	0	0	4.97	2.701	0	0	0	0	0
A4	0	0	0	0	0	0	0	2.701	4.5	0	0	3.02	0	0
B4	0	0	0	0	0	0	2.701	0	0	5.97	3.02	0	0	0
A5	0	0	0	0	0	0	0	0	0	3.02	5.5	0	0	3.308
B5	0	0	0	0	0	0	0	0	3.02	0	0	6.97	3.308	0
A6	0	0	0	0	0	0	0	0	0	0	0	3.308	6.5	0
B6	0	0	0	0	0	0	0	0	0	0	3.308	0	0	7.97

Figure 5.19: Partial vibronic coupling matrix for B_1 mode only with $\hbar\omega$=1 , E_0=1.47 and $c\sqrt{\frac{\hbar}{m\omega}}$=1.91.

	a	b	c	d	e	f	g	h	i	j	k	l	m	n
A0	0.17	0	0	1E-09	5E-15	0	0	2E-12	-0	0	0	-0	6E-13	0
B0	0	2.587	2E-14	0	0	1E-11	2E-07	0	0	5E-07	-0	0	0	6E-10
A1	0	3E-14	-0.66	0	0	1E-13	-0	0	0	-0	-0	0	0	-0
B1	1E-09	0	0	4.483	1E-10	0	0	1E-08	-0	0	0	6E-08	-0	0
A2	5E-15	0	0	1E-10	-0.7	0	0	3E-07	9E-09	0	0	-0	2E-08	0
B2	0	1E-11	1E-13	0	0	6.313	5E-11	0	0	1E-10	-0	0	0	-0
A3	0	2E-07	-0	0	0	5E-11	0.408	0	0	-0	8E-10	0	0	-0
B3	2E-12	0	0	1E-08	3E-07	0	0	7.479	4E-07	0	0	7E-10	5E-10	0
A4	-0	0	0	-0	9E-09	0	0	4E-07	1.134	0	0	1E-10	1E-11	0
B4	0	5E-07	-0	0	0	1E-10	-0	0	0	8.558	-0	0	0	-0
A5	0	-0	-0	0	0	-0	8E-10	0	0	-0	1.555	0	0	-0
B5	-0	0	0	6E-08	-0	0	0	7E-10	1E-10	0	0	10.4	2E-13	0
A6	6E-13	0	0	-0	2E-08	0	0	5E-10	1E-11	0	0	2E-13	5.248	0
B6	0	6E-10	-0	0	0	-0	-0	0	0	-0	-0	0	0	11.51

Figure 5.20: Partial diagonalised vibronic coupling matrix for B_1 mode only with $\hbar\omega$=1 , E_0=1.47 and $c\sqrt{\frac{\hbar}{m\omega}}$=1.91.

	a	b	c	d	e	f	g	h	i	j	k	l	m	n
A0	0.655	0	0	0.204	0.532	0	0	0.026	0.405	0	0	0.002	0.088	0
B0	0	0.613	-0.32	0	0	0.07	0.38	0	0	0.01	-0.4	0	0	8E-04
A1	0	0.28	0.62	0	0	0.226	-0.44	0	0	0.048	0.124	0	0	0.006
B1	-0.16	0	0	0.601	-0.47	0	0	0.137	0.19	0	0	0.016	0.311	0
A2	-0.23	0	0	0.332	0.532	0	0	0.304	-0.47	0	0	0.062	0.308	0
B2	0	-0.27	-0.47	0	0	0.52	-0.02	0	0	0.172	0.287	0	0	0.029
A3	0	-0.07	0.432	0	0	0.337	0.385	0	0	0.297	-0.4	0	0	0.088
B3	0.358	0	0	-0.21	-0.34	0	0	0.536	0.119	0	0	0.195	0.108	0
A4	-0.44	0	0	-0.25	0.257	0	0	0.234	0.238	0	0	0.339	-0.26	0
B4	0	0.26	-0.25	0	0	-0.1	-0.43	0	0	0.408	0.037	0	0	0.235
A5	0	-0.23	0.17	0	0	-0.31	0.44	0	0	0.084	0.301	0	0	0.352
B5	0.308	0	0	0.189	-0.14	0	0	-0.25	-0.37	0	0	0.487	-0.16	0
A6	-0.23	0	0	0.086	0.081	0	0	-0.25	0.438	0	0	0.195	0.317	0
B6	0	-0.03	-0.08	0	0	0.015	-0.29	0	0	-0.3	-0.39	0	0	0.425

Figure 5.21: Partial eigenvector matrix for B_1 mode only with $\hbar\omega$=1 , E_0=1.47 and $c\sqrt{\frac{\hbar}{m\omega}}$=1.91.

The energies of the two mode states are plotted in Fig. 5.22 for $E_0 = 250 \pm 50$ meV as a function of c, to demonstrate the response of the states to the perturbation.

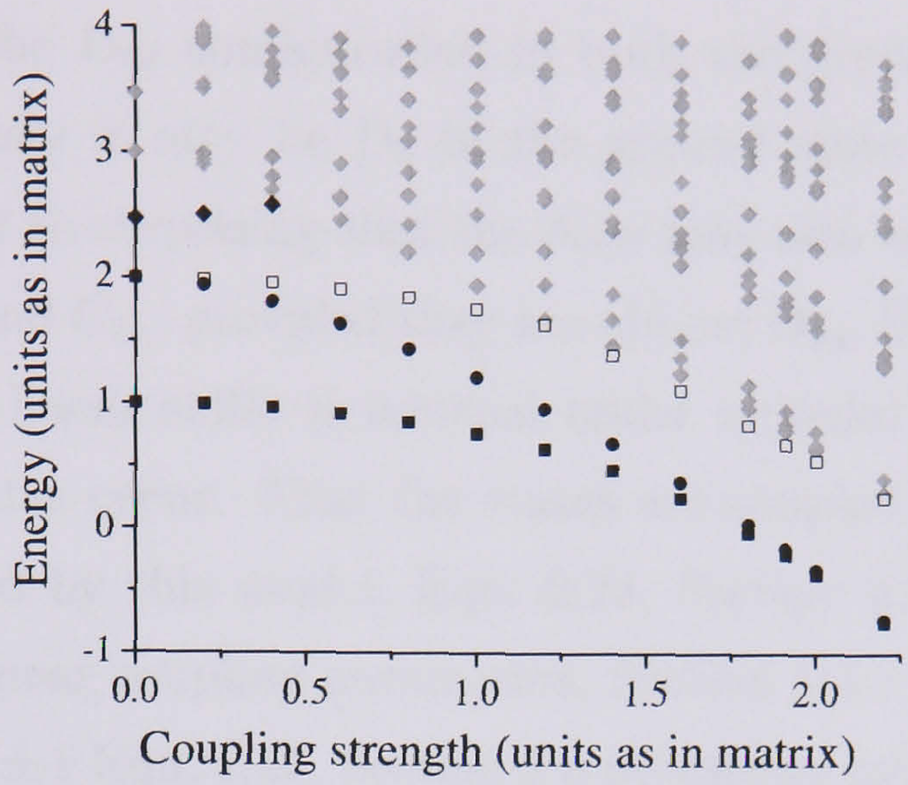

Figure 5.22: Energies of the two-mode coupled vibronic states as a function of coupling strength. A00 (filled squares) and A10 (circles) are repelled down from B10 and B00 (filled diamonds while discernable) respectively. A01 (open squares) behaves as A00 since its one B_2 phonon does not interact with the ground (A and B) states.

Double Minimum.

The splitting in the ground state of the interstitial is the tunnelling splitting arising from the tunnelling motion that is a consequence of the double minimum in the potential surface of $\mathbf{I}^0_{\langle 001\rangle}$, see Fig. 5.15. The splitting represents the uncertainty as to which minimum the defect is actually in since the energy level is not uniquely defined but has a spread equal to the splitting. The two levels represent the symmetric and antisymmetric combination of states giving two distinct states with a separation determined by the time spent in one of the wells. This amount of time, Δt, can therefore be calculated from the energy splitting, ΔE, using the uncertainty relation ($\Delta E \Delta t$ is approximately equal to $\hbar$). The smallest transition energy is 1685 meV while the largest energy splitting representing tunnelling at $\mathbf{I}^0_{\langle 001\rangle}$ is 7.6 meV (in the ground state; there is also tunnelling in the excited state, splitting = 5.0 meV). This means the timescale of the transition is orders of magnitude slower than the rate of tunnelling. So, on the timescale of our observation of the interstitial the average

is observed. This is the D_{2d} configuration in both the ground and excited states, although instantaneously it may be D_2 in the ground state or C_{2v} in the excited state. At least it is not so surprising that the data may also be fitted in terms of the lower symmetries D_2 and C_{2v}, provided they are almost D_{2d}, Sections 5.3.9 and 5.3.8.

To have negligible linear shifts is unusual under uniaxial stress, even where interactions between states occur. That the states are coupled to each other and not to themselves, required by this model, Eqn. 2.26, Section 2.3, is confirmed by the negligible size of the linear coupling parameters, Section 5.3.3. The uncoupled states only interact for $p = n \pm 1$ Eqn. 2.27, Section 2.3 producing two separate progressions of coupled states. This allows the coupled states to repel and the defect to distort.

5.3.11 Spurious Splittings - Some Interesting Observations

In some spectra the 1692 meV line appeared to split into two components. This might be expected for a centre of D_2 symmetry, Section 5.3.8, however it is easy to show that the observed splitting is spurious. If this splitting was due to D_2 symmetry, with $\hat{a}'_1 \neq -\hat{a}''_1$ then under [110] stress the 'a' to 'c' transition induced at defects with orientations 3-6, Table 5.7, would shift at different rates for defects orientated as 3 and 6 than for defects orientated as 4 and 5, due to the difference in magnitude of $(\hat{a}'_1)^2$ and $(\hat{a}''_1)^2$. The shift rates of the two components can be used to calculate $(\hat{a}'_1)^2$ and $(\hat{a}''_1)^2$. From this $(\hat{a}'_1 - \hat{a}''_1)^2$ can be calculated. This is the magnitude of the same perturbation, that should then be experienced by defects with orientations 1 and 2 in the same experiment. Without an applied stress a small intensity i_0 of the 1692 meV line is visible. The value of $(\hat{a}'_1 - \hat{a}''_1)^2$ that fits the splitting observed in the data should induce an intensity $i > 2i_0$ at the maximum stress of this experiment, at an energy hardly shifted from 1692 meV. This should therefore be readily detectable and is not observed.

What then, is the cause of this spurious splitting? The splitting is not observed in all of the relevant experimental runs and differs in extent from one experiment to the next. The sharpest and 'un-split' induced 'a' to 'c' transition is observed in an

experiment conducted on a sample that had been annealed under stress, unfortunately the first effect of annealing a D_2 interstitial under $\langle 110 \rangle$ stress might be expected to be to remove the orientational degeneracy 3/4 and 5/6, Table. 5.7. Re-orientation between equivalent D_2 centres aligned along the same [001] direction in this way requires a far smaller movement of the atoms and no breaking of bonds compared to re-orientation between D_2 centres aligned along different [001] directions. However, another explanation is that since the sample broke during this anneal and had to be re-polished, the faces of the sample were at their best and so the applied stress was at its most uniform. The same sample was then annealed at much higher temperatures (see Section 5.3.2) to compare the annealing behaviour of the 1692 and 1859 meV lines. After this anneal splitting was observed at the 1692 meV induced line and worsened with each anneal. This might be expected if annealing under stress had aligned the defects and annealing at a higher temperature without an applied stress returned them to randomly distributed orientations. However, in the analysis shown above this splitting has been shown not to be due to differing D_2 orientations because no induced intensity is observed under [110] stress in the [001] polarisation, this held true for the annealed sample. A better explanation is that, the surface of the sample was at its most perfect after polishing and deteriorated with annealing, producing an uneven stress leading to spurious splittings. At 77K such splittings would not be resolvable due to increased line width, so this is a hazard of working at such low temperatures and demonstrates a need for scepticism and quantitative analysis when observing some stress split components. The data as a whole needs to be consistent.

During one stress run the 1692 meV induced line was observed to exhibit one component as the applied stress was increased and two components as the stress was removed. This behaviour was entirely repeatable - Fig. 5.23. Note that the GR1 also displays hysteresis in its behaviour. This could be interpreted as deformation of the defect by stress (the deformation known to induce this line, Section 5.3.3) with a barrier to its return to an undeformed state at low temperature. Although this would have to apply to $\mathbf{V}^0$, $\mathbf{I}^0_{\langle 001 \rangle}$ and the defect that gives rise to the 1693 meV line, since

they all display this sort of behaviour. Uniaxial stresses are never perfect in practice, reproducing the exact line shapes from one experiment to the next is difficult. This is why repeated measurements have been made on the subtle features in the 1685 meV region.

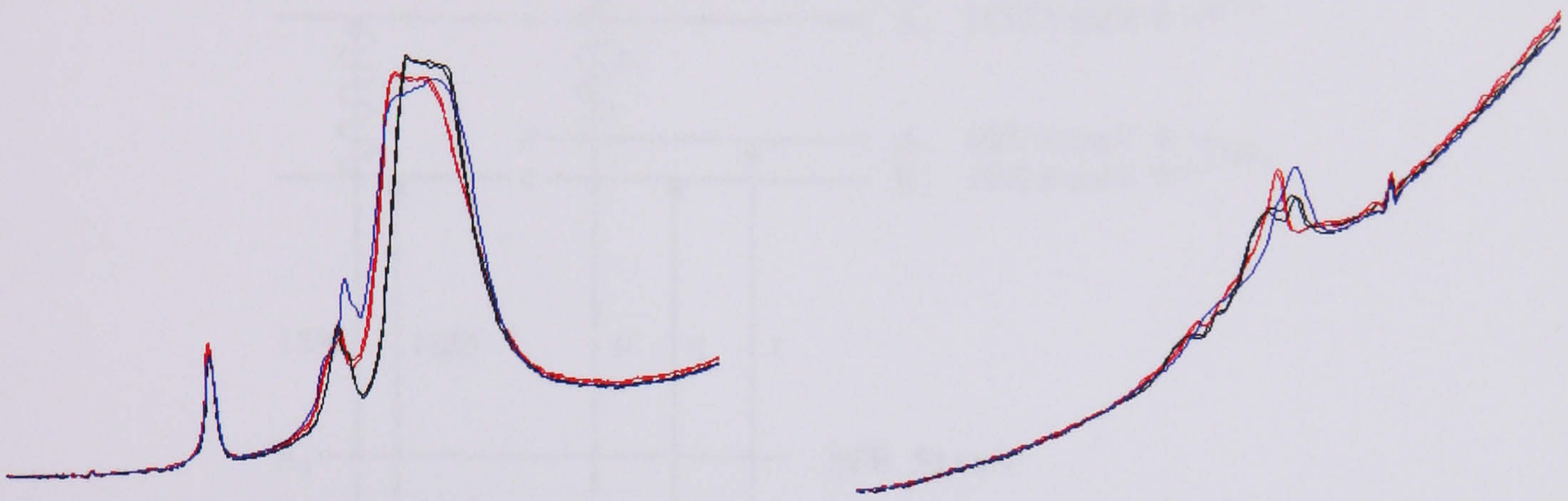

Figure 5.23: Stress splitting at the GR1 (LHS) and 1692 meV stress induced line (RHS): all spectra under the same [001] stress of greater than 1 GPa. The blue spectrum is taken the first time the defect is subjected to the stress, the black spectra were taken after the diamond has been taken up to twice that stress and back down, while the red spectra were taken after taking the diamond down to zero stress and back up.

5.4 Summary

Transitions at $\mathbf{I}^0_{\langle 001\rangle}$ can be induced by stress at 1690, 1692 and 1864 meV. The appearance of lines, their energy shifts and intensity variations under stress can be quantitatively fitted in terms of a defect with D_{2d} symmetry. The states of $\mathbf{I}^0_{\langle 001\rangle}$ interact considerably under symmetry lowering perturbations and suffer negligible first order perturbation by the stress. This work has revealed two previously unseen states of $\mathbf{I}^0_{\langle 001\rangle}$, one electronic, one vibronic. The information gained on the energy states of $\mathbf{I}^0_{\langle 001\rangle}$ is summarised in Fig. 5.24. The data is consistent with $\mathbf{I}^0_{\langle 001\rangle}$ vibrating in a B_1 mode in its ground state between equivalent dynamic distortions of D_2 symmetry

and in a B_2 mode between equivalent distortions of C_{2v} symmetry in an excited state. Any static distortion of $\mathbf{I}^0_{\langle 001\rangle}$ to D_2 or C_{2v} symmetry must be small and any dynamic distortion must be rapid on the timescale of the optical transitions.

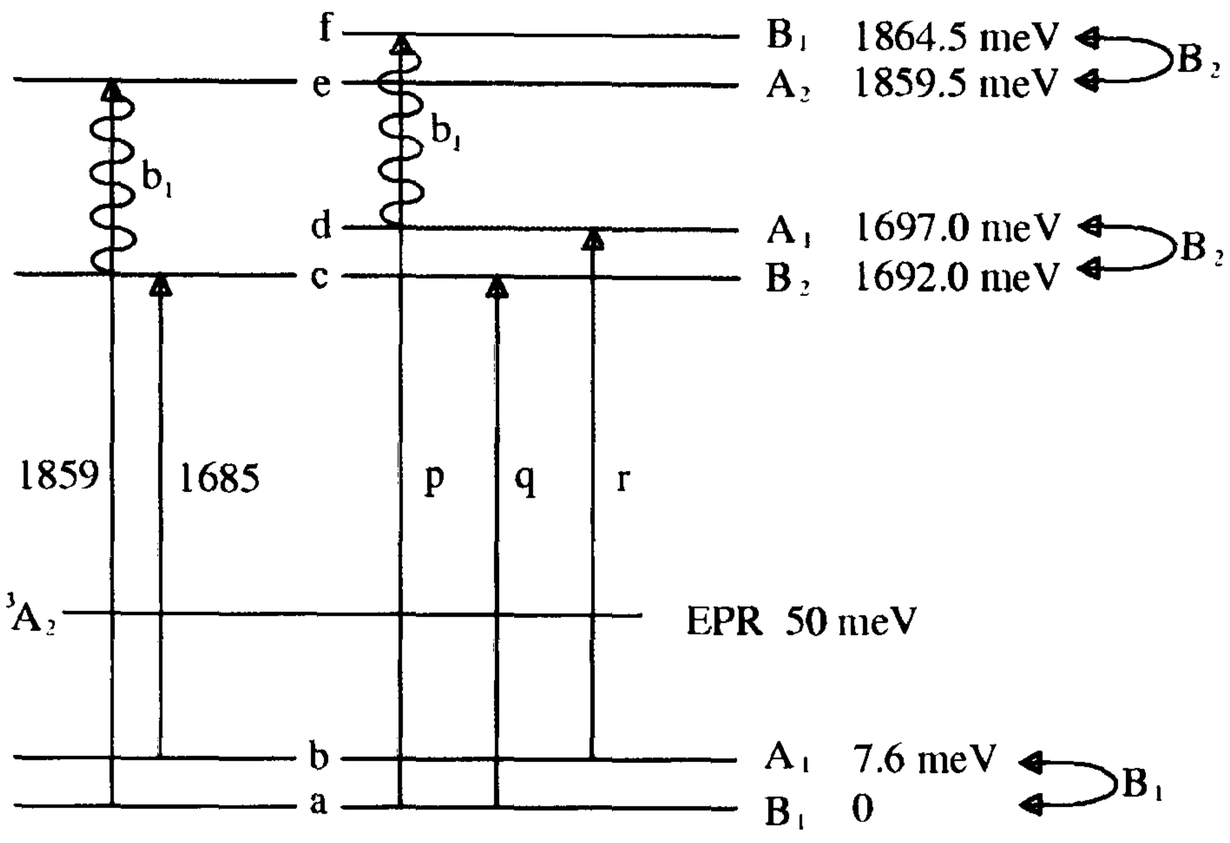

Figure 5.24: Energy Levels of $\mathbf{I}^0_{\langle 001\rangle}$, not to scale. The right hand side depicts information added as a result of work done in this section. Lines represent electronic transitions, wavy lines represent phonons with the indicated symmetry. Transitions p, q and r are stress induced. The choice of ground state symmetry is arbitrary, all other state symmetries follow from it. The symmetry indicated for the deformation required to couple the states and the symmetries of the phonons are independent of the choice of ground state and are definitively determined within the D_{2d} point group formalism.

Chapter 6

3H

One of the defects thought to involve self-interstitials is the 3H centre. The symmetry was investigated by Walker, but his fit required a coincidence in some parameters [81]. To understand the evolution of interstitials it would be helpful to know whether Walker's conclusions were correct. The better samples and techniques available today are used here to re-investigate Walker's conclusions.

6.1 Literature

The 3H defect is produced in diamond by irradiation and enhanced by heat treatment. It produces a sharp zero-phonon line at 2462 meV. Two other distinct defects labelled S1 and H3 also produce lines at this energy, a fact that was the source of some confusion in early studies of 3H [51]. The distinction between 3H and H3 was first made by Davies [82] (since they have different vibronic structures, H3 has considerable vibronic structure to higher energy while 3H has none, they have differing annealing behaviour and because H3 is only produced in type Ia diamond while 3H is produced in all types) and between 3H and S1 by Walker (S1 is only observed in luminescence 3H is also observed in absorption). 3H was named by Walker [81] for case of reference and to highlight both the similarity and the difference between it and H3.

3H is produced in all types of diamond by irradiation, most readily at room

temperature [51] and is the dominant PL in virtually all irradiated diamonds [83], [51, 84, 85]. Its strength is proportional to the nitrogen concentration in type Ia diamond and is particularly strong in type Ib samples, but is depleted in type IIb diamond [51, 85].

Annealing below 600K can enhance 3H [81], annealing to higher temperatures and illumination can bleach it out [81, 85, 83]. In early work there was a report that having annealed out at 600K, 3H may be restored by x-irradiation and is stable up to 900K [81] leading to the conclusion that this is a charge transfer effect. Contrary to this report more recent experiments were not able to recover the luminescence after annealing and X-ray irradiation [85].

3H is known to be highly mobile under the conditions of irradiation [85]. Line scans using photoluminescence microscopy, across a locally irradiated (using a transmission electron microscope) area of diamond, show that 3H luminescence is not confined to the electron irradiated area but extends outside it, even for a low temperature irradiation [85].

The 3H line shifts $+3.8 \pm 0.1$ meV in 99% ^{13}C diamond relative to 2463 meV in diamond of natural abundance isotopic composition [30].

In 50% ^{13}C diamond the highest energy local mode associated with 3H splits into three components, one at the same energy as in natural diamond (217.7 meV) and two others at 213.7 and 209.4 meV [84]. The integrated intensity of the central peak is approximately twice that of either outer peak, which are of approximately equal intensity [84] (1-2-1). The observed ratio between the highest and lowest frequencies is very close to $\sqrt{13/12}$ [84].

3H was studied under uniaxial stress by Walker [81]. The results corresponded well to a centre of C_{2v} symmetry with a $\pi\langle 110\rangle$ oscillator. The full set of standard uniaxial stress experiments were reported in this paper except for [110] stress [001] view [81], which was not done because the sample broke in an earlier experiment (!), the full set of perturbations can be adequately observed without the need for this direction so this should not affect the validity of his conclusions.

The precise atomic configuration of 3H eludes identification although it is generally thought of as an intrinsic defect that involves interstitials.

The 3H luminescence has been related directly to self-interstitials by its mobility upon irradiation and the isotope dependence of its highest energy local mode [84]. Since the self-interstitial is known to consist of a pair of closely situated carbon atoms, the three local modes of highest energy in 50% ^{13}C diamond might be expected to arise from ^{12}C^{12}C, ^{12}C^{13}C, and ^{13}C^{13}C pairs with the ratio between the highest and lowest frequencies being $\sqrt{13/12}$ as is observed for 3H [84]. The identification of $\mathbf{I}^0_{\langle 001\rangle}$ with R2 and the 1.685/1.859 eV lines in absorption, shows that if 3H is an isolated self-interstitial it must have a different structure or be in a different charge state.

3H may be $\mathbf{I}^0_{\langle 001\rangle}$-C-$\mathbf{I}^0_{\langle 001\rangle}$ [86] a second nearest neighbour $\mathbf{I}^0_{\langle 001\rangle}$ pair. Annealing (both isochronal and isothermal) has shown that as the di-interstitial (nearest neighbour $\mathbf{I}^0_{\langle 001\rangle}$ pair) anneals out following 1st order kinetics (indicating that there is no other party involved, no trapping or aggregation, just a simple breaking-up of R1) with an unusually low attempt frequency (ten orders of magnitude smaller than is typical); there is an associated rise in the 3H concentration while the GR1 and isolated $\mathbf{I}^0_{\langle 001\rangle}$ concentrations remain unchanged (indicating a structural change to R1 rather than full dissociation) [86]. The destruction of R1 is permanent. The activation energy for this break-up of the di-interstitial is 0.6 eV, much less than the 1.68 eV migration energy of $\mathbf{I}^0_{\langle 001\rangle}$ so the authors [86] propose it is the energy required to excite R1 to an S=0 level and translate one of the $\mathbf{I}^0_{\langle 001\rangle}$, via a vibrationally assisted jump, into the next lattice site; this would explain the low attempt frequency as well as the low activation energy [86]. According to theoretical calculations [87, 86] $\mathbf{I}^0_{\langle 001\rangle}$-C-$\mathbf{I}^0_{\langle 001\rangle}$ has S=0 and C_{2v} symmetry as does 3H. R1 has S=1 [88, 86] and also has an excited state in the band gap [88, 86].

Although 3H is generally assumed intrinsic, because it appears in all types of diamond, there is one other model proposing that since hydrogen is also common to all types [83] 3H may be a neutral H interstitial incorporated into the lattice during electron irradiation; structural models for this have been considered from theory [89].

Vlasov et al [83] identify a two rate quenching of 3H and say this is consistent with the very low migration energy of H+ predicted from theory [89] in terms of quick loss at traps but slower at surfaces [83]. Also that the donor level at about 3eV predicted from theory [89], is consistent with the ionisation energy of 3H which is between 2.7 and 3.8 eV [90]. C-H-C should give a 3-fold splitting in 50% ^{13}C for local modes [83] as observed at 3H by [84] and H should be depleted in B doped diamond as the donors are trapped by the boron acceptors [89] as is observed experimentally for 3H [51, 85].

3H appears in some (but not all) of the spectra recorded under stress presented in this thesis, permitting new measurements of its uniaxial stress splitting in some directions.

6.2 Uniaxial Stress on the 3H Centre

The splitting and shift in energy of 3H under uniaxial stress is shown in Fig. 6.1 for the $\langle 001 \rangle$ and $\langle 110 \rangle$ stress directions. 3H was not present in the $\langle 111 \rangle$ oriented sample. All the shifts are linear in the stress. The first order perturbations for a centre of C_{2v} symmetry with an $\langle 110 \rangle$ dipole under $\langle 110 \rangle$ and $\langle 001 \rangle$ stress are given in Table 6.1, written out by the same method as used in the $\mathbf{I}^0_{\langle 001 \rangle}$ analysis; without the complication of mixing of states the shifts are linear and so the parameters needed to fit the data are straightforward to write out. This has been done using Walker's [81] (originally Kaplyanskii's [91]) notation, in the last column where:

$$\begin{aligned}
A_1 &= [\langle e|\hat{a_1}|e\rangle - \langle g|\hat{a_1}|g\rangle] \\
A_2 &= [\ \langle e|\hat{a_1'}|e\rangle + \langle e|\hat{a_1''}|e\rangle - \langle g|\hat{a_1'}|g\rangle - \langle g|\hat{a_1''}|g\rangle\ ]/2 \\
A_2 + A_3 &= [\langle e|\hat{a_1'}|e\rangle - \langle g|\hat{a_1'}|g\rangle] \\
A_2 - A_3 &= [\langle e|\hat{a_1''}|e\rangle - \langle g|\hat{a_1''}|g\rangle]
\end{aligned} \tag{6.1}$$

where e represents the excited state and g represents the ground state of the transition. This is also worked out by Mohammed et al [40, 49][1]. The ⟨110⟩ dipole transforms as x or y (B_1 or B_2) so the transition is A to B.

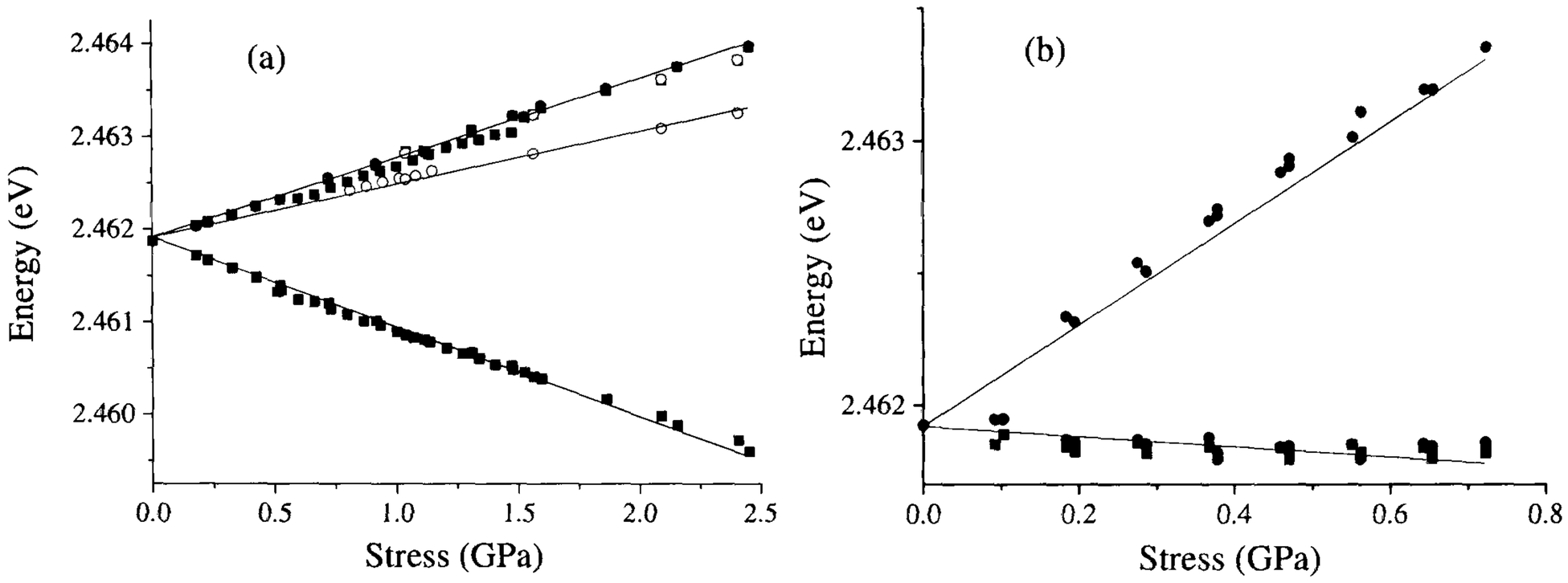

Figure 6.1: Stress splitting at 3H: (a) [110] stress, [110] polarisation (squares) [1$\bar{1}$0] polarisation (open circles), [001] polarisation (filled grey circles). (b) ⟨001⟩ stress, polarisation parallel to stress (squares) and perpendicular (circles).

Walker's values for A_1, A_2 and A_3 ([81], Table 6.2) gave $A_2 - A_3 = (A_1 + A_2)/2$ within experimental error and he did not observe a splitting of these components under [110] stress [1$\bar{1}$0] polarisation. This splitting is observed in the new data of Figs 6.1 and 6.2 strengthening the assignment to C_{2v}.

The intensities of the stress split components do not change as a function of stress or temperature, indicating there are no interacting states and the ground state is non-degenerate, as concluded by Walker [81].

[1] note x or y and z dipoles are the wrong way around in Mohammed's Thesis

Stress	Polarisation	Local Axis Orientation				Stress Parameters			Transformations	Stress Parameters (Walker's Notation)
		defect	x	y	z	s_{xx}	s_{yy}	s_{zz}		
110	[110]	1	110	$\bar{1}10$	001	s	0	0	a_1'	$A_2 + A_3$
	[1-10]	2	$\bar{1}10$	110	00$\bar{1}$	0	s	0	a_1''	$A_2 - A_3$
		3	011	0$\bar{1}$1	100	s/4	s/4	s/2	a_1', a_1'', a_1	$(A_1 + A_2)/2$
	[001], [1-10]	4	01$\bar{1}$	0$\bar{1}\bar{1}$	$\bar{1}$00	s/4	s/4	s/2	a_1', a_1'', a_1	$(A_1 + A_2)/2$
	[110]	5	101	10$\bar{1}$	010	s/4	s/4	s/2	a_1', a_1'', a_1	$(A_1 + A_2)/2$
		6	$\bar{1}$01	$\bar{1}$0$\bar{1}$	0$\bar{1}$0	s/4	s/4	s/2	a_1', a_1'', a_1	$(A_1 + A_2)/2$
001	$\perp$ to stress	1	110	$\bar{1}10$	001	0	0	s	a_1	A_1
	$\parallel$	2	$\bar{1}10$	110	00$\bar{1}$	0	0	s	a_1	A_1
		3	011	0$\bar{1}$1	100	s/2	s/2	0	a_1', a_1''	A_2
	$\perp$ to stress	4	01$\bar{1}$	0$\bar{1}\bar{1}$	$\bar{1}$00	s/2	s/2	0	a_1', a_1''	A_2
		5	101	10$\bar{1}$	010	s/2	s/2	0	a_1', a_1''	A_2
		6	$\bar{1}$01	$\bar{1}$0$\bar{1}$	0$\bar{1}$0	s/2	s/2	0	a_1', a_1''	A_2

Table 6.1: Perturbations under uniaxial stress for differently oriented centres with C_{2v} symmetry and a $\langle 110 \rangle$ dipole.

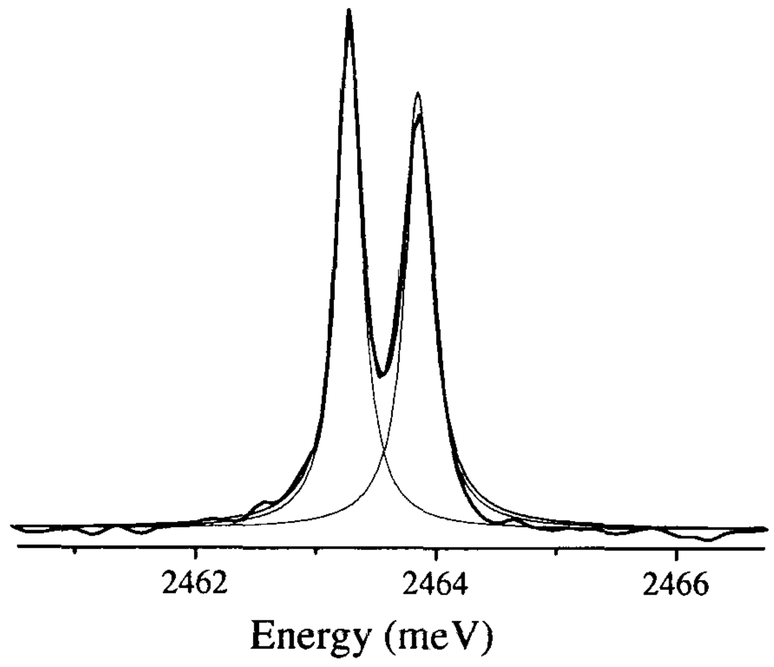

Figure 6.2: Splitting at 3H under [110] stress in $[1\bar{1}0]$ polarisation. Data is shown in black, fit is shown in grey.

Parameter	Walker(meV GPa^{-1})	Current Work(meV GPa^{-1})
A_1	1.8	1.93
A_2	-0.3	-0.19
A_3	-1.2	-0.77
error	±0.3	±0.05

Table 6.2: Stress splitting parameters for the 3H centre. See Eqn. 6.1 for definitions.

6.3 Summary

The improved stress data presented here have shown that the 3H defect has C_{2v} symmetry and a $\langle 110 \rangle$ dipole, in agreement with the results of Walker [81]. All the perturbations are linear in the stress and are fitted with parameters of similar magnitude to those of Walker [81]. Through the application of higher stresses the one stress split component that may be expected for this symmetry that was not resolved by Walker, due to a near coincidence in the parameters (or because he could not measure this direction after a sample broke) has been resolved here under [110] stress $[1\bar{1}0]$ polarisation, Fig. 6.2. This sheds no new light on the exact atomic configuration of the defect but does serve to confirm the symmetry.

Chapter 7

Interstitials in Ib Diamond

In optical absorption spectroscopy, the presence of $\mathbf{I}^0_{\langle 001 \rangle}$ has been quantified using the peak intensity at 1859 meV since $\mathbf{I}^0_{\langle 001 \rangle}$ was identified in the optical absorption spectrum. Where the $\mathbf{I}^0_{\langle 001 \rangle}$ are heavily distorted, this is inappropriate and gives a considerable underestimate of the number of $\mathbf{I}^0_{\langle 001 \rangle}$ present.

Radiation damage in nitrogen containing diamond produces a very different spectrum to that in irradiated pure diamond. Holding to the theme of self-interstitials and their perturbation, this chapter presents a new study of the effect of the presence of nitrogen in diamond, on the production of self-interstitials by irradiation.

It will be shown that absorption by self-interstitials is very different in appearance in 'as irradiated' nitrogen containing diamond, than in the pure diamond considered so far. In fact the presence of the nitrogen has a profound effect on the amount and structure of the defects formed by irradiation in diamond and the way they absorb.

7.1 Literature

To get a good picture of what happens in nitrogen containing diamond when it is irradiated, what is known about the defects concerned and their interactions needs to be reviewed.

Nitrogen Aggregation and Diamond Classification

Nitrogen exists in single substitutional form ($\mathbf{N_S}$) in most untreated synthetic diamonds and may be in the neutral or positive charge state depending on the other defects that are present [92]. Upon annealing, nitrogen can become mobile within the lattice, migrate, meet up and form various types of aggregates. These defects cause characteristic absorption in the one-phonon region of the infrared (IR) spectrum. Absorption in the blue end of the visible spectrum due to the presence of dispersed nitrogen (single substitutional) causes diamonds to be yellow-brown in colour; this colour is reduced on annealing, as aggregation occurs and the concentration of dispersed nitrogen diminishes [93].

Diamonds are classified according to the impurities they contain determined by their IR spectra in the one-phonon region. Diamonds that show negligible absorption in the one phonon region are classified as type IIa ('pure') while diamonds which contain single substitutional nitrogen, sometimes known as C type, are classed type Ib. Although HPHT grown synthetic diamonds can be made to be type IIa if they are grown with nitrogen getters, most HPHT grown synthetic diamonds are type Ib, while few natural diamonds are. This is due to their having been subjected to moderately high temperatures and pressures after their formation, for much longer than can be done in the laboratory, so that any dispersed nitrogen will have long since aggregated. Diamonds containing aggregated nitrogen are classed type Ia.

Aggregation Sequence [94]

Upon annealing, single substitutional nitrogen atoms first meet up to form pairs, the two atoms assuming adjacent substitutional lattice positions. This is called an A aggregate. The additional electron associated with each of the $\mathbf{N_S}$ (relative to carbon) is localised in the bond between the two nitrogen atoms, so that they relax apart along a $\langle 111 \rangle$ direction. This pair is more stable in diamond than $\mathbf{N_S}$ are separately.

Upon further aggregation B and N3 centres are formed. B centres are very stable and consist of four nitrogen atoms and a vacancy, while N3 centres consist of three

nitrogen atoms and a vacancy.

$\mathbf{N_S}$, A and B centres all show characteristic absorption in the one phonon region of the infrared spectrum, (see Fig. 7.1), this can be used to determine their relative concentrations within a given sample. N3 centres do not create absorption in this region [95]. Diamonds containing nitrogen aggregated in mostly A form are classed type IaA and diamonds containing mostly the B aggregate are classed type IaB.

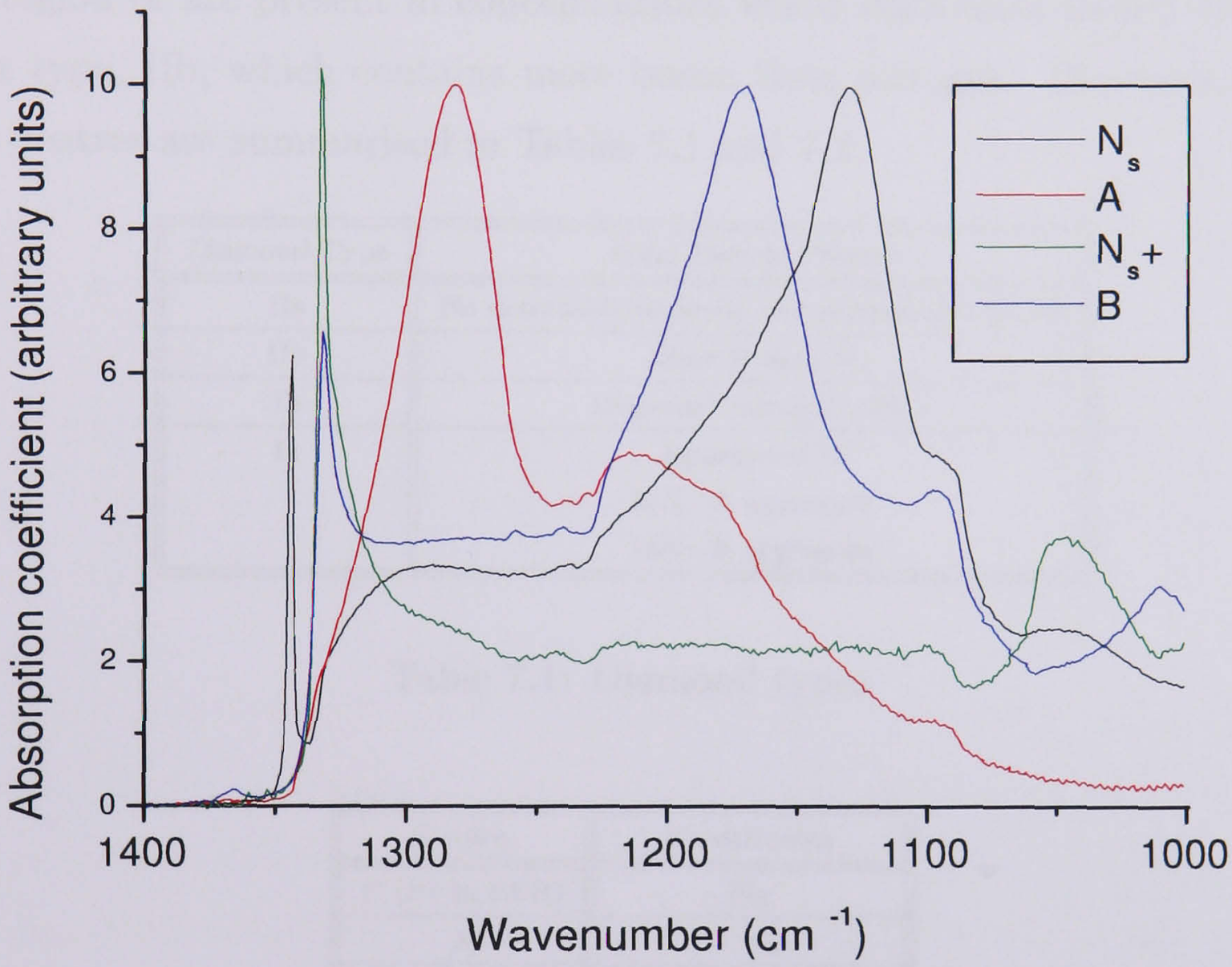

Figure 7.1: One-phonon absorption component spectra due to the presence of nitrogen defects, plotted using the Nitrogen Concentration Wizard (IR spectra decomposition program, D. Fisher (modified A. Smith)). $\mathbf{N_S}$ = single substitutional (type Ib), A = A aggregate (type IaA), B = B aggregate (type IaB), $\mathbf{N_S^+}$ = positively charged single substitutional $\mathbf{N_S}$. Wavenumber scale plotted inversely according to convention.

Another product of nitrogen aggregation, is the appearance in the later stages of aggregation [94], of increased absorption due to platelets, just outside the one-phonon region. The structure of these platelets has not been identified, but they are thought

to be formed from carbon interstitials released by the aggregation of A centres into N3 and B centres (since they contain a vacancy). Platelets can contain nitrogen, although it is not thought to be part of their structure, but to be present as an impurity decorating the defect [94].

To summarise, type I diamonds contain nitrogen, Ib in dispersed form and Ia as aggregates, type IIa are 'pure' (any impurities present do not absorb in the one phonon region or are present in concentrations below detectable levels) and there is a further type, IIb, which contains more boron than nitrogen. Diamond types and nitrogen centres are summarised in Tables 7.1 and 7.2.

Diamond Type	Point Defects Present
IIa	No detectable impurity one-phonon absorption
IIb	More B than N
Ib	Dispersed nitrogen - $\mathbf{N_S}$
Ia	Aggregated N: IaA - A aggregate IaB - B aggregate

Table 7.1: Diamond types

Centre	Constituents
C (P1 in EPR)	$\mathbf{N_S}$
A	2 $\mathbf{N_S}$
B	4 $\mathbf{N_S}$ and a vacancy
N3	3 $\mathbf{N_S}$ and a vacancy

Table 7.2: Some nitrogen centres.

Influence of Radiation Damage and Transition Metals

The presence of vacancies and interstitials has been found to influence the rate at which nitrogen already present in the diamond can aggregate. A number of mechanisms for this interference have been proposed such as; carbon interstitials returning to lattice sites by knocking single substitutional nitrogen atoms out of their lattice

positions, producing nitrogen interstitials [34] which are then highly mobile and can so aggregate more quickly [96, 35, 36]; or in the case of vacancies the formation of nitrogen vacancy complexes [34, 36] that also have an increased mobility within the lattice and so are able to aggregate more quickly.

Nitrogen aggregation can also be influenced by the presence of transition metals such as Ni and Co [34, 35, 36]. The mechanisms behind this influence are not known although it is thought that the transition metals may produce carbon interstitials or vacancies, which in turn influence nitrogen migration.

It has been suggested that Ni occupying a double semi-divacancy position (Ni impurity sitting in the middle between two adjacent, otherwise vacant, lattice sites - octahedral orientation) is formed through negatively charged substitutional Ni, (Ni_S^-, defect NE4, tetrahedral orientation) displacing a neighbouring carbon atom producing an interstitial [34, 35, 36]. These carbon interstitials may go on to enhance aggregation. Nickel is observed in single substitutional form in as-grown diamonds, the semi-divacancy is observed only after annealing. It has also been suggested that during annealing a reversion of the Ni to NE4 [34] or adjustment of other Ni-vacancy complexes [36] may then release vacancies which go on to enhance aggregation. A third mechanism for aggregation enhancement by the presence of transition metals has been proposed as an increased $\mathbf{N}_S^+$ diffusion rate in the Coulomb field of negative charge states of Ni containing centres [34]. In summary, transition metals are known to increase the aggregation rate and cause a deviation from the second order kinetics expected, for two atoms randomly coming across each other [34, 35, 36] and there is evidence to suggest the involvement of an intermediate species, (probably vacancies or interstitials) but no firm evidence has yet been found to confirm these processes.

Vacancies and self-interstitials therefore play a significant and pervasive role in defect reactions in nitrogen containing diamond, so having a good understanding of them in these diamonds is important.

IR - Nitrogen and Nitrogen Aggregate Concentration Determination

To study the interactions between vacancies, interstitials and nitrogen in diamond, it is necessary first to quantify the amount and aggregation state of nitrogen present.

The amount of absorption produced by a defect is proportional to its concentration. The standard IR spectra, shown in Fig. 7.1, for the nitrogen and nitrogen aggregate defects, are used to establish their concentrations. Where more than one of these defects is present in a sample at one time, as is often the case, their relative absorption spectra will add up to give the observed absorption. Establishing their concentrations in a given sample, then requires that the recorded spectrum for that sample, be decomposed to show which absorption features are present and what their intensities are. This is easily done using a program called the Nitrogen Concentration Wizard written in Excel using Visual Basic by David Fisher (DTC Research Centre) and modified by Alex Smith (KCL). Data is loaded into the program and the best least squares fit of the sum of each of the reference spectra to the data, is found as a function of the intensity (proportional to defect concentration) of each of the defect spectra. The fit and its component spectra are then plotted with the data and the defect concentrations are calculated from the peak intensities and are listed in a table below the chart. The lines used in this calculation are shown in the table and the relations between intensity and concentration are given in the introduction of reference [92], which includes a figure showing the spectra. An example output of this program is shown in Fig. 7.2.

The residual between the data and the fit is also plotted; if the fit is good this should purely represent the noise on the data. The errors in the concentrations determined by this method have been estimated from inspection of the residual, for example it was estimated to be about $\pm$ 0.1 cm^{-1} for the C centre, from the data shown in the example output i.e. 105.3 $\pm$ 2.5 ppm of single substitutional nitrogen is present in the sample. This method of concentration determination is subject to baseline errors (significant at low concentrations) and assumes homogeneity, often a false assumption.

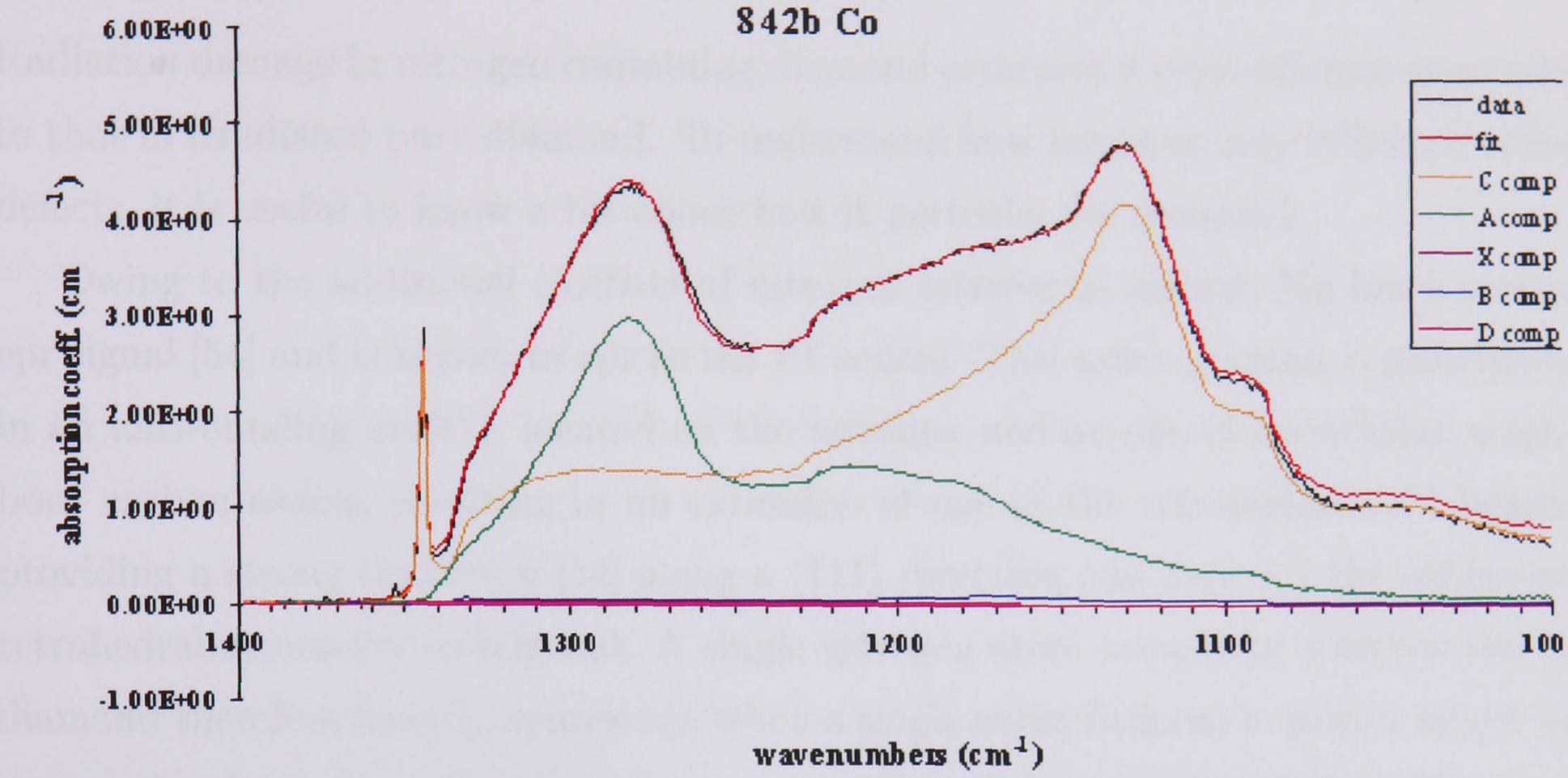

type Ib	$\mu(1130cm^{-1})$	4.21 cm^{-1}	$[N_C]$	105.3 ppm	
type IaA	$\mu(1282cm^{-1})$	2.98 cm^{-1}	$[N_A]$	49.2 ppm	
N^+	$\mu(1332cm^{-1})$	0.00 cm^{-1}	$[N^+]$	0.0 ppm	
type IaB	$\mu(1282cm^{-1})$	0.03 cm^{-1}	$[N_B]$	2.7 ppm	*fit*)
D	65536	0.02 cm^{-1}	$[N_T]$	157.2 ppm	

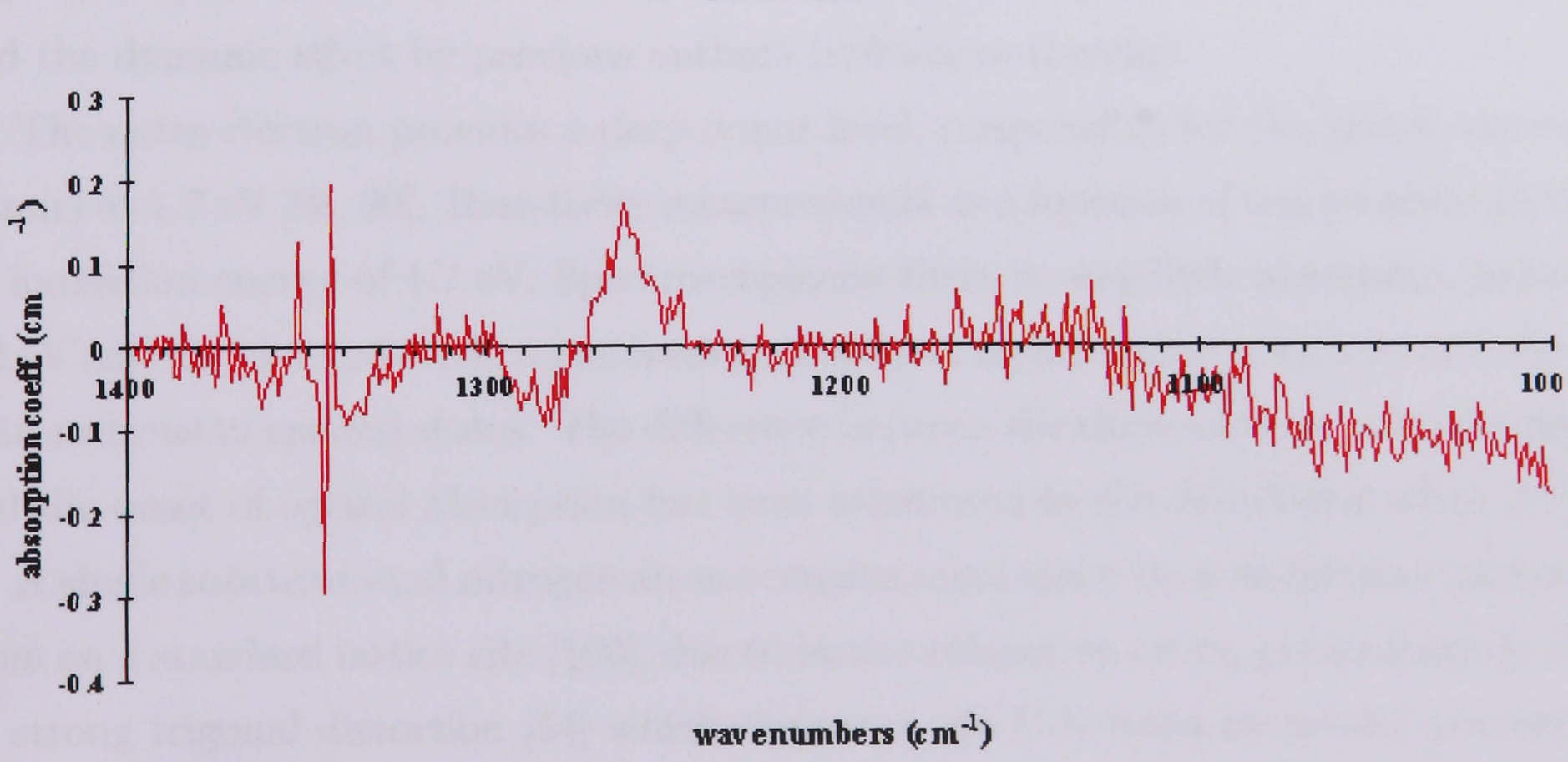

Figure 7.2: Example output of the Nitrogen Concentration Wizard (IR spectra decomposition program, D. Fisher (modified A. Smith)).

The Structure of N_S and the Lattice Response

Radiation damage in nitrogen containing diamond produces a very different spectrum to that in irradiated pure diamond. To understand how nitrogen may influence other defects, it is useful to know a bit about how it perturbs the diamond.

Owing to the additional electron of nitrogen relative to carbon, N_S has a strong epr signal [54] and is known in epr as the P1 centre. This extra electron is principally in an anti-bonding orbital, located on the nitrogen and on one of its nearest neighbour carbon atoms, resulting in an extension of one of the tetrahedral C-N bonds, providing a strong distortion [54] along a $\langle 111 \rangle$ direction and lowering the otherwise tetrahedral symmetry to trigonal. A single nitrogen atom occupying a lattice site in diamond therefore has C_{3v} symmetry, when a single substitutional impurity might be expected to have the same symmetry as a normal lattice site, (which is T_d). There are four equivalent static distortions at low temperature, but when the temperature is high enough, re-orientation may occur between the equivalent distortions, replacing the orientational degeneracy with a vibronic degeneracy and effectively restoring the tetrahedral symmetry [51]. Static re-orientation has been observed by Ammerlaan et al in epr, upon isothermal annealing of stress induced alignment of the centres [97] and the dynamic effect by previous authors (references therein).

The extra electron provides a deep donor level, (responsible for the yellow/brown colour) at 1.7 eV [98, 99]. Resistivity measurements as a function of temperature yield an ionisation energy of 1.7 eV. Spectroscopically there is very little absorption below 2.2 eV and the absorption then increases gradually at higher energies with no evidence of transitions to excited states. The difference between the electrical ionisation energy and the onset of optical absorption has been attributed to the JahnTeller effect [51].

A single substitutional nitrogen atom occupies more space than an intrinsic carbon atom on a standard lattice site [100], due to lattice relaxation owing predominantly to its strong trigonal distortion [54] which elongates one C-N bond by several percent. The exact extent of the relaxation is unclear. Lang et al ([101], 1998) discuss the varying theoretical calculations of the extent of this C-N bond elongation (of between

a few and 30 percent) and compare them to the estimation of 35% made from stress alignment and thermal re-orientation experiments in epr by Ammerlaan et al [97] and to their own measurement of the volume dilation by the nitrogen, (41%, later revised to 35% [100]) suggesting a C-N extension well in excess of this. It is generally agreed that nitrogen produces strain within the lattice. Vacancies may help relieve this strain and so are readily trapped at the nitrogen.

As we will see in the next section, $\mathbf{N_S}$ may interact with a vacancy in diamond and transfer an electron, leaving it positively charged. $\mathbf{N_S^+}$ does not have the additional electron compared to carbon, that $\mathbf{N_S}$ has and so may be expected to retain the tetrahedral symmetry of a standard lattice site. In the absence of the strong trigonal distortion of $\mathbf{N_S}$, $\mathbf{N_S^+}$ may be expected to occupy less space in the lattice and so induce less strain than $\mathbf{N_S}$ [102]. This has implications (which should be noted in this chapter) for the amount and type of strain produced by $\mathbf{N_S}$ when there are vacancies present.

Vacancy - Nitrogen Defect Reactions

This thesis is principally concerned with interstitials and this chapter is no exception. The production (and often fate) of interstitials in diamond is however, inextricably linked to that of the vacancy; so it is helpful to review what is known about the vacancy in nitrogen containing diamond.

Vacancies in diamond are readily trapped [103] upon annealing by nitrogen in many of its forms;

$\mathbf{N_S}$ + V $\rightarrow$ NV (2.156 eV or 575 nm) [104] or NV^- (1.945 eV) [105]

A + V $\rightarrow$ NVN (H3) [106] or NVN^- (H2) [107]

B + V $\rightarrow$ H4, [106]

Collins established that isolated nitrogen atoms are much more efficient at trapping vacancies upon annealing than A or B centres which are similarly efficient [103]. Later, armed with the subsequently determined oscillator strengths of the centres, Davies [30] used this data [103] to determine that the vacancy capture radius around a single substitutional nitrogen atom, is about 20 times larger than around a nitrogen pair (A centre). Davies also calculated that this radius is 1.7 times bigger for an A centre than for a B centre [30]. These radii apply to thermal migration of vacancies. Other work has found that $\mathbf{N_S}$ traps vacancies 8 times more efficiently than A centres [108].

Radiation damage is known to enhance nitrogen aggregation considerably upon annealing, so this relative vacancy trapping efficiency of differing aggregates of nitrogen has been used to explain how vacancies may enhance nitrogen aggregation, via the following mechanism: NV + N → NVN (H3) → V + NN (A aggregate) → NV [103]. The multiple release and re-trapping of vacancies allowed by this mechanism, accounts for the extent of enhancement, by a vacancy concentration which may be very much less than the nitrogen concentration [103].

Influence of Ia Character on the Production of Radiation Damage

It will be shown in this chapter that absorption by self-interstitials is very different in 'as irradiated' Ib diamond, than in IIa diamond. The epr might also be expected to be very different or even absent. To put this into context, it is useful to review what is known and how it was concluded, from the defects that are recognised and can be quantified, as well as those that are missing and the things that are not understood. Detailed early work focussed on IaA diamond, so this is where the discussion will start.

Vacancy production upon irradiation is enhanced as much as 60% by the presence of A aggregates of nitrogen in type IaA diamond compared to type IIa [59]. The enhanced portion, identified via the additional line width (due to the strain) of the GR1, anneals out much more readily (12 times! [59]) than the remainder, leaving the

GR1 narrowed and implying the enhancement is local to the strain source (nitrogen). In fact, using the known stress response to analyse the strain broadened GR1 in these samples, 40% of the vacancies produced in this material are estimated to be within a few atomic sites (0.7 nm) of the nitrogen [59] (roughly 3% of the total volume of the diamond). The authors suggested [59] that the presence of the nitrogen reduced correlated recombination of vacancies with interstitials during irradiation, enhancing the final vacancy concentration. Davies has proposed that [30] since, if we assume that an interstitial halves its kinetic energy each time it collides with lattice atoms, its energy will typically be reduced below its migration barrier of 1.6 eV after only about 4 collisions, then correlated recombination during irradiation is likely to be not insignificant; in a more detailed calculation he showed that the damage without correlated recombination is likely to be only about double that where it is effective [79]. Fast annealing of the extra vacancies in IaA diamond [59] was observed with an activation of 1.6 eV, the authors attributed and matched it to the growth in H3 centres (N-V-N) as the vacancies created nearest to the nitrogen pairs are captured by them. They also showed that the growth of H3 showed the same two speed behaviour so that the fast process must involve the motion of vacancies [59] and not to annihilation with nearby interstitials. Reference [79] contains a more recent A centre /vacancy related discussion of the effect of nitrogen on radiation damage determined in reference [59].

At the time of this work the isolated self-interstitial had not yet been identified and was thought not to be stable at room temperature, a more recent study has shown that interstitial production is also enhanced in IaA diamond [109], by about 60%.

Influence of Ib Character on the Production of Radiation Damage

Recent work by Collins and Dahwich [2], taking advantage of the differing uptake of nitrogen in different growth sectors [5] to study radiation effects on Ib diamond of varying nitrogen concentrations, [2] has shown that the total vacancy production is also enhanced in type Ib diamond. The enhancement was by a factor of 3 with a

concentration of 25 ppm of $\mathbf{N_S}$, a factor of 4 for 75 ppm $\mathbf{N_S}$ and for $[\mathbf{N_S}]$ of about 300 ppm, may be as high as a factor of 5 [2].

In Ib diamond, the production of GR1 falls [30, 58, 110], while the ND1 (negative vacancy, 3.150 eV) increases [110] due to charge transfer from the nitrogen donor. The equilibrium charge state of vacancies is determined by impurities, in IIa diamond the GR1 is prevalent, in Ib diamond the ND1 maybe prevalent (depending on the relative concentrations of the $\mathbf{N_S}$ and $\mathbf{V}$ [71]) and in Ia diamond there is a mixture [59]. The charge state of a single vacancy is influenced by its proximity to the nitrogen donor, the nearer it is to the nitrogen donor the more likely a vacancy is to be negatively charged [111]. A negatively charged vacancy must correspond to an $\mathbf{N_S^+}$, which will therefore be the nearest nitrogen. Since $\mathbf{N_S^+}$ is expected to produce less strain in the lattice than $\mathbf{N_S}$ [102] there may be a sudden change in strain experienced by vacancies from the nitrogen the nearer they get, with coulomb effects also becoming important. This has implications, of potential significance in the analysis later in this chapter, for the amount and type of strain produced by $\mathbf{N_S}$ when there are many vacancies present.

Vacancies migrate in the neutral charge state, negatively charged vacancies must undergo a reversible charge transfer process before migrating, driven by the charge state equilibrium just described [59]. Collins and Dahwich [2] measured the total concentration by inferring (it cannot be measured directly due to other strong broad band absorption in this region in high nitrogen diamond) the negative vacancy (ND1) concentration from the $\mathbf{N_S^+}$ concentration [2]. The authors attributed their enhancement in total vacancy production in Ib diamond, to a reduction in correlated recombination during irradiation, possibly arising from trapping of interstitials by the nitrogen [2]. They found only a weak intensity (compared to that produced in IIa diamond) of the 1859 meV 'line' which grew in intensity upon annealing, reaching a maximum at about 400°C before annealing out [2], and attributed it to the annealing out of the 2.535 meV line thought to be a nitrogen self-interstitial complex.

If the peak intensity at 1859 meV gives an accurate measure of the number of

interstitials and there are more vacancies in this material, this raises the question as to where the corresponding interstitials are. The possibilities are: that they are trapped by the nitrogen, that they are in a different charge state, that they are distorted by strain and so are not contributing to the peak intensity at 1859 meV or some combination of the three. Possible nitrogen interstitial complexes have been identified in optical absorption and appear in these spectra, but it is not known how many are present, since the oscillator strength of the transition, which relates the absorption intensity to the concentration, is not known; in other words, this may account for the missing interstitials or it may not. No optical absorption feature or epr signal has been identified with a charged interstitial, which may not be stable enough to exist; if it does we do not know how to identify, much less quantify, its presence. This chapter will address the third possibility through quantitative comparison of spectra, with simulations produced by modelling the effects of strain.

Self-Interstitial - Nitrogen Complexes

The 2.367 eV line, produced only in Ib diamond by irradiation, was studied in 1979 by Collins and Rafique [112] who speculated that it is most likely a substitutional nitrogen - self-interstitial complex, due to the conditions under which it is created and because the centre is destroyed at much lower temperatures than those at which the vacancy is mobile. The 2.367 eV line was shown to anneal out as a line at 2.535 eV anneals in [112]. Both these lines were observed in the high nitrogen sectors in the recent work by Collins and Dahwich [2]. The 2.535 eV line was plotted annealing out as the 1859 meV 'line' anneals in. This was attributed to the release of interstitials as the 2.535 eV centre breaks up. Other annealing data has also suggested that single substitutional nitrogen efficiently traps interstitials and releases them upon annealing at 400°C [3]. A progressive loss of $\mathbf{N_S^+}$ (or V^-) was also reported by Collins and Dahwich, over the same temperature range (275-400°C), equivalent to a reduction in ND1 of 30% and attributed to annihilation with interstitials as they are released [2]. Since the charge state of a single vacancy is thought to be influenced by its proximity to the

nitrogen donor [111], this might suggest that these separated vacancy-interstitial pairs are near to the nitrogen. There is also a collection of centres found in Ib diamond termed W centres thought to be highly distorted negative vacancies [113].

Recombination Enhanced Diffusion of Self-Interstitials During Irradiation

It has been established [71, 79], that recombination enhanced diffusion (exciton recombination) of interstitial atoms occurs during irradiation, at temperatures above 100K, reducing the final $\mathbf{I}^0_{\langle 001\rangle}$ concentration by a factor of three, relative to the vacancy concentration. The major sinks for the interstitials have not yet been identified [79]. There is no evidence for vacancy recombination enhanced diffusion [71] and there is a significant barrier to vacancy-interstitial recombination in diamond [71].

Imaging of Nitrogen and Radiation Damage Defects

Epr imaging of P1, R2 and R1 defects ($\mathbf{N_S}$, $\mathbf{I}^0_{\langle 001\rangle}$ and $\mathbf{I}^0_{\langle 001\rangle}$ pair respectively) has shown that unlike in type IIa diamond, R1 is not produced upon irradiation in Ib diamond, suggesting that the presence of $\mathbf{N_S}$ (P1) inhibits the ability of $\mathbf{I}^0_{\langle 001\rangle}$ to form pairs [114]. The study found that the concentration of R2 in these regions was unaffected by a local concentration of about 85 ppm $\mathbf{N_S}$. The already broad R2 spectrum broadens considerably in the presence of nitrogen making its concentration harder to determine. Generally speaking relative concentrations of interstitials can be more accurately determined optically due to the unusually large line-width of the R2 spectrum [72, 115].

We will see in the next few sections, from its absorption spectrum, that the concentration of $\mathbf{I}^0_{\langle 001\rangle}$ is heavily affected by the presence of the nitrogen. It will also be shown that most of the $\mathbf{I}^0_{\langle 001\rangle}$ present are heavily distorted with a significant mixing of their states, this may have a profound effect on their epr signal, or even cause it to be absent at the more distorted centres.

7.2 Production of Neutral ⟨001⟩-split Interstitials in the Presence of Increasing Concentrations of Single Substitutional Nitrogen

With the aim of measuring the effect of single substitutional nitrogen on the production of interstitials by electron irradiation, eight Ib samples were selected with a range of $[\mathbf{N_S}]$. Their nitrogen content was measured as described in Section 7.1 and is shown in Table 7.3.

Sample	$[\mathbf{N_S}]$(ppm)	error(ppm)
55902-01	560	12
	533	12
55902-03	401	8
	405	8
	416	8
403002-11-02	129	3
	121	5
403002-11-01	126	5
	118	3
	115	3
s122-iii	8.8	1
	7.6	1
s122-ii	6.0	1

Table 7.3: The concentrations of single substitutional nitrogen present in the samples studied in this section, measured via their IR absorption as described in Section 7.1.

Nitrogen may be grown into and detected optically in diamond to concentrations ranging from a few ppm up to hundreds of ppm. Using Ib samples allows a high degree of control over the precise impurity content. Ia samples may contain predominantly for example A aggregates, but will then also contain a significant proportion of $\mathbf{N_S}$, B aggregates and maybe platelets, since the stages of aggregation are not entirely separable. Ib samples therefore, may be selected to contain only $\mathbf{N_S}$ with great variations in concentration obtainable, providing an ideal and controlled system to

study the effects of impurity content on the production of radiation damage.

Here the samples have approximately 1, 10, 100 and 400 ppm of $\mathbf{N_S}$ (2 samples of each) covering almost 3 orders of magnitude. The four highest concentration samples were single ⟨100⟩ sector cobalt grown samples (they should contain essentially no transition metals [5]) and so are fairly homogeneous. The remaining samples were grown with nitrogen getters, a more difficult growth process and so are visibly inhomogeneous (in colour to the eye); the measured nitrogen concentration is therefore an average and there may be regions of these samples that are nitrogen free.

These samples were electron irradiated at approximately room temperature next to each other so that they received the same dose under the same conditions. A summary of the defect absorption present in these samples after this irradiation is given in Table 7.4.

Line energy(meV)	Defect	~1ppm	~10ppm	~100ppm	~500ppm
1256	H2, -ve charge state of H3 (NVN) [107]	χ	χ	χ	✓
1424	LVM of H2	χ	χ	χ	✓
1498, broad	?	χ	χ	✓	✓
1536, broad	?	χ	χ	✓	✓
1575, broad	?	χ	✓	✓	✓
1633, broad	?	χ	✓	✓	✓
1673	GR1 ($\mathbf{V^0}$)	✓	✓	χ	χ
1740, broad	?	χ	χ	✓	✓
1859	$\mathbf{I}^0_{\langle 001 \rangle}$	✓	✓	-ve feature	-ve feature
1915, 1921	? Same? (seem to thermalise)	✓ weak	✓	χ	χ
2086	595nm	✓	✓	χ	χ
2165, broad	?	χ	✓	✓	✓
2535	Probably nitrogen bound to interstitial carbon [112]	χ	✓	✓	✓
2677, broad	?	χ	✓	✓	χ
2881	GR2 ($\mathbf{V^0}$)	✓	✓	χ	χ
2887	GR3 ($\mathbf{V^0}$)	✓	✓	χ	χ

Table 7.4: Appearance of optical absorption features at 4K in the visible region of irradiated Ib diamonds of varying $\mathbf{N_S}$ concentrations as indicated in ppm.

The GR1 is present in the low nitrogen samples and absent in the high nitrogen

samples, which could well be due to a change in charge state [110]. The 1859 meV line ($\mathbf{I}^0_{\langle 001\rangle}$) is clearly visible in the (inhomogeneous) ~1 and ~10ppm $\mathbf{N_S}$ samples, but appears to be absent in the samples with higher nitrogen concentrations. Instead, these high nitrogen samples feature a step down in the spectrum at 1859 meV, followed by a gentle rise in absorption a few meV to higher energy. This trough like 'negative' absorption feature is present in all four high nitrogen samples, Fig. 7.3. The presence of the nitrogen has clearly had a profound effect on this region of the spectrum.

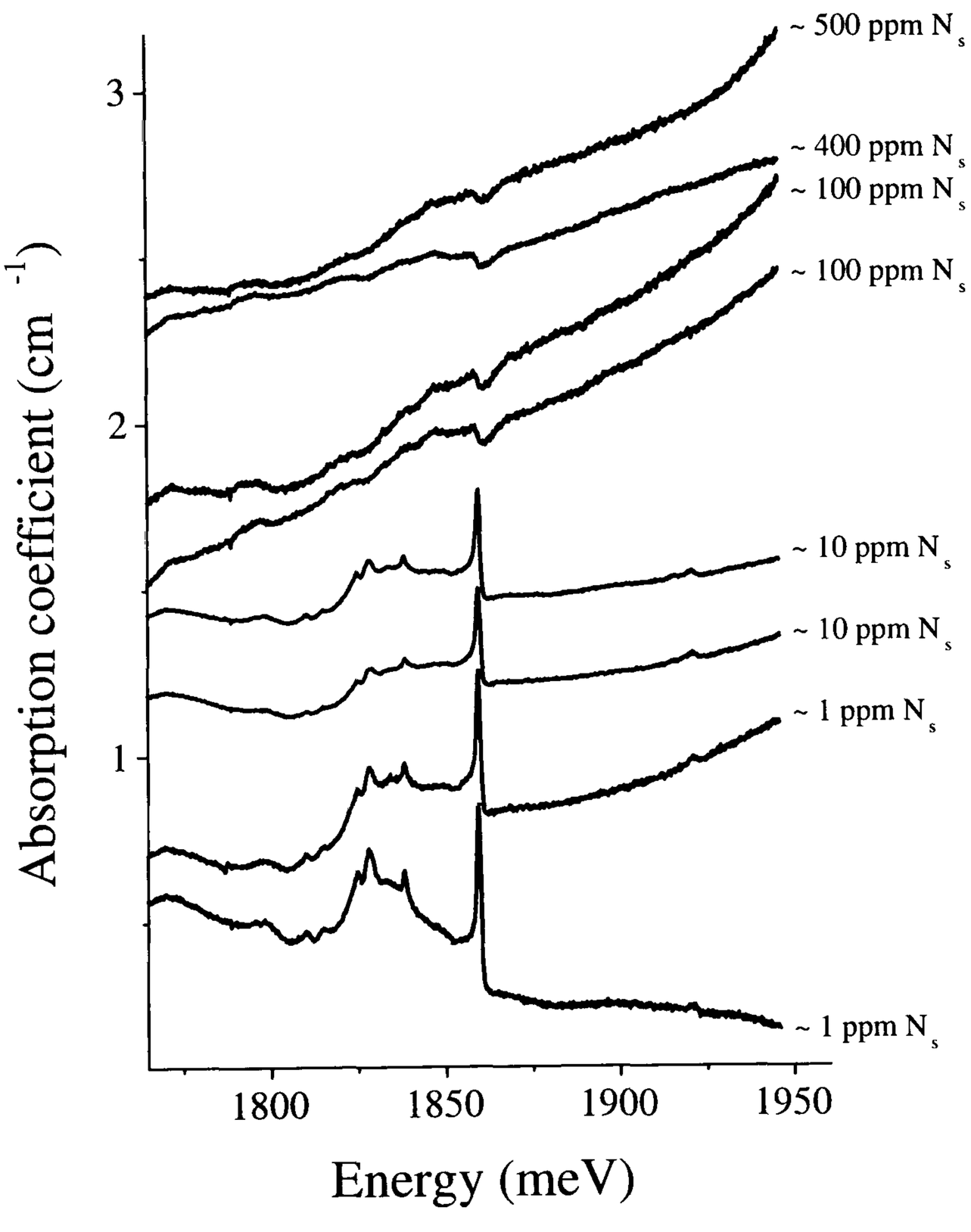

Figure 7.3: Spectra of 8 Ib diamonds with varying $\mathbf{N_S}$ concentrations irradiated simultaneously. Spectra are displaced vertically.

7.2.1 Absorption by Strained $\mathbf{I}^0_{\langle 001 \rangle}$

Nitrogen impurities will introduce strain into the lattice. Using the results of Chapter 5.3 it is easy to model the effect of strain on the spectrum of $\mathbf{I}^0_{\langle 001 \rangle}$. There are negligible first order effects so these can be ignored (see Chapter 5.3): there will be no linear shifts in the energy due to normal stresses. This leaves the two distinct symmetry lowering distortions and their second order effects on the spectrum, due to mixing of the states by shear stresses. These are the distortion in the ground state by an $x^2 - y^2$ type strain and the distortion in the first excited states of $\mathbf{I}^0_{\langle 001 \rangle}$ by an xy type strain.

The $x^2 - y^2$ type distortion mixes the components of the ground state doublet so that the initial state of the 1859 meV transition is repelled to lower energy (Fig. 5.9). This gives rise to an increase in the energy of the 1859 meV transition, that is quadratic in the strain, whilst causing its absorption intensity to fall with increasing magnitude of strain, until it levels out at 50% when the states are fully mixed. Meanwhile, the mixing arising from the distortion, induces the 1692 meV absorption line with a complementary rise in its intensity and matching energy shift.

The xy type distortion mixes the components of the first excited state doublet (and consequently their one phonon replicas) so that the final states of the 1859 and 1864 meV transitions repel to lower and to higher energy respectively (Fig. 5.9) giving rise to a decrease and an increase in their transition energies respectively, again at a rate that is quadratic in the strain. At the same time the mixing causes their transition probabilities to fall/increase (from zero) with increasing magnitude of strain until the states are fully mixed and they are equal. The 1864 is an induced transition that is forbidden in the unperturbed system.

Ignoring first order effects (which are effectively zero, see Chapter 5.3), the energy shift with stress given by Equation 2.15 is $\frac{1}{2}\Delta E \pm \frac{1}{2}\sqrt{(\Delta E)^2 + 4\gamma^2}$ where, (adopting the notation of Chapter 2):

- for an $x^2 - y^2$ stress of magnitude s (under which the mixing is in the ground states (states a and b = g)), $\gamma = b_{ab}s$ and $\Delta E = E_g$

- for an xy stress (under which the mixing is in the middle excited states (states c and d = m)), $\gamma = b_{cd}s$ and $\Delta E = E_m$.
- and the sign before the square root depends on which transition it applies to and which states are being mixed.

Still disregarding the negligible first order parameters, the probability/absorption intensity change with stress given by Equations 2.19 and 2.20 is;

$$\frac{1}{2} \pm 1/\left(2\sqrt{(2\gamma/\Delta E)^2 + 1}\right) \tag{7.1}$$

where the γ and ΔE are as before, the + and - signs are for the 1859 (whose probability falls with stress) and the 1864/1692 (whose probabilities increase with stress) meV transitions respectively.

Consider an intensity of absorption I_s by interstitials under a stress of magnitude s, which is proportional to the number of $\mathbf{I}^0_{\langle 001\rangle}$ under that stress times by the $\cos^2\theta$ or $1 - \cos^2\theta$ probability factor (Eqn. 2.20, Table 5.6) associated with the transition at that stress. For a set value of s this absorption would appear in the spectrum as a lorentzian of the form:

$$\text{absorption value} = \frac{I_s}{(E - E_s)^2 + (w/2)^2} \tag{7.2}$$

where I_s is proportional to the area of lorentzian = intensity of absorption by interstitials under stress s, $w = 1$ meV is the approximate unperturbed width of the 1859 meV line, E is the energy variable and E_s is the perturbed energy of the transition.

For an xy perturbation there are two lines to consider at low temperature. For the 1859 meV transition;

$$I_s = I_0\left(\frac{1}{2} + 1/\left(2\sqrt{(2\gamma/\Delta E)^2 + 1}\right)\right) \tag{7.3}$$

and,

$$E_s = \frac{1}{2}\Delta E - \frac{1}{2}\sqrt{(\Delta E)^2 + 4\gamma^2} \tag{7.4}$$

while for the 1864 meV transition the same is true with the opposite signs before the square roots. The total area of both peaks will equal I_0, the intensity of absorption by the equivalent in unperturbed interstitials, so although its structure will be different, xy strained $\mathbf{I}^0_{\langle 001\rangle}$ produce the same total intensity of absorption in this region as unperturbed $\mathbf{I}^0_{\langle 001\rangle}$.

The x^2-y^2 case does not induce the 1864 meV transition, so under x^2-y^2 strain, the total intensity in the 1859 meV region will fall below that expected for the number of $\mathbf{I}^0_{\langle 001\rangle}$, the remaining intensity will be found were it is induced in the 1692 meV region. Note: The induced intensity in the 1692 meV region must be taken account of to determine the intensity that the 1859 would have had were it unperturbed, but, the 1692 meV induced transition 'borrows' its intensity from the 1685 meV transition, not the 1859, so the induced intensity may not be simply added to the reduced intensity in the 1859 meV region. The difference in oscillator strength between the allowed transition must be taken into account: I_0^{1685} / I_0^{1859} = 0.45±0.05 [47] determined in Section 5.2.1.

Also most of the theory described in this section assumes low temperature because this is the simplest case, however note that the published proportionality constants between the 1859 meV line intensity and $\mathbf{I}^0_{\langle 001\rangle}$ concentration were determined at 77K [28]. Experimentally it is also important to note that in the x^2-y^2 case the stress dependence of the line intensities is highly temperature dependent (Table 5.6).

Combining the Two Perturbations

The effects on the spectrum are more complicated for $\mathbf{I}^0_{\langle 001\rangle}$ that are subjected to both xy and x^2-y^2 types of strain together. If the two types of strain are of similar magnitudes, the energy shifts due to mixing in the ground and excited states add together and may cancel, producing little shift of the 1859meV transition so that it may appear unperturbed. The 1692 and 1864meV transitions will still be induced. The former will shift little while the latter will shift at double pace. The accompanying variations in line intensities are more complicated. When there are perturbations in

both the ground and excited states, the change in transition probabilities ($\cos^2\theta$ or $1-\cos^2\theta$ term) associated with each of the two perturbations, are multiplied to give the total change in transition probability. This can be understood explicitly using the theory of Eqns 2.19 to 2.23 of Section 2.2.4 using the notation of Fig. 5.24 as follows:

$$\begin{aligned}
T_{1859} &= |\int \Psi_g^- (\Delta V) \Psi_e^- dr|^2 \\
&= |\int \left(a^-\psi_a + b^-\psi_b\right) \Delta V \left(e^-\psi_e + f^-\psi_f\right) dr|^2 \\
&= |a^-e^- \int \psi_a \Delta V \psi_e dr + a^-f^- \int \psi_a \Delta V \psi_f dr \\
&\quad + b^-e^- \int \psi_b \Delta V \psi_e dr + b^-f^- \int \psi_b \Delta V \psi_f dr|^2 \\
&= \left(a^-e^-\right)^2 T_{ae} + 0 + 0 + 0 \\
&= \left(1-\cos^2\theta_g\right)\left(1-\cos^2\theta_e\right) T_{ae}
\end{aligned}$$

$$\begin{aligned}
T_{1864} &= |\int \Psi_g^- (\Delta V) \Psi_e^+ dr|^2 \\
&= \left(a^-e^+\right)^2 T_{ae} \\
&= \left(1-\cos^2\theta_g\right)\left(\cos^2\theta_e\right) T_{ae}
\end{aligned}$$

$$\begin{aligned}
T_{1692} &= |\int \Psi_g^- \Delta V \Psi_m^- dr|^2 \\
&= |\int \left(a^-\psi_a + b^-\psi_b\right) \Delta V \left(c^-\psi_c + d^-\psi_d\right) dr|^2 \\
&= \left(b^-c^-\right)^2 T_{bc} \\
&= \left(\cos^2\theta_g\right)\left(1-\cos^2\theta_e\right) T_{bc} \\
&= \left(\cos^2\theta_g\right)\left(1-\cos^2\theta_e\right) 0.45 T_{ae} \qquad (7.5)
\end{aligned}$$

where:

$$\begin{aligned} a^+ &= \cos\theta_g & b^+ &= -\sin\theta_g \\ a^- &= \sin\theta_g & b^- &= \cos\theta_g \end{aligned}$$

$$\begin{aligned} c^+ = e^+ &= \cos\theta_e & d^+ = f^+ &= -\sin\theta_e \\ c^- = e^- &= \cos\theta_e & d^- = f^- &= \cos\theta_e \end{aligned} \tag{7.6}$$

Unfortunately, the total absorption no-longer bears a simple relation to the total $\mathbf{I}^0_{\langle 001\rangle}$ concentration, but will be a little less than or equal to the standard absorption per $\mathbf{I}^0_{\langle 001\rangle}$.

7.2.2 Strain Distributions

If the population of $\mathbf{I}^0_{\langle 001\rangle}$ suffers a distribution of strain then I_0 will be some function of s, $I_0(s)$. A routine has been written which calculates the absorption value (Eqn. 7.2) and sums them for each value of s stepping through the distribution of I_0 in s at a set value of E, giving the total absorption at that energy E, before stepping on to the next value of E and the next, building up a plot of absorption strength against energy, E. The function $I_0(s)$ (the distribution of interstitials with s) may be different for the xy plus x^2-y^2 together, xy and x^2-y^2 strain cases. The distribution in the magnitude and type of shear strain suffered across the population of interstitials is the only variable in the simulation.

Note that at temperatures above about 20K, there may also be features present in the spectrum associated with transitions from the upper ground state. The sensitivity of their intensities to stress and temperature dictate that except at low stresses and at temperatures above 20K they will not be observed. Their appearance can be modelled, but compared to the ground state transitions, yields no new information about the environment of the interstitials. For this reason it is simplest and most accurate to limit the modelling to the 1692, 1859 and 1864 meV lines below 20K.

Simulations of the 1859 meV region are shown in Figs 7.4 to 7.7 for various stress distributions of interstitials. Note, that any intrinsic asymmetry of the 1859 meV line has been neglected. The step observed at 1859 meV and the gentle rise a few meV to higher energy in the spectra of the Ib irradiated diamonds (the 'negative' absorption feature) is clearly characteristic of xy strained $\mathbf{I}^0_{\langle 001 \rangle}$. There can be little $x^2 - y^2$ strain in comparison, since this would fill the 'trough', Fig. 7.7. There must be some $\mathbf{I}^0_{\langle 001 \rangle}$ under no strain since the step is at 1859 meV and not to lower energy. There is also a smooth distribution in the magnitude of the strain since there are no sharp peaks.

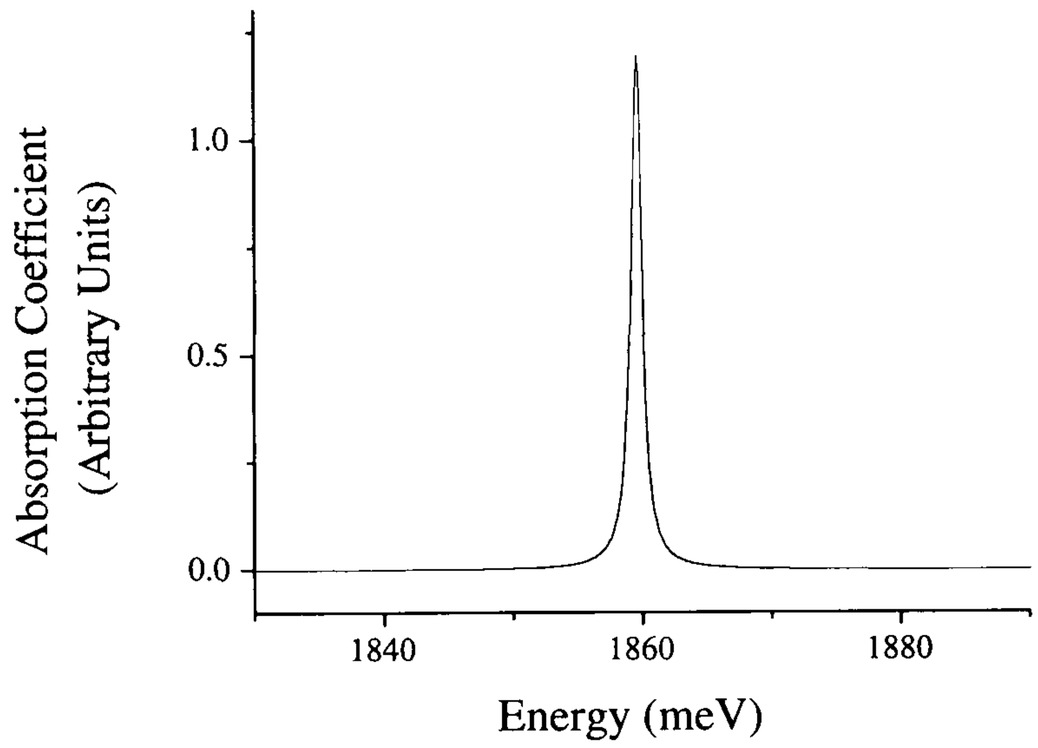

Figure 7.4: Simulation of unstrained $\mathrm{I}^0_{\langle 001 \rangle}$ absorption.

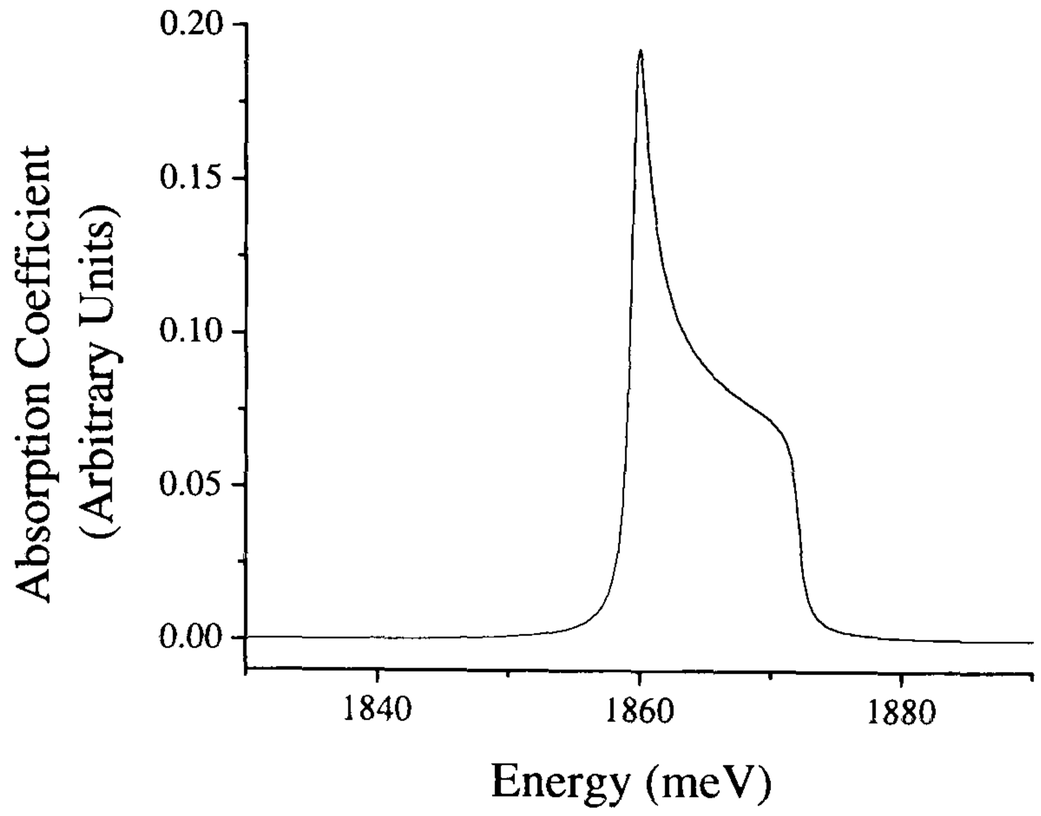

Figure 7.5: The effect of $x^2 - y^2$ stress varying in magnitude from 0 to 4 GPa evenly across a population of interstitials i.e. number of interstitials = constant from 0 to 4 GPa and then zero elsewhere.

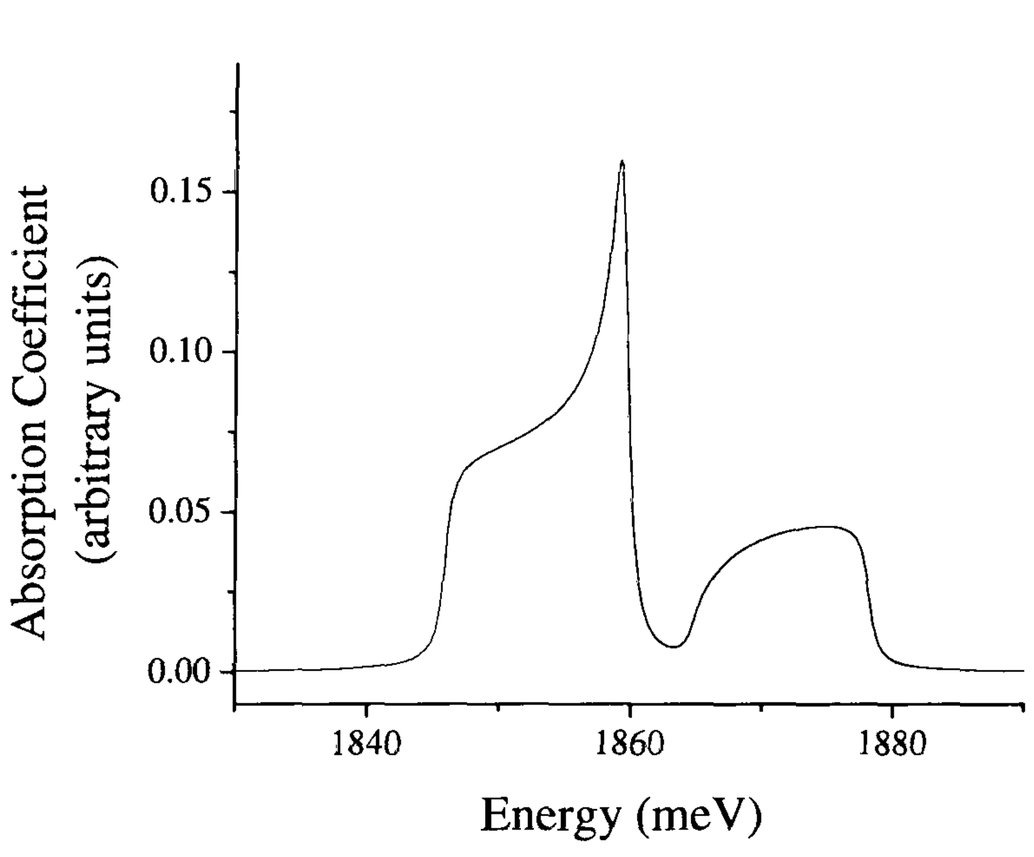

Figure 7.6: The effect of xy stress varying in magnitude from 0 to 4 GPa evenly across a population of interstitials i.e. number of interstitials = constant from 0 to 4 GPa and then zero elsewhere.

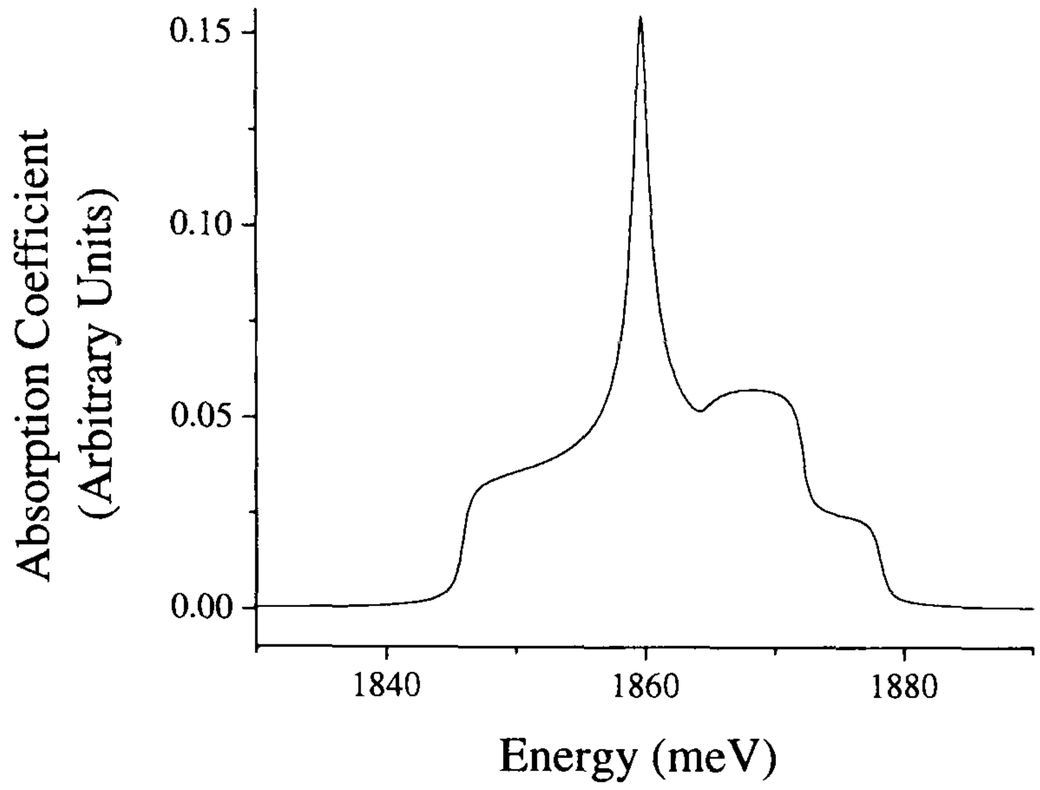

Figure 7.7: Sum of simulations shown in Fig. 7.5 and Fig. 7.6.

It was shown in Section 5.3.6 that internal strain in a IIa sample can produce an $x^2 - y^2$ perturbation (albeit very small - at the limit of detectability). This presumably is produced by $\mathbf{V}^0$ known to have T_d symmetry (Chapter 4). Although it is a substitutional impurity $\mathbf{N}_S$ does not maintain the T_d symmetry of its lattice site, owing to its excess electron it distorts along one of its four bonding $\langle 111 \rangle$ directions, lowering its symmetry to C_{3v}. To a crude approximation the local strain might therefore be regarded as similar in nature to a $\langle 111 \rangle$ stress. Locally this might result in predominantly shear type lattice strain caused by the nitrogen, with a reduced $x^2 - y^2$ component.

Due to the inherent broad nature of the absorption feature and the difficulty in knowing where it ends, fitting a baseline to the interstitial absorption is even more subjective than usual for this region of the spectrum. The only well defined structure is the 'negative' absorption feature, (it is clearly not negative but zero at least) the step is plainly characteristic of $\mathbf{I}^0_{\langle 001 \rangle}$ and so the bottom of the trough by this step is a good place to start. The baselines used are shown in Fig. 7.8.

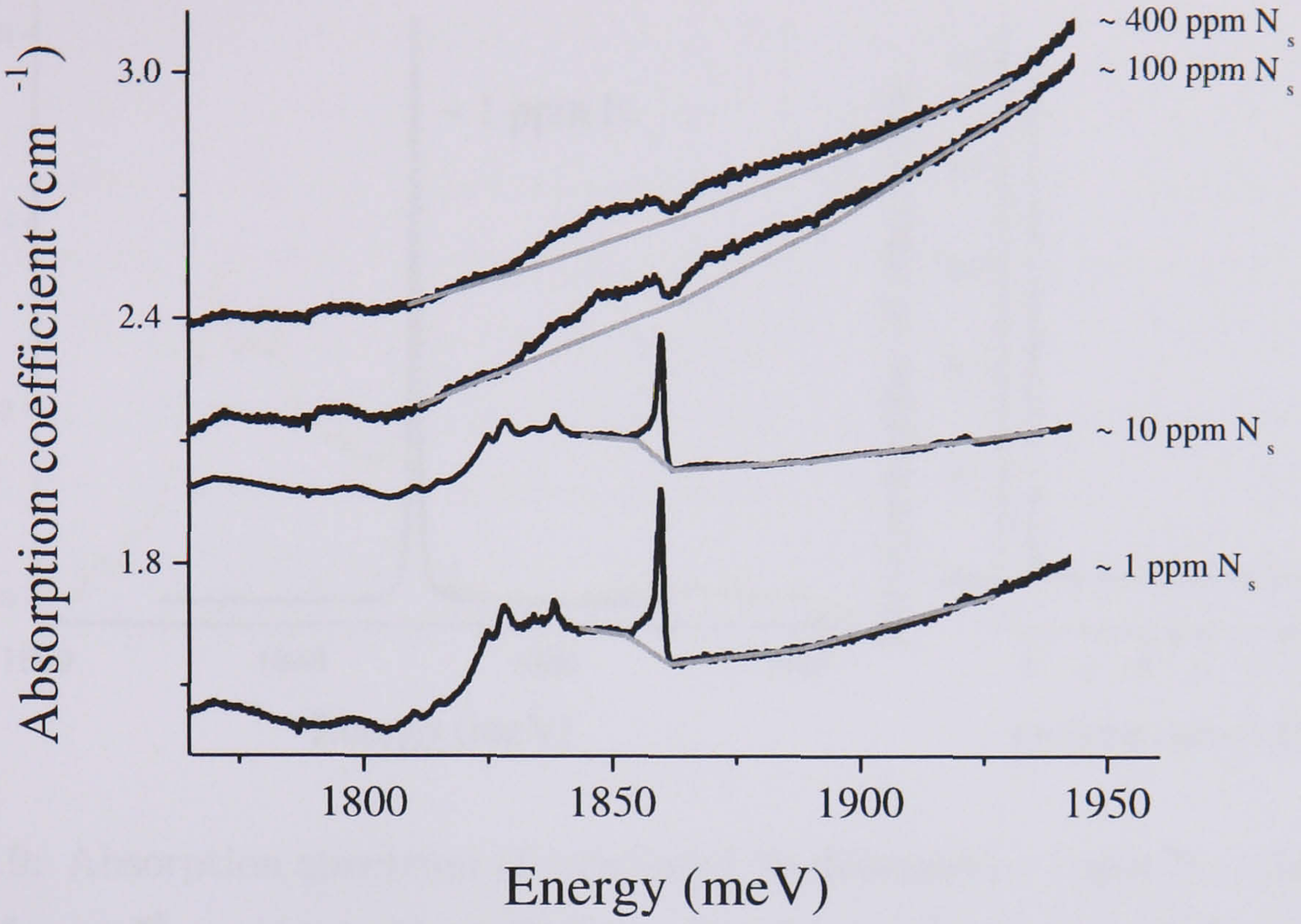

Figure 7.8: Baselines for strained $\mathbf{I}^0_{\langle 001 \rangle}$ spectra. Spectra are displaced vertically.

Having baseline corrected the spectrum, the variable strain distribution can be adjusted to fit the simulation to the data; a fit to the spectrum of one of the lowest concentration of nitrogen samples is shown in Fig. 7.9 and shows there is little or no distortion of the interstitials at this concentration of nitrogen. A fit to the spectrum of one of the samples containing approximately 10 ppm of nitrogen is shown in Fig. 7.10 and shows there is a small amount of strain starting to creep in.

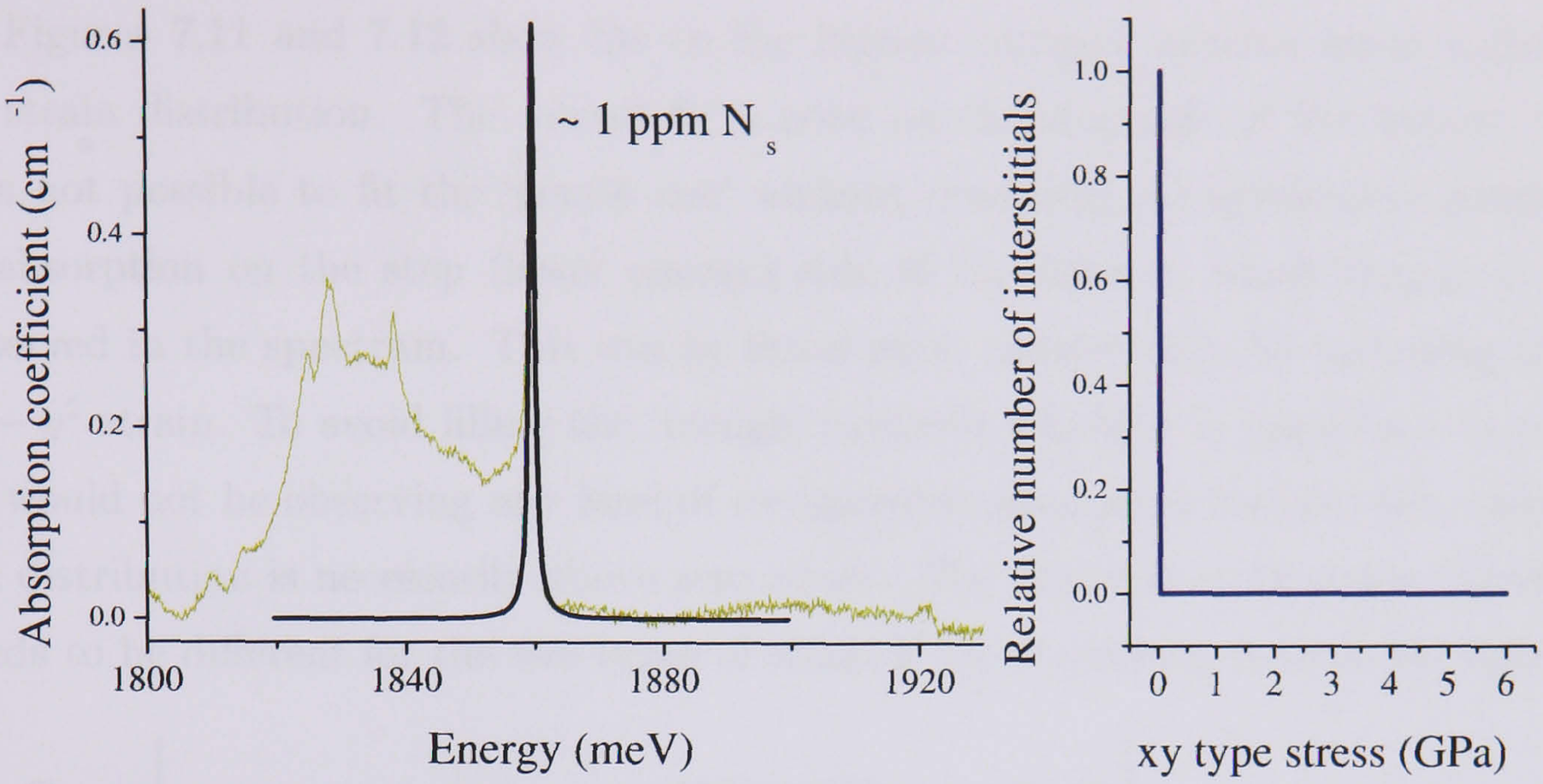

Figure 7.9: Absorption spectrum of irradiated Ib diamond $\sim$ 1ppm $\mathbf{N_S}$. Simulation overlaid for an $\mathbf{I}^0_{\langle 001 \rangle}$ population suffering a distribution in strain as indicated on the right, in this case all the interstitials suffer zero strain. Structure to the left of the peak is due to the GR1.

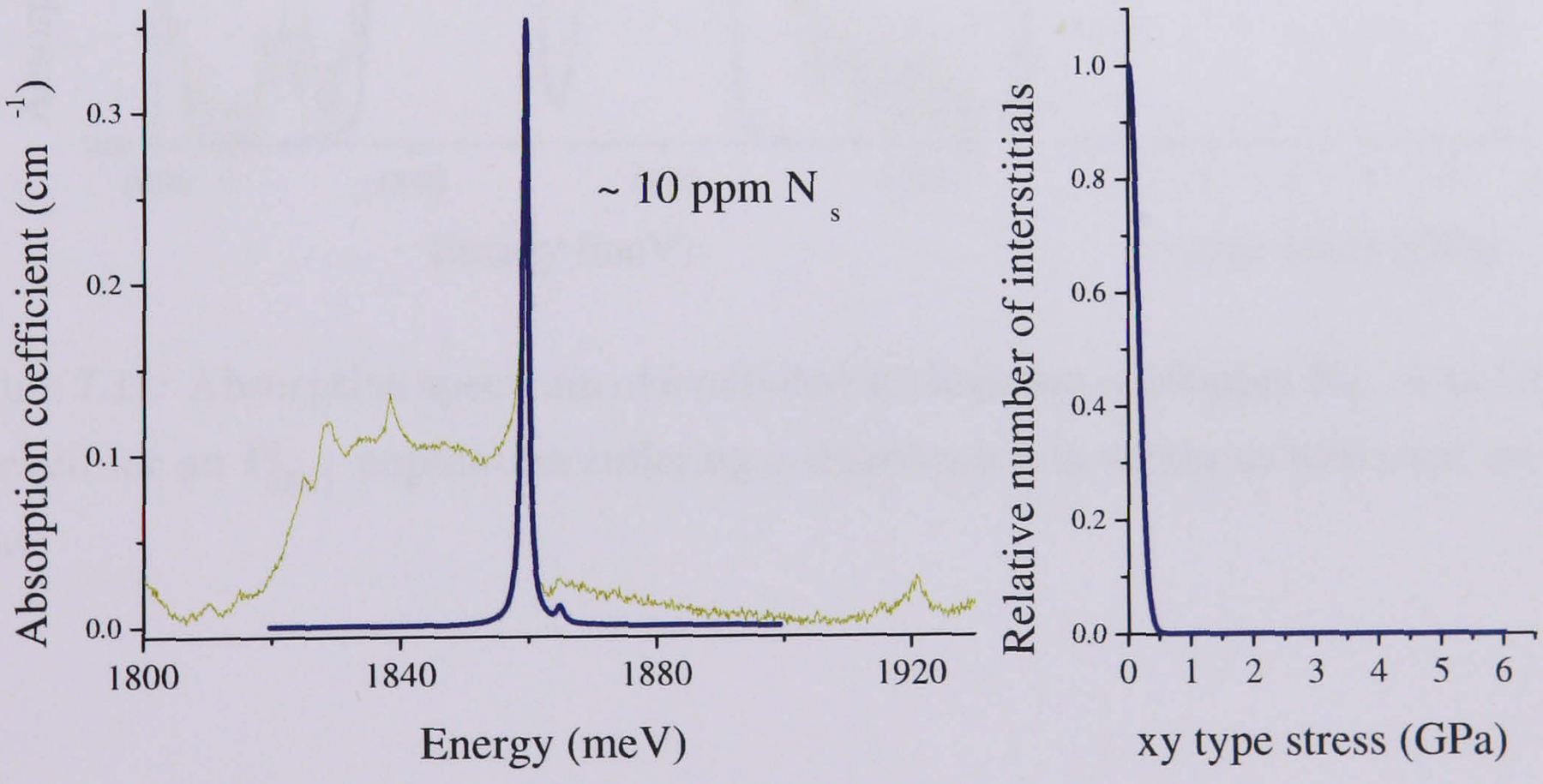

Figure 7.10: Absorption spectrum of irradiated Ib diamond $\sim$ 10ppm $\mathbf{N_S}$. Simulation overlaid for an $\mathbf{I}^0_{\langle 001 \rangle}$ population suffering a distribution in strain as indicated on the right. Structure to the left of the peak is due to the GR1.

Figures 7.11 and 7.12 show fits to the highest nitrogen spectra using a purely xy strain distribution. The overall fit is good on the step side of the feature, but it is not possible to fit the 'gentle rise' without producing a considerable intensity of absorption on the step (lower energy) side of the feature, which simply is not observed in the spectrum. This can be fitted more satisfactorily by including some $x^2 - y^2$ strain. To avoid filling the 'trough' (without which, it is important to note, we would not be observing any kind of recognisable absorption feature) the onset of the distribution is necessarily above zero strain. The distribution of strain therefore needs to be different for the two types of strain if the simulation is to fit the data.

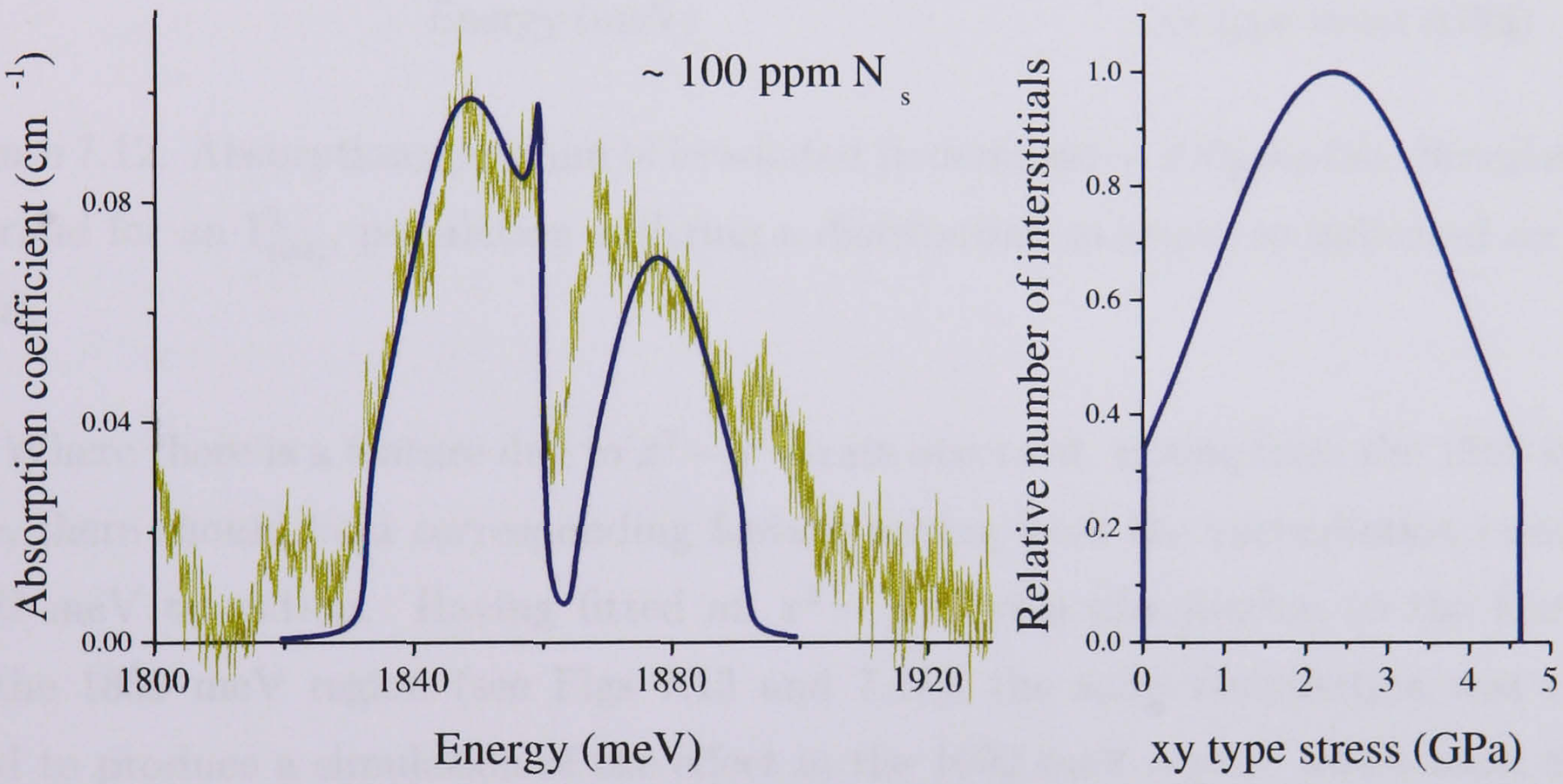

Figure 7.11: Absorption spectrum of irradiated Ib diamond $\sim$ 100ppm $\mathbf{N_S}$. Simulation overlaid for an $\mathbf{I}^0_{\langle 001 \rangle}$ population suffering a distribution in strain as indicated on the right.

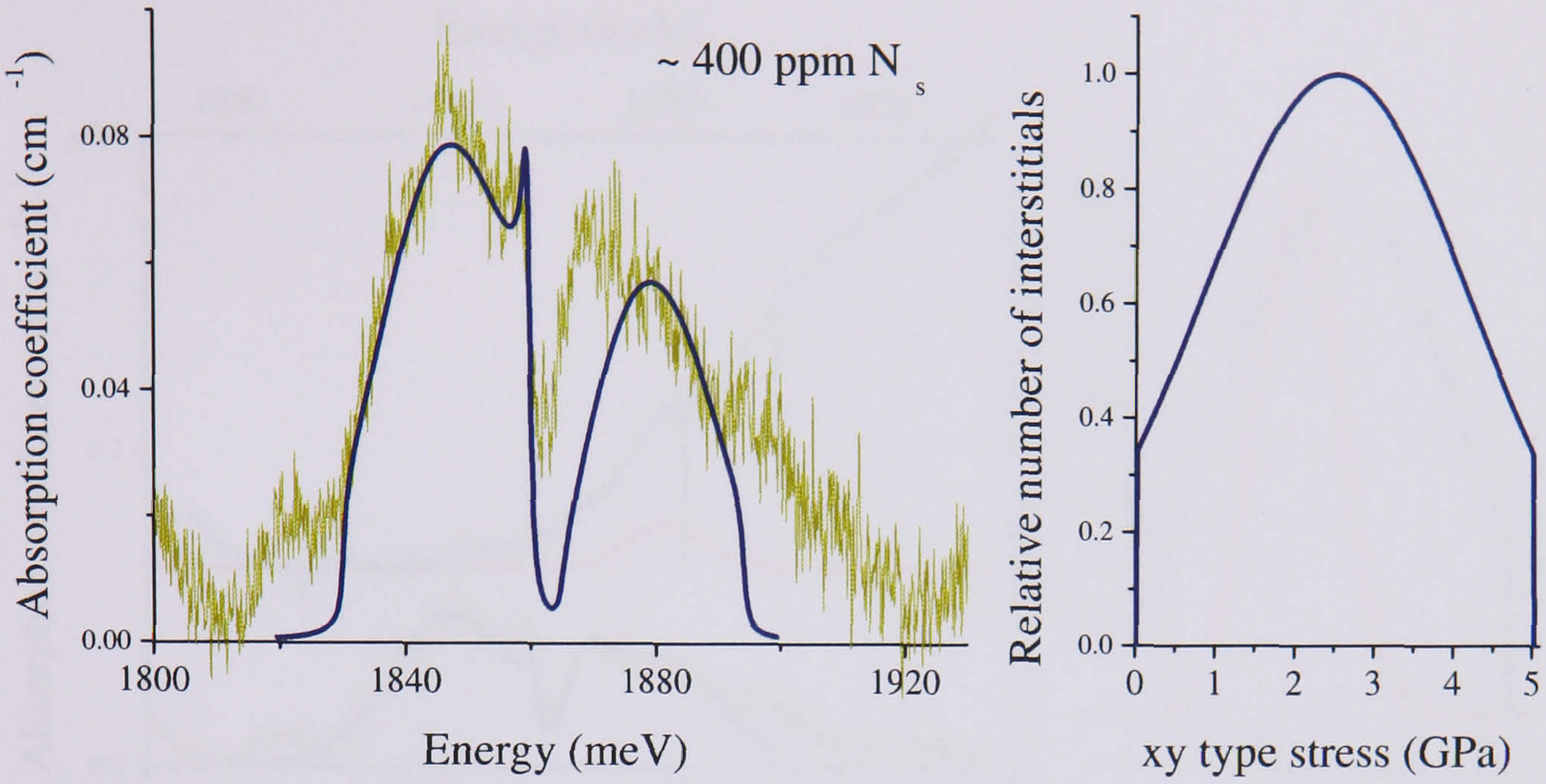

Figure 7.12: Absorption spectrum of irradiated Ib diamond $\sim$ 400ppm $\mathbf{N_S}$. Simulation overlaid for an $\mathbf{I}^0_{\langle 001 \rangle}$ population suffering a distribution in strain as indicated on the right.

Where there is a feature due to $x^2 - y^2$ strain observed, arising from the 1859 meV line, there should be a corresponding feature arising from the perturbation induced 1692 meV transition. Having fitted an $x^2 - y^2$ strain distribution to the feature in the 1859 meV region (see Figs 7.13 and 7.14), the same distribution was then used to produce a simulation of the effect in the 1692 meV region, which must then satisfactorily correspond to the data in this region for the fit to the 1859 meV region to be valid. The simulation and data (not baseline corrected) are shown in Figs 7.13 and 7.14. The overall fit now corresponds well to the data, implying that the strain distributions plotted are reasonable.

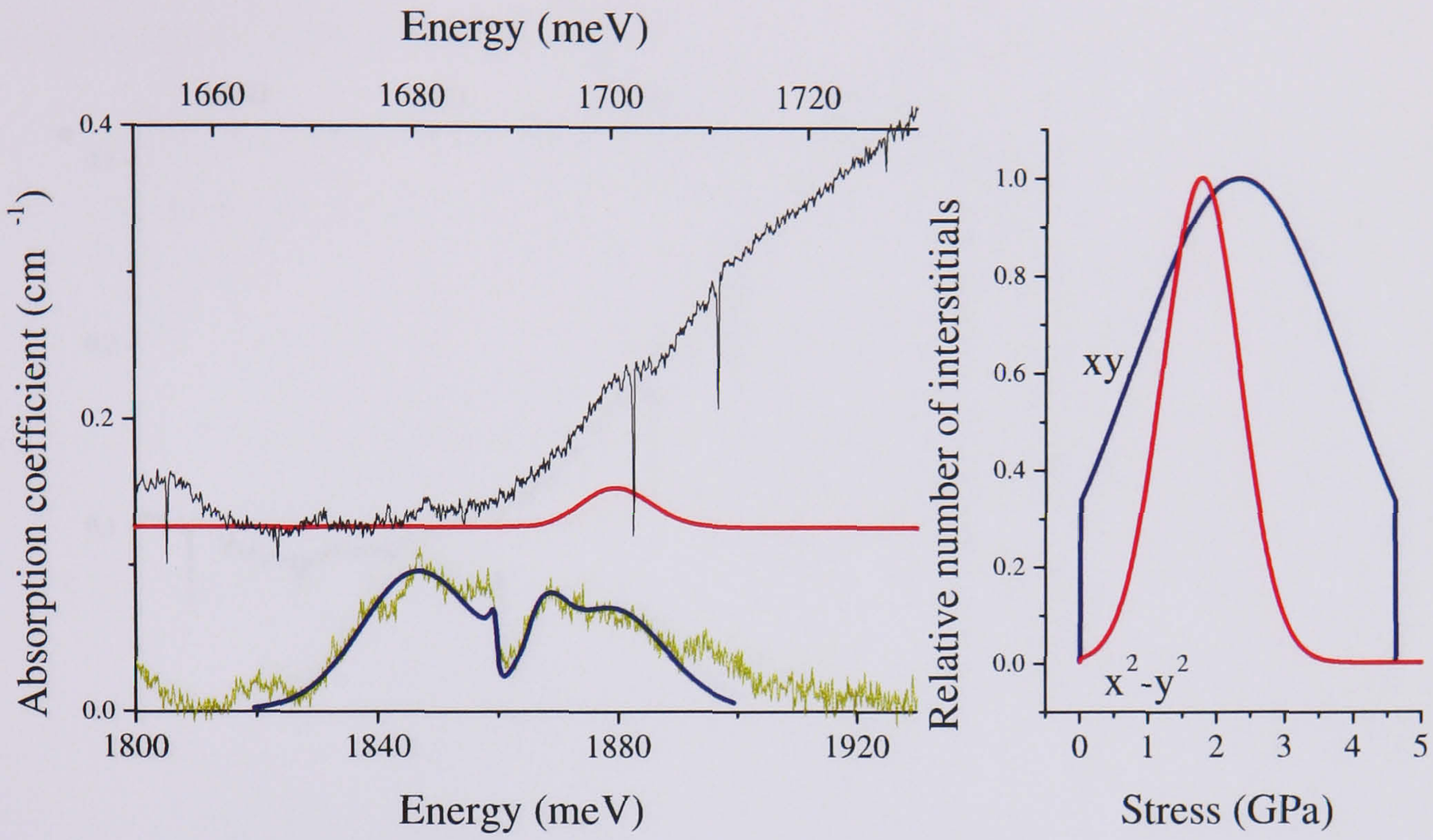

Figure 7.13: Absorption of irradiated Ib diamond $\sim$ 100ppm N_S, top curve is not baseline corrected and corresponds to the top energy axis (sharp features are artifacts). Simulations are overlaid for the sum of absorption by two distinct populations of $\mathbf{I}^0_{\langle 001\rangle}$ suffering distributions in strain as indicated on the right.

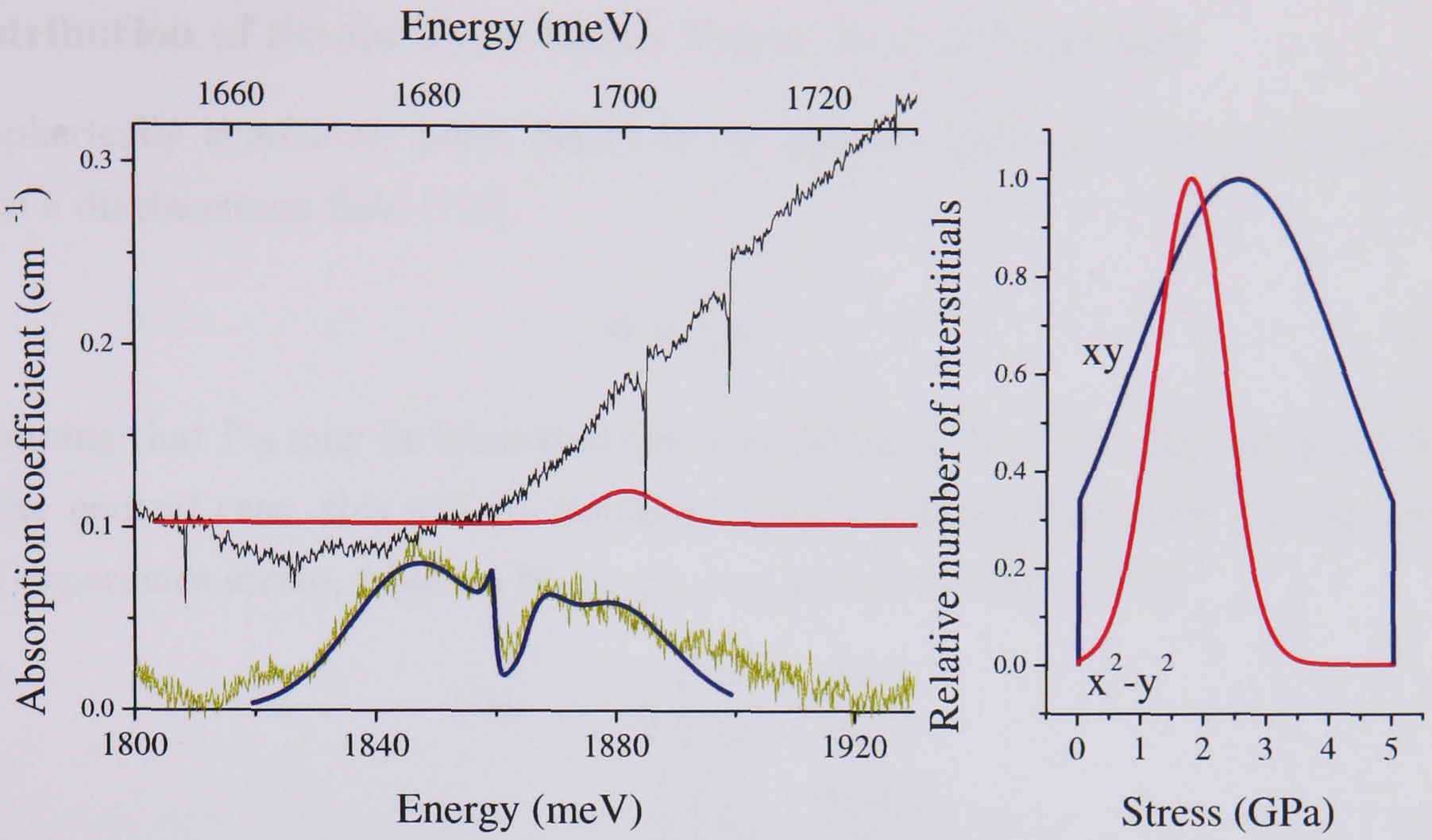

Figure 7.14: Absorption of irradiated Ib diamond $\sim$ 400ppm $\mathbf{N_S}$, top curve is not baseline corrected and corresponds to the top energy axis (sharp features are artifacts). Simulations are overlaid for the sum of absorption by two distinct populations of $\mathbf{I}^0_{\langle 001 \rangle}$ suffering distributions in strain as indicated on the right.

Gaussian functions have been used to represent the strain distributions for ease of plotting, but adjustments to this function may be made to better fit the observed features. The integrity of the fit comes from our ability to use the stress and temperature dependence parameters determined in Chapter 5 to produce a simulation, whose only variable is the distribution in type and magnitude of strain, that can convincingly fit the interdependent features of the spectrum using a reasonable distribution. These interdependent features are that; any feature produced by xy strain broadening the 1859 meV line to lower energy, must be matched by a corresponding feature with an onset at 1864 meV extending to higher energy (see Fig. 7.6) and that any feature produced by an $x^2 - y^2$ strain extending the 1859 meV line to higher energy (see Fig. 7.5) must be accompanied by a corresponding feature extending to higher energy of 1692 meV.

Distribution of Strain Type (Both Types Acting Together)

A spherically symmetric point defect in an infinite elastically isotropic continuum gives a displacement field [116]:

$$\mathbf{u} = \frac{A}{r^3}\mathbf{r} \tag{7.7}$$

Assuming that $\mathbf{N_S}$ may be treated in this way (likely to be a false assumption at least in the neutral case, this will be discussed later) an interstitial placed at the origin will experience strain, from an $\mathbf{N_S}$ at (x_1, x_2, x_3), of the form [116]:

$$\begin{aligned} \epsilon_{ij} &= \frac{1}{2}\left(\frac{\delta u_i}{\delta x_j} + \frac{\delta u_j}{\delta x_i}\right) \\ &= \frac{A}{r^3}\left(\delta_{ij} - \frac{3x_i x_j}{r^2}\right) \end{aligned} \tag{7.8}$$

In terms of the local axes of the interstitial placed at the origin x_1, x_2, x_3 are x, y and z, these are the co-ordinates of the source of the strain, the $\mathbf{N_S}$, relative to the interstitial.

In the xy plane of the $\mathbf{I}^0_{\langle 001\rangle}$, setting $x = r\sin\theta$ and $y = r\cos\theta$ results in,

$$\begin{aligned} \epsilon_{xx} - \epsilon_{yy} &= \frac{3A}{r^3}\cos(2\theta) \\ \epsilon_{xy} &= -\frac{3A}{2r^3}\sin(2\theta) \end{aligned} \tag{7.9}$$

Alternatively, starting from the stress tensor component definition of Section 2.2.3 Eqns 2.1 and 2.2,

$$S_{ij} = |s|\cos\theta_i\cos\theta_j \tag{7.10}$$

Where $\theta_{i/j}$ is the angle between the applied stress s and i/j. $\theta_x = \pi/2 - \theta_y$ and vice versa, giving $\cos\theta_y = \sin\theta_x$ and vice versa so that,

$$\begin{aligned} S_{xx} - S_{yy} &= |s|\cos(2\theta_x) \\ S_{xy} &= \frac{|s|}{2}\sin(2\theta_x) \end{aligned} \tag{7.11}$$

where $|s|$ is the magnitude of stress produced by a defect (in this case nitrogen) making an angle θ_x to the x axis of an interstitial and will depend on A, which is some function of the coupling parameters of the nitrogen and the distance, r, between the two.

The simulations produced so far have fixed θ_x at 0 or $\pi/4$ for a given distribution in the magnitude $|s|$. This relation in θ_x (Eqn. 7.11) allows us to consider the effect of a variation in θ or a deviation in the form of the strain field of the $\mathbf{N_S}$ from Eqn. 7.7; the two are hard to separate. If there is a higher concentration of interstitials suffering from strain associated with one value of θ, than that associated with another value of θ, then this may be due to interstitials being produced preferentially in a certain type of strain field, or it may mean that the strain field is not isotropic and so there are more sites around the $\mathbf{N_S}$ suffering that type of strain than would be expected if the $\mathbf{N_S}$ were a spherical point defect. For $\mathbf{N_S}$ with its strong trigonal distortion, Eqn. 7.7 may not be expected to hold but to be more significant along a $\langle 111 \rangle$ type direction resulting in increased xy type strain (a greater $|s|$ for $\theta_x = \pi/4$ than for $\theta_x = 0$).

The range of angles from 0 to $\pi/4$ covers all the possible $x^2 - y^2$ and xy strain scenarios evenly and z does not need to be considered since there is no significant z perturbation of $\mathbf{I}^0_{\langle 001 \rangle}$. The effect of z is confined to a change in r (which affects $|s|$ see Eqn. 7.11 cf Eqn. 7.10) this may be taken account of in the distribution of $|s|$.

The simulation has been extended using Eqn. 7.11 so that θ_x may be stepped through from 0 to $\pi/4$ and its effects summed for various distributions of number of $\mathbf{I}^0_{\langle 001 \rangle}$ with θ. The distribution of number of $\mathbf{I}^0_{\langle 001 \rangle}$ in $|s|$ may also be varied but is left fixed from one value of θ to the next varying only the total number of $\mathbf{I}^0_{\langle 001 \rangle}$ with θ. The results are shown in Fig. 7.15 (using a distribution in $|s|$ similar to that used for the simulations in Figs 7.5 to 7.7, rather than the gaussian distribution used to produce the simulations in Figs 7.9 to 7.14) and clearly show that there is a significant enhancement of xy type strained interstitials over $x^2 - y^2$ strained interstitials in our spectra. It can also be seen, Fig. 7.15, that the presence of some $x^2 - y^2$ strain can produce a magnitude of broad absorption to the lower energy side of the 1859 meV

line, that is not matched on the higher energy side (see Fig. 7.22 further on, for an experimental occurrence of this).

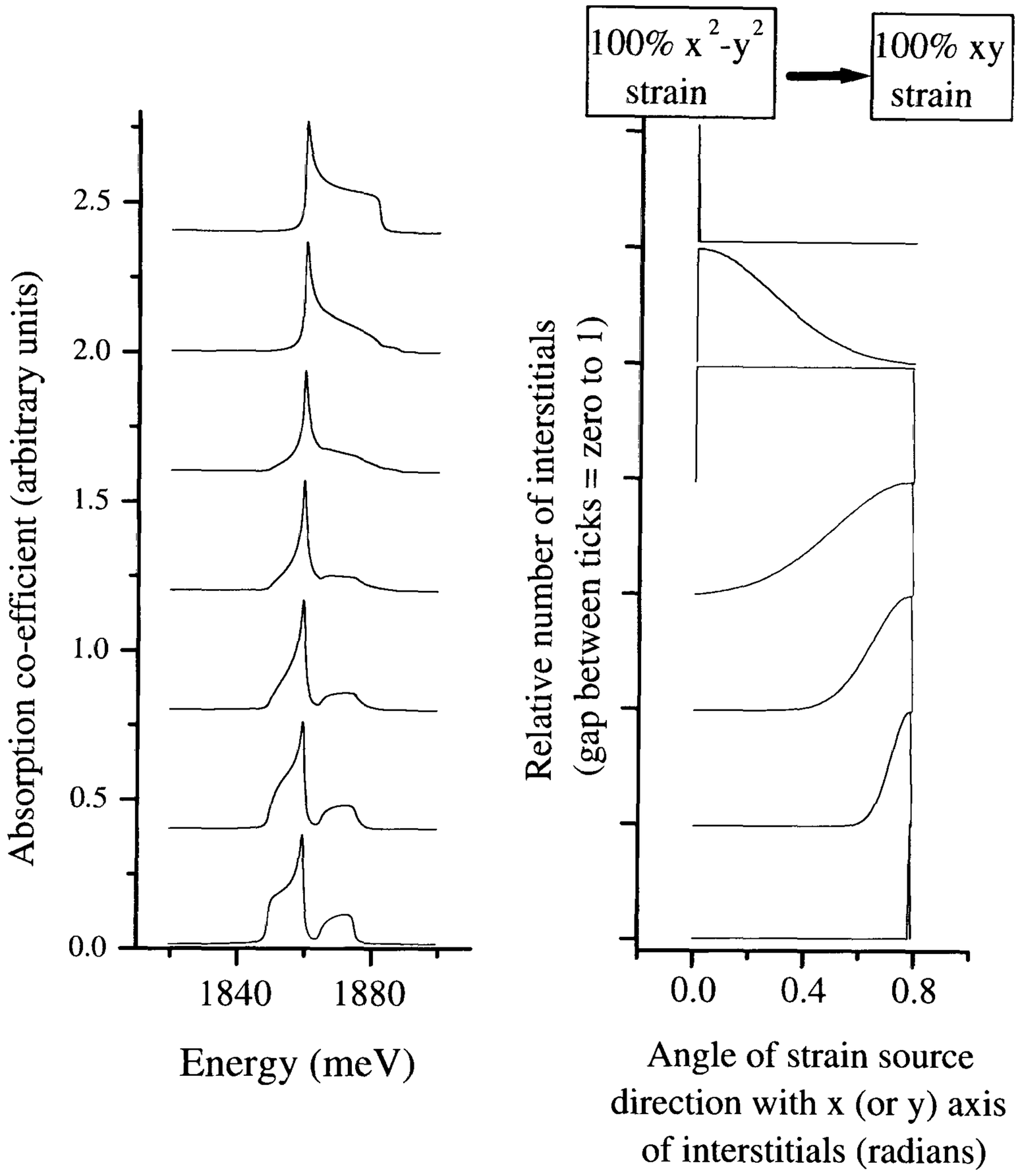

Figure 7.15: LHS: Simulated absorption spectra for $\mathbf{I}^0_{\langle 001 \rangle}$ suffering stress varying in magnitude from 0 to 4 GPa evenly across a population of interstitials i.e. number of interstitials = constant from 0 to 4 GPa and then zero elsewhere. Only the strain type varies from one spectrum to the next as shown on the RHS. Zero corresponds to 100% $x^2 - y^2$ strain, while $\pi/4$ corresponds to 100% xy strain, everything in between represents a mixture varying continuously between the two.

When considering the effects of strain on the interstitials it is worth remembering that nearby nitrogen atoms are unlikely to be the only source. If, as postulated (due to the increase in interstitial and vacancy production rates), the nitrogen acts to prevent correlated recombination, it is likely that the vacancy from which a given interstitial originates is still nearby, certainly nearer than it might be in the absence of the influence of the nitrogen. The strain caused by the vacancy may then have to be taken into account, although total lattice expansion by a vacancy in diamond is generally thought to be negligible [117] so this might not be significant. It is also unclear what the charge state of the nearby nitrogen might be, as discussed in the literature section of this chapter, this is likely to make a big difference to the magnitude and type of strain produced.

7.2.3 The Discrete Lattice

Davies et al [59] estimated the size of A (Eqn. 7.7) for an A centre in diamond to be $A = 1.1 \text{ x } 10^{-31}$ m^3. He defined A as being proportional to the volume change ($\Delta V/V$) of the centre with respect to the pure lattice. Lang et al determined the effective volumes of $\mathbf{N_S}$ and A centres using X-ray diffraction [100]:

$V_N/V_C = 1.35$ and $V_A/V_{C-C} = 1.11$ giving $\Delta V/V$ of 0.35 and 0.11 for $\mathbf{N_S}$ and A centres respectively. A sensible estimate of A (Eqn. 7.7) for $\mathbf{N_S}$ is therefore $A = 1.1$ x 10^{-31} x 0.35 / 0.11 (m^3). The elastic moduli for diamond are [80]: $c_{11} = 1080$ GPa, $c_{12} = 127$ GPa and $c_{44} = 577$ GPa.

With these numbers and Eqn. 7.8 it is now straightforward to estimate the stress in GPa (of whatever type) at any given lattice site resulting from a nearby $\mathbf{N_S}$. This may then be fed directly into the simulation of the last section to determine the effect of the nitrogen on the absorption by an interstitial placed at that site.

The x, y, z co-ordinates of 942 lattice sites reaching out as far as the 36th nearest neighbour, a distance of 1.078 nm, have been calculated and are shown in the Appendix. These give rise to 116 distinctly strained sites; for each of these $x^2 - y^2$ and xy stresses have been calculated in GPa. It is immediately clear from the list, given

the parameters fitted to the data in the last section, that the interstitials cannot be randomly distributed across these sites either as a function of R or type of strain.

A simulation produced from stresses calculated for these discrete sites is shown in Fig. 7.16, overlaid onto two separate experimental spectra for comparison. In producing this simulation a system was devised for weighting the likelihood of a nitrogen being at a given site relative to an interstitial. This consisted of four 'probabilities' that depend on four parameters of a given site and are multiplied to give the total probability for that site, by which the absorption perturbed by the stress at that site was weighted in the simulation. The first parameter is the number of sites suffering identical strain and is determined by the available equivalent sites in the diamond lattice. The remaining three were chosen (by trial and error) as guesses for what the probability might depend on from which we found a good fit; the distributions of probability vs these parameters, was then varied in width and peak position to minimise the least squares fit of the simulation to the data. The sites were weighted in this way, according to the following four parameters;

1. The number of sites suffering the same magnitude and type of strain

2. A gaussian distribution in the probability of an interstitial being created at a site as a function of the magnitude of the $x^2 - y^2$ plus the xy strain at that site. See Fig. 7.17. This assumes that an interstitial is more likely to be created in the strain field of the nitrogen and yet is observed (as an isolated interstitial) only beyond a certain distance from the nitrogen.

3. A decreasing distribution in the probability of an interstitial being created at a site as a function of the square of its z co-ordinate from the nitrogen, see Fig. 7.18. Interstitials ($\langle 100 \rangle$-split) are unperturbed by zz type strains (few are observed unperturbed) and compress the lattice considerably along their z axis, so this distribution assumes that the interstitial would strongly prefer not to orient with its z axis pointing towards the nitrogen strain source.

4. A distribution in the probability of an interstitial being created at a site as

a function of the angle of the direction of the nitrogen strain source to its x or y axis, in other words the ratio of xy to $x^2 - y^2$ type strain, weighted in favour of sites with xy type strain over $x^2 - y^2$ type strain, see Fig. 7.19. This assumes interstitials would rather be created in an xy type strain environment OR compensates for the false assumption of a spherically symmetric nitrogen defect strain source by introducing more xy, $\langle 111 \rangle$ type strain.

The number of interstitials in each of the 116 distinctly strained sites, was weighted according to the product of their relative probabilities of occurring in a particular site, as given by each of these four distributions for that site, see the Appendix.

The resulting simulation (Fig. 7.16) looks plausible. The number of interstitials as a function of distance from the nitrogen is shown in Fig. 7.20, they are a mean distance of 0.72nm from the nitrogen. The available sites are also shown on this figure for comparison of filled to available sites, there is clearly a non-statistical distribution for this assumed strain field.

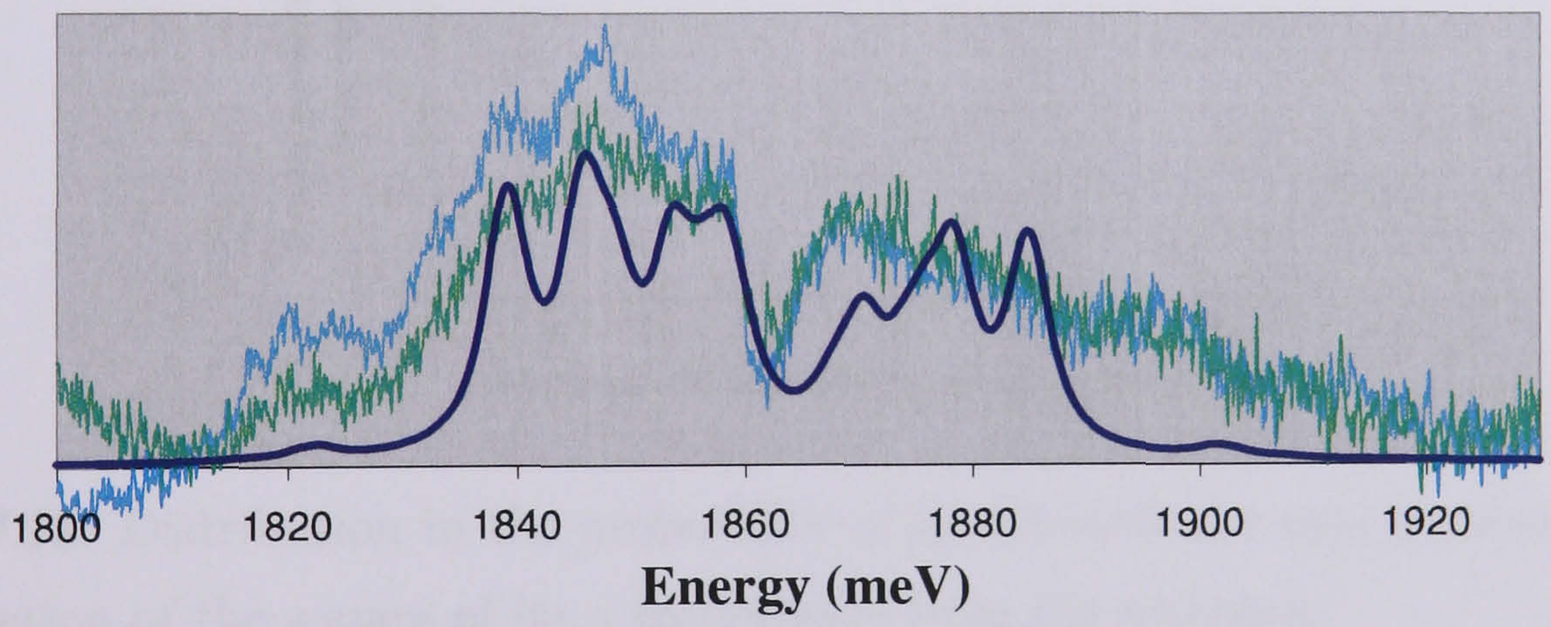

Figure 7.16: A simulation produced from strain calculated for discrete sites overlaid onto two separate experimental spectra for comparison. The sites were weighted according to the four criteria listed in the text.

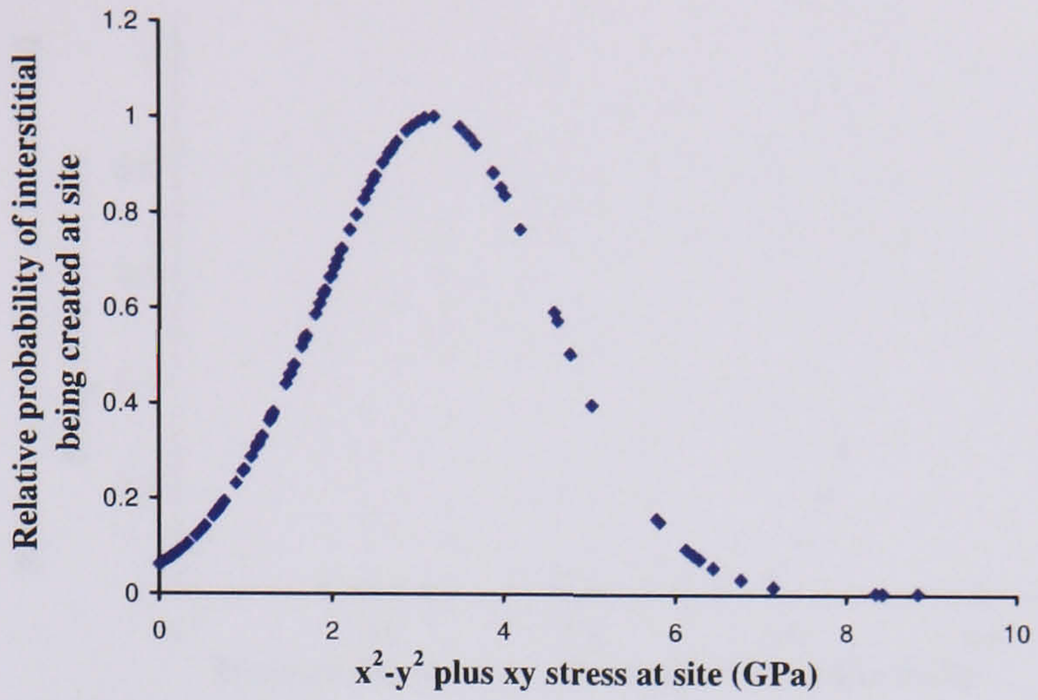

Figure 7.17: Distribution in the probability of an interstitial being created at a site as a function of the magnitude of the $x^2 - y^2$ plus the xy strain at that site.

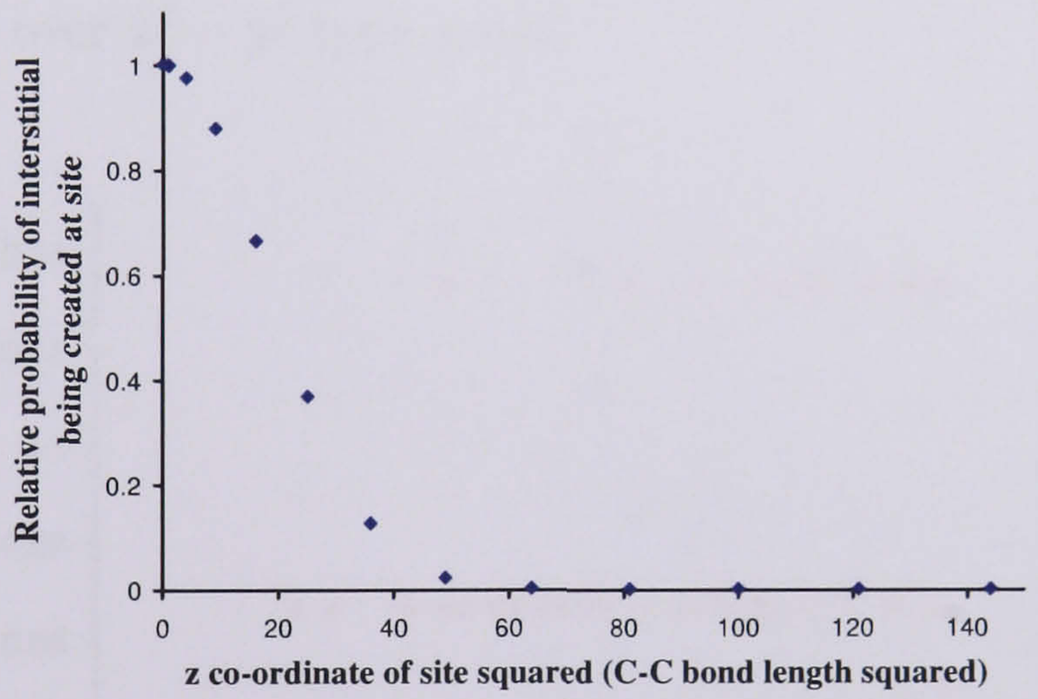

Figure 7.18: Distribution in the probability of an interstitial being created at a site as a function of the square of its z co-ordinate from the nitrogen.

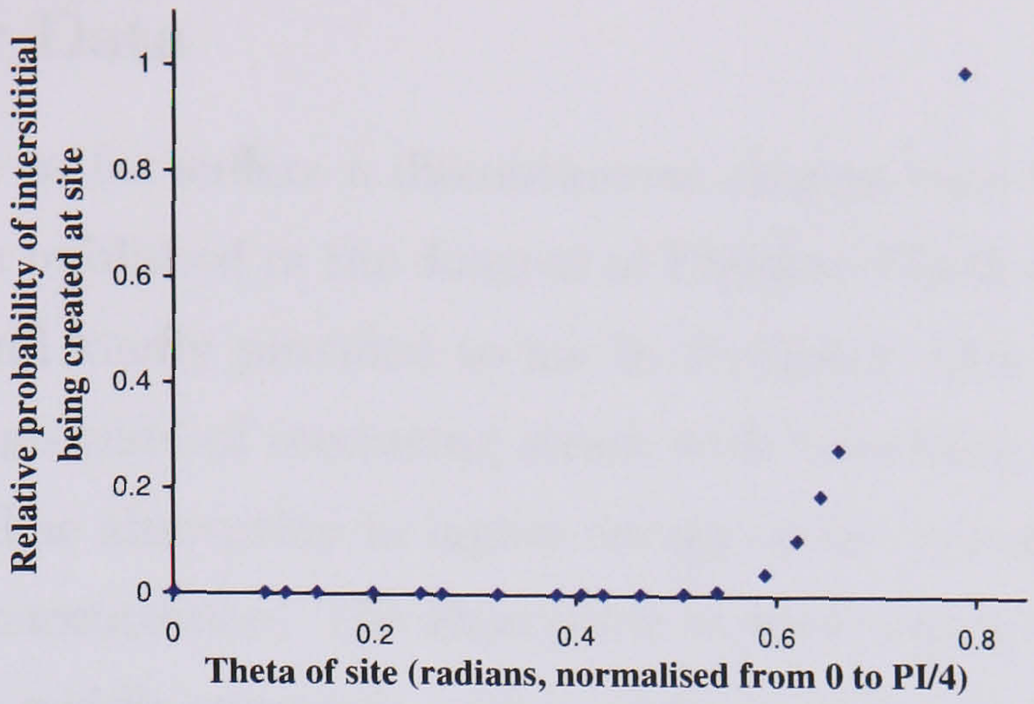

Figure 7.19: Distribution in the probability of an interstitial being created at a site as a function of the angle of the direction of the nitrogen strain source to its x or y axis, in other words the ratio of xy to $x^2 - y^2$ type strain, weighted in favour of sites with xy type strain over $x^2 - y^2$ type strain.

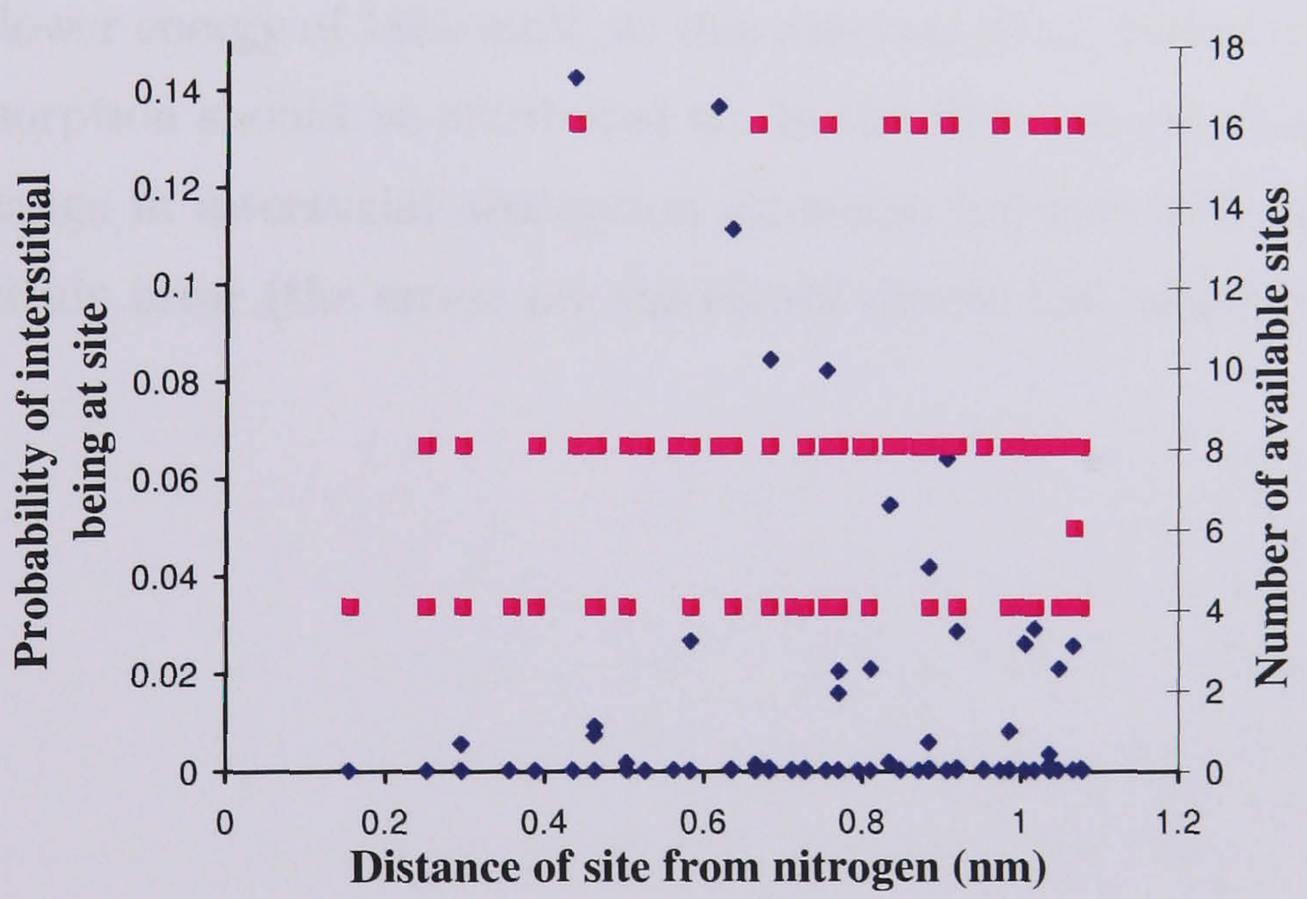

Figure 7.20: Blue diamonds: (left hand y axis) The number of interstitials as a function of distance from the nitrogen, they are a mean distance of 0.72nm from the nitrogen. Pink squares: (right hand y axis) number of available sites for the interstitials as a function of distance from the nitrogen.

7.2.4 Further Data

The data presented so far suffers a discontinuous change between 10 and 100 ppm of nitrogen. Spectra published in the Journal of Physics: Condensed Matter (Collins and Dahwich [2]) and kindly provided to me by Professor Alan Collins, fill the gap showing a clear progression of increasing strain with increasing nitrogen concentration, see Fig. 7.21. The absorption to higher energy of the 'trough' increases steadily with the nitrogen concentration. The absorption to lower energy of 1859 meV seems to be highest in the middle spectrum, which seems to have a higher total interstitial absorption than the highest nitrogen spectrum. This may suggest that interstitial production increases with nitrogen concentration, then, after a point, decreases, perhaps as an equilibrium is reached between increased interstitials produced due to the nitrogen and increased interstitials trapped at the nitrogen. Unfortunately, the presence of the GR1 sideband (albeit reduced and broadened) in the region of the absorption to lower energy of 1859 meV, at this concentration, makes it unclear which defect this absorption should be attributed to. In the data presented in this chapter, there is no change in interstitial absorption intensity, between 100 and 500 ppm of nitrogen, to within error (the errors are significant due to the subjective baseline).

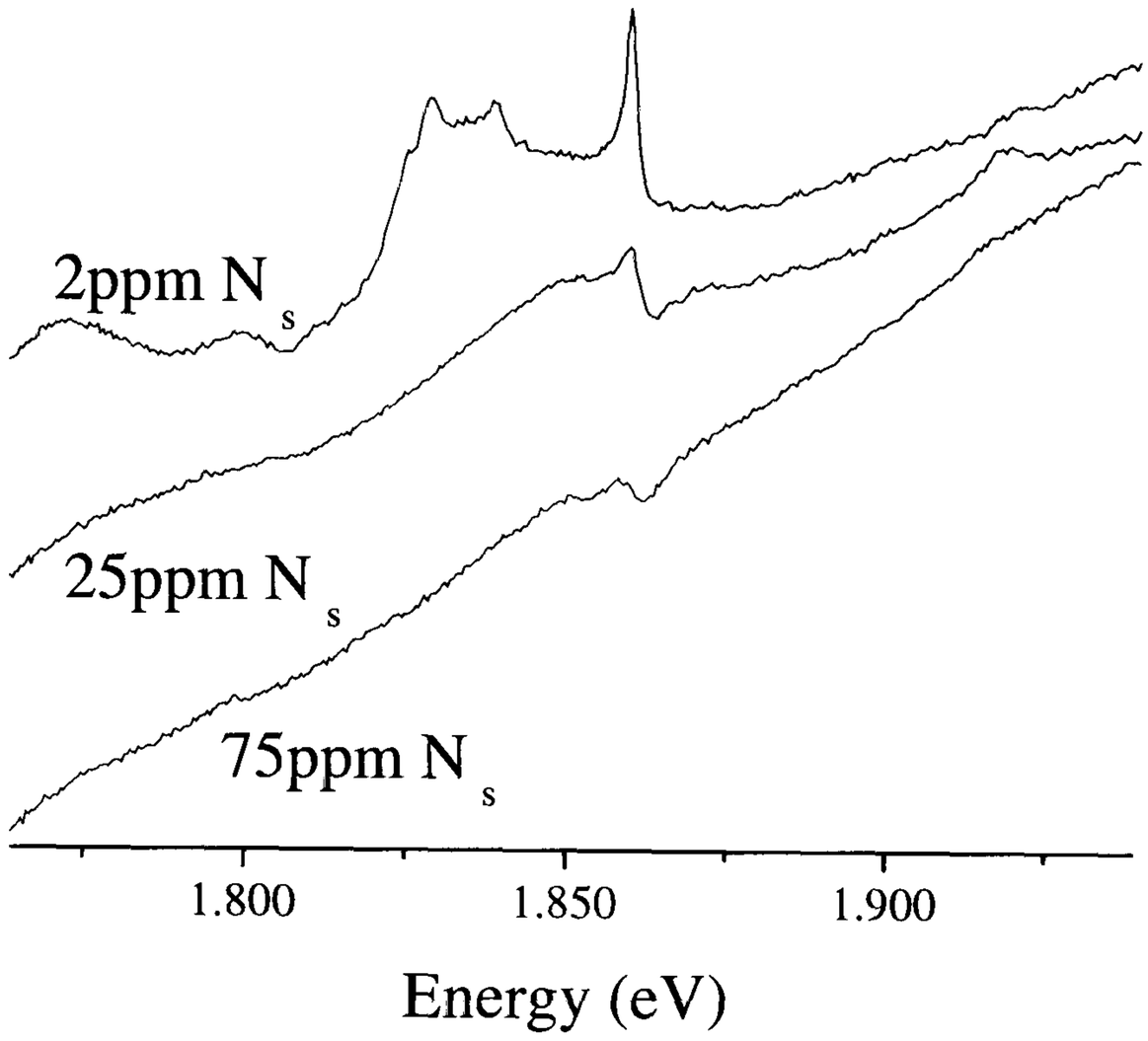

Figure 7.21: Interstitial absorption in irradiated Ib diamond of varying N_S concentration kindly provided by Alan Collins (Collins and Dahwich [2]).

More interesting still is the result of Collins and Dahwich [2] that the 1859 meV line anneals in when irradiated Ib diamond is annealed, this is corroborated and illustrated by data kindly provided to me by Konstantin Iakoubovskii [3] on the annealing progression, of spectra of two irradiated high nitrogen Ib samples, see Figs 7.23 and 7.22. The 'negative' feature is observed in the as irradiated material, but with increasing temperature of anneal the breadth of the absorption to lower energy of the step reduces and the 1859 meV appears and sharpens. Most significantly the intensity of absorption due to unstrained interstitials increases, even the 1685 meV line appears with annealing, until temperatures are reached where all interstitials begin to anneal out. These spectra show that although the majority of interstitials are highly strained in as irradiated material, there is room for them to move to unstrained sections of material and their shape corresponds to a narrowing and shift towards zero of the stress distribution used in the models of the previous sections.

Again, from the absorption to lower energy of 1859 meV (if this may be attributed

to the interstitials) it seems that the concentration of interstitials increases slightly in the middle spectrum. If this is real, it indicates that the total number of 'isolated' interstitials does increase with annealing, perhaps through their release from nitrogen-interstitial complexes. In any case, it is important to note from the data of this chapter that, although the 1859 meV peak is small, as irradiated, there are many more 'isolated' interstitials present in Ib than in equally treated IIa diamond, this will be discussed in the next section. These interstitials are heavily strained and move away from the nitrogen with annealing.

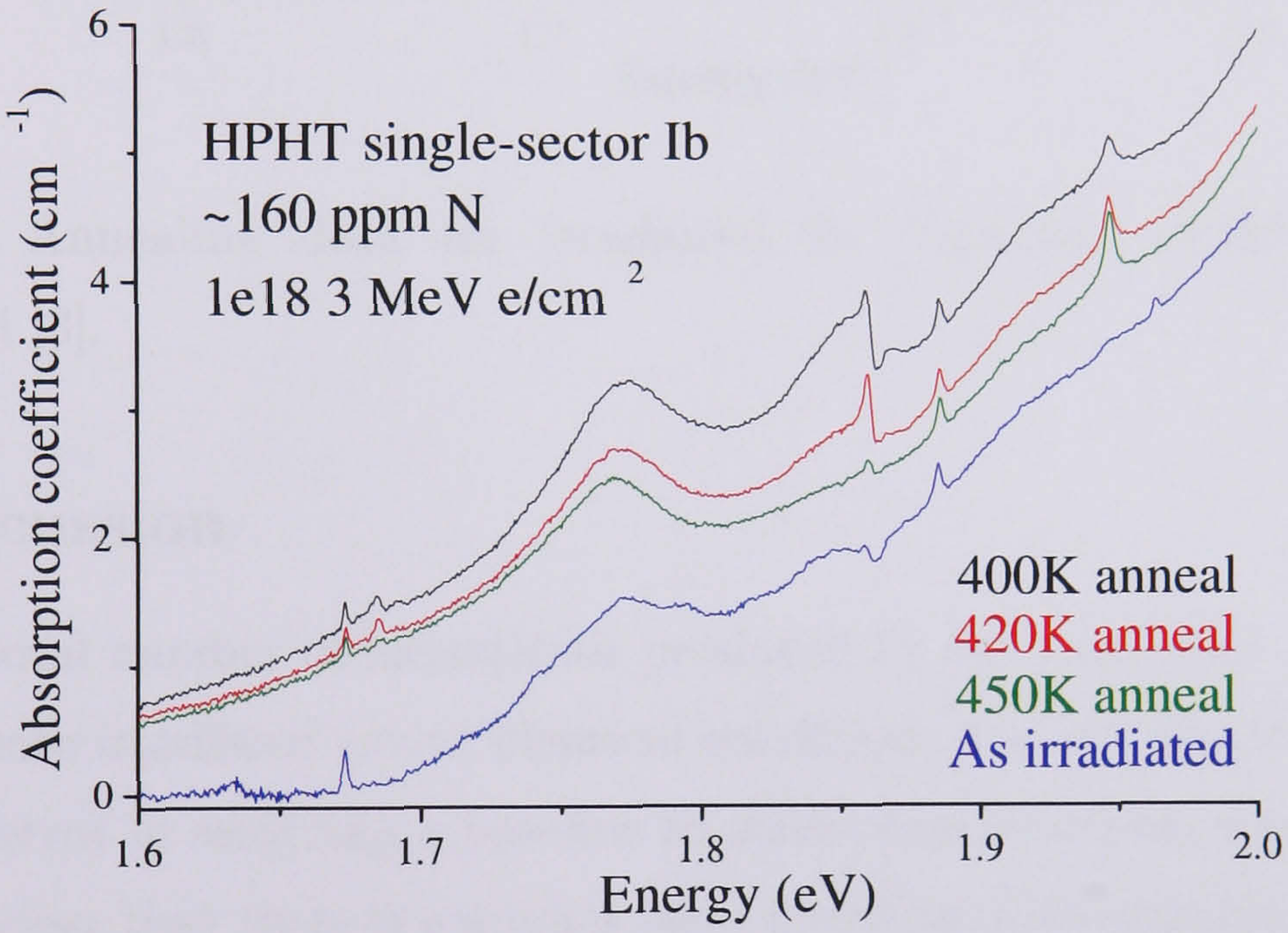

Figure 7.22: Annealing data for irradiated Ib diamond, kindly provided by K.Iakoubovskii [3].

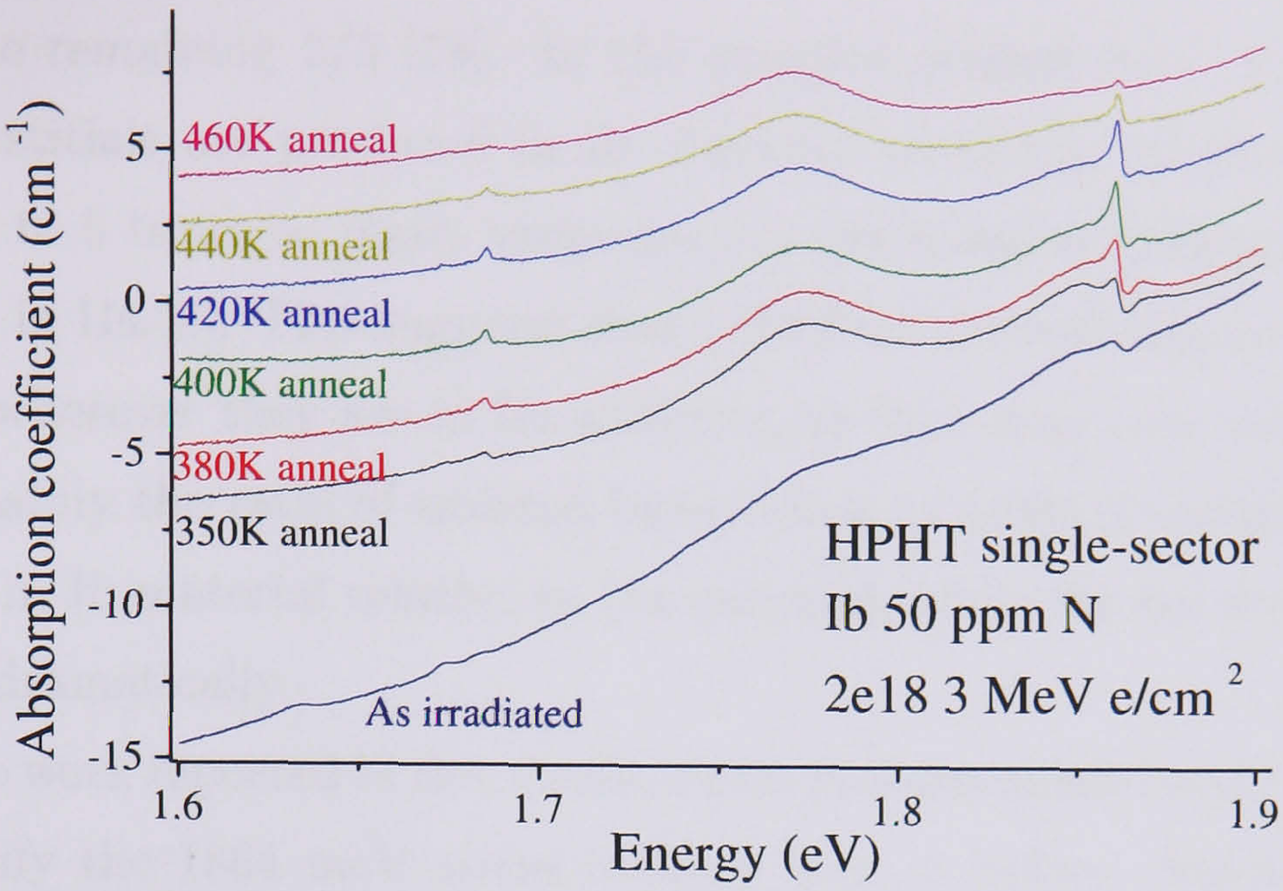

Figure 7.23: Annealing data for irradiated Ib diamond, kindly provided by K.Iakoubovskii [3].

7.2.5 Discussion

Consider the total number of interstitials produced by the irradiation, the 8 samples studied here were irradiated under identical conditions and yet despite the considerable room for error in assigning a baseline to absorption by strained interstitials (see Fig. 7.8), it is clear that there is a greater total intensity of absorption by interstitials in the high nitrogen material, than in the low nitrogen material, where they are easily measured from the sharp line. All this suggests that perhaps interstitials are preferentially created or suffer less correlated recombination during irradiation, within the local strain field of single substitutional nitrogen, but that they may be persuaded to move away from these traps, with a lower activation energy than is required for their mobility in unstrained diamond. Although they are found near to the nitrogen after irradiation in greater numbers than elsewhere, the interstitials therefore prefer not to be trapped at or near to the nitrogen.

In IIa diamond irradiated at room temperature it is known that 1/3 as many isolated neutral interstitials are produced as vacancies [71, 79]. It is not known what

happens to the remaining 2/3 [79]. In the samples studied here, 5 times as many 'isolated' interstitials are produced in Ib diamond as in IIa. Collins and Dahwich found that up to 5 times as many vacancies are produced in (300 ppm of nitrogen) Ib diamond as in IIa [2]. This suggests that 2/3 of the interstitials are still 'missing'. They may be wherever they are in IIa material, or they may now be trapped at the nitrogen. Certainly the ratio of isolated interstitials to isolated vacancies appears to be unchanged in Ib material relative to IIa material, while the total number of each has increased dramatically.

Prior to the work reported in this thesis, stress measurements on the self-interstitial failed to identify the 1864 meV stress induced line, so before obtaining the results of Chapter 5, identifying and quantifying heavily strained interstitials in Ib diamond would have been very difficult. It is clear that where there is a source of considerable strain present measurement of the peak intensity at 1859 meV is insufficient to quantify the number of $\mathbf{I}^0_{\langle 001 \rangle}$ that are present. Most of the $\mathbf{I}^0_{\langle 001 \rangle}$ present are heavily distorted, indicating a significant mixing of their states, this may have a profound effect on their epr signal, or even cause it to be absent at the more distorted centres. Epr may, therefore, be equally unreliable in determining the concentration of R2 centres in these samples.

Previously it has been implied from the apparent reduction in interstitial production in Ib diamond, that at room temperature there may be a stable negatively charged interstitials present, courtesy of the nitrogen donor, that are being missed. But no optical absorption or epr centres have been identified with a negatively charged self-interstitial. This new data suggests that the damage production data may be understood without requiring a negatively charged interstitial. This existence or otherwise of a stable negatively charged interstitial could perhaps be proven by determining and comparing the ND1 and $\mathbf{N}^+_S$ concentrations independently in a high nitrogen Ib diamond, where a negatively charged interstitial should be observed, unless it is unsuccessfully competing with the vacancy to capture the charge.

That the 1859 meV line anneals in when irradiated Ib diamond is annealed, [2], [3],

indicates that although the majority of interstitials are highly strained in as irradiated material (shown by our data), there is room for them to move to unstrained sections of material and that $\mathbf{I}^0_{\langle 001 \rangle}$ prefer to move away from the nitrogen and do so with an activation energy that is lower than for the motion of $\mathbf{I}^0_{\langle 001 \rangle}$ in unstrained material. Vacancies on the other hand are readily trapped by nitrogen [103], more so nitrogen in single substitutional form than as A centres [30]. The factor concerned (a factor of 20 or 8, see literature section) for $\mathbf{N_S}$ vs A centres, is higher than the difference in strain between these centres, suggesting electrostatic attraction plays a role in this. In any case, there is a clear mechanism for the influence of nitrogen on the ability of vacancies and interstitials to separate and it is reasonable that this effect should be greater in type Ib diamond than in type Ia. All this demonstrates clearly that $\mathbf{I}^0_{\langle 001 \rangle}$ suffer considerably less correlated recombination with vacancies during irradiation within the local strain field (although maybe not due to it) of single substitutional nitrogen.

Armed with this new information on interstitials, there are many options for further work to try to clarify the situation. Homogeneity is an issue at low nitrogen concentrations, it is possible that all the absorption at 1859 meV could be coming from regions without nitrogen present, so it would be helpful to determine better the dependence on local concentration, perhaps using some sort of imaging. It would be interesting to irradiate Ib diamond cold, to see how the strain profile and concentration of interstitials changes, when there is expected to be no recombination enhanced diffusion of the interstitials during the irradiation. Further annealing studies may be useful, especially if they encompass all the relevant defects (highlighted in Section 7.1) quantitatively alongside the interstitial and its newly determined perturbation profile.

It's possible that the strain at the vacancy /interstitial is from the interstitial /vacancy nearby, due to a reduction in correlated recombination creating little separated interstitial - vacancy pairs. The lattice expansion due to an interstitial is 20 times more than due to an A centre [117]. If correlated recombination is reduced by the presence of the nitrogen and it has been shown here that the interstitials remain

isolated, then the vacancies and interstitials are likely to be very near to one another and the vacancy is likely to be heavily strained by the interstitial, more so than by the nitrogen. Lattice expansion by a vacancy is thought to be negligible [117], so the dominant influence on the interstitial is still expected to be the nitrogen.

The reduction in correlated recombination may be due to the influence of the $\mathbf{N_S}$ on charge state. It will be much less in type Ia because A centres have less of an effect, but still significant because many $\mathbf{N_S}$ will still be present. Irradiating samples under uniaxial stress may help to identify the effect of the magnitude and type of strain on interstitial and vacancy production, to establish if strain is the cause of the enhanced production.

7.3 Summary

Neutral isolated self-interstitial production in diamond is enhanced by as much as a factor of 5 in the vicinity of single substitutional nitrogen (mean 0.72nm away). The interstitials in this material are almost all highly strained and produce an absorption spectrum of a very different form to that in pure diamond. The concentration of these interstitials and their strain profile are readily determined from the resulting spectrum, the absorption is characterised by a step down in absorption at 1859 meV followed by a gentle rise very few meV to higher energy and otherwise consists of broad absorption tens of meV wide. Care must therefore be taken in determining the presence and quantity of $\mathbf{I}^0_{\langle 001\rangle}$ in Ib diamond using optical spectroscopy and even epr, where the traditional signal is also likely to be heavily altered or even absent.

Chapter 8

Conclusions

The stress splitting at the GR1 as determined by Davies and Penchina [1] has been reproduced and successfully used as a standard to calibrate stresses applied to diamond, resulting in the self-consistent measured stress response at other centres.

The $\langle 001 \rangle$ split interstitial consists of two principal atoms sharing a lattice site split along $\langle 001 \rangle$ [28]. In its ground state, on the timescale of optical measurements, this configuration has its highest possible symmetry (D_{2d}). This means that on average, each of the two bonds made to nearest neighbours by each of the two principal atoms has the same length and makes the same angle to the crystal axes. This configuration is distorted dynamically to lower D_2 or to C_{2v} symmetries in its ground and excited states respectively, by one or the other of two distinct vibrations of the centre. These vibrations are between equivalent distortions so the higher (D_{2d}) symmetry is observed on average. The energy of $\mathbf{I}^0_{\langle 001 \rangle}$ is lowered by the distortion significantly and this process occurs even for zero point vibrations.

Along its [001] principal axis, $\mathbf{I}^0_{\langle 001 \rangle}$ exhibits a 'hard' response to stress and is hardly perturbed to first order by stresses from any direction; the energy levels of $\mathbf{I}^0_{\langle 001 \rangle}$ are only perturbed appreciably when it is distorted by a second order perturbation. $\mathbf{I}^0_{\langle 001 \rangle}$ is readily distorted to the lower D_2 or C_{2v} symmetries by very little strain ($\sim$6 meV GPa^{-1}) making the defect soft to these two particular distortions. Vibrations produce instantaneous strains orders of magnitude greater than those applied in these

experiments so this demonstrates the power of vibrations of the correct symmetry to produce distortions of $\mathbf{I}^0_{\langle 001\rangle}$ and lower its energy.

The external strains applied in these experiments may also be very small compared to local perturbations that are present within the lattice. It has been demonstrated that under a perturbing strain, forbidden transitions are induced at $\mathbf{I}^0_{\langle 001\rangle}$ producing two types of interdependent features in the spectrum. Transitions are induced from the ground state of $\mathbf{I}^0_{\langle 001\rangle}$ at 1864(+) meV by $\langle 110\rangle$ directed shear type strains and at 1692(+) meV by $\langle 100\rangle$ directed $x^2 - y^2$ type strains (distortions to C_{2v} symmetry and to D_2 symmetry respectively, where the + indicates that the energy increases with increasing strain). In a highly strained environment these distortions lower the energy of $\mathbf{I}^0_{\langle 001\rangle}$. Any broadening of the 1859 meV line to lower energy produced by xy type strain, must be matched by a corresponding feature with an onset at 1864 meV, extending to higher energy and any broadening of the 1859 meV line to higher energy, produced by an $x^2 - y^2$ type strain, must be accompanied by a corresponding feature extending to higher energy of 1692 meV.

In Ib diamonds containing a high concentration of single substitutional nitrogen, a broad feature is observed in the absorption spectrum with a dip in the middle, consisting of a step down at 1859 meV and a gentle rise at 1864 meV. This dip may be the only clearly discernable feature in this region and has been identified with the presence of highly strained $\mathbf{I}^0_{\langle 001\rangle}$. This feature is observed even in the absence if a resolved line at 1685 or 1859 meV, so in nitrogen containing diamond there may be a considerable concentration of interstitials present, without its characteristic absorption lines at 1859 and 1685 meV being observed.

The results of Chapter 5, have been used to simulate the effect of strain on the absorption by $\mathbf{I}^0_{\langle 001\rangle}$, the result fits well to the data. The integrity of the fit comes from our ability to use the stress and temperature dependence parameters determined in this thesis, for the 1685 and 1859 meV absorption lines to produce a simulation, whose only variable is the strain distribution, that can convincingly fit the interdependent features of the spectrum using a reasonable distribution of strain. Previous stress

measurements on the 1859 meV line [51] failed to identify the 1864 meV stress induced line, which forms the high energy wall of the trough, so before obtaining the results of this work, identifying and quantifying heavily strained interstitials in Ib diamond would have been very difficult.

Fitting simulations to the data clearly show an enhancement in $\mathbf{I}^0_{\langle 001\rangle}$ concentration in Ib diamond over IIa diamond irradiated under the same conditions. The enhancement is by a factor of about 5, much greater than the enhancement reported in IaA material [59]. That the 1859 meV line anneals in when irradiated Ib diamond is annealed, [2], [3], indicates that although the majority of interstitials are highly strained in as irradiated material (shown by our data), there is room for them to move to unstrained sections of material. All this demonstrates clearly that $\mathbf{I}^0_{\langle 001\rangle}$ suffer considerably less correlated recombination with vacancies during irradiation, in the presence of single substitutional nitrogen and end up, non-statistically distributed, within the local strain field of the nitrogen.

The apparent reduction in $\mathbf{I}^0_{\langle 001\rangle}$ production in Ib diamond, judged by the intensity of the 1859 meV absorption line, has indicated that there may be stable negatively charged interstitials present, courtesy of the nitrogen donor, that are being missed (unseen). But no optical absorption or epr centres have been identified with a negatively charged self-interstitial. This new data suggests that the damage production data may be understood without requiring a negatively charged interstitial.

This identification of strained $\mathbf{I}^0_{\langle 001\rangle}$ has implications for sample characterisation and defect reaction studies. Since $\mathbf{I}^0_{\langle 001\rangle}$ was identified, many studies of its production and interactions have relied upon identifying its concentration via the intensity of the 1859 meV peak in optical absorption. This work has shown that in some samples this may give a considerable underestimate. The dimensions of this newly identified feature, may also now be used to characterise the distribution and type of strains experienced by $\mathbf{I}^0_{\langle 001\rangle}$ in a sample, so that its local environment may be studied more fully. This provides a new tool for identifying the roles of $\mathbf{I}^0_{\langle 001\rangle}$ and $\mathbf{V}^0$ in defect processes.

Identifying other forms of the interstitial may be similarly useful. This work has confirmed, without the requirement for a coincidence in parameters, that the 3H defect has C_{2v} symmetry with a $\langle 110 \rangle$ dipole, re-enforcing the result of Walker [29]. The stress parameters give the response to perturbation, these are small compared to those at vacancy related centres in diamond showing that the defect gives a 'hard' response to stress and adding to evidence that this is an interstitial related centre. The configuration of the 3H defect, however, remains controversial and is likely to be no less so for this confirmation of 30 year old results!

8.1 Further Work

In the nitrogen study, homogeneity was an issue at low nitrogen concentrations, it is possible that all the absorption at 1859 meV could be coming from regions without nitrogen present, so it would be helpful to determine better the dependence on local concentration by using more local measurements.

It would be interesting to irradiate Ib diamond cold, to see how the strain profile and concentration of interstitials changes, when there is expected to be no exciton recombination enhanced diffusion of the interstitials. Irradiating samples under uniaxial stress may help to identify the effect of the magnitude and type of strain on interstitial and vacancy production.

Further annealing studies of irradiated Ib diamond may be useful in the light of these new discoveries, to encompass all the relevant defects quantitatively, alongside the interstitial and its perturbation profile. Annealing the samples used here, isothermally, may help to compare the number of interstitials, vacancies and nitrogen-interstitial / nitrogen-vacancy complexes annealing out (or in) fast, with those annealing more slowly and changes in their strain profiles with annealing. It would be helpful to know more about the role of the charge state of the nitrogen and vacancy as well as the strain. Measuring epr under uniaxial stress would be useful in identifying the impact of Ib character on the R2 signal.

Appendix

x	y	z	R(nm)	nn	xx-yy	xy	no. sites	Sxx-Syy (GPa)	Sxy (GPa)	Weighting
1	1	1	0.154	1	0	1	4	0.00	165.88	0.0000
2	2	0	0.251	2	0	4	4	0.00	57.14	0.0000
2	0	2	0.251	2	4	0	8	94.38	0.00	0.0000
1	1	-3	0.295	3	0	1	4	0.00	6.44	0.0054
3	1	-1	0.295	3	8	3	8	85.14	19.33	0.0000
4	0	0	0.356	4	16	0	4	66.73	0.00	0.0000
3	3	1	0.388	5	0	9	4	0.00	14.79	0.0000
3	1	3	0.388	5	8	3	8	21.71	4.93	0.0000
2	2	4	0.436	6	0	4	8	0.00	3.67	0.1429
4	2	2	0.436	6	12	8	16	18.16	7.33	0.0000
1	1	5	0.462	7	0	1	4	0.00	0.68	0.0073
3	3	-3	0.462	7	0	9	4	0.00	6.14	0.0091
5	1	1	0.462	7	24	5	8	27.06	3.41	0.0000
4	4	0	0.503	8	0	16	4	0.00	7.14	0.0015
4	0	4	0.503	8	16	0	8	11.80	0.00	0.0000
5	3	-1	0.526	9	16	15	8	9.43	5.35	0.0000
5	1	-3	0.526	9	24	5	8	14.14	1.78	0.0000
3	1	-5	0.526	9	8	3	8	4.71	1.07	0.0000
6	2	0	0.562	10	32	12	8	13.51	3.07	0.0000
2	0	6	0.562	10	4	0	8	1.69	0.00	0.0000
6	0	2	0.562	10	36	0	8	15.19	0.00	0.0000

Figure 8.1: List (part 1/3) of 942 (first 36 nearest neighbours) lattice sites surrounding an interstitial. The co-ordinates 'x', 'y' and 'z' represent displacement of the site along the direction of the x, y and z local axes of the interstitial respectively and are scaled such that 1, 1, 1 represents the standard C-C bond in diamond. 'R' represents the shortest distance from the interstitial to the site in nm and 'nn' stands for nearest neighbour, 'nn' = 5 for example represents sites that are the 5th nearest neighbour to the interstitial, of all the sites in terms of 'R'. The number of sites with similar 'x', 'y' and 'z' and identical $xx-yy$ and xy are listed under 'no. sites' and the stress of $xx-yy$ and xy types are listed under 'Sxx-Syy' and 'Sxy' respectively, as experienced by the interstitial, originating from a $\mathbf{N_S}$ placed at the listed site. There are 116 distinctly strained sites. Finally the 'weighting' column shows the relative number of $\mathbf{N_S}$ found at the site used to plot the simulation shown in Fig. 7.16 of Chapter 7 and calculated according to the model described in the text of Section 7.2.2.

x	y	z	R(nm)	nn	xx-yy	xy	no. sites	Sxx-Syy (GPa)	Sxy (GPa)	Weighting
3	3	5	0.583	11	0	9	4	0.00	1.92	0.0267
5	3	3	0.583	11	16	15	8	5.64	3.20	0.0000
4	4	4	0.616	12	0	16	8	0.00	2.59	0.1370
1	1	-7	0.635	13	0	1	4	0.00	0.14	0.0002
5	5	1	0.635	13	0	25	4	0.00	3.48	0.1116
7	1	-1	0.635	13	48	7	8	11.04	0.97	0.0000
5	1	5	0.635	13	24	5	8	5.52	0.70	0.0000
6	4	2	0.665	14	20	24	16	3.64	2.64	0.0013
6	2	4	0.665	14	32	12	16	5.82	1.32	0.0000
4	2	6	0.665	14	12	8	16	2.18	0.88	0.0000
5	5	-3	0.683	15	0	25	4	0.00	2.42	0.0847
7	3	1	0.683	15	40	21	8	6.39	2.03	0.0000
5	3	-5	0.683	15	16	15	8	2.56	1.45	0.0005
7	1	3	0.683	15	48	7	8	7.67	0.68	0.0000
3	1	7	0.683	15	8	3	8	1.28	0.29	0.0000
8	0	0	0.711	16	64	0	4	8.34	0.00	0.0000
3	3	-7	0.728	17	0	9	4	0.00	0.63	0.0004
7	3	-3	0.728	17	40	21	8	4.65	1.48	0.0000
2	2	8	0.754	18	0	4	8	0.00	0.24	0.0000
6	6	0	0.754	18	0	36	4	0.00	2.12	0.0825
8	2	2	0.754	18	60	16	16	5.83	0.94	0.0000
6	0	6	0.754	18	36	0	8	3.50	0.00	0.0000
5	-5	-5	0.770	19	0	-25	4	0.00	1.33	0.0159
7	5	-1	0.770	19	24	35	8	2.10	1.86	0.0204
7	1	-5	0.770	19	48	7	8	4.21	0.37	0.0000
5	1	-7	0.770	19	24	5	8	2.10	0.27	0.0000
8	4	0	0.795	20	48	32	8	3.58	1.45	0.0000
4	0	8	0.795	20	16	0	8	1.19	0.00	0.0000
8	0	4	0.795	20	64	0	8	4.78	0.00	0.0000
1	1	9	0.810	21	0	1	4	0.00	0.04	0.0000
7	5	3	0.810	21	24	35	8	1.63	1.44	0.0210
7	3	5	0.810	21	40	21	8	2.72	0.87	0.0000
5	3	7	0.810	21	16	15	8	1.09	0.62	0.0000
9	1	1	0.810	21	80	9	8	5.44	0.37	0.0000
6	6	4	0.834	22	0	36	8	0.00	1.28	0.0547
6	4	6	0.834	22	20	24	16	1.18	0.85	0.0016
9	3	-1	0.848	23	72	27	8	3.89	0.88	0.0000
9	1	-3	0.848	23	80	9	8	4.33	0.29	0.0000
3	1	-9	0.848	23	8	3	8	0.43	0.10	0.0000
4	4	8	0.871	24	0	16	8	0.00	0.46	0.0000
8	4	4	0.871	24	48	32	16	2.27	0.92	0.0001
3	3	9	0.885	25	0	9	4	0.00	0.24	0.0000
5	5	-7	0.885	25	0	25	4	0.00	0.66	0.0004
7	7	1	0.885	25	0	49	4	0.00	1.30	0.0419
7	5	-5	0.885	25	24	35	8	1.05	0.93	0.0058
9	3	3	0.885	25	72	27	8	3.15	0.72	0.0000
7	1	7	0.885	25	48	7	8	2.10	0.19	0.0000
8	6	2	0.907	26	28	48	16	1.08	1.13	0.0643
10	2	0	0.907	26	96	20	8	3.72	0.47	0.0000
8	2	6	0.907	26	60	16	16	2.32	0.38	0.0000
6	2	8	0.907	26	32	12	16	1.24	0.28	0.0000
2	0	10	0.907	26	4	0	8	0.15	0.00	0.0000
10	0	2	0.907	26	100	0	8	3.87	0.00	0.0000
7	7	-3	0.920	27	0	49	4	0.00	1.07	0.0286
9	5	1	0.920	27	56	45	8	2.02	0.98	0.0004
7	3	-7	0.920	27	40	21	8	1.44	0.46	0.0000
9	1	5	0.920	27	80	9	8	2.89	0.20	0.0000
5	1	9	0.920	27	24	5	8	0.87	0.11	0.0000
9	5	-3	0.953	28	56	45	8	1.69	0.82	0.0003
9	3	-5	0.953	28	72	27	8	2.17	0.49	0.0000
5	3	-9	0.953	28	16	15	8	0.48	0.27	0.0000
10	4	2	0.974	29	84	40	16	2.27	0.66	0.0000
10	2	4	0.974	29	96	20	16	2.60	0.33	0.0000
4	2	10	0.974	29	12	8	16	0.32	0.13	0.0000
1	1	-11	0.986	30	0	1	4	0.00	0.02	0.0000
7	7	5	0.986	30	0	49	4	0.00	0.76	0.0080
7	5	7	0.986	30	24	35	8	0.61	0.54	0.0002
8	8	0	1.006	31	0	64	4	0.00	0.89	0.0262
8	0	8	1.006	31	64	0	8	1.47	0.00	0.0000

Figure 8.2: List (part 2/3) of 942 lattice sites surrounding an interstitial.

x	y	z	R(nm)	nn	xx-yy	xy	no. sites	Sxx-Syy (GPa)	Sxy (GPa)	Weighting
5	5	9	1.018	32	0	25	4	0.00	0.33	0.0000
9	7	-1	1.018	32	32	63	8	0.70	0.83	0.0292
9	5	5	1.018	32	56	45	8	1.22	0.59	0.0001
11	3	1	1.018	32	112	33	8	2.44	0.43	0.0000
11	1	3	1.018	32	120	11	16	2.61	0.14	0.0000
9	1	-7	1.018	32	80	9	8	1.74	0.12	0.0000
7	1	-9	1.018	32	48	7	8	1.04	0.09	0.0000
3	1	11	1.018	32	8	3	8	0.17	0.04	0.0000
6	6	8	1.037	33	0	36	8	0.00	0.43	0.0000
10	6	0	1.037	33	64	60	8	1.27	0.72	0.0011
8	6	6	1.037	33	28	48	16	0.55	0.58	0.0033
6	0	10	1.037	33	36	0	8	0.71	0.00	0.0000
10	0	6	1.037	33	100	0	8	1.98	0.00	0.0000
3	3	-11	1.048	34	0	9	4	0.00	0.10	0.0000
9	7	3	1.048	34	32	63	8	0.60	0.72	0.0209
11	3	-3	1.048	34	112	33	8	2.10	0.37	0.0000
9	3	7	1.048	34	72	27	8	1.35	0.31	0.0000
7	3	9	1.048	34	40	21	8	0.75	0.24	0.0000
0	0	12	1.067	35	0	0	6	0.00	0.00	0.0000
8	8	4	1.067	35	0	64	8	0.00	0.67	0.0256
8	4	8	1.067	35	48	32	16	0.82	0.33	0.0000
12	0	0	1.067	35	144	0	4	2.47	0.00	0.0000
7	7	-7	1.078	36	0	49	4	0.00	0.48	0.0003
11	5	-1	1.078	36	96	55	8	1.56	0.54	0.0000
11	1	-5	1.078	36	120	11	8	1.96	0.11	0.0000
5	1	-11	1.078	36	24	5	8	0.39	0.05	0.0000
						sum =	942			

Figure 8.3: List (part 3/3) of 942 lattice sites surrounding an interstitial.

Bibliography

[1] G Davies and C M Penchina. *Proc. R. Soc. Lond. A.*, 338:359–374, 1974.

[2] A T Collins and Ahmad Dahwich. *J. Phys.: Condens. Matter, Letter to the editor*, 15:L591–L596, 2003.

[3] K Iakoubovskii and A Stesmans. *Physical Review B*, 66:045406, 2002.

[4] W A Bassett F P Bundy, M S Weathers, R J Hemley, H K Mao, and A F Goncharov. *Carbon*, 34:141–153, 1996.

[5] R C Burns, J O Hansen, R A Spits, M Sibanda, C M Welbourn, and D L Welch. *Diamond and Related Materials*, 8:14331437, 1999.

[6] S C Lawson and H Kanda. *Journal of Applied Physics*, 73:3967, 1992.

[7] Devashish Choudhary and Jayesh Bellare. *Ceramics International*, 26:73–85, 2000.

[8] P May. *Phil. Trans. R. Soc. Lond.*, 358:473–495, 2000.

[9] S Tong Leea, Zhangda Linb, and Xin Jiangc. *Materials Science and Engineering*, 25:123–154, 1999.

[10] Alix Gicquel, Khaled Hassouni, Francois Silva, and Jocelyn Achard. *Current Applied Physics*, 1:479–496, 2001.

[11] S E Coe and R S Sussmann. *Diamond and Related Materials*, 9:1726–1729, 2000.

[12] R Sauer. *Cryst. Res. Technol.*, 34:227–241, 1999.

[13] H.A. Naseem A.P. Malshe W.D. Brown, R.A. Beera. *Surface and Coatings Technology*, 86-87:698–707, 1996.

[14] M N Touzelbaev and K E Goodson. *Diamond and Related Materials*, 7:1–14, 1998.

[15] S Koizumi, M Kamo, Y Sato, S Mita, A Sawabe, A Reznik, C Uzan-Saguy, and R Kalish. *Dia. and Rel. Mat.*, 7:540–544, 1998.

[16] S Koizumi, K Watanabe, M Hasegawa, and H Kanda. *Science*, 292:1899–1902, 2001.

[17] J Isberg, J Hammersberg, E Johansson andT Wikstrom, D J Twitchen, A J Whitehead, S E Coe, and G A Scarsbrook. *Science*, 297:1670–1672, 2002.

[18] P R Chalker. *Thin Solid Films*, 343-344:616–622, 1999.

[19] Stefan K.Estreicher. *Materials Today*, June:26–35, 2003.

[20] Ties Behnke, Alexander Oh, Albrecht Wagner, Wolfram Zeuner, Andrea Bluhm, Claus-Peter Klages, Mario Paul, and Lothar Schafer. *Diamond and Related Materials*, 7:1553–1557, 1998.

[21] W Adam, E Berdermann, P Bergonzo, G Bertuccio, F Bogani, E Borchi, A Brambilla, M Bruzzi, C Colledani, J Conway, P Dangelo, W Dabrowski, P Delpierre, A Deneuville, W Dulinski, B van Eijk, A Fallo Pirollo, P Polesello, M Procario, J L Riester, S Roe, L Rousseau, F Fizzotti, F Foulon, M Fried, K K Gan, E Gheeraert, E Grigoriev, G Hallewell, S Han, F Hartjes, J Hrubec,

D Husson, H Kagan, D Kania, J Kaplon, C Karl, R Kass, M Krammer, A Logiudice, R Lu, C Manfredotti, D Meier, M Mishina, L Moroni, A Oh, L S Pan, M Pernicka, A Peitz, A Rudge, J Russ, S Sala, M Sampietro, S Schnetzer, S Sciortino, H Stelzer, R Stone, B Suter, R J Tapper, R Tesarek, M Trawick, W Trischuk, D Tromson, E Vittone, A M Walsh, R Wedenig, P Weilhammer, C White, W Zeuner, M Zoeller, A Fenyvesi, J Molnar, and D Sohler. *Nuclear Instruments and Methods in Physics Research A*, 434:131–250, 1999.

[22] W Adam, E Berdermann, P Bergonzo, G Bertuccio, F Bogani, E Borchi, A Brambilla, M Bruzzi, C Colledani, J Conway, P Dangelo, W Dabrowski, P Delpierre, A Deneuville, W Dulinski, B van Eijk, A Fallo Pirollo, P Polesello, M Procario, J L Riester, S Roe, L Rousseau, F Fizzotti, F Foulon, M Fried, K K Gan, E Gheeraert, E Grigoriev, G Hallewell, S Han, F Hartjes, J Hrubec, D Husson, H Kagan, D Kania, J Kaplon, C Karl, R Kass, M Krammer, A Logiudice, R Lu, C Manfredotti, D Meier, M Mishina, L Moroni, A Oh, L S Pan, M Pernicka, A Peitz, A Rudge, J Russ, S Sala, M Sampietro, S Schnetzer, S Sciortino, H Stelzer, R Stone, B Suter, R J Tapper, R Tesarek, M Trawick, W Trischuk, D Tromson, E Vittone, A M Walsh, R Wedenig, P Weilhammer, C White, W Zeuner, M Zoeller, A Fenyvesi, J Molnar, and D Sohler. *Nuclear Instruments and Methods in Physics Research A*, 447:244–250, 2000.

[23] S Prawer. *Diamond and Related Materials*, 4:862–872, 1995.

[24] Rafi Kalish. *Applied Surface Science*, 117/118:558–569, 1998.

[25] A T Collins. *Dia. And Rel. Mat.*, In Press, 2003.

[26] G D Watkins. *phys. stat. sol. (a)*, 186:167–176, 2001.

[27] E C Reynhardt and G L High. *Progress in Nuclear Magnetic Resonance Spectroscopy*, 38:37–81, 2001.

[28] D C Hunt, D J Twitchen, M E Newton, J M Baker, T R Anthony, W F Banzoler, and S S Vagarli. *Phys. Rev. B*, 61:3863, 2000.

[29] J Walker. *J. Phys. C: Solid state Phys.*, 10:3867, 1977.

[30] Gordon Davies. *Physica B*, 273-274:15–23, 1999.

[31] A T Collins, G Davies, and G S Woods. *J. Phys. C*, 21:1363–1376, 1988.

[32] G Davies. *Rep. Prog. Phys.*, 44:788–830, 1981.

[33] G. Davies, H Nazare, and M F Hamer. *Proc. R. Soc. Lond. A.*, 351:245–265, 1976.

[34] V A Nadolinny, A P Yelisseyev, J M Baker, D J Twitchen, M E Newton, B N Feigelson, and O P Yuryeva. *Diamond and Related Materials*, 9:883, 2000.

[35] D Fisher and S C Lawson. *Diamond Related Materials*, 7:299, 1998.

[36] I Kiflawi, H Kanda, and A Mainwood. *Diamond Related Materials*, 7:327, 1998.

[37] C D Clark and J Walker. *Proc. R. Soc. Lond. A.*, 334:241–257, 1973.

[38] G Davies. *Semiconductors and Semimetals*, 51B:chapter 1, 1998.

[39] Gary J Hawkins. *PhD Thesis, Reading*, 1998.

[40] K Mohammed, G Davies, and A T Collins. *J. Phys. C: Solid State Phys.*, 15:2779–2788, 1982.

[41] A A Kaplyanskii. *Optika i Spectroskopija*, 16:1031–1044, 1964.

[42] A A Kaplyanskii. *Optika i Spectroskopija*, 16:602–614, 1964.

[43] P W Atkins. *Molecular Quantum Mechanics, Oxford University Press*, Second Edition:349, 1983.

[44] edited by R Berman. *Physical Properties of Diamond, Oxford.*

[45] private communication Gordon Davies.

[46] J P Goss. *Thesis University of Exeter*, 1997.

[47] G Davies, H Smith, and H.Kanda. *Phys. Rev. B*, 62:1528, 2000.

[48] M J Neves M H Nazare and G Davies. *Phys. Rev. B*, 43:14196, 1991.

[49] Khalid Mohammed. *PhD Thesis, King's College London*, 1982.

[50] J R Hook and H E Hall. *Solid State Physics*, Second Edition:122, 1991.

[51] J Walker. *Rep. Prog. Phys.*, 42:1605, 1979.

[52] group theory lecture notes Gordon Davies.

[53] PerkinElmer Website. *http://www.perkinelmer.com/*, 1998-2004.

[54] W V Smith, P P Sorokin, L L Gelles, and G J Lasher. *Phys. Rev*, 115:1546, 1959.

[55] J A van Wyk, O D Tucker, M E Newton, J M Baker, G S Woods, and P Spear. *Phys. Rev B*, 52:12657, 1995.

[56] J Isoya, H Kanda, Y Uchida, S C Lawson, S Yamaski, H Itoh, and Y Morita. *Phys Rev B*, 45:1436, 1992.

[57] A Pu, T Bretagnon, D Kerr, and S Dannefaer. *Diamond and Related Materials*, 9:1450–1463, 2000.

[58] D J Twitchen, D C Hunt, V Smart, M E Newton, and J M Baker. *Diamond and Related Materials*, 8:1572–1575, 1999.

[59] G Davies, S C Lawson, A T Collins, A Mainwood, and S J Sharp. *Phys Rev B*, 46:13157, 1992.

[60] J Walker, L A Vermeulen, and C D Clark. *Proceedings of the Royal Society of London Series A Mathematical and Physical Sciences*, 341:252–266, 1974.

[61] J E Field. *The Properties of Natural and Synthetic Diamond, 2nd ed., Academic Press*, 1992.

[62] C Weigel, D Peak, J W Corbett, G D Watkins, and R P Messmer. *Phys. Rev. B*, 8:2906, 1973.

[63] J C Bourgoin and J W Corbett. *Physics Letters A*, 38 number 2:135–137, 1972.

[64] A Mainwood, F P Larkins, and A M Stoneham. *Solid State Electronics*, 21:1431–1433, 1978.

[65] S J Breuer and P R Briddon. *Phys. Rev. B*, 51:p6984, 1995.

[66] L H Li and J E Lowther. *J. Phys. Chem Solids*, 58:1607–1610, 1997.

[67] D Saada, J Adler, and R Kalish. *International Journal of modern physics C*, 9:61–69, 1998.

[68] J P Goss, R Jones, T D Shaw, M J Rayson, and P R Briddon. *Phys. Stat. Sol*, 186:215–220, 2001.

[69] J P Goss, B J Coomer, R Jones, T D Shaw, P R Briddon, M Rayson, and S Oberg. *Phys. Rev. B*, 63:195208, 2001.

[70] L Allers, A T Collins, and J Hiscock. *Diamond and Related Materials*, 7:228–232, 1998.

[71] M E Newton, B A Campbell, D J Twitchen, J M Baker, and T R Anthony. *Diamond and Related Materials*, 11:618–622, 2002.

[72] D C Hunt. *DPhil Thesis, Oxford*, 1999.

[73] C D Clark and J Walker. *Diamond Research*, 1:975–995, 1972.

[74] G Davies. *Phd Thesis, King's College London*, 1970.

[75] L W Song and G D Watkins. *Phys. Rev B*, 42:5759, 1990.

[76] X D Zhan and G D Watkins. *Phys. Rev B*, 47:6363–6380, 1993.

[77] J Kulda, B Darner, B Roessli, H Sterner, R Bauer, Th May, K Karch, P Pavone, and D Strauch. *Solid State Communications*, 99:799–802, 1996.

[78] A Mainwood, A T Collins, and P Woad. *Mater. Sci Forum*, 29:143–147, 1994.

[79] G Davies, B Campbell, A Mainwood, M Newton, M Watkins, H Kanda, and T R Anthony. *Phys. Stat sol. (a)*, 186:187–198, 2001.

[80] R Vogelgesang, A K Ramdas, S Rodriguez, M Grims-ditch, and T Anthony. *Phys. Rev. B*, 54:3989, 1996.

[81] J Walker. *Inst. Phys. Conf. Ser.*, 23:chapter 4 p317, 1975.

[82] G Davies. *Proc. R. Soc. Lond. A.*, 336:507–523, 1974.

[83] I I Vlasov, V G Ralchenko, and E Goovaerts. *Phys. Stat. Sol. (a)*, 193:489493, 2002.

[84] J W Steeds, S Charles, T J Davis, A Gilmore, J Hayes, D Pickard, and J E Butler. *Diamond and Related Materials*, 8:94100, 1999.

[85] J W Steeds, T J Davis, S J Charles, J M Hayes, and J E Butler. *Diamond and Related Materials*, 8:1847–1852, 1999.

[86] D J Twitchen, M E Newton, J M Baker, T R Anthony, and W F Banholzer. *J. Phys: Condens. Matter*, 13:2045–2051, 2001.

[87] J P Goss, B J Coomer, R Jones, T D Shaw, P R Briddon, M Rayson, and S Oberg. *Diamond and Related Materials*, 10:434–438, 2001.

[88] D J Twitchen, M E Newton, J M Baker, O D Tucker, T R Anthony, and W F Banholzer. *Physical Review B*, 54:6988, 1996.

[89] J P Goss, R Jones, M I Heggie, C P Ewels, P R Briddon, and S Oberg. *Phys Rev B*, 65:115207, 2002.

[90] I I Vlasov, V G Ralchenko, and V I Konov. *Phys. Stat. Sol. (a)*, 186:221, 2001.

[91] A A Kaplyanskii. *Opt. Spectros.*, 16:329–37, 1964.

[92] Damian C Hunt Simon C Lawson, David Fisher and Mark E Newton. *J. Phys. Condens. Matter*, 10:6171–6180, 1998.

[93] Zengdu Qi Trevor Evans and Jacqueline Maguire. *J . Phys. C : Solid State Phys., Letter to the editor*, 14:L379–L384, 1981.

[94] I Kiflawi and Bruley. *Diamond and Related Materials*, 9:87, 2000.

[95] edited J E Field T Evans. *The Properties of Natural and Synthetic Diamond, Academic Press*, chapter 6, 1992.

[96] I Kiflawi, A Mainwood, H Kanda, and D Fisher. *Physical Review B*, 54:16719, 1996.

[97] C A J Ammerlaan and E A Burgemeister. *Physical Review Letters*, 47:954–957, 1981.

[98] R G Farrer. *Solid State Commun.*, 7:685, 1969.

[99] L A Vermeulen and R G Farrer. *Diamond Research*, pages 18–23, 1975.

[100] G Pang A R Lang. *Philosophical Transactions: Mathematical, Physical and Engineering Sciences*, 356:1397–1419, 1998.

[101] A P W Makepeace W Wierzchowski C M Welbourn A R Lang, M Moore. *Philosophical Transactions: Physical and Engineering Sciences*, 337:497–520, 1991.

[102] private communication M E Newton.

[103] A T Collins. *J. Phys. C: Solid St. Phys.*, 13:2641–50, 1980.

[104] Y Mita. *Physical Review B*, 53:11360, 1996.

[105] G Davies and M F Hamer. *Proceedings of the Royal Society of London, Series A, Mathematical and Physical Sciences*, 348:285–298, 1976.

[106] G Davies. *J . Phys. C: Solid St. Phys*, 5:2534–42, 1972.

[107] A T Collins S C Lawson, Gordon Davies and A Mainwood. *J. Phys. Condens. Matter*, 4:3439–3452, 1992.

[108] Konstantin Iakoubovskii and Guy J Adriaenssens. *J. Phys.: Condens. Matter*, 13:60156018, 2001.

[109] K Iakoubovskii, I Kiflawi, K Johnston, A Collins, G Davies, and A Stesmans. *Physica B*, 340-342:67–75, 2003.

[110] G Davies. *Nature*, 269:498–500, 1977.

[111] Alan T Collins. *J. Phys.: Condens. Matter*, 14:37433750, 2002.

[112] A T Collins and S Rafique. *Proc. R. Soc. Lond. A.*, 367:81–97, 1979.

[113] J E Lowther and J A van Wyk. *Phys Rev B*, 49:11010, 1994.

[114] G A Watt, M E Newton, and J M Baker. *Diamond and Related Materials*, 10:1681–1683, 2001.

[115] D J Twitchen. *D. Phil. Thesis, University of Oxford*, 1997.

[116] G Davies. *J . Phys. C: Solid State Phys.*, 3:2474, 1970.

[117] R Jones J P Goss and P R Briddon. *Phys. Rev. B*, 65:035203, 2001.